Fully Kinetic Simulations of Microscale Turbulence in Space and Astrophysical Plasmas

Daniel Grošelj

München 2018

Fully Kinetic Simulations of Microscale Turbulence in Space and Astrophysical Plasmas

Daniel Grošelj

Dissertation
an der Fakultät für Physik
der Ludwig–Maximilians–Universität
München

vorgelegt von
Daniel Grošelj
aus Lafayette, USA

München, den 28.11.2018

Erstgutachter: Prof. Dr. Hartmut Zohm
Zweitgutachter: Prof. Dr. Jörg Büchner
Tag der mündlichen Prüfung: 11. Januar 2019

Contents

Zusammenfassung **viii**

Abstract **ix**

1 Introduction **1**
1.1 Turbulence in astrophysical plasmas 2
1.2 The solar wind 3
1.3 Scope of this Thesis 5

2 Kinetic modeling and simulation of weakly collisional plasmas **7**
2.1 The Vlasov-Maxwell system 7
2.2 The PIC fully kinetic simulation method 11
2.2.1 Overview of the numerical scheme 11
2.2.2 Discrete particle effects and noise in PIC simulations 13
2.3 Reduced-kinetic models 16
2.3.1 Hybrid model with kinetic ions and fluid electrons 17
2.3.2 Gyrokinetics 18
2.3.3 Kinetic reduced electron heating model (KREHM) 21

3 The phenomenology of astrophysical plasma turbulence **23**
3.1 Kolmogorov's approach to turbulence 23
3.2 MHD range theories 27
3.2.1 Goldreich-Sridhar '95: The critical balance conjecture 29
3.2.2 A remark on GS95: The local character of the anisotropy 31
3.2.3 Boldyrev '06: Dynamic alignment 31
3.3 The kinetic range: Kinetic Alfvén wave turbulence 35
3.3.1 Electron reduced MHD 36
3.3.2 Remarks on the ERMHD model 40
3.3.3 Spectral scaling predictions 43
3.3.4 Prior evidence in support of KAW turbulence 46
3.3.5 Alternatives to the KAW turbulence phenomenology 49

4 Turbulence simulations with OSIRIS **53**
4.1 Code overview . . . 53
4.2 Problem-specific performance tests . . . 54
4.3 Design of the physical simulation setup . . . 56
4.4 Choice of numerical parameters . . . 60

5 Comparison of kinetic models in collisionless plasma turbulence **65**
5.1 Problem description and simulation setup . . . 66
5.2 Results . . . 68
5.2.1 Spatial field structure and intermittency . . . 69
5.2.2 Global energy budget . . . 72
5.2.3 Spectral features . . . 75
5.2.4 Non-thermal fluctuations in the particle distribution function . . . 79
5.3 Summary and conclusions . . . 81

6 3D fully kinetic study of kinetic Alfvén turbulence **85**
6.1 Simulation details . . . 86
6.2 Results . . . 87
6.2.1 Spatio-temporal evolution . . . 87
6.2.2 Turbulent spectra and spectral ratios . . . 88
6.2.3 Local scale-dependent anisotropy . . . 90
6.2.4 Impact of cross-helicity on the sub-ion scale turbulence . . . 93
6.2.5 Lagrangian particle statistics . . . 94
6.3 Summary and conclusions . . . 99

7 Kinetic turbulence in astrophysical plasmas: waves and/or structures? **101**
7.1 Methods . . . 102
7.1.1 Driven 3D fully kinetic simulation . . . 102
7.1.2 Spacecraft data . . . 104
7.1.3 Wavelet scale decomposition . . . 105
7.1.4 Generalized field ratios . . . 107
7.2 Results . . . 108
7.2.1 Scale-dependent flatness . . . 110
7.2.2 Spatial field structure and local wavelet spectra . . . 111
7.2.3 Wavelet cross coherence . . . 113
7.2.4 Spectral field ratios of the large-amplitude structures . . . 114
7.3 Discussion . . . 115
7.4 Summary . . . 118

8 Conclusions **121**
8.1 Summary . . . 121
8.2 Outlook . . . 123

A An initial condition for decaying 3D turbulence simulations 127

B External turbulence forcing implementation in OSIRIS 131

C List of plasma parameters 135

Bibliography 137

Acknowledgements 165

Zusammenfassung

Turbulenz ist der natürliche Zustand vieler Weltraum und astrophysikalischen Plasmen mit geringer Stoßfrequenz. Bekannte Beispiele sind der erdnahe Sonnenwind, sowie auch weiter entfernte astrophysikalische Systeme wie das warme interstellare Medium, heiße Akkretionsscheiben und Galaxienhaufen. In turbulenten Plasmen mit geringer Stoßfrequenz wird theoretisch angenommen, was auch durch Beobachtungen dokumentiert ist, dass sich die elektromagnetische Energiekaskade jenseits des magnetohydrodynamischen Inertialbereichs auf kinetische Plasmaskalen ausweitet. Beim Übergang in den kinetischen Bereich, unterhalb des Ionengyroradius und der Ionen-Skintiefe, werden die Eigenschaften der Turbulenz im Vergleich zu der magnetohydrodynamischen Turbulenz wesentlich verändert. Die Natur der Turbulenz auf kinetischen Skalen wird derzeit aktiv erforscht, mit wichtigen Folgen für die allgemeinen thermodynamischen Eigenschaften von Plasmen mit geringer Stoßfrequenz.

In der vorliegenden Dissertation werden grundlegende numerische Untersuchungen von Mikroskalen-Turbulenzen im Weltraum und astrophysikalischen Plasmen durchgeführt. Dies umfasst eine Reihe von getriebenen und zerfallenden elektromagnetischen Turbulenzsimulationen in zwei und drei räumlichen Dimensionen. Die dreidimensionalen Turbulenzsimulationen mit vollkinetischen Ionen und Elektronen sind unter den ersten ihrer Art in diesem Bereich. Unsere Ergebnisse werden detailliert mit vereinfachten reduziert-kinetischen Modellen, bestehenden Theorien und Daten aus dem Weltall verglichen, damit die Schlüsselprozesse, die die Entwicklung des komplexen vollkinetischen turbulenten Systems beeinflussen, klar identifiziert werden können.

Unsere Hauptergebnisse beinhalten Folgendes. Wir führen einen direkten Vergleich von vollkinetischen, gyrokinetischen und hybrid-kinetischen Modellen in einem zweidimensionalen turbulenten Aufbau durch. Im Vergleich mit gyrokinetischen Ergebnissen zeigen wir, dass die turbulenten Fluktuationen im Falle von typischen Sonnenwindparametern den Charakter von kinetischen Alfvén-Wellen besitzen. Außerdem heben wir die Stärken und Beschränkungen von reduzierten kinetischen Modellen hervor. Insbesondere quantifizieren wir die Auswirkungen von Effekten kinetischer Elektronen auf turbulente Spektren auf Sub-Ionenskalen und den Einfluss von Fluktuationen mit endlichen Amplituden auf die Ionenheizung. Danach präsentieren wir eine Reihe von dreidimensionalen massiv-parallelen vollkinetischen Simulationen. Mit Hilfe dieser Simulationen demonstrieren wir die natürliche Entwicklung von Plasma-Turbulenz auf Sub-Ionenskalen, in Abstimmung mit der häufig diskutierten Phänomenologie der kinetischen Alfvén-Wellen-Turbulenz. Schließlich bestimmen wir eine Reihe von neuen diagnostischen Maßnahmen und wir analysieren kinetische Simulationsdaten sowie *in situ* Beobachtungsdaten, um den Zusammenhang zwischen wellenförmigen Eigenschaften und der Formierung von turbulenten Stukturen auf kinetischen Skalen von Weltraumplasmen zu erforschen. Die dreidimensionale kinetische Simulation stimmt gut mit Daten von Raumsonden überein und unsere neuen diagnostischen Maßnahmen zeigen, dass die turbulenten Strukturen mit hohen Amplituden selbst Zeichen linearer Wellen aufweisen. Unsere Ergebnisse fördern das theoretische Verständnis von Mikroskalen-Turbulenzen im Weltraum und astrophysikalischen Plasmen mit geringer Stoßfrequenz und bringen Licht in die derzeit stattfindenden Debatten in diesem Bereich.

Abstract

Turbulence is the natural state of many weakly collisional space and astrophysical plasmas. Prominent examples range from the near-Earth solar wind, to more distant astrophysical systems such as the warm interstellar medium, hot accretion flows, and galaxy clusters. In low-collisionality turbulent plasmas, it is anticipated theoretically and documented observationally that the electromagnetic energy cascade extends beyond the inertial, magnetohydrodynamic range into the plasma kinetic range of scales. Upon transition into the kinetic range, below the ion gyroradius and the ion inertial scale, the character of the turbulence changes significantly compared to the magnetohydrodynamic turbulence. The nature of this kinetic-scale turbulence is presently the subject of ongoing investigations, with important implications for the general thermodynamic properties of weakly collisional plasmas.

In this Thesis, we perform first principles numerical investigations of microscale space and astrophysical plasma turbulence. This includes a set of forced and decaying electromagnetic turbulence simulations, in both two and three spatial dimensions. The three-dimensional turbulence simulations with fully kinetic ions and electrons are among the first of their kind in this field. Our results are compared in detail with simplified reduced-kinetic models, existing theories, and spacecraft observations in order to clearly identify the key physical processes that govern the evolution of the complex fully kinetic turbulent system.

Our main results include the following. We carry out a direct comparison of the fully kinetic, gyrokinetic and hybrid-kinetic models in a turbulent, two-dimensional setup. Via comparison with gyrokinetic results, we show that the turbulent fluctuations are predominantly of kinetic Alfvén wave type for typical solar wind parameters. We also highlight the strengths and limits of reduced-kinetic approximations. In particular, we quantify the impact of electron kinetic effects on the sub-ion range turbulent spectra and the influence of finite-amplitude fluctuations on bulk ion heating. Next, we present a set of three-dimensional, massively parallel fully kinetic turbulence simulations. In terms of three-dimensional simulations, we demonstrate the natural development of sub-ion scale plasma turbulence, consistent with the frequently debated phenomenology of kinetic Alfvén wave turbulence. Finally, we define a set of novel diagnostic measures and we jointly analyze kinetic simulation and *in situ* observational data to study the relation between wavelike properties and structure formation in kinetic range space plasma turbulence. The three-dimensional kinetic turbulence simulation yields favorable agreement with spacecraft measurements and our new diagnostic measures show that the large-amplitude turbulent structures themselves carry a linear wave signature. Our results facilitate a progress in the theoretical understanding of microscale turbulence in weakly collisional space and astrophysical plasmas and shed light on some of the ongoing debates in the field.

Chapter 1

Introduction

We are all familiar with turbulence from our experience with fluid motion in everyday life. Intuitively, we are aware that turbulence can be easily created by an instability or an external force, leading to the development of fine velocity structures over a broad range of scales. While the seemingly unpredictable evolution of turbulent fluid flows is yet to be fully understood, it is well known that the sharp spatial variations of the velocity field are ultimately smeared out by molecular viscosity, and it is for this reason that the swirling motion of the fluid eventually dissipates and comes to rest. But imagine instead turbulence in an ionized gas—a plasma. Contrary to turbulence in regular fluids, electromagnetic phenomena, accompanied by a large variety of waves, play a crucial role in plasma turbulence [1, 2]. Moreover, many natural plasmas are hot and diffuse, meaning that they are weakly collisional. In low-collisionality plasmas, the turbulent energy cascade is able to reach the microscopic kinetic scales, where a fluid description breaks down and a kinetic approach has to be used instead. In the latter case, it is not at all obvious how the turbulent motions evolve and dissipate at the plasma microscales.

The majority of baryonic matter in the Universe is in the form of a plasma. Many of these astrophysical plasmas are inherently turbulent. Due to its ubiquitous presence, plasma turbulence is believed to play an important role in the evolution of magnetic fields, which permeate the Universe, and in the transport of energetic particles, heat, and momentum. However, straightforward theoretical analysis has proven difficult due to the immense complexity of turbulent interactions between fields and particles, especially in weakly collisional regimes. For this reason, high-performance plasma simulations have become an indispensable tool in the area, alongside theoretical and observational efforts. In this Thesis we present a series of such simulations, with main application to kinetic-scale turbulence in the solar wind. Below, we explain some of the main motivations for this work based on a set of examples from the field.

1.1 Turbulence in astrophysical plasmas

Astrophysical plasma turbulence is involved in a variety of fundamental processes, including bulk ion and electron heating [3–8], non-thermal particle acceleration [9], magnetic field generation by dynamo action [10–12], and magnetic reconnection [13–16]. The above-mentioned phenomena govern the conversion between different forms of energy. For instance, bulk heating and non-thermal particle acceleration convert the energy of the turbulent fields into internal (both thermal and non-thermal) particle energy, dynamo action involves the amplification of a seed magnetic field by fluid motions, and magnetic reconnection converts magnetic energy into particle kinetic energy. Essentially, turbulence serves as an important mediator in these processes by shaping the spatial field structures and redistributing energy among different scales, which quite often greatly enhances the efficiency of the conversion between different forms of energy. The exact details of the energy partitioning are of course situation dependent. Let us give some examples.

In the context of turbulent heating, hot accretion flows on to black holes, such as the Sagittarius A* at the center of our galaxy, represent a particularly intriguing example [3, 17]. Hot accretion disks can be studied by analyzing their electromagnetic radiation spectra, emitted from the electrons. Ions, on the other hand, do not contribute significantly to the radiation because they are much heavier. Observations combined with simplified models imply that the plasma in hot accretion flows maintains a two-temperature state, with ions much hotter than electrons. In conjunction, the so-called magnetorotational instability drives a weakly collisional, turbulent energy cascade that heats the ions and the electrons. Accurate predictions of the ion-electron heating ratio and of the resulting electromagnetic radiation thus ultimately require kinetic modeling and simulation of weakly collisional, magnetized plasma turbulence [3, 6, 18].

Turbulence also plays an important role in the interstellar space of our galaxy, which is filled with a mixture of neutral gas, plasma, and dust grains [19]. The interstellar medium has many phases, the most relevant of which is in our context the warm ionized phase. Turbulence in the interstellar medium can be inferred from radio wave propagation measurements [20], which reveal broad power-law spectra of the electron density, extending down to the ion kinetic scales below the collisional mean free path [19–21]. Present observations do not provide enough detail to clearly identify a possible presence of sub-ion scale interstellar turbulence, although it has been suggested that the much better studied case of solar wind turbulence could provide some relevant hints in this respect [20].

Finally, an interesting set of turbulent environments includes high-energy astrophysical objects that shine bright over a broad range of the electromagnetic spectrum, such as pulsar wind nebulae or relativistic jets from active galactic nuclei [22]. An iconic example is the Crab Nebula supernova remnant [23], powered by a magnetized rotating neutron star (i.e., pulsar) that drives a relativistic stream of electron-positron plasma (Fig. 1.1). The observed electromagnetic radiation spectra from the pulsar wind imply that the charged particles undergo non-thermal acceleration to ultra-relativistic energies. A physical explanation of the latter ultimately requires an understanding of kinetic plasma physics. Among other possibilities, kinetic turbulence recently emerged as a viable candidate for non-thermal

particle acceleration in pulsar wind nebulae [9].

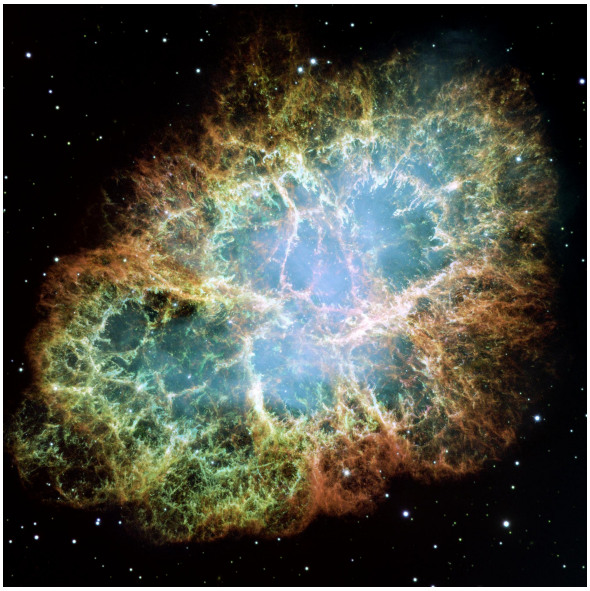

Figure 1.1: Hubble image of the turbulent Crab Nebula supernova remnant. Image credit: NASA, ESA and Allison Loll/Jeff Hester (Arizona State University). Acknowledgement: Davide De Martin (ESA/Hubble).

Unfortunately, we cannot study distant astrophysical systems *in situ* and remote observations are necessarily based on a set of modeling assumptions. On the other hand, the solar wind in our heliosphere readily provides an excellent laboratory to study weakly collisional plasma turbulence [24]. This deserves a separate discussion given below.

1.2 The solar wind

The solar wind is a supersonic stream of plasma, expanding outwards from the Sun [25]. It is a magnetized plasma. On one end, the magnetic field lines are anchored in the photosphere of the rotating Sun, whereas further away the lines are dragged radially outwards by the expanding plasma flow. In this process, a spiral-shaped interplanetary magnetic field structure is created, as first predicted by Parker [26] in the late 1950s. The solar wind is also a dilute and weakly collisional plasma with a mean free path of about one astronomical unit (AU). A set of typical plasma parameters of the near-Earth solar wind is given in Table 1.1. The stream of the interplanetary plasma is commonly divided into two types: the slow and the fast. The fast wind is launched from the locations of open magnetic field lines, typically close to the magnetic poles of the Sun. It reaches velocities up to about 800 km/s. The slow wind, on the other hand, originates from regions closer to the Sun's equator and exhibits reversals in the large-scale magnetic field polarity. It reaches velocities around 400 km/s at one AU. The wind serves as a medium for the transport of magnetic

disturbances created at the Sun throughout the entire solar system, thus directly impacting the magnetospheres of the planets. For our home planet, this interaction is of considerable significance and may cause harmful damage to satellites or even to electrical power grids, in the case of more violent magnetic events (e.g., coronal mass ejections) at the Sun. To prevent harmful events, significant efforts are underway to better understand and model the solar wind and its interaction with the Earth's magnetosphere, with the ultimate goal for more accurate space weather prediction. The evolution of the solar wind is, however, affected by a range of kinetic plasma phenomena. An improved fundamental understanding of these kinetic processes in turbulent plasmas is therefore also of practical interest.

n	T_i	B_0	λ_{mfp}	ρ_i	ρ_e	λ_D	T_i/T_e	β_i
~ 10 cm^{-3}	~ 10 eV	$\sim 10^{-4}$ G	~ 1 AU	~ 40 km	~ 1 km	~ 10 m	~ 1	~ 1

Table 1.1: Some typical plasma parameters of the near-Earth free streaming solar wind [25, 27]: number density n, ion temperature T_i, magnetic field strength B_0, collisional mean free path λ_{mfp}, ion thermal gyroradius ρ_i, electron thermal gyroradius ρ_e, plasma Debye length λ_D, ion-electron temperature ratio T_i/T_e, and the ion beta $\beta_i = 8\pi n T_i/B_0^2$.

Perhaps the most immediate consequence of turbulence in the solar wind is the nontrivial dependence of the plasma temperature profile on the distance from the Sun [24, 28]. Some early models tried to predict the solar wind evolution in terms of a simple adiabatic expansion [29]. However, spacecraft measurements show that the plasma temperature decreases much more slowly than predicted by an adiabatic expansion [30], suggesting the presence of a significant heating mechanism. It was first proposed by Coleman [31] that the heating could be attributed to the turbulent conversion of electromagnetic fluctuations into heat. Nowadays, the turbulent heating paradigm is a well-established fact, but the kinetic details of ion and electron heating are still not fully understood in the case of the solar wind, as well as in low-collisionality astrophysical plasmas generally. As a minimum prerequisite for predicting the collisionless interactions between fields and particles and the resulting ion and electron heating, it is necessary to characterize and understand the type of electromagnetic fluctuations present at kinetic scales [4, 5, 32].

Thanks to high-resolution spacecraft measurements, the electromagnetic turbulent fluctuations can be studied *in situ* in the solar wind over a broad range of scales, from the large energy containing scales, deep into the turbulence kinetic dissipation range [33]. By measuring the frequency of the fluctuations f, as the wind streams at a supersonic speed V past the spacecraft, the wavenumber k in the plasma rest frame can be inferred by invoking the Taylor hypothesis [34]: $k \approx 2\pi f/V$. The hypothesis rests on the assumption that the frequencies in the plasma rest frame are much smaller than the frequencies in the spacecraft frame and it is well satisfied for most relevant types of turbulent fluctuations [35]. Present state-of-the-art observations show that the solar wind is indeed highly turbulent and exhibits power-law fluctuation spectra over a broad range of scales (Fig. 1.2). Moreover, below the ion kinetic scales the spectral slope of the measured magnetic energy spectrum steepens,

thus indicating the presence of a new type of turbulent energy cascade. Much progress on the topic has been made in recent years on the basis of spacecraft observations [32] and numerical simulations (e.g., [36–40]). There is hope that lessons learned from detailed measurements of the solar wind could be applied as well to other turbulent astrophysical plasmas, which cannot be studied *in situ*. However, even in the case of the solar wind a comprehensive theoretical understanding of kinetic-scale turbulence is still lacking.

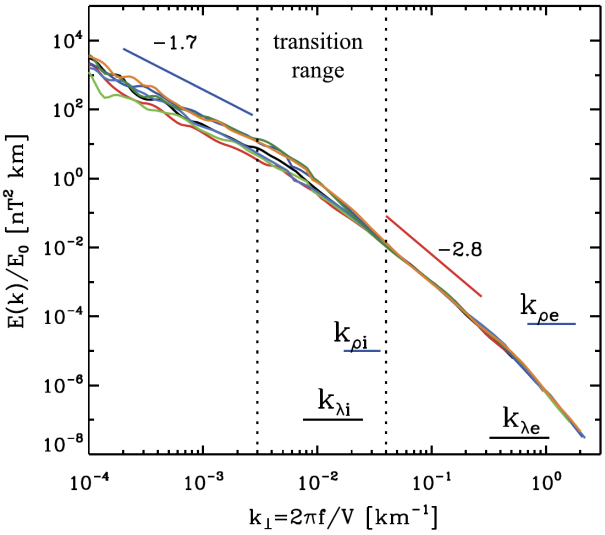

Figure 1.2: Spacecraft measurements of the magnetic energy spectrum plotted versus the wavenumber $k_\perp$, inferred from the spacecraft frame frequency f. The turbulence transitions into a different regime below the ion gyroradius scale ($k_\perp \gtrsim 1/\rho_i$). The new regime is manifested in a change of the spectral slope on the logarithmic graph. Image credit: Alexandrova *et al.* [41].

1.3 Scope of this Thesis

First principles numerical studies of plasma turbulence represent a significant challenge from the simulation and data analysis perspective. For this reason, many previous works resorted to various physically motivated simplifications of the first principles kinetic description. This includes reduced-kinetic descriptions, such as gyrokinetics [5, 36, 39, 42, 43] and hybrid models with fluid electrons [38, 44–47]. Another common approximation is the restriction to a two-dimensional geometry [38, 48, 49]. Significant concerns have been raised by different authors regarding these approximations [50–52]. Moreover, no general consensus presently exists in the community regarding the validity of theoretical and numerical results obtained from different types of simplified plasma descriptions.

It is the purpose of this Thesis to perform first principles studies of space and astrophysical plasma turbulence over the kinetic range of scales. By including the full range of electromagnetic and kinetic phenomena without *ad hoc* approximations, our main goal is to

identify the essential processes that govern the evolution of microscale plasma turbulence, in regimes reminiscent of the observationally accessible solar wind. To be more specific, we identify the dominant type(s) of wavelike fluctuations that participate in the sub-ion scale turbulent dynamics and we characterize their spectral scalings and anisotropy. We also extract signatures of different types of turbulent heating channels, which may or may not be properly represented in a given reduced-kinetic model. Finally, we investigate the relationship between wavelike features and kinetic-scale turbulent structures, detected ubiquitously in spacecraft observations and numerical simulations [53]. Nonlinear turbulent structure formation, frequently associated with the phenomenon of intermittency, may lead to an enhanced dissipation of weakly collisional plasma turbulence [37, 38, 54, 55] and/or significantly affect the turbulence statistical scaling properties [56–58]. It is therefore of considerable interest to understand how (and if at all) turbulent, kinetic-scale structure formation could be interpreted in terms of some of the well-known, wavelike kinetic turbulence phenomenologies [4, 5, 59].

The rest of this Thesis is structured as follows. In Chapter 2 we outline the basic framework for the kinetic description and simulation of weakly collisional plasmas. This includes the Klimontovich-Maxwell and Vlasov-Maxwell systems of equations and an overview of the particle-in-cell plasma simulation method. In addition, we also introduce the commonly used gyrokinetic and hybrid-kinetic (with fluid electrons) approximations. Phenomenological models of astrophysical plasma turbulence are reviewed in Chapter 3. We start with a concise review of the widely influential work of Kolmogorov and his contemporaries on Navier-Stokes fluid turbulence, followed by a description of the phenomenology of inertial range, magnetohydrodynamic plasma turbulence. Finally, we introduce the presently known phenomenologies of kinetic-scale turbulence in astrophysical plasmas. A considerable emphasis is put on the frequently debated kinetic Alfvén wave (KAW) turbulence model [4, 5]. We review the basic properties of KAW turbulence and previous works in support of the phenomenology. We also discuss the criticism and known alternatives to the KAW turbulence phenomenology. A more technical description of our massively parallel kinetic turbulence simulations is given in Chapter 4. There, we introduce the OSIRIS plasma simulation code [60, 61] and we comment on the choice of the physical and numerical simulation parameters. Our main results are featured in Chapters 5, 6, and 7. In Chapter 5 we present the first direct comparison of the prominent fully kinetic, gyrokinetic, and hybrid-kinetic plasma models in a turbulent setup, relevant to space and astrophysical plasmas. The comparison is carried out in two-dimensional geometry. In Chapter 6, we move on to three-dimensional fully kinetic simulations of kinetic-scale plasma turbulence with the aim to demonstrate the natural development of a KAW turbulent cascade from first physics principles, under typical solar wind conditions. Finally, in Chapter 7 we perform a joint analysis of *in situ* space turbulence measurements and fully kinetic simulation data to investigate the interplay between wavelike signatures and large-amplitude turbulent structures in kinetic plasma turbulence. A summary of the main results of this Thesis and a future outlook are given in Chapter 8.

Chapter 2

Kinetic modeling and simulation of weakly collisional plasmas

Due to recent advances in state-of-the-art computational techniques, it is now possible to study weakly collisional, kinetic plasma turbulence in the full six-dimensional particle phase space, with self-consistent electromagnetic interactions, taking place over a wide range of scales. This Thesis features some of the first such simulations in the context of sub-ion range turbulence in solar wind plasmas. Before we present our main results in Chapters 5, 6, and 7, we briefly summarize here the basic kinetic equations for a plasma and relate these to the fully kinetic particle-in-cell (PIC) simulation scheme [62, 63], appropriate for the study of nearly collisionless plasmas, such as the turbulent solar wind [28]. No attempt is made to give a comprehensive review and further information can be found in Refs. [62–69]. Throughout the following chapters, we frequently reference various typical plasma scales and parameters, the definitions of which are given in Appendix C.

2.1 The Vlasov-Maxwell system

The main theoretical basis for the interpretation of our results is the kinetic, Vlasov-Maxwell system of equations. The Vlasov equation is obtained in the so-called collisionless approximation [70], frequently used for the study of nearly collisionless plasmas, characterized by very large values of the plasma parameter $\Lambda = 4\pi n_0 \lambda_D^3 \gg 1$, where λ_D is the Debye length and n_0 is the mean particle density (see also Appendix C). Let us briefly sketch how the Vlasov equation emerges from a more general kinetic plasma description in the collisionless limit.

One way to introduce the plasma kinetic description is to follow the Klimontovich approach [64, 70, 71], which starts from a system of discrete charged particles in their self-generated, microscopic electromagnetic fields. This is complementary to the approach based on the BBGKY (Bogoliubov, Born, Green, Kirkwood, Yvon) hierarchy, which starts with the Liouville equation for the N-particle joint probability density [65]. The Klimontovich

formalism is based on the microscopic phase-space density [64, 70]:

$$\mathcal{N}_s(\mathbf{r},\mathbf{p},t) = \sum_{i=1}^{N_s} \delta\Big(\mathbf{r}-\mathbf{r}_{si}(t)\Big)\,\delta\Big(\mathbf{p}-\mathbf{p}_{si}(t)\Big), \tag{2.1}$$

where the index i runs over all the N_s particles of species s, $\mathbf{r}_{si}$ is the particle position, and $\mathbf{p}_{si}$ its (relativistic) momentum. The relevant force acting on the particles is the Lorentz force and the equations of motion are

$$\frac{\mathrm{d}\mathbf{r}_{si}}{\mathrm{d}t} = \mathbf{v}_{si} = \frac{\mathbf{p}_{si}}{\sqrt{m_s^2 + p_{si}^2/c^2}}, \qquad \frac{\mathrm{d}\mathbf{p}_{si}}{\mathrm{d}t} = q_s\left[\mathbf{E}^{\mathrm{m}}(\mathbf{r}_{si}) + \frac{\mathbf{v}_{si}}{c}\times\mathbf{B}^{\mathrm{m}}(\mathbf{r}_{si})\right], \tag{2.2}$$

where $\mathbf{v}_{si}$ is the particle velocity, m_s is the species mass, q_s denotes the species charge, c is the speed of light, and $\mathbf{E}^{\mathrm{m}}$, $\mathbf{B}^{\mathrm{m}}$ are the microscopic electromagnetic fields produced by the particles. The evolution of the electromagnetic fields is governed by the Maxwell equations:

$$\frac{\partial\mathbf{E}^{\mathrm{m}}}{\partial t} = c\,\nabla\times\mathbf{B}^{\mathrm{m}} - 4\pi\mathbf{J}^{\mathrm{m}}, \qquad \nabla\cdot\mathbf{E}^{\mathrm{m}} = 4\pi\rho^{\mathrm{m}}, \tag{2.3}$$

$$\frac{\partial\mathbf{B}^{\mathrm{m}}}{\partial t} = -\,c\,\nabla\times\mathbf{E}^{\mathrm{m}}, \qquad \nabla\cdot\mathbf{B}^{\mathrm{m}} = 0, \tag{2.4}$$

where $\mathbf{J}^{\mathrm{m}} = \sum_s q_s \int \mathbf{v}\mathcal{N}_s\,\mathrm{d}^3\mathbf{p}$ is particle electric current density and $\rho^{\mathrm{m}} = \sum_s q_s \int \mathcal{N}_s\,\mathrm{d}^3\mathbf{p}$ is the charge density. The two Maxwell equations involving the divergence terms are satisfied implicitly provided that they hold at some initial reference time $t = 0$. Equations (2.1)–(2.4), together with the definitions of $\mathbf{J}^{\mathrm{m}}$ and ρ^{m}, form a closed set. The plasma dynamics arising from such description is generally nonlinear as a result of the interaction between the charged particles and their self-generated fields.

The equations of motion can be written in an alternative form in terms of the microscopic phase-space density. Upon taking the time derivative of $\mathcal{N}_s(\mathbf{r},\mathbf{p},t)$ and using (2.2) we obtain the Klimontovich equation [64]:

$$\frac{\partial\mathcal{N}_s}{\partial t} + \mathbf{v}\cdot\frac{\partial\mathcal{N}_s}{\partial\mathbf{r}} + q_s\left(\mathbf{E}^{\mathrm{m}} + \frac{\mathbf{v}}{c}\times\mathbf{B}^{\mathrm{m}}\right)\cdot\frac{\partial\mathcal{N}_s}{\partial\mathbf{p}} = 0. \tag{2.5}$$

This shows that the microscopic density is conserved along the particle orbits in the six-dimensional phase space. The total number of plasma particles of any given species is macroscopically large and one therefore needs to adopt a statistical description. The single-particle distribution function $f_s(\mathbf{r},\mathbf{p},t)$—a key quantity in plasma kinetic theory—may be defined via a statistical ensemble average of the microscopic phase-space density [65, 71]:

$$f_s(\mathbf{r},\mathbf{p},t) = \langle\mathcal{N}_s(\mathbf{r},\mathbf{p},t)\rangle_{\mathrm{en.}} \tag{2.6}$$

The single-particle distribution function is proportional to the probability to find a particle of type s in a small volume of phase space around $(\mathbf{r},\mathbf{p})$. A statistical description of the

particle dynamics can be obtained by taking the ensemble average of Eq. (2.5), which yields the plasma kinetic equation [64]:

$$\frac{\partial f_s}{\partial t} + \mathbf{v}\cdot\frac{\partial f_s}{\partial \mathbf{r}} + q_s\left(\mathbf{E}+\frac{\mathbf{v}}{c}\times\mathbf{B}\right)\cdot\frac{\partial f_s}{\partial \mathbf{p}} = -q_s\frac{\partial}{\partial \mathbf{p}}\cdot\left\langle\left(\delta\mathbf{E}+\frac{\mathbf{v}}{c}\times\delta\mathbf{B}\right)\delta\mathcal{N}_s\right\rangle_{\text{en.}}, \tag{2.7}$$

where $\mathbf{E} = \langle\mathbf{E}^{\text{m}}\rangle_{\text{en.}}$ and $\mathbf{B} = \langle\mathbf{B}^{\text{m}}\rangle_{\text{en.}}$ are the smooth, self-consistent fields. The quantities $\delta\mathbf{E} = \mathbf{E}^{\text{m}} - \mathbf{E}$, $\delta\mathbf{B} = \mathbf{B}^{\text{m}} - \mathbf{B}$, and $\delta\mathcal{N}_s = \mathcal{N}_s - f_s$ are the statistical deviations from the ensemble averaged values. The term on the right-hand side of (2.7) is the collision integral [65, 70]. It leads to irreversible entropy production in states away from thermal equilibrium. The irreversibility arises from the averaging of the (reversible) microscopic dynamics, leading to the loss of information in the mean-field description. Naturally, the smooth electromagnetic fields still obey the Maxwell equations with the microscopic current and density replaced by their ensemble averaged counterparts. Eq. (2.7) is not closed because it involves the undetermined fluctuations ($\delta\mathbf{E}$, $\delta\mathbf{B}$, and $\delta\mathcal{N}_s$) in the collision integral. In order to obtain a closed set of equations in terms of f_s, $\mathbf{E}$, and $\mathbf{B}$ alone, one needs to approximate the right-hand side. In the case of Coulomb interactions, a common choice is to adopt a Fokker-Planck type collision operator [70, 72, 73]:

$$C[f_s] = \sum_{s'}\left[-\frac{\partial}{\partial \mathbf{p}}\cdot\left(\mathbf{A}_{ss'}f_s\right) + \frac{1}{2}\frac{\partial^2}{\partial \mathbf{p}\partial \mathbf{p}} : \left(\mathsf{D}_{ss'}f_s\right)\right], \tag{2.8}$$

where $\mathbf{A}_{ss'}$ is the friction coefficient, $\mathsf{D}_{ss'}$ is the diffusion tensor, and the sum over s' runs over all the particle species. The Fokker-Planck operator assumes the dominance of small-angle particle scatterings. This is motivated by the fact that the mean particle separation in a weakly coupled ($\Lambda \gg 1$) plasma is much larger than the distance at which the electrostatic interaction energy would exceed the mean kinetic energy. The friction and diffusion coefficients are generally position, momentum, and time dependent and may be expressed as integrals of $f_{s'}$ [65, 73]. Looking at expression (2.8), it is worth noticing that the strength of the collisional term may be locally enhanced by sharp gradients of f_s in momentum space.

In hot and/or diffuse, weakly coupled plasmas the collisional relaxation time for the approach towards equilibrium is much longer than the characteristic time of the collective response [66, 74]. Many space and astrophysical plasmas are naturally found in such weakly collisional state [5]. Prominent examples include the solar wind [28], hot accretion flows [17], and galaxy clusters [75]. A popular approximation for weakly collisional plasmas is to set $1/\Lambda = 0$, which amounts to neglecting any discrete particle effects. The kinetic equation then reduces to the well-known Vlasov equation:

$$\frac{\partial f_s}{\partial t} + \mathbf{v}\cdot\frac{\partial f_s}{\partial \mathbf{r}} + q_s\left(\mathbf{E}+\frac{\mathbf{v}}{c}\times\mathbf{B}\right)\cdot\frac{\partial f_s}{\partial \mathbf{p}} = 0. \tag{2.9}$$

The Vlasov equation describes plasma kinetics in the collisionless regime, where the collective response is assumed to completely dominate over the discrete particle effects on any time

scale of interest. For the sake of completeness, let us also write the Maxwell equations for the self-consistent fields:

$$\frac{\partial \mathbf{E}}{\partial t} = c\,\nabla \times \mathbf{B} - 4\pi \sum\nolimits_s q_s \int \mathbf{v} f_s \,\mathrm{d}^3\mathbf{p}\,, \qquad \nabla \cdot \mathbf{E} = 4\pi \sum_s q_s \int f_s \,\mathrm{d}^3\mathbf{p}\,, \tag{2.10}$$

$$\frac{\partial \mathbf{B}}{\partial t} = -\,c\,\nabla \times \mathbf{E}, \qquad \nabla \cdot \mathbf{B} = 0. \tag{2.11}$$

The Vlasov-Maxwell system of equations is the basic starting point for the interpretation of the fully kinetic simulations of solar wind turbulence presented in this Thesis. The system is fully kinetic in the sense that the distribution function of each species is evolved in the full six-dimensional phase space without any *a priori* restrictions for the self-consistent dynamics.[1] In principle, only the fully kinetic description can properly, and simultaneously, capture all the potentially relevant processes that can take place in a weakly collisional, turbulent plasma. This includes, for example, the high-frequency whistler waves [80–84], electron and ion Landau damping [4, 40, 54, 85–88], collisionless magnetic reconnection [16, 89–92], kinetic instabilities [11, 93–95], or non-thermal particle acceleration [9, 96]. The reader may find it useful to notice that the Vlasov-Maxwell system is mathematically identical to the Klimontovich-Maxwell equations. The only difference from the latter is the smoothness of the initial condition [71]. Numerically solving Eqs. (2.9)–(2.11) is in general a very challenging computational task, even with present state-of-the-art computational resources. Here, we employ massively parallel PIC simulations to accomplish the task. Some general aspects of the PIC scheme are briefly discussed in Sec. 2.2. More technical details on how we coped with the main computational challenges, specific to the kinetic plasma turbulence studied in this Thesis, are given in Chapter 4.

It is worth mentioning an important theoretical shortcoming in strictly describing turbulent, weakly collisional plasmas with the Vlasov equation, which was clearly emphasized in the literature only more recently [5, 69, 97, 98]. Namely, collisions in a plasma with $\Lambda \gg 1$ are truly very weak as long as the distribution function is not too far from Maxwellian. On the other hand, the Vlasov equation may locally develop distinct non-Maxwellian features with very fine structures in both configuration and momentum space. These fine, phase-space structures may locally greatly enhance the collisionality and lead to significant entropy production on dynamically relevant time scales [69, 97]. The situation resembles the so-called dissipative anomaly in hydrodynamic turbulence [99, 100], where kinetic energy dissipation remains finite in the limit of vanishing viscosity due to the emergence of large spatial gradients in the fluid velocity. In a weakly collisional plasma, one can similarly imagine collisional effects as an entropy production source, which prevents unlimited filamentation of f_s [5, 98, 101]. On the other hand, on phase-space scales larger than those with sufficiently large gradients for collisions to become important, the dynamics is still effectively of the Vlasov type and it is not particularly sensitive to the exact form of the collision operator [69, 102, 103]. The Vlasov equation is therefore still a key concept for

[1] Our use of the term "fully kinetic" throughout this whole Thesis is in this sense consistent with the presently common terminology in the kinetic plasma simulation community [40, 76–79].

the study of weakly collisional plasmas, as long as we keep in mind that the phase-space filamentation of f_s cannot be indefinite and is ultimately balanced by collisional effects. In computer simulations, finite resolution always precludes such unlimited filamentation of the particle distribution function and any numerical scheme for the Vlasov equation always comes with some form of numerical collisionallity (or phase-space diffusion), which effectively coarse grains or smooths the particle distribution at the smallest computationally accessible scales. As discussed below, the PIC simulation method employed in this Thesis is no exception to that [63, 68, 104, 105].

2.2 The PIC fully kinetic simulation method

Let us now summarize the main features of the PIC simulation method, employed here for the study of kinetic range solar wind turbulence. One of the most distinct features of the standard PIC method [62, 63] is its representation of the distribution function with a collection of macroparticles of fixed shape. As a consequence, the distribution function may be evolved by following the motions of the computational particles, whereas the Maxwell equations are solved on a discretized spatial grid. Here we mainly focus on the implications of representing the distribution function with a set of computational macroparticles, since this is the feature most specific to particle-based simulations. Numerical effects related to space and time discretization errors [63] are touched upon only briefly.

2.2.1 Overview of the numerical scheme

In the standard PIC method [62, 63], the particle distribution function is represented with a set of M_s charged macroparticles or clouds as [67]

$$\widetilde{f}_s(\mathbf{r},\mathbf{p},t) = \sum_{j=1}^{M_s} N_{sj}\, S\Big(\mathbf{r}-\mathbf{r}_{sj}(t)\Big)\, \delta\Big(\mathbf{p}-\mathbf{p}_{sj}(t)\Big), \tag{2.12}$$

where N_{sj} can be regarded as the number of physical particles in the j-th cloud with charge density $\rho_{sj}(\mathbf{r}) = q_s N_{sj} S(\mathbf{r}-\mathbf{r}_{sj})$. The set of variables $\{\mathbf{r}_{sj}(t), \mathbf{p}_{sj}(t)\}$ determines the positions and momenta of the clouds. The characteristic size of the macroparticles is effectively determined by the spatial extent of the particle shape $S(\mathbf{r})$. Motivated by numerical and physical considerations, this size is typically chosen to be comparable to the Debye length [63]. In order for the representation (2.12) to be meaningful, $S(\mathbf{r})$ should have a finite support and satisfy: $S(\mathbf{r}) \geq 0$, $S(-\mathbf{r}) = S(\mathbf{r})$, and $\int \mathrm{d}^3\mathbf{r}\, S(\mathbf{r}) = 1$. Most PIC codes employ b-splines for the particle shape [63, 67], a common choice being splines of order zero. Higher order, smoother splines have many favorable properties, such as reduced grid aliasing effects [63, 106], although they require more floating point operations per time step. All simulations presented in this Thesis employ either linear or quadratic splines for $S(\mathbf{r})$.[2]

[2]Note that the PIC interpolation functions, for interpolating $\mathbf{J}$, $\mathbf{E}$, and $\mathbf{B}$, to/from the regular grid points, are approximated by splines of one order higher than $S(\mathbf{r})$ [67]. That is, linear and quadratic b-spline shapes yield, respectively, quadratic and cubic spline interpolation functions.

It follows from the numerical distribution function representation (2.12) that the Maxwell equations take the explicit form:

$$\frac{\partial \mathbf{E}}{\partial t} = c\,\nabla \times \mathbf{B} - 4\pi \sum_{s,j} \mathbf{v}_{sj}\, q_s N_{sj} S(\mathbf{r} - \mathbf{r}_{sj}), \quad \nabla \cdot \mathbf{E} = 4\pi \sum_{s,j} q_s N_{sj} S(\mathbf{r} - \mathbf{r}_{sj}), \tag{2.13}$$

$$\frac{\partial \mathbf{B}}{\partial t} = -\,c\,\nabla \times \mathbf{E}, \qquad \nabla \cdot \mathbf{B} = 0, \tag{2.14}$$

where $\mathbf{J} = \sum_{s,j} \mathbf{v}_{sj}\, q_s N_{sj} S(\mathbf{r} - \mathbf{r}_{sj})$ is the current density and $\rho = \sum_{s,j} q_s N_{sj} S(\mathbf{r} - \mathbf{r}_{sj})$ is the charge density. The finite element representation can be exploited when solving for $\widetilde{f}_s$. Because the shape of the macroparticles is fixed, it is sufficient to numerically solve the equations of motion for the charge cloud centers instead of solving for $\widetilde{f}_s$ directly. This effectively amounts to solving for $\widetilde{f}_s$ in a Lagrangian particle frame. The equations of motion for the cloud centers are

$$\frac{\mathrm{d}\mathbf{r}_{sj}}{\mathrm{d}t} = \mathbf{v}_{sj}, \qquad \frac{\mathrm{d}\mathbf{p}_{sj}}{\mathrm{d}t} = q_s \left[\overline{\mathbf{E}}(\mathbf{r}_{sj}) + \frac{\mathbf{v}_{sj}}{c} \times \overline{\mathbf{B}}(\mathbf{r}_{sj}) \right], \tag{2.15}$$

where

$$\overline{\mathbf{E}}(\mathbf{r}_{sj}) = \int \mathrm{d}^3\mathbf{r}'\, \mathbf{E}(\mathbf{r}') S(\mathbf{r}' - \mathbf{r}_{sj}), \qquad \overline{\mathbf{B}}(\mathbf{r}_{sj}) = \int \mathrm{d}^3\mathbf{r}'\, \mathbf{B}(\mathbf{r}') S(\mathbf{r}' - \mathbf{r}_{sj}) \tag{2.16}$$

are the convolved electromagnetic fields, evaluated at each cloud position [62, 67]. The convolved fields appearing in the equations of motion determine the total force on each macroparticle, obtained via an integration over the (fixed) macroparticle shape. Equations (2.13)–(2.16) form a closed set for the PIC fully kinetic, electromagnetic simulation model.

In short summary, Eqs. (2.13)–(2.16) are numerically solved in a cyclic fashion as follows. First, the computational particles are advanced to the next time step according to (2.15). This involves an interpolation of the fields in (2.16) to each particle's position to determine the force. A time centered, second-order finite difference scheme, known as the Boris push [63, 107], is usually used to advance the particle coordinates. Once the particle phase-space coordinates have been updated, the particle electric current density is deposited on the computational grid for the Maxwell equations (2.13) and (2.14). If the electric current deposit is charge-conserving [108, 109], the charge density need not be calculated explicitly. If that is not the case, the charge density is needed to correct the electrostatic field so as to conserve the charge [63]. The Maxwell equations are typically integrated on a staggered grid for $\mathbf{E}$ and $\mathbf{B}$ (so-called Yee mesh [107]), using a second-order, space and time centered leapfrog scheme. The above process is then repeated at the next time step, and so on. Schematically, the scheme may be illustrated with a diagram shown in Fig. 2.1. Although conceptually simple, efficient PIC code implementations, appropriate for modern high-performance simulations, are a technically challenging task and typically require several years of code development and optimization [60, 61, 76, 110].

The finite differencing of spatial and time derivatives introduces artificial numerical effects. For example, the plasma dispersion properties are modified at large wavenumbers

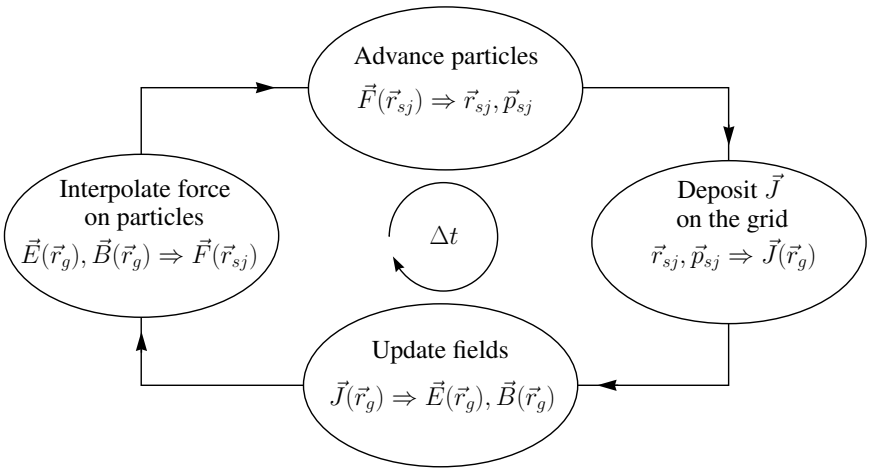

Figure 2.1: Schematic illustration of the PIC numerical integration loop. The scheme is typically second-order accurate in both space and time.

and/or frequencies. Moreover, in explicit time integration schemes, the time step and grid spacing need to be chosen sufficiently small to avoid artificial numerical heating and instabilities. In the standard, second-order explicit PIC scheme, the time step Δt and grid spacings $(\Delta x, \Delta y, \Delta z)$ should satisfy [63, 107]:

$$c\Delta t \left(\frac{1}{\Delta x^2} + \frac{1}{\Delta y^2} + \frac{1}{\Delta z^2} \right)^{1/2} < 1, \qquad \Delta t \omega_{pe} < 2, \qquad \Delta x, \Delta y, \Delta z \lesssim \pi \lambda_D, \tag{2.17}$$

where ω_{pe} is the electron plasma frequency and λ_D is the Debye shielding distance. The expression on the left side of (2.17) is the Courant–Friedrichs–Lewy (CFL) condition and prevents light waves from propagating over more than one grid cell during a single step. It is not particularly recommended to over-satisfy the CFL condition, because time steps just below the CFL threshold yield a better numerical match for the light wave dispersion [107]. For the remaining two conditions in (2.17), it is advisable to be well within the stability region. This also means that the Debye scale has to be at least marginally resolved $(\Delta x \simeq \lambda_D)$, even if it is otherwise of no special interest.

2.2.2 Discrete particle effects and noise in PIC simulations

Solutions of the kinetic equations obtained from PIC methods are affected by random statistical noise, originating from the discrete nature of the computational particles. In order to better illustrate the nature of the PIC noise and its origin, it is instructive to consider a spatially coarse-grained Klimontovich-Maxwell system of equations. In particular, it is of interest to consider a spatial coarse-graining operation, defined as a convolution with the particle shape factor appearing in (2.12):

$$\overline{f}(\mathbf{r}) = \int \mathrm{d}^3\mathbf{r}' \, f(\mathbf{r}') S(\mathbf{r}' - \mathbf{r}), \tag{2.18}$$

where f is some arbitrary function. For the purpose of our discussion, we can suppose that $S(\mathbf{r})$ has a characteristic spatial extent comparable to λ_D. In the latter case, the coarse-graining smooths out any spatial fluctuations within a Debye sphere, affected by discrete particle effects in a plasma, while preserving the self-consistent plasma fluctuations at scales larger than λ_D.

By applying the coarse graining to the Klimontovich equation (2.5), we obtain after straightforward calculation:

$$\frac{\partial \overline{\mathcal{N}}_s}{\partial t} + \mathbf{v} \cdot \frac{\partial \overline{\mathcal{N}}_s}{\partial \mathbf{r}} + q_s \left(\mathbf{E} + \frac{\mathbf{v}}{c} \times \mathbf{B} \right) \cdot \frac{\partial \overline{\mathcal{N}}_s}{\partial \mathbf{p}} = C_s + \epsilon_s, \tag{2.19}$$

where

$$\overline{\mathcal{N}}_s(\mathbf{r}, \mathbf{p}, t) = \sum_{i=1}^{N_s} S\Big(\mathbf{r} - \mathbf{r}_{si}(t)\Big)\, \delta\Big(\mathbf{p} - \mathbf{p}_{si}(t)\Big), \tag{2.20}$$

$$C_s = -q_s \frac{\partial}{\partial \mathbf{p}} \cdot \sum_i \left(\delta\mathbf{E}(\mathbf{r}_{si}) + \frac{\mathbf{v}}{c} \times \delta\mathbf{B}(\mathbf{r}_{si}) \right) S\Big(\mathbf{r} - \mathbf{r}_{si}\Big)\, \delta\Big(\mathbf{p} - \mathbf{p}_{si}\Big), \tag{2.21}$$

$$\epsilon_s = -q_s \frac{\partial}{\partial \mathbf{p}} \cdot \sum_i \left(\Delta\mathbf{E}(\mathbf{r}_{si},\, \mathbf{r}) + \frac{\mathbf{v}}{c} \times \Delta\mathbf{B}(\mathbf{r}_{si},\, \mathbf{r}) \right) S\Big(\mathbf{r} - \mathbf{r}_{si}\Big)\, \delta\Big(\mathbf{p} - \mathbf{p}_{si}\Big), \tag{2.22}$$

and

$$\mathbf{E} = \overline{\mathbf{E}^{\mathrm{m}}}, \qquad \mathbf{B} = \overline{\mathbf{B}^{\mathrm{m}}}, \tag{2.23}$$

$$\delta\mathbf{E} = \mathbf{E}^{\mathrm{m}} - \overline{\mathbf{E}}, \qquad \delta\mathbf{B} = \mathbf{B}^{\mathrm{m}} - \overline{\mathbf{B}}, \tag{2.24}$$

$$\Delta\mathbf{E}(\mathbf{r}',\, \mathbf{r}) = \overline{\mathbf{E}}(\mathbf{r}') - \mathbf{E}(\mathbf{r}), \qquad \Delta\mathbf{B}(\mathbf{r}',\, \mathbf{r}) = \overline{\mathbf{B}}(\mathbf{r}') - \mathbf{B}(\mathbf{r}). \tag{2.25}$$

The advective terms on the left-hand side of the coarse-grained equation (2.19) represent the Vlasov-like part of the dynamics, whereas the right-hand side represents discrete particle effects. Such interpretation of the above terms is only of qualitative type, because a coarse graining over a volume of a Debye sphere is not exactly the same as an ensemble average, used to obtain the plasma kinetic equation. Only the smoothed electromagnetic fields, $\mathbf{E}$ and $\mathbf{B}$ (2.23), appear on the left-hand side of (2.19). They satisfy the usual Maxwell equations with smooth sources $\rho = \overline{\rho^{\mathrm{m}}}$ and $\mathbf{J} = \overline{\mathbf{J}^{\mathrm{m}}}$. The terms C_s and ϵ_s on the right-hand side are different in nature. The former (C_s) explicitly accounts for the influence of the microscopic fields on the coarse-grained dynamics. It could be regarded as an effective collisional-like term. The second term (ϵ_s) is only a very small correction, accounting for the fact that the coarse-grained fields themselves can slightly vary on the scale of the smoothing volume, so that each portion of plasma within that volume feels a slightly different coarse-grained force.

We may proceed as above and derive in addition an explicit expression for the evolution of $\widetilde{f}_s$ (2.12) by taking its time derivative. The end result may be written as

$$\frac{\partial \widetilde{f}_s}{\partial t} + \mathbf{v} \cdot \frac{\partial \widetilde{f}_s}{\partial \mathbf{r}} + q_s \left(\mathbf{E} + \frac{\mathbf{v}}{c} \times \mathbf{B} \right) \cdot \frac{\partial \widetilde{f}_s}{\partial \mathbf{p}} = \epsilon_s, \tag{2.26}$$

where, in analogy with (2.22), we have

$$\epsilon_s = -q_s \frac{\partial}{\partial \mathbf{p}} \cdot \sum_j \Big(\Delta\mathbf{E}(\mathbf{r}_{sj},\, \mathbf{r}) + \frac{\mathbf{v}}{c} \times \Delta\mathbf{B}(\mathbf{r}_{sj},\, \mathbf{r}) \Big)\, N_{sj}\, S\Big(\mathbf{r} - \mathbf{r}_{sj}\Big)\, \delta\Big(\mathbf{p} - \mathbf{p}_{sj}\Big), \tag{2.27}$$

and $\Delta\mathbf{E}(\mathbf{r}_{sj},\, \mathbf{r})$, $\Delta\mathbf{B}(\mathbf{r}_{sj},\, \mathbf{r})$ are given by (2.25). Eq. (2.26) is the PIC numerical equivalent of the Vlasov equation. Same as in (2.19), the ϵ_s term is only a minor correction. It has a vanishing space average and varies on a scale comparable to the cloud size. Its origin is related to the assumed non-deformability of the cloud shape [68, 111]. Without the implicit constraint, any charge cloud would very slowly deform as a result of slight field variations on scales comparable to its own size. This subtle effect is not accounted for in the PIC method [68, 111]. For this reason, the numerical distribution function representation (2.12) does not precisely satisfy a Vlasov equation at any arbitrary point, although it still does so "on average" [67]. More specifically, Eq. (2.26) multiplied in the first instance by $\mathbf{r}$ and in the second one by $\mathbf{p}$, followed by an integration over phase space, yields the two sets of equations (2.15) for the macroparticle orbits [67]. Minor local correction terms, similar to ϵ_s, appear also in the local momentum and energy balance expressions [111]. The local corrections vary on a scale comparable to the cloud size and vanish when integrated over $\mathbf{r}$, so that the total momentum and energy are conserved.[3]

Interestingly, the PIC distribution function representation (2.12) could be alternatively interpreted in terms of the coarse-grained particle density (2.20) [68]. In particular, $\tilde{f}_s$ could be constructed as a random subsample ($M_s \ll N_s$), drawn from the coarse-grained distribution $\overline{\mathcal{N}}_s$, with modified weights to preserve the original particle number. This implies that the PIC distribution function representation is in a strict sense not a proper ensemble averaged quantity, but corresponds rather to a particular realization of a numerical experiment [68]. The larger the statistical sample of computational particles, the less apparent is this formal distinction. Comparing the PIC equivalent of the Vlasov equation (2.26) to the coarse-grained Klimontovich equation (2.19), we also see that they are structurally equivalent, except for the right-hand side collisional-like term depending on the microscopic fields (C_s), which has disappeared. Indeed, discrete particle effects are generally much weaker in a computer plasma model with finite-size macroparticles than in a real plasma with pointlike charges [62, 63, 104]. This property is at the basis of the PIC method because it makes kinetic, Vlasov-like phenomena accessible to particle-based simulations, where the number of computational particles is in practice limited by the availability of memory and computing time [62, 63]. Evidently, the quality of momentum-space resolution does not improve by giving the computational particles a finite size, and therefore, the macroparticle number still needs to be chosen with care in order to properly capture kinetic effects, such as Landau damping [112, 113]. Moreover, collisional-like effects in PIC simulations are only reduced by the finite macroparticle size but not eliminated [68, 104, 105, 114, 115]. The PIC

[3]Evidently, this does not account for numerical integration effects, related to a finite grid resolution and finite time stepping, which may not ideally conserve the total momentum and/or energy. Such space and time discretization effects, discussed at length in Ref. [63], can be made negligible with an appropriate choice of the numerical simulation parameters.

distribution function representation (2.12) is smooth only in configuration space, whereas in momentum space, it is essentially a collection of sharp, δ-function spikes. The discrete nature of the computational particles gives rise to an effective numerical collisionality and drives random thermal fluctuations in the electromagnetic fields [62, 63, 68]. These random field fluctuations, referred to as PIC noise, can deteriorate the self-consistent, Vlasov-like part of the electromagnetic response.

PIC noise may be reduced by increasing the number of computational particles, which in turn improves the momentum space statistics. However, the random statistical fluctuations decrease only slowly with the particle count. For macroparticle sizes comparable to λ_D, the noise amplitude scales roughly as $\sim 1/\sqrt{N_D}$, where N_D is the number of computational particles in a Debye sphere [68, 105, 116]. It is therefore often worth considering additional noise reduction techniques [40]. In this Thesis, we employ two such techniques (see also Chapter 4). The first approach pertains to the choice of the particle shape. The smoother the particle shape, the weaker are the discrete noise effects [63, 105]. More specifically, high-order quadratic or cubic spline interpolation (corresponding, respectively, to linear or quadratic spline particle shapes) tends to give lower noise levels than the more frequently used linear interpolation [106, 117]. Another relatively effective method is short-time averaging of the simulation output data [40, 118]. Indeed, PIC noise often dominates on much shorter time scales than the characteristic time of the main plasma phenomenon under question. Under such circumstances, the noise may be further reduced by averaging the simulation results over the short time scales of the random fluctuations, while preserving the slower time scales of interest [40].

A significant reduction of PIC noise can be also achieved by relaxing the cloud non-deformability constraint, allowing the shape to dynamically evolve in phase space. However, in the latter case the PIC simulation scheme has to be replaced by a more general and technically advanced formulation [119, 120], which is able to self-consistently evolve the shape of the phase-space elements. A promising method of this kind recently emerged in cosmological, Vlasov-Poisson simulations [120, 121]. First attempts to adapt the method to kinetic plasma simulations have already been made [122], although it is presently unclear if the heavily reduced noise properties could outweight the increased numerical complexity of the scheme.

2.3 Reduced-kinetic models

As we have already emphasized, fully kinetic studies of plasma turbulence are currently a major theoretical and computational challenge. In view of these circumstances, several previous works on the subject have resorted to various simplifications of the first principles fully kinetic description [4, 5, 11, 18, 38, 39, 42, 44, 46, 85, 87, 123–125]. The presently most prominent reduced models are, in particular, the hybrid-kinetic (HK) model with fully kinetic ions and fluid electrons [44, 126–128] and the gyrokinetic (GK) model [129–131]. We do not limit ourselves here to an exclusive analysis of fully kinetic simulations only, but we instead also borrow the simulation data from reduced-kinetic models and directly

compare these against our own results. This allows us to firmly identify the most essential types of kinetic physics that govern the kinetic range turbulence in various regimes studied. In view of these model comparisons, which are presented in Chapter 5 (see also Ref. [40]), we briefly introduce below the HK and GK models, as well as a reduced GK model.

2.3.1 Hybrid model with kinetic ions and fluid electrons

The HK model is a quasi-neutral, non-relativistic model with kinetic ions and fluid electrons. Several versions of the model exist, depending on how exactly the electrons are treated within the fluid description. In the standard HK model [44, 45], the electrons are treated as a massless fluid, so that their inertia may be neglected. The main assumptions of the standard HK model can be stated as follows:

- Charge quasi-neutrality ($\rho \approx 0$): $k\lambda_D,\ \omega/\omega_{pe} \ll 1$,
- Non-relativistic limit: $\omega/(kc) \ll 1$,
- Massless electrons: $m_e/m_i \ll 1$,

where ω and k represent, respectively, a characteristic frequency and wavenumber of the process studied. By definition of quasi-neutrality, the ion density n_i and electron density n_e are assumed equal, while at the same time the electrostatic part of the electric field on scales $k\lambda_D,\ \omega/\omega_{pe} \ll 1$ is retained. The kinetic equation to be solved is the Vlasov equation (2.9) for the ion distribution function $f_i(\mathbf{r}, \mathbf{v}, t)$. As usual, the magnetic field is advanced using Faraday's law:

$$\frac{\partial \mathbf{B}}{\partial t} = -c\nabla \times \mathbf{E}. \tag{2.28}$$

On the other hand, because the displacement current is neglected in the non-relativistic limit, one cannot use Ampere's law to determine the evolution of $\mathbf{E}$. Instead, the $\mathbf{E}$ field is obtained at any instant of time from a generalized Ohm's law:

$$\mathbf{E} + \frac{\mathbf{u}_i \times \mathbf{B}}{c} - \frac{\mathbf{J} \times \mathbf{B}}{n_i e c} = -\frac{\nabla p_e}{n_i e} + \eta \mathbf{J}, \tag{2.29}$$

where $n_i = \int f_i \mathrm{d}^3\mathbf{v}$ is the ion (electron) density, $\mathbf{u}_i = (1/n_i)\int \mathbf{v} f_i \mathrm{d}^3\mathbf{v}$ is the ion fluid velocity, $\mathbf{J} = (c/4\pi)\nabla \times \mathbf{B}$ is the electric current, p_e is the electron pressure, η is the (numerical) resistivity, and $e = |q_e|$ is the elementary charge. The left-hand side gives the electric field in the electron fluid frame $\mathbf{E}' = \mathbf{E} + \mathbf{u}_e \times \mathbf{B}/c$, where $\mathbf{u}_e = \mathbf{u}_i - \mathbf{J}/(n_i e)$ is the electron flow velocity. The right-hand side gives the nonideal contributions to the electric field. Based on the smallness of the mass ratio, nonideal contributions stemming from electron inertia and anisotropic electron pressure effects are neglected. Finally, in order to obtain a closed set of equations, an equation of state is needed for the electron pressure. To this end, the electrons are usually assumed to be isothermal, such that $p_e = n_i T_{0e}$, where T_{0e} is the (constant) electron temperature, measured in energy units.

Sometimes, an alternative version of Ohm's law is used in the HK model, which accounts for electron inertia (e.g., [40, 128]). Upon assuming quasi-neutrality, the electron inertia may be expressed from the two-fluid equations with an isotropic electron pressure. This leads to an Ohm's law of the form

$$\left(1 - d_e^2 \nabla^2\right)\mathbf{E} = -\frac{\mathbf{u}_e \times \mathbf{B}}{c} - \frac{\nabla p_e}{n_i e} + \eta \mathbf{J} - \frac{m_e}{m_i}\left\{\frac{\mathbf{u}_i \times \mathbf{B}}{c} - \frac{1}{n_i e}\nabla \cdot \left[m_i n_i (\mathbf{u}_i \mathbf{u}_i - \mathbf{u}_e \mathbf{u}_e) + \mathsf{P}_i\right]\right\}, \quad (2.30)$$

where $\mathsf{P}_i = m_i \int (\mathbf{v} - \mathbf{u}_i)(\mathbf{v} - \mathbf{u}_i) f_i \mathrm{d}^3\mathbf{v}$ is the ion pressure tensor and d_e is the electron inertial length. The added terms compensate for the missing electron inertia contribution (equal to $-(m_e/e)\mathrm{d}\mathbf{u}_e/\mathrm{d}t$) on the right-hand side of (2.29). The version of Ohm's law given by Eq. (2.30) was used to produce the HK simulation data that are included, for reference, in Chapter 5 as part of the model comparison. We mention that the addition of electron inertia is not fully consistent with the isotropic electron pressure assumption, unless the electron gyroradius ρ_e is much smaller than d_e. In the opposite case, one would strictly speaking also need to include electron finite-Larmor-radius (FLR) corrections for the pressure.

The HK model is expected to be applicable in the non-relativistic regime, over the range of scales where electron kinetic physics need not be explicitly considered for the process being studied. It can be typically applied at scales larger or similar to the ion kinetic scales. Given its reduction in computational cost compared to the fully kinetic model, the advantage of the HK model is the possibility to simulate relatively large-sized systems, coupled with ion kinetic physics. In particular, the HK model is a good tool for studying inertial, MHD range turbulence and its transition into the kinetic range, where the cascaded energy may become subject to significant ion damping [38, 46, 132–134]. With some caution the model may be also applied somewhat below the ion kinetic scales, provided that electron kinetic effects remain negligible. Contrary to a common view from the literature, we show in Chapter 5 that electron kinetic effects can be noticed already slightly below the ion scales of kinetic plasma turbulence.

2.3.2 Gyrokinetics

The standard GK model [129–131, 135] is obtained from the fully kinetic description in the limit of low-frequency, low-amplitude, anisotropic fluctuations in magnetized plasmas. The fluctuating quantities are expanded in terms of a small ordering parameter $\epsilon \ll 1$, and only the lowest order terms are kept in the expansion. GK was traditionally developed in the context of magnetic confinement fusion [129]. Much later, it was adapted for the study of magnetized astrophysical plasmas [4, 5, 131]. Naturally, we will focus here on its astrophysics context. The main assumptions of the standard GK model may be stated as follows:[4]

[4] In principle, a different ordering parameter may be used separately for each fluctuating quantity [130]. Here, we use for simplicity the same "ϵ" for all.

- Small-amplitude, low-frequency, anisotropic fluctuations:
  $\delta f_s/F_{0s} \sim \delta B/B_0 \sim c\,\delta E_\perp/(B_0 v_{\mathrm{th},i}) \sim \omega/\Omega_{ci} \sim k_\parallel/k_\perp \sim \epsilon$,
- Strong magnetization: $\rho_i/L \ll 1$,
- Non-relativistic limit: $v_{\mathrm{th},s}/c \ll 1$,

where F_{0s} is the background particle distribution function, B_0 is the background magnetic field, δf_s is the perturbed part of the distribution, δB is the fluctuating magnetic field, $\delta E_\perp$ is the perpendicular electric field, L is a macroscopic length scale for the variation of B_0, ω is a characteristic fluctuation frequency, and $k_\parallel$, $k_\perp$ are, respectively, characteristic parallel and perpendicular wavenumbers with respect to the mean magnetic field direction. The remaining quantities introduced above are the ion thermal gyroradius ρ_i, the ion cyclotron frequency Ω_{ci}, and the species thermal velocity $v_{\mathrm{th},s}$ (see Appendix C). Similar to the HK model, the above assumptions also imply charge quasi-neutrality. The typical field-perpendicular scales are usually taken to be of the order of the ion gyroradius, $k_\perp \rho_i \sim 1$, which then also implies that $k_\parallel \rho_i \sim \epsilon$. In turbulent space and astrophysical plasmas, L can be associated with the outer scale of MHD range turbulence [131]. Since the outer scale mean field variations cannot be assumed anisotropic, we then also require $k_\parallel L \gg 1$ [5]. That is, we consider the fluctuations well below the MHD outer scale, where an anisotropy is expected to develop naturally [136].

Modern formulations of gyrokinetic equations involve Lagrangian and Hamiltonian Lie-transform perturbation methods [130], most notably with application to fusion plasmas. For our purpose, we follow a more traditional formulation of Howes *et al.* [131], which can be viewed as an adaptation of the original work of Frieman and Chen [129] to astrophysical plasmas in a homogeneous background in slab geometry. Below, we merely summarize the main equations. Further details can be found in Ref. [131].

The gyrokinetic equations are solved in a reduced, five-dimensional phase space. The reduction to five dimensions is made possible by averaging over the fast particle cyclotron motion, leaving only one degree of freedom for the field-perpendicular motion. To this end, the ring average at fixed particle gyrocenter is introduced as

$$\langle a \rangle_{\mathbf{R}_s} = \frac{1}{2\pi} \oint \mathrm{d}\theta \; a\left(\mathbf{R}_s - \frac{\mathbf{v} \times \hat{\mathbf{e}}_z}{\Omega_{cs}}, \mathbf{v}, t \right), \tag{2.31}$$

where $\mathbf{R}_s = \mathbf{r} + (\mathbf{v} \times \hat{\mathbf{e}}_z)/\Omega_{cs}$ is the particle gyrocenter position, θ is the gyroangle, $\hat{\mathbf{e}}_z = \mathbf{B}_0/B_0$ is the unit vector in the mean field (z) direction, and $a(\mathbf{r}, \mathbf{v}, t)$ is some arbitrary function. The above reduction yields the new phase-space coordinates $(\mathbf{R}_s, \mu_s, v_\parallel)$, where $\mu_s = m_s v_\perp^2/2B_0$ is the magnetic moment and $v_\parallel = \mathbf{v} \cdot \hat{\mathbf{e}}_z$ is the velocity along the mean field. The particle magnetic moment is an (adiabatic) invariant to lowest order in the expansion. Next, the gyrocenter distribution function h_s is introduced, which can be written to order ϵ as

$$h_s(\mathbf{R}_s, \mu_s, v_\parallel, t) = \delta f_s(\mathbf{r}, \mathbf{v}, t) + \frac{q_s \delta\varphi(\mathbf{r}, t)}{T_{0s}} F_{0s}(v), \tag{2.32}$$

where $\delta\varphi$ is the perturbed electrostatic potential and T_{0s} is the species background temperature. The distribution of particle gyrocenters is independent of the gyrophase angle at fixed $\mathbf{R}_s$. The second term on the right-hand side accounts for the Boltzmann part of the response to the electrostatic potential. Written in terms of h_s, the reduced kinetic equation takes the form

$$\frac{\partial h_s}{\partial t} + v_\parallel \hat{\mathbf{e}}_z \cdot \frac{\partial h_s}{\partial \mathbf{R}_s} + \frac{c}{B_0}\Big\{\langle\chi\rangle_{\mathbf{R}_s},\, h_s\Big\} - q_s \frac{\partial \langle\chi\rangle_{\mathbf{R}_s}}{\partial t}\frac{F_{0s}}{T_{0s}} = C[h_s], \tag{2.33}$$

where $\{\langle\chi\rangle_{\mathbf{R}_s},\, h_s\} = \hat{\mathbf{e}}_z \cdot (\partial\langle\chi\rangle_{\mathbf{R}_s}/\partial\mathbf{R}_s \times \partial h_s/\partial\mathbf{R}_s)$ is the Poisson bracket, $\chi = \varphi - \mathbf{v}\cdot\mathbf{A}/c$ is the gyrokinetic potential, and $C[h_s]$ is a (linearized) collision operator. The kinetic equation for h_s is supplemented with the Maxwell equations for the self-consistent fields. Since the sources in the Maxwell equations are written in the physical particle coordinates, we need to introduce the gyro-average at a fixed particle position:

$$\langle a\rangle_{\mathbf{r}} = \frac{1}{2\pi}\oint \mathrm{d}\theta\; a\left(\mathbf{r} + \frac{\mathbf{v}\times\hat{\mathbf{e}}_z}{\Omega_{cs}}, \mathbf{v}, t\right), \tag{2.34}$$

where $a(\mathbf{R}_s, \mathbf{v}, t)$ is a function of the gyrocenter position and $\mathbf{v} = v_\parallel\hat{\mathbf{e}}_z + v_\perp(\cos\theta\hat{\mathbf{e}}_x + \sin\theta\hat{\mathbf{e}}_y)$. For the electrostatic potential, the Maxwell equations translate into a quasi-neutrality condition,

$$\sum_s q_s \delta n_s = \sum_s \left(-\frac{q_s^2 n_{0s}}{T_{0s}}\varphi + q_s \int \mathrm{d}^3\mathbf{v}\,\langle h_s\rangle_{\mathbf{r}}\right) = 0, \tag{2.35}$$

and the vector potential is determined from a pre-Maxwell version of Ampere's law:

$$-\nabla_\perp^2 A_\parallel = \sum_s \frac{4\pi}{c} q_s \int \mathrm{d}^3\mathbf{v}\, v_\parallel \langle h_s\rangle_{\mathbf{r}}, \tag{2.36}$$

$$\nabla_\perp \delta B_\parallel = -\hat{\mathbf{e}}_z \times \nabla_\perp^2 \mathbf{A}_\perp = \sum_s \frac{4\pi}{c} q_s \int \mathrm{d}^3\mathbf{v}\,\langle(\hat{\mathbf{e}}_z \times \mathbf{v}) h_s\rangle_{\mathbf{r}}. \tag{2.37}$$

Equations (2.31)–(2.37) constitute the GK model for a homogeneous plasma in slab geometry, as detailed in Howes *et al.* [131]. It is worth emphasizing that the expansion parameter ϵ does not appear explicitly in the equations solved by GK codes. Instead, all expressions and quantities are rescaled by their appropriate power of ϵ. No inconsistency occurs due to such rescaling, since only quantities of the same order in ϵ are kept in any equation. From the rescaled equations, one may *a posteriori* recover any quantity in absolute physical units by choosing a representative value for ϵ.

The GK description is relevant to low-frequency, strongly magnetized plasma turbulence. The assumption of small fluctuations and strong anisotropy might seem severely restrictive at first glance. Observational, theoretical, and numerical results strongly suggest that the MHD range turbulence in magnetized astrophysical plasmas is predominantly low-frequency, Alfvénic, and increasingly anisotropic with decreasing scale ([5, 32, 131, 136–140], see Chapter 3). Because the turbulent energy cascade time decreases with scale, the

fluctuating magnetic fields at large scales appear nearly constant on the time scale of the much smaller-sized eddies. Furthermore, the scale-dependent fluctuation amplitudes decrease as the energy is anisotropically cascaded to higher perpendicular wavenumbers. These circumstances imply that the small-scale fluctuations (measured relative to a *local* mean background) eventually fulfill the GK ordering. Thus, even though the turbulent fluctuations just below L might be large and nearly isotropic, the GK description is still relevant at scales much smaller than L, provided that ρ_i/L is sufficiently small [131]. There are several potential caveats to that, some of which are critically examined in this Thesis. For example, while it is true that most of the energy in MHD range turbulence is carried by low-frequency fluctuations [141], the situation is presently less clear in the wave-dispersive kinetic range ($k_\perp \rho_i \gtrsim 1$), where high-frequency waves such as ion Bernstein modes [40, 142] or whistlers [81, 84, 143, 144] might be potentially relevant. Furthermore, the probability distribution functions of the turbulent fluctuations around $k_\perp \rho_i \sim 1$ are known to be inherently non-Gaussian [53, 78, 145, 146], such that a certain fraction of the fluctuations significantly exceeds the root-mean-square value. Thus, it may happen that a certain fraction of the small-scale eddies does not satisfy the GK ordering, even if this ordering is otherwise well satisfied on average. As was recently suggested [55], the presence of heavy-tailed, non-Gaussian fluctuations around $k_\perp \rho_i \sim 1$ may significantly enhance the importance of kinetic effects beyond GK, such as stochastic ion heating [147, 148]. Another potentially problematic aspect is the definition of the background distribution function F_{0s}. Due to the low collisionality, the background particle distributions in astrophysical plasmas are typically anisotropic and non-Maxwellian [28, 149]. Such non-equilibrium particle distributions may drive various kinetic plasma instabilities [93, 95, 133, 150], which are beyond the scope of the GK model. Very recently, a generalized GK framework for astrophysical plasmas with anisotropic background distributions was introduced [151]. To our knowledge, the model has not yet been applied to kinetic range turbulence studies.

2.3.3 Kinetic reduced electron heating model (KREHM)

In Chapter 5, we also include for reference simulation data from the so-called kinetic reduced electron heating model (KREHM) [102], which is obtained from the GK description in the low plasma beta limit [102]. The formal low beta restriction takes the form

$$\sqrt{\beta_e} \sim \sqrt{m_e/m_i} \ll 1, \tag{2.38}$$

where β_e is the electron beta and m_e/m_i is the electron-ion mass ratio. The ion beta may be either comparable to or somewhat smaller than the electron beta. That is, the ion-electron temperature ratio is a free parameter of order unity or smaller. Note that, even though the plasma beta is assumed small, KREHM primarily concerns small-scale fluctuations with $k_\perp \rho_i \sim 1$. Due to the low beta assumption, the ions have thermal velocities much smaller then the Alfvén speed and cannot efficiently exchange energy with the electromagnetic fluctuations, so that the ion heating is ordered out of the model. The only ion kinetic effect that remains are ion FLR corrections in the GK equation for the electrostatic potential.

On the other hand, the electrons are treated in the drift-kinetic approximation, valid for $k_\perp \rho_e \ll 1$, which retains electron heating via the Landau damping channel [101, 102]. The electron drift-kinetic equation can be written as

$$\frac{\mathrm{d}g_e}{\mathrm{d}t} + v_\parallel \nabla_\parallel \left(g_e - \frac{\delta T_{\parallel e}}{T_{0e}} F_{0e} \right) - \left(1 - \frac{2v_\parallel^2}{v_{\mathrm{th},e}^2} \right) F_{0e} \nabla_\parallel \frac{e}{cm_e} d_e^2 \nabla_\perp^2 A_\parallel = C[g_e], \tag{2.39}$$

where

$$g_e(\mathbf{r}, \mathbf{v}, t) = \delta f_e(\mathbf{r},\, \mathbf{v}, t) - \left[\delta n_e(\mathbf{r}, t)/n_0 + 2v_\parallel u_{\parallel e}(\mathbf{r}, t)/v_{\mathrm{th},e}^2 \right] F_{0e}(v) \tag{2.40}$$

is the modified perturbed distribution function [102], $C[g_e]$ is a collision term,

$$\frac{\mathrm{d}}{\mathrm{d}t} = \frac{\partial}{\partial t} + \frac{c}{B_0}\{\varphi, \dots\}, \qquad \nabla_\parallel = \frac{\partial}{\partial z} - \frac{1}{B_0}\{A_\parallel, \dots\}, \tag{2.41}$$

are, respectively, the total time derivative and the derivative along the *total* magnetic field, and $\{P, Q\} = \hat{\mathbf{e}}_z \cdot (\nabla_\perp P \times \nabla_\perp Q)$ is the Poisson bracket. All other symbols have their standard meanings as in previous sections (see also Appendix C). The modified distribution g_e is free from any density and fluid velocity contributions [101]. The density fluctuations, δn_e, and the parallel vector potential, $d_e^2 \nabla_\perp^2 A_\parallel = (m_e c/e) u_{\parallel e}$, are evolved separately with a set of fluidlike equations [102, 152]:

$$\frac{1}{n_0}\frac{\mathrm{d}\delta n_e}{\mathrm{d}t} = -\nabla_\parallel \frac{e}{cm_e} d_e^2 \nabla_\perp^2 A_\parallel, \tag{2.42}$$

$$\frac{\mathrm{d}}{\mathrm{d}t}(A_\parallel - d_e^2 \nabla_\perp^2 A_\parallel) = -c\frac{\partial \varphi}{\partial z} + \frac{cT_{0e}}{e}\nabla_\parallel \left(\frac{\delta n_e}{n_0} + \frac{\delta T_{\parallel e}}{T_{0e}} \right). \tag{2.43}$$

Finally, assuming singly charged ions, the electrostatic potential and the density are related by $\delta n_e = (n_0 e/T_{0i})(\widehat{\Gamma}_0 - 1)\varphi$, where $\widehat{\Gamma}_0$ is the inverse Fourier transform of $\Gamma_0 = I_0(k_\perp^2 \rho_i^2/2)\exp(-k_\perp^2 \rho_i^2/2)$ and $I_0(z)$ is the modified Bessel function. Because the equations do not explicitly depend on velocities perpendicular to the mean magnetic field, the perpendicular motion may be integrated out, leaving only the parallel velocity dependence for g_e. As shown in Ref. [102], g_e can be then conveniently expanded in a Hermite polynomial basis for $v_\parallel$.

KREHM was primarily designed to capture the essential physics of magnetic reconnection in low-beta, magnetized plasmas [102, 152]. The low-beta assumption is, however, not typical for astrophysical plasmas. In our case, the KREHM simulation data are included mainly to clarify the impact of (finite) plasma beta and of electron Landau damping on the turbulent cascade.

Chapter 3

The phenomenology of astrophysical plasma turbulence

Despite decades of research, our present understanding of astrophysical plasma turbulence is predominantly based upon a set of phenomenological models, whereas exact analytical results are only few [69, 153–156]. Such models are typically obtained from a set of reasonable, thought not rigorously justified, simplifying assumptions. These, in turn, enable one to obtain approximate turbulence scaling predictions. It is for this reason that detailed numerical simulations have become an indispensable tool in the field, since they provide critical tests for existing theories and inspire the design of more refined models. The presently leading theories of MHD range turbulence have been quite extensively examined in simulations [138, 139, 157–160], but only few stringent tests of kinetic range models have been made so far. This Thesis represents some of the first attempts along these lines, in terms of first principles, three-dimensional (3D) kinetic simulations [78, 161]. Below, we summarize the basic phenomenology of astrophysical plasma turbulence, as envisioned by some of the presently leading models.

3.1 Kolmogorov's approach to turbulence

Most of the existing theories of astrophysical plasma turbulence can be viewed as adaptations of Kolmogorov's 1941 original work (hereafter, K41 [162, 163]) on hydrodynamic, high Reynolds number turbulence. We therefore first summarize the main features of the celebrated K41 theory. It is fair to mention that the type of turbulence analysis commonly attributed to Kolmogorov was around the same time independently pursued by several of his contemporaries, such as Obukhov [164], von Weizsäcker [165], Heisenberg [166], and Onsager [167], although the K41 theory is the one that is most widely known.

The relevant equation for incompressible, unmagnetized turbulent flows is the Navier-Stokes equation

$$\frac{\partial \mathbf{u}}{\partial t} + \mathbf{u} \cdot \nabla \mathbf{u} = -\nabla p + \nu \nabla^2 \mathbf{u} + \mathbf{f}, \tag{3.1}$$

where $\mathbf{u}$ is the fluid velocity, p is the kinematic pressure, ν is the kinematic viscosity, and $\mathbf{f}$ is an external force driving the turbulence. The strength of the nonlinear term relative to the dissipative term is quantified by the Reynolds number $R = L\delta u_L/\nu$, where L is a characteristic flow scale and δu_L is a characteristic velocity. Turbulence concerns regimes with very large Reynolds numbers, where the dissipative term is weak on the scale L. As is customary, the dynamics is often considered in a periodic domain. The turbulent field is then conveniently represented with a Fourier series as

$$\mathbf{u}(\mathbf{r}, t) = \sum_{\mathbf{k}} \mathbf{u}_{\mathbf{k}}(t) \exp(\mathrm{i}\, \mathbf{k} \cdot \mathbf{r}), \tag{3.2}$$

where $\mathbf{u}_{\mathbf{k}}(t)$ is the complex amplitude of the Fourier mode with wave vector $\mathbf{k}$. The Fourier representation gives a convenient scale decomposition for $\mathbf{u}$, with each wavenumber inversely proportional to a characteristic scale: $\ell \sim 1/k$. Generally speaking, the correspondence between Fourier wavenumbers and different scales (in real space) should be taken with some caution. This is due to the Fourier uncertainty principle ($\Delta x \Delta k > C$) [168, 169], which shows that a sharply localized signal in spectral space is completely delocalized in real space. Thus, one should not directly associate single Fourier modes with turbulence scales in situations where the local, real space structure of the turbulent field matters. An example is provided by the novel analysis presented in Chapter 7, where a wavelet decomposition is employed to circumvent the pitfalls of the standard Fourier analysis. Putting this technicality aside for now, we only note here that each scale should be in principle related to a spectral band of logarithmic width in Fourier space, rather than to a thin shell of wavenumbers.

Turbulence can be described as a self-organized, nonlinear redistribution of energy across different scales, aimed at enhancing the energy dissipation in a nominally weakly dissipative system. Central to the turbulence is therefore the scale-dependent energy conservation law. In spectral space, the energy balance takes the form

$$\frac{\partial E(\mathbf{k})}{\partial t} = T(\mathbf{k}) - D(\mathbf{k}) + P(\mathbf{k}), \tag{3.3}$$

where $E(\mathbf{k})$ is the energy density of a given mode, $T(\mathbf{k})$ is the nonlinear energy transfer into/from that mode, $D(\mathbf{k})$ is the dissipation, and $P(\mathbf{k})$ is the energy injection rate from the external force. For Navier-Stokes turbulence, the terms may be written as (e.g., [170–172]):

$$E(\mathbf{k}) = \frac{1}{2}|\mathbf{u}_{\mathbf{k}}|^2, \qquad D(\mathbf{k}) = 2\nu k^2 E(\mathbf{k}), \tag{3.4}$$

$$T(\mathbf{k}) = -\sum_{\mathbf{p}+\mathbf{q}=\mathbf{k}} \mathrm{Im}\Big\{(\mathbf{k}\cdot\mathbf{u}_{\mathbf{q}})(\mathbf{u}_{\mathbf{p}}\cdot\mathbf{u}_{-\mathbf{k}})\Big\}, \qquad P(\mathbf{k}) = \mathrm{Re}\Big\{\mathbf{f}_{\mathbf{k}}\cdot\mathbf{u}_{-\mathbf{k}}\Big\}. \tag{3.5}$$

In real space, the dissipative term takes the form

$$D(\mathbf{r}) = 2\nu\, \mathsf{S}\!:\!\mathsf{S}, \tag{3.6}$$

where $\mathsf{S} = [(\nabla\mathbf{u}) + (\nabla\mathbf{u})^{\mathrm{T}}]/2$ is the symmetrized strain rate tensor. Essentially, the dissipation may be locally enhanced by large-amplitude, small-scale velocity gradients. It is

instructive to consider a cumulative energy balance up to a given wavenumber scale k by summing Eq. (3.3) over all modes $\mathbf{k}'$ with $|\mathbf{k}'| \leq k$. This leads to [99]:

$$\frac{\partial \mathcal{E}(k)}{\partial t} = -\Pi(k) - \mathcal{D}(k) + \mathcal{P}(k), \tag{3.7}$$

where $\mathcal{E}(k)$ is the cumulative energy content up to scale k, $\mathcal{D}(k)$ is the cumulative dissipation, $\mathcal{P}(k)$ is the cumulative energy injection, and $\Pi(k)$ is the net energy transfer to wavenumbers larger than k. Let $\ell_{\min} \sim 1/k_{\max}$ be the smallest physical scale of the system. In steady state, we would have by means of energy conservation:

$$P = \mathcal{P}(k_{\max}) = \mathcal{D}(k_{\max}) = D, \qquad \Pi(k_{\max}) = 0, \tag{3.8}$$

where P and D are, respectively, the total energy injection and dissipation rates. The existence of such a steady state, regardless of the smallness of the viscosity, is fundamental to the K41 phenomenological theory of turbulence. Indeed, present results on the subject strongly suggest that the turbulent dissipation maintains a finite value in the limit when $\nu \to 0$ [99, 100, 173]. This implies that the energy must be nonlinearly transferred from the weakly dissipative scale L to ever smaller scales, until the dissipation eventually becomes significant at a scale $\ell_\nu \ll L$.[1] On the other hand, in the intermediate range of scales between L and ℓ_ν, known as the inertial range, no significant dissipation or energy injection occurs. This led Kolmogorov to the key conjecture that the inertial range is characterized solely by the constant rate of energy flux, controlled by the large-scale energy injection, or equivalently by the small-scale, ν-independent dissipation. The statistical properties in the inertial range may be then deduced from simple scaling arguments. We may summarize the assumptions leading to the Kolmogorov-like phenomenological predictions as follows:[2]

- Statistical isotropy, homogeneity, and scale invariance,
- Constant energy flux across scales,
- Scale locality of interactions.

The first two assumptions are motivated by the conjectured existence of finite dissipation in the large Reynolds number limit, and by the large scale separation between the injection and dissipation scale in that same limit. The assumption of scale locality may be, for example, motivated by noticing that the nonlinear transfer (see Eqs. (3.5)) into mode $\mathbf{k}$ from modes $\mathbf{p}, \mathbf{q}$ must satisfy: $\mathbf{p} + \mathbf{q} = \mathbf{k}$. Thus, if at some instance in time the energy fills up the spectral space up to a given k, the nonlinear term can redistribute that energy at most up to $2k$ but not further. It is possible to make the scale locality argument more rigorous [168, 174]. To conclude, we summarize the Kolmogorov-like phenomenological picture of turbulence in Fig. 3.1.

[1] In Navier-Stokes turbulence, this is made possible by the vortex stretching term in the vorticity equation, $\mathsf{S} \cdot (\nabla \times \mathbf{u})$, by which the large-scale eddies perform deformation work on the smaller-scale vortices.

[2] Note that in the original K41 theory [162, 163], these assumptions were formulated somewhat differently.

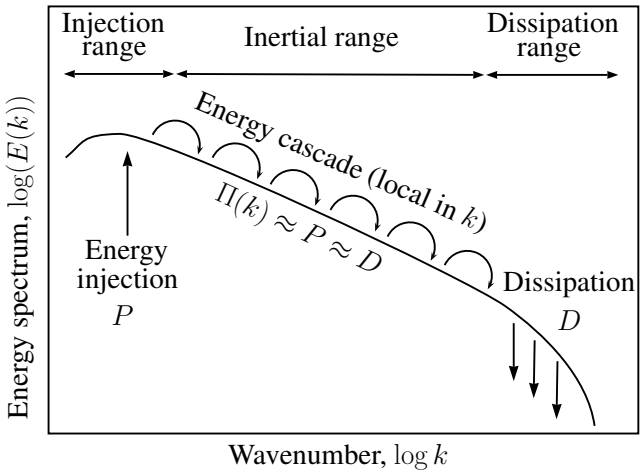

Figure 3.1: Illustration of the turbulent energy cascade, embraced in the works of Kolmogorov and his contemporaries. The notion of a "cascade" in fluid turbulence is commonly attributed to Richardson [175]. $E(k)$ is the one-dimensional energy spectrum, obtained by integrating the 3D spectrum over all possible wave vector directions at a fixed $k = |\mathbf{k}|$.

Given the assumptions introduced above, the statistics of the turbulent velocity field in the inertial range may be obtained from simple scaling arguments as follows. Let δu_ℓ be a velocity fluctuation at scale $\ell \sim 1/k$. By locality of interactions, the energy flux across ℓ can be estimated from δu_ℓ and ℓ alone as

$$\Pi_\ell \sim \frac{\delta u_\ell^2}{\tau_{c,\ell}} \sim \frac{\delta u_\ell^3}{\ell}, \tag{3.9}$$

where $\tau_{c,\ell} = \ell/\delta u_\ell$ is the energy cascade time, i.e. the time it takes to pass the energy across scale ℓ. On dimensional grounds, the cascade time must equal the characteristic nonlinear time $\tau_{\mathrm{nl},\ell}$, simply because there is no other alternative to construct a time scale from δu_ℓ and ℓ alone. Since the inertial range flux equals the energy injection from scale L, we can also estimate $\Pi_\ell \sim \delta u_L^3/L$. Thus, the inertial range velocity scaling is given by

$$\delta u_\ell \sim \left(\frac{\ell}{L}\right)^{1/3} \delta u_L. \tag{3.10}$$

For second-order statistics, it is customary to represent the scaling in terms of the one-dimensional (1D) energy spectrum $E(k)$, defined in the continuous limit as

$$E = \int_0^\infty E(k)\,\mathrm{d}k = \int_0^\infty \frac{\mathrm{d}\mathcal{E}(k)}{\mathrm{d}k}\,\mathrm{d}k\,, \tag{3.11}$$

where E is the total energy. The 1D energy spectrum is described by the celebrated five-thirds law:

$$E(k) \propto k^{-5/3}, \tag{3.12}$$

which is obtained from (3.10) by noticing that $E(k) \propto \delta u_k^2/k$, with $k \sim 1/\ell$.[3] All presently leading models of astrophysical plasma turbulence follow the same line of reasoning to obtain the energy spectrum, albeit with a few very important modifications specific to magnetized plasmas.

A significant challenge for Kolmogorov-like phenomenological turbulence theories is to account for the inherent violation of statistical scale invariance in turbulent flows, known as the phenomenon of intermittency [53, 99]. In short, the scaling (3.9) may be in fact formulated much more rigorously (e.g., see [99] and references therein), but only in the sense of statistical mean values for Π_ℓ and δu_ℓ^3. However, to straightforwardly obtain the scalings of arbitrary moments of δu_ℓ, it is necessary to assume that the entire distribution of Π_ℓ is scale independent. As it turns out, this is generally not the case because the dissipation is concentrated in fine-scale, intermittent structures and its statistical distribution as seen on different scales is non-universal. In practice, intermittency leads to the gradual emergence of heavy-tailed, non-Gaussian probability distribution functions with decreasing scale. Intermittency corrections therefore tend to be more pronounced for high-order moments of δu_ℓ, which are more sensitive to the large values at the tails of the probability distribution.

3.2 MHD range theories

Let us now consider inertial range turbulence in magnetized plasmas, above the ion and electron kinetic scales, where the turbulence can be approximately described with the magnetohydrodynamic (MHD) equations [32, 176, 177]. Recent advances in MHD turbulence studies have provided valuable hints for interpreting certain aspects of the kinetic-scale simulations presented in this Thesis. For this reason, we briefly summarize here the current state of the art in MHD turbulence. As is often done, we restrict the discussion to the incompressible part of the dynamics. It can be argued *a posteriori* that the turbulent cascade is dominated by the incompressible Alfvénic fluctuations, which passively mix the subdominant compressive modes [2, 139, 178–181]. The fluid equations of incompressible MHD can be written as

$$\frac{\partial \mathbf{u}}{\partial t} + \mathbf{u}\cdot\nabla\mathbf{u} = \frac{1}{4\pi\rho_m}\mathbf{B}\cdot\nabla\mathbf{B} - \nabla p + \nu\nabla^2\mathbf{u} + \mathbf{f}, \tag{3.13}$$

$$\frac{\partial \mathbf{B}}{\partial t} + \mathbf{u}\cdot\nabla\mathbf{B} = \mathbf{B}\cdot\nabla\mathbf{u} + \eta\nabla^2\mathbf{B}, \tag{3.14}$$

where $\mathbf{u}$ is the fluid velocity, $\mathbf{B}$ is the magnetic field, $\mathbf{f}$ is an external force, ν is the kinematic viscosity, η is the magnetic diffusivity, ρ_m is the mass density, and p is the total pressure (kinetic plus magnetic) divided by ρ_m. Compared to the Navier-Stokes equation (3.1), an additional dimensionless parameter emerges—the magnetic Reynolds number,

[3] The conversion comes from the fact that δu_ℓ is usually considered as a high-pass filtered field with a cutoff scale $k \sim 1/\ell$, whereas $E(k)$ is obtained by summing the energy over thin spectral shells of fixed width. Thus, there is a factor of $1/k$ in the conversion. Alternatively, the same conversion is also obtained if δu_ℓ is defined via a band-pass filter of width proportional to its center wavenumber k.

$R_m = L\delta u_L/\eta$. Naturally, the regime of interest here is the one where $R, R_m \gg 1$. It is instructive to rearrange Eqs. (3.13) and (3.14) into a symmetric form. To this end, we introduce the following notation:

$$\mathbf{B} = \mathbf{B}_0 + \sqrt{4\pi\rho_m}\,\mathbf{b}, \qquad\qquad \mathbf{z}^{\pm} = \mathbf{u} \pm \mathbf{b}, \tag{3.15}$$

where $\mathbf{B}_0$ is the uniform mean magnetic field, $\mathbf{b}$ is the rescaled fluctuating field, and $\mathbf{z}^{\pm}$ are the Elsässer variables [182]. Note that $\mathbf{b}$ has the physical units of velocity. In terms of the newly introduced variables, we can rewrite Eqs. (3.13) and (3.14) into

$$\frac{\partial \mathbf{z}^{\pm}}{\partial t} \mp \mathbf{v}_A \cdot \nabla \mathbf{z}^{\pm} + \mathbf{z}^{\mp} \cdot \nabla \mathbf{z}^{\pm} = -\nabla p + \frac{\nu+\eta}{2}\nabla^2 \mathbf{z}^{\pm} + \frac{\nu-\eta}{2}\nabla^2 \mathbf{z}^{\mp} + \mathbf{f}, \tag{3.16}$$

where $\mathbf{v}_A = \mathbf{B}_0/\sqrt{4\pi\rho_m}$ is the Alfvén speed. In the plasma rest frame, Eq. (3.16) admits general solutions of the form $\mathbf{z}^{\pm} = \mathbf{g}(\mathbf{r} \mp \mathbf{v}_A t)$, with either $\mathbf{z}^{+} = 0$ or $\mathbf{z}^{-} = 0$. Such solutions correspond to non-interacting Alfvén wave packets, of arbitrary shape, propagating either upward or downward the mean magnetic field with a speed v_A. In such states, $\mathbf{u}$ and $\mathbf{b}$ are either exactly aligned or anti-aligned, and the nonlinear term is identically zero. Thus, in incompressible MHD turbulence the nonlinear interaction is essentially restricted to counterpropagating Alfvén wave packets. In addition, it is worth noting that, in the absence of dissipation and forcing, Eq. (3.16) separately conserves the mean Elsässer energies $E^{\pm} = \langle |\mathbf{z}^{\pm}|^2 \rangle/2$. The total energy E and cross-helicity H_c are as well ideally conserved quantities, because they are obtained from linear combinations of $E^{\pm}$ as

$$E = \langle |\mathbf{u}|^2 + |\mathbf{b}|^2 \rangle/2 = (E^{+} + E^{-})/2, \qquad H_c = \langle \mathbf{u} \cdot \mathbf{b} \rangle = (E^{+} - E^{-})/2. \tag{3.17}$$

Attempts to determine the statistical properties of MHD range turbulence have mainly followed the line of reasoning of Kolmogorov. Following his ideas, one is tempted to write

$$\Pi \sim \frac{E_\lambda}{\tau_{c,\lambda}}, \tag{3.18}$$

where λ is some inertial range scale, E_λ is the scale-dependent energy, Π is the (constant) energy flux, and $\tau_{c,\lambda}$ is the energy cascade time. Here we are met with some ambiguity, since it is not *a priori* clear how $\tau_{c,\lambda}$ should be defined or which energy to take. Apart from the nonlinear times $\tau^{\pm}_{\mathrm{nl},\lambda} \sim \lambda/\delta z^{\mp}_{\lambda}$, the system also contains the linear Alfvén wave-crossing time scales $\tau^{\pm}_{A,\ell^{\pm}_{\parallel}} \sim \ell^{\pm}_{\parallel}/v_A$, where $\ell^{\pm}_{\parallel}$ is a characteristic field-parallel scale of a given wave packet. There is no firm basis for assuming isotropy, i.e. $\lambda \sim \ell^{\pm}_{\parallel}$, although this was done in early models of MHD turbulence [183, 184]. Indeed, already some early simulations and observations [137, 185, 186], made over two decades ago, showed that MHD plasma turbulence is inherently anisotropic with respect to the mean magnetic field direction, with most of the energy contained in the nearly field-perpendicular wavenumbers. This empirical fact suggests that λ should be identified as the field-perpendicular scale. What then still remains to be determined are the dependence of $\ell^{\pm}_{\parallel}$ on λ and the energy cascade times.

3.2.1 Goldreich-Sridhar '95: The critical balance conjecture

A far-reaching idea for the resolution of the ambiguities in determining the MHD turbulence cascade time and its anisotropy was introduced in the 1995 work of Goldreich and Sridhar (GS95, [136]), which was preceded by their 1994 paper on weak MHD turbulence [187]. GS95 first restricts the discussion to so-called balanced regimes with $E^+ \sim E^-$. This appears to be at present an almost inevitable simplifying assumption, which renders the time scales of δz^+ and δz^- equal to order unity. Thus, either of the two fields may be used to estimate the nonlinear time and the energy at a given scale. To determine the cascade time, GS95 makes the key conjecture that ratio of linear to nonlinear times is a constant of order unity:

$$\chi \sim \frac{\tau_{A,\ell_\parallel}}{\tau_{\mathrm{nl},\lambda}} \sim 1. \tag{3.19}$$

Relation (3.19) is known as the *critical balance conjecture* and the ratio χ is the *nonlinearity parameter*. The conjecture allows to identify the energy cascade time $\tau_{c,\lambda}$ with either of the two MHD time scales ($\tau_{\mathrm{nl},\lambda}$ or $\tau_{A,\ell_\parallel}$). The general idea of critical balance is also a key concept in most phenomenological models of kinetic range plasma turbulence (see Sec. 3.3).

Theoretical arguments, although lacking a rigorous proof, in support of critical balance can be given by considering the opposite cases of over-strong turbulence with $\chi \gg 1$ or weak turbulence with $\chi \ll 1$ [188]. The hypothetical over-strong regime can be dismissed based on a causality argument [189, 190] as follows. Physically, $\chi \gg 1$ implies nearly two-dimensional (2D) turbulent structures with $\ell_\parallel \gg \ell_* \sim v_A \tau_{\mathrm{nl},\lambda}$. The information between two perpendicular planes cannot propagate faster than at the speed v_A so that $\ell_* \sim v_A \tau_{\mathrm{nl},\lambda}$ is the maximal parallel coherence length on the time scale $\tau_{\mathrm{nl},\lambda}$. Beyond this point, the fluctuations decorrelate, which means that $\chi \gg 1$ is effectively unsustainable and we must have $\chi \lesssim 1$. The case $\chi \ll 1$ is more subtle and may be treated analytically in the weak turbulence formalism [191, 192]. At a qualitative level, the key aspect to consider is the weak interaction between two Alfvén-wave modes with wave vectors $\mathbf{k}_1 = \mathbf{k}_{\perp 1} + \mathbf{k}_{\parallel 1}$ and $\mathbf{k}_2 = \mathbf{k}_{\perp 2} + \mathbf{k}_{\parallel 2}$, producing a mode with wave vector $\mathbf{k}_3 = \mathbf{k}_{\perp 3} + \mathbf{k}_{\parallel 3}$, where the subscripts "$\parallel$" and "$\perp$" denote, respectively, the components parallel and perpendicular to $\mathbf{B}_0$. Such interaction must satisfy a resonance condition [185, 193]: $\mathbf{k}_1 + \mathbf{k}_2 = \mathbf{k}_3$ and $\omega_A(\mathbf{k}_1) + \omega_A(\mathbf{k}_2) = \omega_A(\mathbf{k}_3)$, where $\omega_A(\mathbf{k}) = |k_\parallel| v_A$ is the Alfvén wave frequency. The resonance can only be satisfied if $k_{\parallel 1} = k_{\parallel 3}$ and $k_{\parallel 2} = 0$. Thus, the weak interaction is mediated by zero-frequency modes and it does not increase $k_\parallel$. If we treat the angle between $\mathbf{k}_{\perp 1}$ and $\mathbf{k}_{\perp 2}$ as a random, uniformly distributed variable, we also have one average $k_{\perp 3} > k_{\perp 1}, k_{\perp 2}$. This shows that there is on average an energy cascade in $k_\perp$ only. Using $\lambda \sim 1/k_\perp$ and $\ell_\parallel \sim 1/k_\parallel$, we see that χ must grow with $k_\perp$, unless $\delta z_{k_\perp}$ decays as $\sim 1/k_\perp$ or faster, which corresponds to a perpendicular wavenumber spectrum of the form $E^\pm(k_\perp) \propto k_\perp^{-3}$ or steeper. Analytical calculations and numerical simulations show that the (balanced) weak turbulence spectrum is given by $E^\pm(k_\perp) \propto k_\perp^{-2}$ [191, 192, 194, 195]. Therefore, the nonlinearity parameter increases with $k_\perp$ until $\chi \sim 1$, where the turbulence is no longer weak. In conclusion, as argued above, critical balance is the natural state of MHD turbulence, since $\chi \ll 1$ and $\chi \gg 1$ are both asymptotically unsustainable.

Using the GS95 critical balance conjecture (3.19), alongside with the scale locality assumption, the energy spectrum of incompressible MHD turbulence and its anisotropy can be straightforwardly determined.[4] By approximating the energy cascade time in (3.18) with the nonlinear time $\tau_{\mathrm{nl},\lambda} \sim \lambda/\delta z_\lambda$, we recover a Kolmogorov-like scaling:

$$\delta z_\lambda \sim \left(\frac{\lambda}{L}\right)^{1/3} \delta z_L, \tag{3.20}$$

where L is the outer scale of the turbulence. Unlike in unmagnetized hydrodynamic turbulence, λ is measured here perpendicular to the mean magnetic field direction. The corresponding GS95 energy spectrum of balanced, incompressible MHD turbulence as a function of $k_\perp$ is

$$E^{\pm}(k_\perp) \propto k_\perp^{-5/3}. \tag{3.21}$$

Because $E = (E^+ + E^-)/2$, the total energy spectrum $E(k_\perp)$ takes the same form as $E^{\pm}(k_\perp)$. It is worth noting that the critical balance conjecture is not invoked explicitly to obtain $E^{\pm}(k_\perp)$, but only implicitly as a justification for the choice $\tau_{c,\lambda} \sim \tau_{\mathrm{nl},\lambda}$. Next, using the perpendicular scaling (3.20) and critical balance (3.19), we obtain the GS95 turbulence anisotropy prediction:

$$\ell_\parallel \sim \lambda^{2/3} L^{1/3} (v_A/\delta z_L). \tag{3.22}$$

In spectral space, this corresponds to $k_\parallel \propto k_\perp^{2/3}$, where $k_\parallel$ is a characteristic parallel wavenumber at perpendicular scale $\lambda \sim 1/k_\perp$.[5] Finally, the 1D energy spectrum as a function of $k_\parallel$ is

$$E^{\pm}(k_\parallel) \propto k_\parallel^{-2}. \tag{3.23}$$

This is obtained by inserting the linear time $\tau_{A,\ell_\parallel} \sim \ell_\parallel/v_A$ as the cascade time into (3.18).

In summary, the GS95 model predicts a Kolmogorov-like perpendicular energy spectrum and provides an explanation for the observed scale-dependent anisotropy of MHD turbulence based on the critical balance conjecture. Some years after the GS95 model emerged, the $k_\parallel \propto k_\perp^{2/3}$ anisotropy scaling was indeed confirmed in numerical simulations [138, 157, 199], within the computational limits of high-performance simulations around that time. Moreover, the $E^{\pm}(k_\parallel) \propto k_\parallel^{-2}$ spectrum is presently supported by state-of-the-art solar wind observations and simulations [140, 181, 200, 201]. On the other hand, simulations following the GS95 work showed that the total energy spectrum with respect to $k_\perp$ is better described by $E(k_\perp) \propto k_\perp^{-3/2}$, contrary to the predicted $E(k_\perp) \propto k_\perp^{-5/3}$ [157, 202]. The discrepancy prompted a revision of the model, which was eventually introduced in 2006 by Boldyrev (see Sec. 3.2.3).

[4] See Refs. [196, 197] for recent results on the scale locality of MHD turbulence. In short, the dominant scale interactions in MHD turbulence are essentially local, although perhaps to a slightly lesser degree than in Navier-Stokes turbulence.

[5] The $k_\parallel \propto k_\perp^{2/3}$ scaling was also obtained in a paper by Higdon [198], which preceded the GS95 model.

3.2.2 A remark on GS95: The local character of the anisotropy

It is worth commenting on an additional aspect of the GS95 model, which was swept under the rug in the preceding section. A point of frequent confusion throughout the years (even recently) has been the anisotropy relation $k_\parallel(k_\perp)$. How exactly should "$k_\parallel$" and "$k_\perp$" be understood here and measured? The original work of GS95 did not say how. In some works (e.g., [203, 204]) following GS95, the anisotropy was calculated based on the global mean magnetic field direction $\mathbf{B}_0$. This yielded results that were at odds with the $k_\parallel \propto k_\perp^{2/3}$ prediction. However, it was realized by Cho and Vishniac [138] that the anisotropy should be calculated with respect to a *local* mean magnetic field at a given perpendicular scale $\lambda \sim 1/k_\perp$. The motivation to do so is sketched in Fig. 3.2 and can be explained as follows. Consider a coarse-grained magnetic field $\mathbf{B}_{0,\lambda}$ at a scale λ. Such a field can be defined, for example, via a moving average over a volume of linear size λ. The coarse-grained field $\mathbf{B}_{0,\lambda}$ contains the global mean field $\mathbf{B}_0$ as well as the fluctuating field $\delta\mathbf{B}$ from scales somewhat larger than λ. Let $\ell_{0,\lambda}$ and $\tau_{0,\lambda}$ be some arbitrary space and time scale of the coarse-grained field $\mathbf{B}_{0,\lambda}$. We can estimate $\ell_{0,\lambda} \gtrsim 2\lambda$ and $\tau_{0,\lambda} \gtrsim 2^{2/3}\tau_{A,\ell_\parallel}$ (using (3.19) and (3.20)). In fact, because the fluctuation amplitude grows with scale, the dominant contribution to $\mathbf{B}_{0,\lambda}$ comes from scales satisfying the strong inequalities: $\ell_{0,\lambda} \gg \lambda$ and $\tau_{0,\lambda} \gg \tau_{A,\ell_\parallel} \sim \tau_{\mathrm{nl},\lambda}$. Thus, the coarse-grained field is essentially scale-separated from the dynamics on scale λ and may act as a *local* mean field on δz_λ. In other words, an isolated wave packet $\delta z(\lambda, \ell_\parallel)$ with a perpendicular size λ and parallel coherence length $\ell_\parallel$ will travel along and align itself with $\mathbf{B}_{0,\lambda}$ (see Fig. 3.2). The parallel coherence length $\ell_\parallel \sim 1/k_\parallel$ should be therefore measured along the local mean field $\mathbf{B}_{0,\lambda}$ at any given scale $\lambda \sim 1/k_\perp$. Failure to do so will result in an underestimate of the anisotropy, because any path between two perpendicular planes, taken along the local field lines, is generally longer than the path taken along the global magnetic field. It is important to note that $k_\parallel$ has to be measured locally even if the mean fluctuation amplitude $\epsilon \approx \delta B/B_0$ is asymptotically small, whenever $k_\parallel/k_\perp$ is of the same order as ϵ [205].[6] When the local mean magnetic field direction is used, the anisotropy of MHD turbulence closely matches the predicted $k_\parallel \propto k_\perp^{2/3}$ relation [138, 157, 199]. In the author's opinion, the importance of measuring the anisotropy locally cannot be overemphasized. The reason we discuss here this rather technical aspect in detail is because it emerges again in studies of kinetic range turbulence (see Sec. 3.3). In particular, in Chapters 6 and 7 we present first estimates of the *local* scale-dependent anisotropy, obtained from forced and decaying, fully kinetic simulations of sub-ion scale plasma turbulence.

3.2.3 Boldyrev '06: Dynamic alignment

As explained above, the GS95 model introduced some highly significant ideas, but it gives by no means a precise description of incompressible MHD turbulence. In particular, the total energy spectra obtained from numerical simulations seem to be closer to $E(k_\perp) \propto k_\perp^{-3/2}$ than to the predicted $E(k_\perp) \propto k_\perp^{-5/3}$ [157, 158, 202]. A resolution of the dilemma was

[6] In contrast, $\mathbf{k}_\perp$ can be measured perpendicular to $\mathbf{B}_0$ to lowest order in $\epsilon \approx \delta B/B_0$.

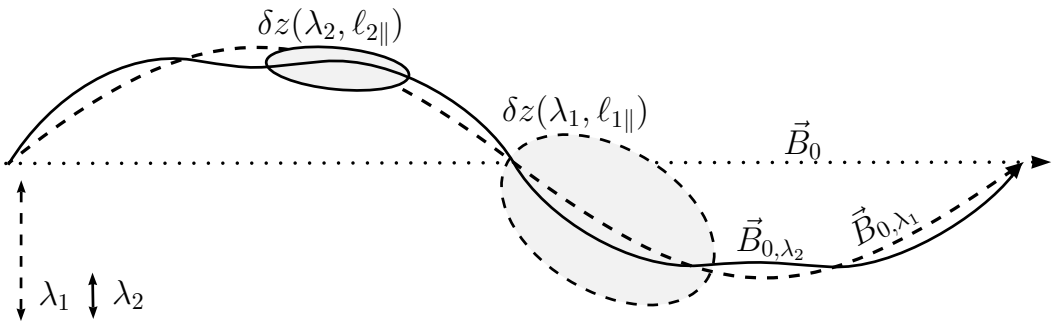

Figure 3.2: The local, scale-dependent anisotropy of magnetized plasma turbulence. In the figure, λ_1 and λ_2 are the perpendicular scales of two different eddies, which are aligned with the directions of $\mathbf{B}_{0,\lambda_1}$ and $\mathbf{B}_{0,\lambda_2}$, respectively. Similar drawings can be found in Refs. [138, 199].

proposed in 2006 by Boldyrev (B06, [206]). The starting point for the B06 model is an improved estimate of the nonlinear term in Eq. (3.16) on scale λ given by

$$|\delta\mathbf{z}_\lambda^\mp \cdot \nabla \delta\mathbf{z}_\lambda^\pm| \sim \frac{\sin\theta_\lambda}{\lambda}|\delta\mathbf{z}_\lambda^\mp||\delta\mathbf{z}_\lambda^\pm| \sim \frac{|\delta\mathbf{z}_\lambda^\pm|}{\tau_{\mathrm{nl},\lambda}^\pm}, \tag{3.24}$$

where θ_λ is a scale-dependent angle between $\delta\mathbf{z}_\lambda^+$ and $\delta\mathbf{z}_\lambda^-$. As argued by Boldyrev [206] (see also Beresnyak [207]), the correction is dynamically significant even on average. This can be qualitatively explained as follows. First, because of the strong anisotropy, the so-called pseudo-Alfvén modes with polarizations parallel to $\mathbf{B}_0$ are dynamically insignificant, since they are coupled only via the weak parallel gradients [136, 158]. What then remains are shear Alfvén fluctuations, $\mathbf{z}_\perp^\pm$, which are 2D solenoidal (i.e., $\nabla_\perp \cdot \mathbf{z}_\perp^\pm = 0$) and thus exhibit the strongest gradients in the transverse, field-perpendicular directions determined by $\mathbf{B}_0 \times \mathbf{z}_\perp^\pm$. This already implies that the GS95 estimate $|\delta\mathbf{z}_\lambda^\mp \cdot \nabla\delta\mathbf{z}_\lambda^\pm| \sim (1/\lambda)|\delta\mathbf{z}_\lambda^\mp||\delta\mathbf{z}_\lambda^\pm|$ is accurate only if $\delta\mathbf{z}_\lambda^-$ and $\delta\mathbf{z}_\lambda^+$ are nearly perpendicular. Secondly, MHD turbulence is in fact 3D anisotropic, due to its tendency to form strong electric currents sheets [13, 157, 208–210]. For the structures to be sheetlike, the wave packets need to maintain a fluctuation-direction (parallel to $\delta\mathbf{z}_{\perp\lambda}^\pm$) correlation length ξ longer than λ.[7] However, this is sustainable only if the distance ξ does not fall much outside the *locally* correlated region of $\delta\mathbf{z}_\lambda^\mp$ (see Fig. 3.3).[8] Otherwise, the sheetlike eddies would quickly decorrelate due to nonlinear interaction with different, non-coherent $\delta\mathbf{z}_\lambda^\mp$ fluctuations. Since we consider structures on scale λ and because the $\delta\mathbf{z}_\lambda^\mp$ vector forms an angle θ_λ with the $\delta\mathbf{z}_\lambda^\pm$ vector, the correlation distance can be estimated as $\xi \approx \lambda/\sin\theta_\lambda$. Thus, we see that $\sin\theta_\lambda \approx \lambda/\xi$ can be alternatively interpreted as the aspect ratio of the (sheetlike) structures.

In order to fix the spectral scalings, an estimate of θ_λ as a function of λ only is needed. This is obtained in B06 based on an uncertainty principle [158, 206], related to the stochastic

[7] Otherwise the structures would be tubes with $\xi \approx \lambda \ll l_\parallel$.

[8] This heuristic argument is implicitly based on the assumption that the turbulence is strong and scale-local.

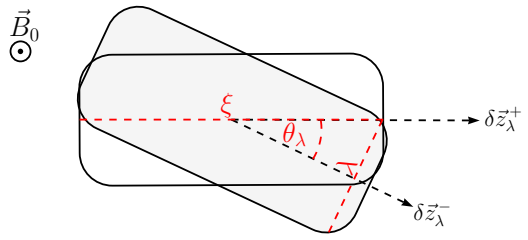

Figure 3.3: Sketch of the local (in space) interaction of $\delta\mathbf{z}_\lambda^+$ with $\delta\mathbf{z}_\lambda^-$, which constrains the fluctuation-direction correlation length ξ. The argument can be reversed for the interaction of $\delta\mathbf{z}_\lambda^-$ with $\delta\mathbf{z}_\lambda^+$, and therefore, ξ should be roughly the same for both. Note that the *local* nonlinear time should be defined separately for each field as $\tau_{\mathrm{nl},\lambda}^{\pm} \approx \lambda/(\sin\theta_\lambda \delta z_\lambda^{\mp})$, regardless if the turbulence is globally balanced, $\langle(\delta z_\lambda^+)^2\rangle \approx \langle(\delta z_\lambda^-)^2\rangle$, or not.

wandering of field lines within the structures. The reasoning goes as follows. Due to the mutual shearing of the Elsässer fields (or alternatively, due to the shearing of magnetic field lines by the velocity field), it is reasonable to expect that MHD turbulence tries to achieve maximal alignment at each scale.[9] However, perfect alignment ($\theta_\lambda = 0$) cannot be reached due to the angular uncertainty, associated with turbulent field line wandering:

$$\frac{\delta b_\lambda}{v_A} \sim \frac{\delta z_\lambda}{v_A} \propto \sin\theta_\lambda. \tag{3.25}$$

The above determines the scaling of the alignment angle uniquely and allows for a constant and finite energy flux across scales. Relation (3.25) should be understood in the sense of "typical" fluctuations.[10] By estimating the energy flux in the usual way as $\Pi \sim \delta z_\lambda^2/\tau_{\mathrm{nl},\lambda} \sim \delta z_{\ell_\parallel}^2/\tau_{A,\ell_\parallel}$ and using (3.25), we then immediately obtain the scalings:

$$\delta z_\lambda \propto \lambda^{1/4}, \qquad \delta z_{\ell_\parallel} \propto \ell_\parallel^{1/2}, \qquad \ell_\parallel \propto \lambda^{1/2}, \qquad \sin\theta_\lambda \propto \lambda^{1/4}. \tag{3.26}$$

The corresponding 1D energy spectra are

$$E(k_\perp) \propto k_\perp^{-3/2}, \qquad E(k_\parallel) \propto k_\parallel^{-2}. \tag{3.27}$$

As in GS95, these scalings are formally obtained for globally balanced regimes. Apart from the modified nonlinear time definition, $\tau_{\mathrm{nl},\lambda} \sim \lambda/(\delta z_\lambda \sin\theta_\lambda)$, the above derivation is analogous to GS95 and still invokes the critical balance conjecture (3.19).

Several recent works seem to support the $E(k_\perp) \propto k_\perp^{-3/2}$ and $\sin\theta_\lambda \propto \lambda^{1/4}$ scalings [158–160, 212, 213], although some of these studies have been questioned by Beresnyak

[9] This was mainly motivated in B06 based on the properties of decaying MHD turbulence, which typically favors maximally aligned states, $\mathbf{u} = \pm\mathbf{b}$, in the long-time limit due to the slow decay of the mean cross-helicity H_c [211]. It was then proposed that a similar effect develops locally in driven turbulence. However, an alternative motivation that does not appeal to the global cross-helicity dynamics has been given recently [57, 58].

[10] Locally, one should take $\max\{\delta z_\lambda^+, \delta z_\lambda^-\}/v_A \propto \sin\theta_\lambda$ [160].

[214, 215].[11] The consistency with the $\ell_\parallel \propto \lambda^{1/2}$ prediction is perhaps even less clear, mainly because it is challenging to estimate the anisotropy with sufficient accuracy to be able to claim that the scaling is more consistent with either B06 or GS95. Finally, we emphasize that the "average" alignment angle is very sensitive to the exact method of averaging, because the higher-amplitude fluctuations tend to be much more aligned [159, 160]. Moreover, it turns out that the probability distribution function of $\sin\theta_\lambda$ is scale-dependent [159, 160, 207]. This led to an interesting recent development, where the dynamic alignment is reinterpreted as an intermittency effect [57, 58].

We have discussed the alignment in terms of $\delta\mathbf{z}^+_\lambda$ and $\delta\mathbf{z}^-_\lambda$, although it may be also formulated in terms of $\delta\mathbf{u}_\lambda$ and $\delta\mathbf{b}_\lambda$ [158, 212]. Simulations show that these two angles are similar [160]. What is interesting in the context of this Thesis is that the alignment between $\delta\mathbf{u}_\lambda$ and $\delta\mathbf{b}_\lambda$, combined with its intermittent character, implies that the turbulent structures tend to *locally* restore the linear Alfvén wave polarization, $\delta\mathbf{u}_\lambda \approx \pm\delta\mathbf{b}_\lambda$, leading to a progressive weakening of the nonlinearity. In the language of critical balance, dynamic alignment can be in this sense viewed as the "last resort" of strongly nonlinear MHD turbulence to preserve the linear footprint of Alfvén waves, even within the large-amplitude structures. Indeed, the crude GS95 estimate (without alignment) $\tau_{\mathrm{nl},\lambda} \sim \lambda/\delta z_\lambda$ would imply that the local nonlinear time is significantly accelerated within the most intense structures with a large δz_λ. However, this does not seem to occur because the above-average amplitudes are compensated by the stronger alignment, which maintains $\tau_{\mathrm{nl},\lambda} \sim \tau_{A,\ell_\parallel}$. Evidence for such interpretation is provided in the recent work of Mallet *et al.* [159], which shows that the entire distribution of the (local) nonlinearity parameter, $\chi^\pm = \tau^\pm_{A,\ell_\parallel}/\tau^\pm_{\mathrm{nl},\lambda} = \ell^\pm_\parallel \delta z^\mp_\lambda \sin\theta_\lambda/(v_A\lambda)$, is scale-independent, even though the turbulent fields analyzed have strongly intermittent, scale-dependent statistics. In Chapter 7, we demonstrate the possibility of a similar effect in kinetic range plasma turbulence. There, the electron fluid velocity and the magnetic field preferentially align in a scale-dependent and intermittent manner, similar to the alignment between $\delta\mathbf{u}_\lambda$ and $\delta\mathbf{b}_\lambda$ in MHD turbulence.

To conclude, we emphasize that even MHD range plasma turbulence is presently an active area of research with many unknowns [32]. Even though considered highly significant by many experts, the GS95 and B06 models are not universally appreciated at present. Moreover, the GS95 and B06 phenomenologies fail to describe at least two significant and measurable effects: (i) the global imbalance between the E^+ and E^- Elsässer energies, and (ii) the scale-dependence of the residual energy $E_r = (\langle|\delta\mathbf{u}_\lambda|^2\rangle - \langle|\delta\mathbf{b}_\lambda|^2\rangle)/2$ [32, 217–219]. Globally imbalanced regimes are by construction outside the scope of GS95 or B06. The degree of imbalance may be quantified with the normalized cross-helicity $\sigma_c = (E^+ - E^-)/(E^+ + E^-)$, which takes values between -1 and 1. Especially the fast streams of the solar wind frequently exhibit high degrees of imbalance [32, 218]. To account

[11] Beresnyak's claims have been, in turn, questioned as well [158]. A possible resolution of the controversy is provided by Refs. [15, 216]. There, it is argued that the $E(k_\perp) \propto k_\perp^{-3/2}$ spectrum is genuine, but the scaling of the dissipation cutoff with the magnetic Reynolds number R_m may be more consistent with GS95. Moreover, if R_m is *very* large, the $E(k_\perp) \propto k_\perp^{-3/2}$ range may transition into a steeper power law at some critical $k_\perp$.

for the imbalance, various extended models have been proposed, with σ_c as an additional free parameter (e.g., [220, 221]). The residual energy is a scale-dependent quantity and may be quantified with a dimensionless ratio given by $\sigma_r = (\langle|\delta\mathbf{u}_\lambda|^2\rangle - \langle|\delta\mathbf{b}_\lambda|^2\rangle)/(\langle|\delta\mathbf{u}_\lambda|^2\rangle + \langle|\delta\mathbf{b}_\lambda|^2\rangle)$. Observations and simulations of MHD range turbulence indicate that the magnetic and kinetic energy spectra differ [213, 222, 223]. In particular, the magnetic spectrum is typically closer to $E_b(k_\perp) \propto k_\perp^{-5/3}$, whereas the velocity spectrum is usually better described by $E_u(k_\perp) \propto k_\perp^{-3/2}$, and it contains slightly less energy on average. This leads to a nontrivial residual energy spectrum. Roughly speaking, it is not difficult to see why the magnetic and velocity spectra need not be the same. The MHD equations (3.13) and (3.14) are non-symmetric in $\mathbf{u}$ and $\mathbf{b}$ and the nonlinearity is already substantially weakened in any state satisfying $\delta\mathbf{u}_\lambda \approx \pm C_\lambda \delta\mathbf{b}_\lambda$, where C_λ is some correction term of order unity. Therefore, there is no firm basis to argue that the magnetic and velocity spectra are in exact equipartition. Similar as for the imbalance, certain extended models have been proposed to explain the residual energy (e.g., [222, 224]). The results of this Thesis suggest that an analogous effect may exist in kinetic plasma turbulence. There, the linear physics of kinetic Alfvén waves would imply an exact equipartition between the density and perpendicular magnetic field fluctuations. However, for presumably similar reasons as in MHD turbulence, exact equipartition is not observed and the density spectrum is typically slightly shallower than the perpendicular magnetic spectrum (see Chapters 6 and 7).

3.3 The kinetic range: Kinetic Alfvén wave turbulence

Finally, we turn to the phenomenology of weakly collisional plasma turbulence in the kinetic range (at scales below the ion thermal gyroradius), which is at the main focus of this Thesis. Since even the MHD range turbulence is presently not fully understood, it should be of no surprise that the kinetic range is accordingly even less understood and explored. Various phenomenologies or, more loosely speaking, viewpoints for interpreting the kinetic range turbulence have been advocated [4, 5, 16, 38, 53, 59, 69, 80, 86, 225]. It is worth mentioning that this presently ongoing debate on the subject has led to a certain amount of controversy [50, 188, 226, 227].

For starters, it may be useful to recall that a proper description of kinetic scale turbulence generally requires a self-consistent description of fields and particles, which generalizes the notion of a turbulent cascade to the entire phase-space of the particle distribution function f_s [69, 228]. The fluidlike part of the cascade then becomes intertwined with the velocity-space fluctuations in the particle distribution. The internal energy of the species, which includes both thermal and non-thermal fluctuations, should be therefore considered explicitly alongside the electromagnetic and species fluid kinetic energy. How the (conserved) total energy is redistributed among these different forms and how the non-thermal energy fluctuations thermalize and heat the turbulent plasma is a key question of considerable practical interest [3, 8, 18, 24]. It seems likely that the problem of kinetic range plasma

turbulence can be generally "solved" only by means of nonlinear kinetic simulations, whereas theoretical predictions inevitably require certain simplifying assumptions. There is presently no general consensus within the astrophysical and space plasma turbulence community as to which approximations are acceptable and which not [5, 38, 42, 50, 52, 188, 229], in part, because the different turbulence modeling approaches are rarely compared [40, 230–232]. This gap has been partially filled by the study presented in Ref. [40], led by the author (see Chapter 5). Alternatively, one may adhere to the view that a theoretical framework for kinetic plasma turbulence should be established from basic principles. In this context, we point the reader to the recent work of Eyink [69], where bounds for the kinetic turbulence scaling exponents are established rigorously. While very significant at a fundamental level, the derived bounds are in practice not particularly restrictive [69]. To obtain a more concrete set of scaling predictions, it may as well be that a phenomenological approach is ultimately inevitable.

In the following, we focus on one particular phenomenology [4, 5, 56, 59, 86, 233], which has attracted considerable attention in recent years [36, 39, 40, 42, 43, 78, 88, 145, 234–239]. This is the phenomenology of kinetic Alfvén wave (KAW) turbulence. The model was originally introduced about a decade ago in the works of Schekochihin *et al.* [5] and Howes *et al.* [4]. Later, the original phenomenology was refined and/or extended by different authors, including Howes *et al.* [233], Boldyrev and Perez [56], Boldyrev *et al.* [59], and Passot and Sulem [86]. Essentially, common to all variants of the KAW turbulence model is the assumption that the sub-ion scale electromagnetic turbulence is strongly anisotropic, low-frequency, and in an approximate state of critical balance between the linear (KAW) and nonlinear time. At a conceptual level, the model can be viewed as an adaptation of the ideas of GS95 to the kinetic range, where the plasma waves are generally dispersive and may be subject to significant collisionless damping via wave-particle interactions [52, 143, 240]. In the sections below, we qualitatively explain some of the main features of KAW turbulence, followed by a short review of previous evidence in support of the phenomenology. We also address the criticism and known alternatives to the KAW turbulence model.

3.3.1 Electron reduced MHD

In general, the phenomenology of KAW turbulence is relevant (if considered as such) only over a finite range, between the ion and electron kinetic scales, the extent of which is limited by the square root of the proton-electron mass ratio: $\sqrt{m_p/m_e} \approx 43$. In order to precisely determine all the features of KAW turbulence and its kinetic coupling with ions and electrons, one needs to numerically solve the kinetic equations (e.g., [36, 39, 42, 233]).[12] However, a set of simplified, fluidlike equations can be obtained in the asymptotic limit

$$1/\rho_i \ll k_\perp \ll 1/\rho_e, \tag{3.28}$$

[12]KAW turbulence is believed to be well described by gyrokinetics, where KAWs are the only relevant linear modes at sub-ion scales [4, 5]. On the other hand, whether or not KAW turbulence actually develops naturally in the general fully kinetic description has been a longstanding open question, which is addressed for the first time in this Thesis.

assuming $k_\parallel \ll k_\perp$ and $\beta_s = 8\pi n_0 T_{0s}/B_0^2 \sim 1$, where β_s is the species beta, ρ_i is the ion thermal gyroradius, and ρ_e is the electron thermal gyroradius (see Appendix C). The fluidlike equations are known as the equations of *electron reduced MHD* (ERMHD) [5]. ERMHD does *not* provide a precise or even fully satisfactory description of KAW turbulence, since it does not represent the particle velocity space and the associated wave-particle interactions. On the other hand, its simplicity leads to a physically illuminating, phenomenological picture of the KAW turbulence dynamics. It can be therefore still considered as a valuable starting point. The numerous limitations of ERMHD or of gyrokinetics, where KAW turbulence is as well a natural consequence of the model assumptions [4], can ultimately only be surpassed by fully kinetic simulations, such as the ones presented in this Thesis. In the following, we sketch the derivation of the ERMHD equations. Further details can be found in Refs. [5, 59, 241].

The ERMHD equations may be obtained rigorously from the gyrokinetic model in the idealized asymptotic limit (3.28) [5]. However, a more intuitive derivation based on the magnetic induction equation and on the first moments of the Vlasov equation is also possible and this is the approach outlined here [59, 241]. We start with the induction equation and with the force balance for the electrons:

$$\frac{\partial \mathbf{B}}{\partial t} = -c\nabla \times \mathbf{E}, \qquad -n_e e\left(\mathbf{E} + \frac{\mathbf{u}_e \times \mathbf{B}}{c}\right) - \nabla p_e = 0, \tag{3.29}$$

where n_e is the electron density, $\mathbf{u}_e$ is the electron fluid velocity, and $p_e = n_e T_{0e}$ is the isothermal electron pressure. The electron inertia is neglected by assuming low-frequency dynamics ($\omega \ll k_\parallel v_{\mathrm{th},e}$) at perpendicular wavenumber scales $k_\perp \ll 1/\rho_e$.[13] The isothermal electron closure may be justified within the framework of gyrokinetics, where it can be shown to result from a zeroth-order expansion in $(m_e/m_i)^{1/2}$ [5]. The main equations of ERMHD correspond to the projections of Eqs. (3.29) onto the *total* magnetic field direction:

$$\frac{\partial B_\parallel}{\partial t} = \hat{\mathbf{e}}_\parallel \cdot \left[\nabla \times (\mathbf{u}_e \times \mathbf{B})\right], \qquad -n_e e E_\parallel - T_{0e}\, \hat{\mathbf{e}}_\parallel \cdot \nabla n_e = 0, \tag{3.30}$$

where $B_\parallel = \hat{\mathbf{e}}_\parallel \cdot \mathbf{B}$, $E_\parallel = \hat{\mathbf{e}}_\parallel \cdot \mathbf{E}$, and $\hat{\mathbf{e}}_\parallel = \mathbf{B}/|\mathbf{B}|$ is the unit vector parallel to $\mathbf{B}$. Above, we used the second equation in (3.29) to express the electric field in the magnetic induction equation. To proceed, we use the vector identity $\nabla \times (\mathbf{u}_e \times \mathbf{B}) = -\mathbf{B}\nabla \cdot \mathbf{u}_e + \mathbf{B} \cdot \nabla \mathbf{u}_e - \mathbf{u}_e \cdot \nabla \mathbf{B}$, and we express $E_\parallel$ in terms of the electrostatic potential φ and parallel vector potential $A_\parallel$ as $E_\parallel = -\hat{\mathbf{e}}_\parallel \cdot \nabla\varphi - (1/c)\partial A_\parallel/\partial t$. We also use the electron continuity equation,

$$\frac{\partial n_e}{\partial t} + \mathbf{u}_e \cdot \nabla n_e = -n_e \nabla \cdot \mathbf{u}_e, \tag{3.31}$$

to express $\nabla \cdot \mathbf{u}_e$. Essentially, the fluid motions are not assumed to be incompressible, so as to allow for density fluctuations, which are supported by the low-frequency response of the

[13] The condition $\omega \ll k_\parallel v_{\mathrm{th},e}$ implies low-frequency dynamics for parallel as well as perpendicular electron motion, since we are assuming strong anisotropy: $k_\parallel/k_\perp \ll 1$.

(spatially non-magnetized) ions. With the use of these additional relations, we obtain

$$\frac{\partial B_\parallel}{\partial t} = \frac{B_\parallel}{n_e}\left(\frac{\partial n_e}{\partial t} + \mathbf{u}_e \cdot \nabla n_e\right) + \mathbf{B} \cdot \nabla u_{\parallel e} - \mathbf{u}_e \cdot \nabla B_\parallel, \tag{3.32}$$

$$\frac{1}{c}\frac{\partial A_\parallel}{\partial t} = -\hat{\mathbf{e}}_\parallel \cdot \nabla\varphi + \frac{T_{0e}}{n_e e}\,\hat{\mathbf{e}}_\parallel \cdot \nabla n_e. \tag{3.33}$$

Equations (3.32) and (3.33) can be simplified by adopting the ordering

$$b/B_0 \sim \delta n_e/n_0 \sim k_\parallel/k_\perp \ll 1, \tag{3.34}$$

where n_0 is the mean density, B_0 is the mean field strength, δn_e is the fluctuating density, and b is the fluctuating magnetic field. That is, the turbulent fluctuations are assumed to be small compared to the background and of similar order as $k_\parallel/k_\perp$. This is supported by recent solar wind observations [32, 242] and can be physically motivated by the fact that we consider kinetic range turbulence, where the *scale-dependent* fluctuation amplitudes are expected to be small [4], since they feed on the fluctuations at the very tail of the inertial MHD range. Similarly, the $k_\parallel/k_\perp \ll 1$ assumption is motivated by the fact that MHD turbulence becomes increasingly more anisotropic at smaller scales, so that by the time when kinetic scales are reached, the strong anisotropy assumption is justified. We mention that "small" fluctuations do *not* necessarily imply a state of weak wave turbulence [243]. Indeed, the adopted scalings yield $bk_\perp \sim k_\parallel B_0$, which is typical for strong turbulence characterized by critical balance [4, 5, 59, 136]. With the above simplifications in mind, (3.32) and (3.33) become:

$$\frac{\partial}{\partial t}\left(\frac{b_\parallel}{B_0} - \frac{n_e}{n_0}\right) = \nabla_\parallel u_{\parallel e} - \mathbf{u}_{\perp e} \cdot \nabla_\perp \left(\frac{b_\parallel}{B_0} - \frac{n_e}{n_0}\right), \tag{3.35}$$

$$\frac{1}{c}\frac{\partial A_\parallel}{\partial t} = \nabla_\parallel \left(\frac{T_{0e}}{n_0 e} n_e - \varphi\right), \tag{3.36}$$

where $\mathbf{b} = \mathbf{B} - B_0\,\hat{\mathbf{e}}_z$ is the fluctuating part of the magnetic field, $\nabla_\perp = \hat{\mathbf{e}}_x\partial/\partial x + \hat{\mathbf{e}}_y\partial/\partial y$, and

$$\nabla_\parallel = \hat{\mathbf{e}}_\parallel \cdot \nabla = \frac{\partial}{\partial z} + \frac{\mathbf{b}_\perp}{B_0} \cdot \nabla \tag{3.37}$$

is the derivative along the *local* magnetic field line. In the same ordering, the electron flow can be approximated as

$$\mathbf{u}_{\perp e} \approx \hat{\mathbf{e}}_z \times \frac{c}{B_0}\nabla_\perp \left(\varphi - \frac{T_{0e}}{n_0 e} n_e\right), \tag{3.38}$$

$$u_{\parallel e} \approx -\frac{c}{4\pi n_0 e}\nabla_\perp^2 \psi. \tag{3.39}$$

Above, we introduced the flux function $\psi = -A_\parallel$, and we used $u_{\parallel e} \approx -J_\parallel/(n_0 e)$, where $\mathbf{J}_\parallel = c/(4\pi)\nabla_\perp \times \mathbf{b}_\perp = c/(4\pi)\nabla_\perp \times (\hat{\mathbf{e}}_z \times \nabla_\perp \psi)$ is the parallel electric current, to relate

$u_{\parallel e}$ to ψ. To obtain a closed system of equations, we use the perpendicular force balance condition for the ions and for the bulk plasma:

$$n_0 e(-\nabla_\perp \varphi) - \nabla_\perp p_i = 0, \tag{3.40}$$

$$\frac{1}{c}\mathbf{J}_\perp \times B_0 \hat{\mathbf{e}}_z - \nabla_\perp (p_i + p_e) = 0, \tag{3.41}$$

where p_i is the ion pressure and $\mathbf{J}_\perp$ is the perpendicular current. We consider singly charged ions ($q_i = e$) for simplicity and the plasma is treated as quasi-neutral: $n_i \simeq n_e$. The above is obtained by assuming that the perpendicular ion dynamics is low-frequency ($\omega \ll k_\perp v_{\mathrm{th},i}$) at scales $k_\perp \gg 1/\rho_i$, where the ions are (spatially) non-magnetized. Note that the parallel ion motion need not satisfy an equivalent low-frequency condition [59]. On the slow time scale and over short distances compared to ρ_i, perpendicular gradients of the ion temperature may be neglected and the pressure term in (3.40) can be approximated as $\nabla_\perp p_i \approx T_{0i} \nabla_\perp n_e$, where T_{0i} is the background ion temperature. Equation (3.40) then translates into a Boltzmann response for the ion (electron) density:

$$n_e \approx n_0 \left(1 - \frac{e}{T_{0i}}\varphi\right). \tag{3.42}$$

The perpendicular pressure balance (3.41) can be accordingly written as

$$\nabla_\perp \frac{b_\parallel}{B_0} = -\frac{4\pi n_0 (T_{0i} + T_{0e})}{B_0^2} \nabla_\perp \frac{n_e}{n_0} = -\frac{\beta_i + \beta_e}{2} \nabla_\perp \frac{n_e}{n_0}. \tag{3.43}$$

Using (3.42) we can also eliminate φ from (3.38) and approximate the perpendicular electron flow velocity as

$$\mathbf{u}_{\perp e} \approx -\hat{\mathbf{e}}_z \times \frac{c B_0 (\beta_i + \beta_e)}{8\pi n_0 e} \nabla_\perp \frac{n_e}{n_0}. \tag{3.44}$$

Finally, with the help of (3.39) and (3.42)–(3.44), we can rearrange the equations (3.35) and (3.36) into

$$\frac{\partial n_e}{\partial t} = \frac{c}{4\pi e \left[1 + (\beta_i + \beta_e)/2\right]} \nabla_\parallel \nabla_\perp^2 \psi, \tag{3.45}$$

$$\frac{\partial \psi}{\partial t} = -\frac{c B_0^2 (\beta_i + \beta_e)}{8\pi n_0^2 e} \nabla_\parallel n_e. \tag{3.46}$$

The above constitutes a closed system of equations for the flux function $\psi = -A_\parallel$ and for the electron density n_e. These are the main equations of ERMHD.[14] It is instructive to

[14]The ERMHD model may be formulated in terms of different quantities (cf., Refs. [5, 59, 241]). Here, we obtain the variant from Boldyrev *et al.* [59].

represent the equations in a dimensionless form, using the following normalizations:

$$t' = \frac{v_A}{\rho_i}\sqrt{\frac{1+\beta_e/\beta_i}{2+\beta_i+\beta_e}}\,t, \tag{3.47}$$

$$\mathbf{r}' = \frac{\mathbf{r}}{\rho_i}, \tag{3.48}$$

$$\psi' = \frac{\psi}{B_0\rho_i}, \tag{3.49}$$

$$n_e' = \left[\frac{\beta_i+\beta_e}{2}\left(1+\frac{\beta_i+\beta_e}{2}\right)\right]^{1/2}\frac{n_e}{n_0}, \tag{3.50}$$

where $v_A = B_0/\sqrt{4\pi n_0 m_i}$ is the Alfvén speed. In the above units, the ERMHD equations take a simple form [59]:

$$\frac{\partial n_e'}{\partial t'} = \nabla_\parallel' \nabla_\perp'^2 \psi', \tag{3.51}$$

$$\frac{\partial \psi'}{\partial t'} = -\nabla_\parallel' n_e', \tag{3.52}$$

where

$$\nabla_\parallel' = \frac{\partial}{\partial z'} + \left(\hat{\mathbf{e}}_z \times \nabla_\perp' \psi'\right)\cdot \nabla_\perp'. \tag{3.53}$$

The dimensionless version reflects the fact that the low-frequency turbulent dynamics in the asymptotic limit (3.28) is free from any characteristic scales. The choice of normalization, leading to the above form, is not unique because either the reference length scale or the time scale may be chosen arbitrarily. More specifically, the ERMHD equations are invariant under the simultaneous rescaling: $t \to \alpha^2 t$, $\mathbf{r} \to \alpha \mathbf{r}$, $\psi \to \alpha\psi$, with arbitrary α. Indeed, we use here a normalization slightly different from the one given in Ref. [59], but we still obtain the same dimensionless form. The equations are also invariant under the rescaling: $t \to \epsilon t$, $z \to \epsilon z$, $n_e \to n_e/\epsilon$, $\psi \to \psi/\epsilon$ [56, 59]. Thus, even though we physically assume the ordering (3.34), we may always renormalize the parallel (z) direction and the (small) fluctuations in such a way that $k_z \sim \psi \sim \delta n_e \sim 1$ [59].

3.3.2 Remarks on the ERMHD model

In the previous section, we outlined the derivation of a set of fluidlike equations, which can be used to roughly describe the very basic features of KAW turbulence. We now discuss some general properties of ERMHD and its limitations.

Essential in the derivation is the low-frequency assumption, which renders the ion response dynamically important and gives rise to significant density fluctuations. This is in contrast with alternative kinetic range models, such as whistler wave turbulence [80, 244, 245], where the ions form a static, neutralizing background and density fluctuations are negligible. In more technical terms, Eqs. (3.45) and (3.46) are obtained by assuming,

at the same time, $\mathbf{u}_i \approx 0$ and $\nabla \cdot \mathbf{u}_i = \nabla \cdot \mathbf{u}_e \neq 0$ [5, 241]. The divergence term is, however, not calculated directly from the fluid velocity, but it is instead determined from the electron continuity equation (3.31). Considering that $\mathbf{b}_\perp = \hat{\mathbf{e}}_z \times \nabla_\perp \psi$, it is also evident that KAW turbulence inherently couples the Alfvénic (polarized perpendicularly to $\mathbf{B}_0$) and compressive fluctuations. This property differs substantially from the phenomenology of MHD range turbulence (see Sec. 3.2), where the Alfvénic part is essentially decoupled.

Another interesting aspect, pointed out by Howes *et al.* [4] and Boldyrev *et al.* [59], is that it is not strictly necessary for the characteristic frequencies to satisfy $\omega/\Omega_{ci} \ll 1$ (as in gyrokinetic theory) for the phenomenology of KAW turbulence to be relevant.[15] What is required is that the fluctuations are strongly anisotropic, small amplitude, and satisfy $\omega \ll k_\perp v_{\mathrm{th},i}$, $k_\parallel v_{\mathrm{th},e}$, which is enough to ensure that the fluctuations are in perpendicular pressure balance between the kinetic and magnetic pressures. This property is evident in the linear kinetic dispersion solutions of Sahraoui *et al.* [246] and López *et al.* [240], where the KAW branch is shown to smoothly extend to frequencies above the ion cyclotron frequency, provided that the propagation angle is fairly oblique and the beta is close to unity or higher.[16] In terms of linear theory, the continuation to frequencies above Ω_{ci} is made possible by the (generalized) ion Bernstein modes, which merge into a single branch with the KAW, when $k_\parallel/k_\perp \ll 1$ and $\beta_i \gtrsim 1$ [240].

As shown in the next section, it is possible to construct a kinetic range turbulence phenomenology by following the approach of GS95. Essential for such a phenomenology are the properties of linear waves, supported by the dynamics. By dropping the nonlinear terms (this amounts to replacing $\nabla_\parallel$ with $\partial/\partial z$), it is readily seen that Eqs. (3.45) and (3.46) support linear solutions with a dispersion relation

$$\omega_{KAW} = \pm\sqrt{\frac{1+\beta_e/\beta_i}{2+\beta_i+\beta_e}}\, k_z v_A k_\perp \rho_i. \tag{3.54}$$

In the normalized units, the above translates into $\omega'_{KAW} = \pm k'_z k'_\perp$. This is the analytical dispersion relation of the KAW for $1/\rho_i \ll k_\perp \ll 1/\rho_e$ [4, 5, 59, 131]. The wave is dispersive and has a group velocity given by

$$\mathbf{v}_g = \pm v_A \rho_i \sqrt{\frac{1+\beta_e/\beta_i}{2+\beta_i+\beta_e}}\left(k_z\, \mathbf{k}_\perp/k_\perp + k_\perp\, \hat{\mathbf{e}}_z\right). \tag{3.55}$$

Since $k_z/k_\perp \ll 1$, the wave packets disperse primarily along $\mathbf{B}_0 = B_0\hat{\mathbf{e}}_z$. The polarization satisfies

$$\left[\frac{\beta_i+\beta_e}{2}\left(1+\frac{\beta_i+\beta_e}{2}\right)\right]^{1/2}\frac{\delta n_{e,\mathbf{k}}}{n_0} = \pm\frac{k_\perp \psi_{\mathbf{k}}}{B_0}. \tag{3.56}$$

[15] As explained in Howes *et al.* [4], the cyclotron resonance of the KAW, while present, is relatively weak and it occupies a very narrow frequency gap for $k_\perp \gg 1/\rho_i$.

[16] Sahraoui *et al.* [246] call the part above Ω_{ci} "Alfvén-whistler" modes. This distinction is perhaps slightly unnecessary, since the so-called "Alfvén-whistler" modes share all the basic properties of KAWs below Ω_{ci} and they differ from the classical whistler modes, which do not satisfy the perpendicular pressure balance [247].

In terms of the magnetic field perturbations, the above implies right-hand elliptical polarization along the direction of $\mathbf{k}_\perp$ (assuming $\omega, k_z > 0$) [5]:

$$\mathbf{b}_\mathbf{k} = \mathrm{i}k_\perp \psi_\mathbf{k} \left[\hat{\mathbf{e}}_z \times \mathbf{k}_\perp / k_\perp + \mathrm{i} \left(\frac{\beta_i + \beta_e}{2 + \beta_i + \beta_e} \right)^{1/2} \hat{\mathbf{e}}_z \right] = \mathbf{b}_{\perp,\mathbf{k}} + \mathbf{b}_{\parallel,\mathbf{k}}. \tag{3.57}$$

Similarly, $\mathbf{E}_{\perp,\mathbf{k}}$ is right-hand elliptically polarized in the direction of $\mathbf{B}_0$, i.e., it rotates in the electron sense [5, 248, 249]. In analogy with Alfvén waves in MHD, a single KAW packet with a fixed $k_\perp$ is essentially an exact nonlinear solution of Eqs. (3.45) and (3.46), since the nonlinear terms vanish whenever (3.56) is satisfied in a single $k_\perp$ shell [5]. This gives additional credibility to the KAW-like picture of kinetic range turbulence because it implies a certain robustness of the wavelike solutions. It is also useful to observe that the ERMHD equations exhibit two ideal conserved quantities [5, 59]:

$$E'_{KA} = \int \left(|\nabla'_\perp \psi'|^2 + |\delta n'_e|^2 \right) \mathrm{d}^3\mathbf{r}' = \int \left(|\mathbf{b}'_\perp|^2 + |\delta n'_e|^2 \right) \mathrm{d}^3\mathbf{r}' \,, \tag{3.58}$$

$$H'_{KA} = \int \psi' \delta n'_e \, \mathrm{d}^3\mathbf{r}' \,, \tag{3.59}$$

where E'_{KA} is the kinetic-Alfvén energy, H'_{KA} is the so-called cross-correlation, and the primes denote the normalizations (3.47)–(3.50). The kinetic-Alfvén energy is the kinetic range, fluidlike analog of the cascaded energy in MHD turbulence. It is important to mention that E'_{KA} is not *a priori* related to any wave activity. Instead, it merely gives the appropriate definition of the total energy for the nonlinear equations (3.51) and (3.52). Due to perpendicular pressure balance (3.43), the constancy of H'_{KA} implies a conservation of the helicity of magnetic fluctuations: $H = \int \mathbf{A} \cdot \mathbf{b} \, \mathrm{d}^3\mathbf{r} \approx \int A_\parallel b_\parallel \, \mathrm{d}^3\mathbf{r}$ [5].

In the physical limit in which the ERMHD equations are obtained, the KAW is the only relevant linear mode at sub-ion scales. This is true also in the more general gyrokinetic approximation (for a homogeneous plasma in slab geometry), of which ERMHD is a special limiting case [5, 131]. Beyond gyrokinetics, it is not obvious that KAW-like fluctuations should dominate the kinetic range and various alternatives have been considered [52, 83, 142, 143, 250], such as the high-frequency whistler waves [81, 83, 84, 143]. Even if the turbulent fluctuations are indeed predominantly low-frequency, the much simplified ERMHD model still neglects several important effects. It does not describe the damping of the turbulent cascade, which involves purely kinetic effects, such as Landau damping [4, 18, 54, 85, 98], stochastic heating [147, 148], or non-thermal particle acceleration [49, 96, 251].[17] The asymptotic linear dispersion (3.54) neglects as well any corrections originating from the proximity of ion and electron scales. It is also assumed that the background particle distributions are isotropic Maxwellians; a situation not typical in space and astrophysical plasmas [17, 28, 75].[18] Non-equilibrium background distributions can potentially excite various kinetic instabilities [93], which may impact the KAW turbulence

[17] For numerical reasons, the ERMHD equations are in practice supplemented with *ad hoc* dissipation terms, in order to smooth out the numerical solutions at the smallest resolved scales [56, 59].

[18] For a generalization of the KAW turbulence phenomenology to bi-Maxwellian, pressure anisotropic

dynamics. All of the above features can be generally captured only within the fully kinetic framework, employed in this Thesis. The results presented here provide evidence, for the first time based on first principles kinetic simulations, that the basic phenomenological picture of KAW turbulence (as deduced from ERMHD and gyrokinetics) holds well beyond its formal limit of applicability (see Chapters 5, 6, and 7).

3.3.3 Spectral scaling predictions

Upon invoking the critical balance conjecture [136], it is possible to obtain heuristic scaling predictions for KAW turbulence [4, 5, 59]. The relevant linear mode is the KAW and the cascaded energy is the kinetic-Alfvén energy density $E'_{KA} = |\mathbf{b}'_\perp|^2 + |\delta n'_e|^2$. The phenomenological spectral estimates are limited to the fluidlike part of the KAW cascade and turbulent dissipation is typically included merely as a refinement of the basic predictions [4, 36, 86]. There is no straightforward way to self-consistently incorporate ion and electron heating into the KAW turbulence predictions, which is one of the reasons why nonlinear kinetic simulations are so essential [36, 43, 78, 98, 252]. The standard predictions are obtained as follows. First, it is assumed that the partitioning of turbulent energy between magnetic field and density fluctuations is determined by the linear properties of KAWs. This implies that

$$\frac{b^2_{\perp\lambda}}{B_0^2} \sim \left[\frac{\beta_i+\beta_e}{2}\left(1+\frac{\beta_i+\beta_e}{2}\right)\right]\frac{\delta n^2_{e,\lambda}}{n_0^2} \sim \left(\frac{2+\beta_i+\beta_e}{\beta_i+\beta_e}\right)\frac{b^2_{\parallel\lambda}}{B_0^2}, \tag{3.60}$$

where $\lambda \sim 1/k_\perp$ is a field-perpendicular scale. This shows that the energy partitioning in KAW turbulence strongly depends on the plasma beta. In the normalized units, the above becomes $b'^2_{\perp\lambda} \sim \delta n'^2_{e,\lambda} \sim b'^2_{\parallel\lambda}$.[19] The scaling relation (3.60) should be understood in the sense of typical fluctuations at each scale. In a system consisting of many KAWs with different phases, there is no guarantee that (3.60) will be satisfied locally (in real space), except for the perpendicular pressure balance (3.43), which implies

$$\frac{b_{\parallel\lambda}(\mathbf{r})}{B_0} \approx -\frac{\beta_i+\beta_e}{2}\frac{\delta n_{e,\lambda}(\mathbf{r})}{n_0}. \tag{3.61}$$

The perpendicular pressure balance is a quite general signature of low-frequency dynamics, not exclusively limited to KAWs. On the other hand, it is still a fairly stringent condition at sub-ion scales, since it eliminates high-frequency phenomena, such as whistler waves [81, 83, 84, 143], which do not fulfill the presure balance [247].

plasmas see the recent work of Kunz *et al.* [151]. There, it is shown that the KAW dynamics is sensitive to the electron pressure anisotropy but not to the ion one. Moreover, significant qualitative changes (compared to the isotropic case) are seen either for large betas ($\beta \gtrsim 10$) or for strong electron pressure anisotropies ($|P_{\perp,e}/P_{\parallel,e}| \gtrsim 2$).

[19] Note that the normalization for $b_\parallel$ is different than the one for $b_\perp$ [161, 241].

Based on a Kolmogorov-like approach, the (constant) kinetic-Alfvén energy cascade rate in the range $\rho_e \ll \lambda \ll \rho_i$ is estimated as

$$\Pi'_{KA} \sim \frac{\psi'^2/\lambda'^2}{\tau'_{c,\lambda}} \sim \frac{\delta n'^2_{e,\lambda}}{\tau'_{c,\lambda}}, \tag{3.62}$$

where $\tau'_{c,\lambda}$ is the (normalized) energy cascade time. In the spirit of critical balance, it is assumed that either the linear or the nonlinear time may be used as the cascade time. Taking into account that $\psi'_\lambda/\lambda' \sim \delta n'_{e,\lambda}$, we can roughly estimate the nonlinear time from (3.51) or (3.52) as $\tau'_{\mathrm{nl},\lambda} \sim \lambda'^3/\psi'_\lambda$. By balancing the linear and nonlinear terms in (3.53) we can also estimate $1/k'_\parallel \sim \ell'_\parallel \sim \lambda'^2/\psi'_\lambda \sim \lambda'/\delta n'_{e,\lambda}$. The latter is the critical balance statement for KAW turbulence [4, 5, 78, 241, 253].[20] It implies a balance between the two derivatives in (3.53), such that $B_0 k_\parallel \sim k_\perp b_{\perp k_\perp}$ (in physical units). Employing the above-mentioned relations, the scalings follow immediately [4, 5, 59]:

$$\delta n_{e,\lambda} \propto \lambda^{2/3}, \qquad \delta n_{e,\ell_\parallel} \propto \ell_\parallel^2, \qquad \ell_\parallel \propto \lambda^{1/3}. \tag{3.63}$$

In spectral space, the above becomes:

$$E_{KA}(k_\perp) \propto k_\perp^{-7/3}, \qquad E_{KA}(k_\parallel) \propto k_\parallel^{-5}, \qquad k_\parallel \propto k_\perp^{1/3}, \tag{3.64}$$

where $E_{KA}(k_\perp)$ and $E_{KA}(k_\parallel)$ are, respectively the perpendicular and parallel wavenumber spectra of the kinetic-Alfvén energy. The predicted kinetic range spectrum is steeper than the one in the MHD range and it is somewhat more anisotropic. Similar qualitative features are also predicted by alternative kinetic range models (see Sec. 3.3.5). The above estimates are obtained by neglecting any dissipative effects. A simple, *ad hoc* inclusion of dissipation in the form of linear Landau damping yields an exponential fall off for the $k_\perp^{-7/3}$ spectrum, upon approaching electron scales [4]. It is also worth emphasizing that $k_\parallel$ should be measured here with respect to the *local* mean magnetic field direction [78, 138, 205, 241, 245], for the same reasons as in MHD range turbulence (see Sec. 3.2.2).

As explained in the next section, a number of recent observational and computational studies (including this Thesis) shows that the partitioning between the density and magnetic fluctuations is indeed consistent with the beta-dependent KAW polarization properties, as described by relation (3.60). On the other hand, the measured $k_\perp$ spectra are approximately of power-law type, with typical spectral exponents around -2.8 [27, 36, 235, 254, 255]; a value considerably steeper than the predicted $-7/3$. The discrepancy led to several complementary revisions of the original KAW turbulence phenomenology [56, 86, 233]. Refined models generally fall into two camps. They either attempt to explain the additional spectral steepening in terms of collisionless wave damping, or they continue to favor a fluidlike approach and discuss the implications of turbulent structure formation and intermittency. Howes *et al.* [233] relax the strict critical balance assumption and take into account nonlocal shearing by large-scale fluid motions, which may become significant

[20] Here, we mention that critical balance is an assumption *not* hardwired by default into ERMHD, or gyrokinetics for that matter [5, 205].

when the cascade is weakened due to linear Landau damping. Similarly, Passot and Sulem [86] account for ion temperature homogenization along the field lines, induced by Landau damping. Common to both of these models is the emergence of near power-law spectra in the sub-ion range, with typical spectral exponents reasonably close to the observed values. The predicted spectra are *not* universal but depend on the relative strength of the damping. In contrast, Boldyrev and Perez [56] obtain universal, modified spectral predictions within the scope of ERMHD. Based on their simulation results, they conjecture that KAW turbulence is strongly intermittent and concentrated in 2D structures with a volume filling ratio proportional to λ. The filling ratio correction yields an energy spectrum of the form $E_{KA}(k_\perp) \propto k_\perp^{-8/3}$, which is closer to observations and simulations. The anisotropy scaling is in this case given by $k_\parallel \propto k_\perp^{2/3}$ [56].

Presently, the debate concerning the exact scaling of the sub-ion range energy spectrum is far from settled, even within the scope of KAW turbulence alone. It seems reasonable to suppose that damping as well as intermittency need to be taken into account for a precise prediction of the turbulence spectrum over the range $1/\rho_i \lesssim k_\perp \lesssim \min\{1/\rho_e, 1/d_e\}$, where KAWs may exist. However, we wish to caution the reader that (speculative) arguments against the urge to include either damping or kinetic-scale intermittency can be made as well.[21] It is worth to briefly mention these here.

Concerning damping, it has been recently argued that Landau damping in a turbulent plasma may be inefficient at scales much larger than the species Larmor radius [181, 256]. The physics behind such "fluidization" of kinetic turbulence is based on a stochastic version of the so-called plasma echo [257], which is suspected to occur due to the coupling between linear phase mixing and nonlinear advection by the turbulent flow. Some evidence for the fluidization effect is provided by recent observations and simulations of solar wind turbulence at scales larger or comparable to the ion Larmor radius [177, 181, 258]. At scales between the ion and electron gyroradius, which are at the main focus of this work, it is yet to be clarified if electron Landau damping can be suppressed in a turbulent setting. Several works are somewhat at odds with the latter possibility [40, 85, 88, 98, 259], although it is too early to make a definitive conclusion. For the ions, it is established theoretically [5, 228, 260], at least within the context of gyrokinetics, that the parallel phase mixing (i.e., Landau damping) is overtaken by the nonlinear perpendicular phase mixing at scales $k_\perp \gg 1/\rho_i$. This is supported by kinetic simulations [98, 261, 262]. The nonlinear phase mixing is manifested as a phase-space cascade of entropy fluctuations, which receive energy from the turbulence around the transition into the sub-ion range [5, 228]. From there on, the electromagnetic KAW turbulence is essentially decoupled from the ion phase-space cascade [5]. We do not investigate the ion entropy cascade in this work. In addition, the ions may be also subject to stochastic heating [147, 148]. The latter mechanism is expected to be isolated to scales comparable to the ion gyroradius.

Regarding intermittency, the observational studies of Kiyani *et al.* [146, 254] and Chen *et*

[21] To avoid confusion, we note that while the damping of the electromagnetic cascade is inevitable, it is presently not well understood *where* (in scale) significant damping occurs and how the released energy is dissipated [18, 43, 98, 181, 256].

al. [263] suggest that the sub-ion scale density and magnetic fluctuations have non-Gaussian probability distributions with nearly scale-independent shapes, implying that an unknown process may be limiting the turbulence volume filling ratio from below.[22] These findings are consistent with the Cluster spacecraft data analysis, performed by the author, and presented in Chapter 7. The near statistical self-similarity is at odds with the intermittency correction of Boldyrev and Perez [56], which assumes that the volume filling fraction varies linearly with scale in the sub-ion range. Thus, the most straightforward way to incorporate intermittency does not seem to be particularly well motivated by observations. On the other hand, intermittent corrections, commonly associated with turbulent structures [53], may be still significant when considering the possible nonlocal couplings with the MHD and electron scales. For example, a number of works indicated a tendency toward current sheet formation in sub-ion scale plasma turbulence [48, 78, 85, 158, 264], similar to that in MHD turbulence. If the forming current sheets were to be disrupted by the collisionless tearing instability [16, 102, 265, 266], significant nonlocal couplings could emerge and possibly alter the shape of the energy spectrum [16, 91, 267].[23] As a side note, it is also worth mentioning that the saturation of the sub-ion scale intermittency is not seen in existing simulations ([40, 46–48, 161, 269], see Chapter 7), presumably due to the limited size of the simulation domains.

To conclude we note that, while there exist several complementary models for predicting the exact form of the KAW turbulence spectrum, a common denominator to all is the assumption that the fluctuations are low-frequency, strongly anisotropic, as anticipated by critical balance, and in approximate equipartition between the density and perpendicular magnetic field energy (in appropriately normalized units). Much of the data analysis presented in this Thesis is focused on the latter properties.

3.3.4 Prior evidence in support of KAW turbulence

Before the work of this Thesis, evidence in support of the KAW turbulence phenomenology was mainly based on spacecraft observations [145, 235–238, 270, 271], gyrokinetic [36, 43, 205], and generalized fluid simulations [88, 241, 253]. Some evidence was also available from hybrid-kinetic simulations [47, 144, 272]. In contrast, it was never investigated whether a critically balanced KAW cascade develops naturally in a first principles, 3D kinetic description. This goal was accomplished within the scope of this Thesis [78, 161]. In this respect, it is worth to briefly discuss the accomplishments as well as the limitations of previous works.[24]

Considerable progress on the subject has been achieved by means of *in situ* solar wind observations [32, 238]. Nevertheless, observational studies are often limited to single-point

[22] Note that the volume filling ratio is related to the inverse of the kurtosis of the probability distribution function [53].

[23] Interestingly, the collisional tearing instability in MHD turbulence has been considered as a limiting factor for the volume filling ratio ([268], see also Ref. [263]). It may be worth considering an analogous possibility for kinetic range, collisionless plasma turbulence.

[24] This is not meant to undermine the importance of previous works, of course.

spacecraft measurements of magnetic field [146, 205, 236, 273] and/or density fluctuations [145, 255], which do not allow for detailed investigations of the 3D structure of the kinetic turbulence. Multispacecraft techniques (e.g., using the four Cluster [274] or MMS [275] spacecraft) are possible [235, 276–278], but these are generally constrained to only four-point measurements. Moreover, multispacecraft techniques applied to present data tend to have a rather limited accuracy at sub-Larmor scales [276, 277, 279]. Observational studies of kinetic turbulence require also a very careful selection of measurement intervals, in order to isolate the turbulence from other processes that might be taking place in space plasmas [247, 276, 278, 280]. This limits the amount of data suitable for analysis. For these reasons, simulations have become an indispensable supporting source of information, since they can be performed in a much more controlled setting without the pitfalls of experimental measurement uncertainties. Previous simulations targeting KAW turbulence have been mostly performed using the gyrokinetic model [36, 39, 42, 43, 98]. This led to a certain amount of criticism [38, 50, 226], based on the fact that several potentially relevant physical effects are ruled out from gyrokinetics. Other works focusing on KAW turbulence employed ERMHD or Landau-fluid models [56, 88, 241, 253], which are as well based on a series of simplifying assumptions. The possibility of a transition into a KAW cascade was also considered in 2D [144, 272] and, very recently, 3D hybrid-kinetic simulations [47, 134]. Concerns have been raised [52] even for the hybrid modeling approach, due to its neglect of electron kinetic physics.

From the data analysis perspective, a very frequently employed diagnostic for testing the presence of KAW-like turbulent fluctuations are the ratios of the 1D (perpendicular) wavenumber spectra [40, 143–146, 205, 236]. This includes, in particular, the magnetic compressibility $C_\parallel = |b_\parallel|^2/|b|^2$ and the electron compressibility $C_e = |\delta n_e/n_0|^2/\,|b/B_0|^2$ [59, 143]. In general, $C_\parallel$ and C_e are functions of scale [40, 143, 205]. In the asymptotic limit (3.28), the ratios for KAWs can be expressed analytically as (cf., Eq. (3.60))

$$C_\parallel = \frac{|b_\parallel|^2}{|b|^2} = \frac{\beta}{2+2\beta}, \qquad \widetilde{C}_\parallel = \frac{|b_\parallel|^2}{|b_\perp|^2} = \frac{\beta}{2+\beta}, \tag{3.65}$$

$$C_e = \frac{|\delta n_e/n_0|^2}{|b/B_0|^2} = \frac{2}{\beta(1+\beta)}, \qquad \widetilde{C}_e = \frac{|\delta n_e/n_0|^2}{|b_\perp/B_0|^2} = \frac{4}{\beta(2+\beta)}, \tag{3.66}$$

where $\beta = \beta_i + \beta_e$ is the total plasma beta. We also list the modified ratios, $\widetilde{C}_\parallel$ and $\widetilde{C}_e$, with $|b_\perp|^2$ in the denominator. Although the standard definitions are more common, the modified versions are more natural for testing the presence of KAWs, since $b_\parallel$ and $b_\perp$ scale differently with beta. Beyond the asymptotic limit (3.28), more accurate linear predictions can be obtained by numerically solving the kinetic plasma dispersion relation [40, 52, 143, 205]. Numerical solutions show that the asymptotic predictions (3.65) and (3.66) can be typically considered as reasonable approximations of the exact linear solutions for $\beta \sim 1$ plasmas over the range were KAWs exist [40, 237]. It is also of interest to consider the ratio of the perpendicular electric to perpendicular magnetic field spectrum [40, 78, 234], which can be

expressed for a KAW (in the limit (3.28)) as

$$C_A(k_\perp) = \frac{|E_\perp\, c/v_A|^2}{|b_\perp|^2} = \frac{\beta_i (k_\perp \rho_i)^2}{\beta(2+\beta)}. \tag{3.67}$$

Finally, the remaining option is the ratio $C_p = |\delta n_e/n_0|^2 / |b_\parallel/B_0|^2$ [40, 78, 144]. The latter is predicted by the perpendicular pressure balance (3.61), which is a quite general signature of low-frequency dynamics not exclusive to KAWs. If satisfied, the perpendicular pressure balance directly relates the density and parallel magnetic field fluctuations in real space and provides as such a much stronger link between the two fields than the spectral ratios.

A number of previous works found reasonable agreement between the turbulence spectral ratios and linear KAW predictions [144–146, 205, 236, 238, 272]. Among these works, it is worth pointing out the study of Chen *et al.* [145], which was the first observational determination of the (modified) electron compressibility ratio $\widetilde{C}_e$. Unlike the magnetic compressibility, the electron compressibility of the KAW (for $\beta \sim 1$) greatly exceeds the values expected by the alternative whistler wave turbulence model [59, 80, 83, 84, 143, 245]. An additional advantage is that the $\widetilde{C}_e$ ratio strongly depends on the β and it can be measured relatively far into the sub-ion range. According to the solar wind observations by Chen *et al.* [145], the kinetic range normalized ratio of $|\delta n_e'|^2$ to $|b_\perp'|^2$ matches the linear KAW predictions reasonably well over a range of different betas, with a mean value of $|\delta n_e'|^2/|b_\perp'|^2 \approx 0.75$. Qualitatively similar results were obtained from generalized fluid and reduced-kinetic simulations [47, 56, 144, 272]. A number of observational and computational studies found accordingly reasonable agreement with linear predictions for the magnetic compressibility [47, 146, 236, 237]. On the other hand, the agreement between the turbulence spectral ratios and linear theory is often only an approximate one [145, 146] and it is difficult to make a conclusion on the importance of wavelike features based on the spectral ratios alone [238, 272]. For instance, already a naive guess based on the natural normalizations (3.47)–(3.50) would be that $|\delta n_e'|^2 \sim |b_\perp'|^2$, without ever explicitly looking for linear wave solutions.[25] Some much-needed additional evidence has been so far obtained from estimates of the frequency-wavenumber spectra [88, 205, 235] and of the *local* anisotropy [241, 253, 276]. Complementary results in support of the phenomenology are also provided by observational studies of the magnetic helicity spectra [270, 271, 281] around $k_\perp \rho_i \approx 1$, which may be related to the right-hand elliptical polarization of the KAW [282].

While the kinetic range spectral ratios were considered in numerous works, only a few studies attempted to estimate the *local* spectral anisotropy, $k_\parallel(k_\perp)$. Cho and Lazarian [241, 245] estimated the local anisotropy in electron MHD and ERMHD fluid simulations, Chen *et al.* [276] and Podesta [201] gave approximate observational constraints, TenBarge *et al.* [43, 205] indirectly inferred the anisotropy from the frequency spectrum of gyrokinetic turbulence, and Sulem *et al.* [253] gave estimates based on Landau fluid simulations. These works generally obtained results broadly consistent with a critically balanced cascade of

[25] It is fair to mention that without linearization this is not more than a good guess. The nonlinear ERMHD equations cannot be brought into a symmetric form for n_e' and $\mathbf{b}_\perp'$.

KAWs. The simulations presented in this Thesis paved the way towards first direct estimates of $k_\parallel(k_\perp)$, obtained from fully kinetic simulations of sub-ion range turbulence [78, 161]. Such measurements are crucial for testing kinetic range theories that assume strong anisotropy and critical balance. The $k_\perp$ spectra alone are insufficient to establish a strong link with theory.

Finally, studies based on spectral properties alone may be criticized for ignoring (real space) turbulent structures, related to higher-order statistics and intermittency [53]. To overcome the latter limitation, we introduce in this Thesis a new set of generalized field ratios, which can be viewed as appropriate extensions of the standard field ratios to higher-order statistics (see Chapter 7). The generalized ratios were applied by the author to fully kinetic simulation and spacecraft data [161], and yielded results consistent with the KAW turbulence phenomenology.

3.3.5 Alternatives to the KAW turbulence phenomenology

In the previous sections, we focused almost exclusively on the theory of KAW turbulence, which might give the misleading impression that no other alternatives exist. It should be emphasized that the phenomenology of KAW turbulence represents just one out of several viewpoints that have been advocated in the community in recent years. For the sake of clarity, we discuss in the following some of the main alternatives.

In the context of wavelike interpretations, whistler wave turbulence [59, 80, 81, 143, 244, 245] is the main alternative to KAW turbulence. A proper description of whistler turbulence, accounting for kinetic effects such as damping and instabilities [93, 143], requires fully kinetic simulations [81–83]. Nevertheless, in analogy with KAW turbulence, an approximate qualitative understanding may be established based on a simple fluid equation, known as the equation of electron MHD. The model is readily obtained from equations (3.29), which are also the starting point for the ERMHD model. However, the derivation follows a different, much more straightforward path [59, 80, 241, 283]. The ions are assumed to be completely immobile such that both $\mathbf{u}_i$ and $\nabla \cdot \mathbf{u}_i$ can be neglected. We may thus set $\mathbf{u}_e \approx -\mathbf{J}/(n_0 e) = -c/(4\pi n_0 e)\nabla \times \mathbf{B}$, which immediately leads to

$$\frac{\partial \mathbf{B}}{\partial t} = -\frac{c}{4\pi n_0 e}\nabla \times [(\nabla \times \mathbf{B}) \times \mathbf{B}]\,. \tag{3.68}$$

This is the equation of electron MHD [283].[26] It is applicable in the limit of cold ions with $kv_{\mathrm{th},i} \ll \omega$ [59] at scales $1/d_i \ll k \ll 1/d_e$, $1/\rho_e$, but without assuming a strong spectral anisotropy as in ERMHD. By linearizing Eq. (3.68), the well-known dispersion relation of the whistler wave is obtained:

$$\omega_{WW} = \pm k_z v_A k d_i, \tag{3.69}$$

[26] The model may be extended to scales below d_e by including the effects of the electron inertia [244, 247]. Here we restrict the discussion to scales above d_e.

where we used the relation $v_A d_i = cB_0/(4\pi n_0 e)$. Solutions of a kinetic dispersion relation analysis, formally obtained in the asymptotic limit (3.28) and assuming $\beta_s \sim 1$, yield the following magnetic and electron compressibility predictions [59]:

$$C_\parallel = \frac{|b_\parallel|^2}{|b|^2} = \frac{k_\perp^2}{2k^2}, \qquad C_e = \frac{|\delta n_e/n_0|^2}{|b/B_0|^2} = \frac{1}{2k_z^4 d_i^4}. \tag{3.70}$$

The predicted damping rates imply that whistlers tend to be rather strongly damped for $k_z d_i \lesssim 1$ and $\beta_i \sim 1$, which imposes practical limits on their obliquity and compressibility [59, 229].[27] Moreover, for very oblique angles, the MHD fast modes transition at kinetic scales into ion Bernstein modes rather than into whistlers [40, 229, 237, 240]. A key difference between whistlers and KAWs in $\beta \sim 1$ plasmas is the electron compressibility, which is expected to be much smaller for whistler waves than KAWs [59, 145, 247]. The expectation is consistent with numerical solutions of the full kinetic dispersion relation [143]. Being of high-frequency, whistler waves also do not fulfill the perpendicular pressure balance relation (3.61).

A number of authors argued that whistler turbulence, if present at sub-ion scales, might be weak [59, 81, 284]. The weak turbulence regime was considered by Galtier and Bhattacharjee [80], who obtained a magnetic energy spectrum of the form $E_b(k_\perp) \propto k_\perp^{-5/2}$, assuming strong anisotropy $k_\parallel \ll k_\perp$, which is possible if $k_\perp d_i \gg 1$. On the other hand, if we allow for the possibility that whistler turbulence is strong, the spectrum can be obtained based on a set of heuristic arguments [245]. Unlike in KAW turbulence, the natural cascaded quantity is the total fluctuating magnetic field energy. The energy cascade rate is then $\Pi_W \sim (v_A/B_0)^2 b_\ell^2/\tau_c$, where τ_c is the cascade time and $\ell \sim 1/k$. The nonlinear time can be estimated from (3.68) as $\tau_{\rm nl} \sim (B_0/v_A d_i)\,\ell^2/b_\ell$ and the linear time is $\tau_W \sim \ell_\parallel \ell/(v_A d_i)$, where $\ell_\parallel \sim 1/k_\parallel$. In wavelike turbulence models, the cascade time can be generally estimated as $\tau_c \sim \chi^{-2}\,\tau_W$, where $\chi \sim \tau_W/\tau_{\rm nl}$ is the nonlinearity parameter [2, 80, 245]. The value of χ can be understood as the fractional change of energy during each wave scattering. $N \sim \chi^{-2}$ interactions are necessary to transfer the energy across a given scale if the changes accumulate as a random walk. Strong turbulence is achieved when $\chi \sim 1$ and in this case $\tau_c \sim \tau_{\rm nl} \sim \tau_W$. The spectral scalings of strong whistler turbulence can be therefore estimated as

$$E_W(k) \propto k^{-7/3}, \qquad E_W(k_\parallel) \propto k_\parallel^{-5}, \qquad k_\parallel \propto k^{1/3}, \tag{3.71}$$

where $E_W(k)$ and $E_W(k_\parallel)$ are, respectively, the 1D k and $k_\parallel$ spectra of the total magnetic energy. The predictions are exactly analogous to the standard KAW turbulence predictions (3.64), except for the change $k_\perp \to k$. This is only a minor difference, since it is clear from $k_\parallel \propto k^{1/3}$ that any initially isotropic state will eventually evolve towards strong anisotropy at small scales, such that $k \sim k_\perp$. The predictions (3.71) are consistent with numerical

[27] The whistler linear (ion) damping rate is approximately $|\gamma/\omega_{WW}| \approx 2\sqrt{\pi} k_z d_i \beta_i^{-3/2} \exp(-k_z^2 d_i^2/\beta_i)$ [59], which gives an order-of-magnitude estimate $|\gamma/\omega_{WW}| \gtrsim 1$ for $k_z d_i \lesssim 1$, unless $\beta_i \ll 1$ (the $\beta_i \gg 1$ case is restricted due to $k v_{{\rm th},i} \ll \omega$).

simulations of electron MHD turbulence [241, 244, 245]. The qualitative similarity between heuristic estimates of strong KAW and whistler-wave turbulence spectra shows that care has to be taken to clearly distinguish between the two competing models.

Observational data on kinetic range solar wind turbulence tends to be more consistent with the polarization properties of KAWs [145, 235, 236, 238], but there also exist studies in support of whistler waves [84, 285–288]. While the existence of whistlers in the turbulent solar wind is hardly disputable, their origin is an open question [287–289]. Existing studies imply that whistlers may not be present ubiquitously throughout the heliosphere, since they are detected in around 10% of intervals (close 1 AU) [287]. In conjunction, the electron heat flux instability has been considered as a possible source of whistler waves [93, 287–289]. Thus, whistler waves may not be an inherent property of the transition from MHD to kinetic range turbulence, but might instead be specific to intervals with linearly unstable electron velocity populations with fastest growing modes close to $kd_i \sim 1$ [289]. Starting from initially Maxwellian ion and electron velocity distributions, we do not find evidence of whistler waves in the kinetic simulations presented in Chapters 5, 6, and 7. In this sense, our results implicitly support the idea that preexisting, strongly unstable (electron) velocity distributions might be needed to generate sub-ion scale whistler waves. Another point worth acknowledging is the interesting possibility of a transition into whistler turbulence close to electron scales and beyond [225, 226, 247]. Little is known observationally and theoretically about sub-electron scale kinetic turbulence in space plasmas, but based on existing knowledge it may be judged that the conditions at sub-electron scales might be more favorable towards whistler turbulence [82, 84, 247, 290].

In the realm of linear wave physics, whistler waves and KAWs are not the only possibility and other types of waves, such as ion Bernstein modes [40, 142, 286] or kinetic slow modes [291], have also been considered.[28] Ion Bernstein modes may be of particular interest, since they exist at highly oblique angles, where they can couple to fast magnetosonic modes as well as to KAWs [142]. In Chapter 5 we present some numerical evidence for such mode coupling in a (moderately) low-β_i, turbulent plasma [40].

Finally, there exists another common view in the community, which is in sharp contrast with wavelike interpretations of turbulence. In particular, a number of authors argue that the kinetic range turbulence is hardly related to any wave activity and that an interpretation should be instead given in terms of nonlinear turbulence dynamics, scale-to-scale energy transfers, and intermittency [37, 38, 50, 53, 227, 269, 292]. A major motivation for the view is the fact that by the time that kinetic scales are reached, the turbulent energy has already cascaded over the entire MHD inertial range and has naturally developed distinct turbulent structures, leading to heavy-tailed non-Gaussian fluctuations and intermittency [53, 176]. This puts to question perturbative approaches such as gyrokinetics [4, 5, 50], where the kinetic fluctuations are expanded around a mean background to lowest order in the small parameter. Based on experience from (resistive) MHD turbulence, authors not in favor of the wavelike viewpoint also frequently argue that the turbulent dissipation

[28] It is worth mentioning that the kinetic slow mode is expected to be strongly damped at sub-ion scales, unless $T_e \gg T_i$ [143, 229].

of the nearly collisionless cascade should be concentrated in the vicinity of turbulent structures [48, 269, 292, 293]. Since no straightforward expression for dissipation in a nearly collisionless plasma exists, a number of works aimed to identify correlations between various "dissipation proxies" and coherent turbulent structures [48, 269, 292, 294]. While it is intuitively clear that intense structures may contribute to enhanced heating [55, 85, 295], establishing a direct link locally in space can be somewhat ambiguous, since the energy conversion between the electromagnetic and fluid energy, $\mathbf{J} \cdot \mathbf{E}$, and the species fluid and internal energy, $\mathsf{P}_s : \nabla \mathbf{u}_s$, are not sign-definite [69, 292]. Moreover, unlike in collisional MHD where the transfer is instantly converted to heat via resistivity and viscosity, in a nearly collisionless plasma, the energy transfer and the subsequent (partial) thermalization via collisions (or perhaps, in a coarse-grained sense [69]) will be generally displaced from each other in space and time [98, 101, 296]. More generally, establishing concrete kinetic turbulence scaling predictions without any reference to linear physics has proven difficult. To our knowledge, a rare exception to that is the recent work of Eyink [69], where a "4/5th-law" for anomalous entropy production is obtained, together with theoretical bounds for the turbulence scaling exponents. In the opinion of the author, it is not *a priori* evident that turbulent structure formation is a sign of reduced wavelike activity. Indeed, a number of recent works on MHD turbulence [57, 58, 297] interpret turbulent structure formation as a natural consequence of interaction between Alfvén wave packets. In Chapter 7 we try break from a presently common view that interprets kinetic-scale waves and turbulent structures as nearly exclusive to each other and we discuss instead an alternative unifying interpretation, supported by a state-of-the-art analysis of kinetic simulation and observational data [161].

Chapter 4

Turbulence simulations with OSIRIS

OSIRIS is a fully kinetic, fully explicit, fully relativistic particle-in-cell (PIC) code, designed for modern high-performance simulations [60, 61, 298]. The code is officially developed and distributed by the OSIRIS Consortium, consisting of University of California, Los Angeles and Instituto Superior Técnico, Lisbon. We would like to take the opportunity to very kindly acknowledge the OSIRIS Consortium for providing access to the OSIRIS framework. Traditionally used for *ab initio* kinetic studies of plasma wakefield accelerators, the code has recently found application in a wide range of kinetic plasma physics problems (e.g., [78, 299–302]). Among these numerous new applications are also the kinetic simulations of solar wind turbulence presented in this Thesis. Most of the simulations presented here required state-of-the-art computing resources, access to which has been granted on the basis of independently reviewed research proposals. Below, we briefly introduce some of the main OSIRIS features, followed by a more detailed technical description of the simulation setups, used to produce the results presented in Chapters 5, 6, and 7.

4.1 Code overview

In its essence, the default numerical scheme employed in OSIRIS is the standard version of the PIC method, as described in the well-known literature on the subject [62, 63]. As such, the default numerical scheme is explicit and features second-order, space and time centered finite-difference derivatives. The finite-difference time domain method is used to solve the Maxwell equations on a staggered Yee grid for the fields, and the particles are advanced using the Boris push (see also Sec. 2.2). A large number of different boundary conditions are supported, but in this Thesis we always use periodic boundaries in all spatial directions. The initial conditions for the fields may be specified in several ways, including explicit mathematical expressions. Similarly, the particle initialization supports different types of velocity distributions. For reference, we list here the default normalizations used

in the code:

$$t' = t\omega_{pe}, \qquad \mathbf{r}' = \mathbf{r}/d_e, \tag{4.1}$$

$$\rho'_s = \rho_s/(en_0), \qquad \mathbf{p}'_{sj} = \mathbf{p}_{sj}/(m_s c) = \gamma_{sj}\mathbf{v}_{sj}/c, \tag{4.2}$$

$$\mathbf{E}' = \frac{e}{m_e c\omega_{pe}}\mathbf{E}, \qquad \mathbf{B}' = \frac{e}{m_e c\omega_{pe}}\mathbf{B}, \tag{4.3}$$

$$m'_s = m_s/m_e, \qquad q'_s = q_s/e. \tag{4.4}$$

All symbols above have standard meanings as in previous chapters (see also Appendix C). Real particle charges and masses have to be specified only occasionally (e.g., with explicit binary collisions); otherwise the normalized species mass-to-charge ratio, m'_s/q'_s, is sufficient to determine the dynamics.

Critical for the simulation efficiency and accuracy are the sophisticated numerical optimizations and computational strategies built on top of the core algorithm. A distinct feature is the support for efficient high-order (quadratic and cubic) particle spline interpolation, combined with a charge-conserving current deposit [108, 109]. This allows for improved energy conservation and reduced particle noise compared to low-order splines [298]. The numerical self-heating, related to grid aliasing effects, may be reduced even further with binomial (compensated) low-pass filters [63], applied to the fields. The code is parallelized using MPI [303] domain decomposition, together with added support for OpenMP shared memory parallelism on each MPI node. Floating point operations are performed in double precision by default, although the user can also choose single precision. A significant computational speedup is achieved with low-level hardware optimized vector instructions (SIMD) for CPUs. More recently, support for GPU parallelization was added. A large number of diagnostics for fields and particles are supported, all of which are stored in the HDF5 data format. Altogether, the above features make OSIRIS an extremely mature code that can scale efficiently to over a million CPU cores [61]. Nevertheless, state-of-the-art massively parallel production runs still require a very careful design of the simulation setup for optimal results. This typically involves a suite of system-specific and problem-specific code performance and numerics tests, in order to find the optimal configuration which works best for a specific problem on a specific supercomputer. Below, we give some examples from the simulation runs performed in the scope of this Thesis.

4.2 Problem-specific performance tests

In this section, we give for reference an example of a problem-specific code performance test, which was carried out by the author as part of a preparatory access to the Shaheen II Cray XC40 system at the KAUST Supercomputing Laboratory. Scaling studies were also carried out on the Hydra cluster at the Max Planck Computing and Data Facility (not shown here), in preparation for production runs on the SuperMUC system at the Leibniz-Rechenzentrum. Quite often, the problem-specific performance tests are a necessary prerequisite for obtaining access to leadership computing resources.

A representative, three-dimensional (3D) simulation with periodic boundaries in all directions was chosen as the basis for the test. The computational grid size was 1920^3, with 64 particles per cell per species. Cubic spline interpolation was used. These settings resemble the actual large-scale production runs (see Sec. 4.4). To obtain realistic estimates, diagnostics for fields and particles were used during the scaling tests. The diagnostics included electromagnetic field data (written only at the start of each test run) and particle track data with about 8,000 tracks per species. The latter diagnostic was optimized to achieve good performance during runtime. First, a series of small simulations was performed to find the optimal parallelization strategy. Best results were obtained for a hybrid MPI/OpenMP parallelization, running 2 threads per MPI task. Using these settings, a strong scaling test was conducted for the large problem, by performing a series of runs from 27,648 to 131,072 CPU cores. The results are shown in Fig. 4.1 and demonstrate an almost ideal scaling over the range studied. Additional information is given in Table 4.1. A high computational performance was achieved thanks to the hardware optimized vector instructions (AVX SIMD) for CPUs, which are readily available as part of OSIRIS. For our specific problem type, the simulations also benefited from the large availability of memory per CPU ($\approx$ 4 GB) on Shaheen II, which can accommodate a large number of computational particles. The results in Table 4.1 are comparable to those reported by the main code developers for similar systems [61].

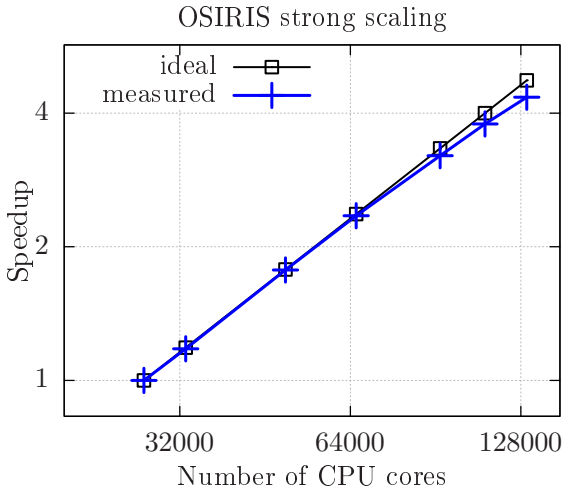

Figure 4.1: Strong scaling of OSIRIS on a Cray XC40 from 27,648 to 131,072 CPU cores.

Another critical aspect for the success of massively parallel simulations is efficient handling of data output to the file system. Frequent output of large amounts of data can deteriorate the performance significantly. Rather than categorically outputting a large number of different data, one is faced with the necessity to carefully decide in advance which particular diagnostics are needed and how frequently they should be saved. Similarly, very frequent output of code checkpoints is not feasible in large-scale simulations. On the other hand, whenever the data output is necessary, it is crucial that the operation is done

Num. of cores	Part. pushed per second	Speedup	Time spent on node boundary updates
27,648	$72 \cdot 10^9$	1.	7.9%
32,768	$85 \cdot 10^9$	1.18	8.0%
49,152	$128 \cdot 10^9$	1.77	8.3%
65,536	$169 \cdot 10^9$	2.35	8.4%
92,160	$231 \cdot 10^9$	3.21	9.8%
110,592	$273 \cdot 10^9$	3.78	9.8%
131,072	$313 \cdot 10^9$	4.35	10.9%

Table 4.1: Performance of OSIRIS on the Shaheen II Cray XC40 system. The timings represent averages across all MPI nodes. Each simulation ran for a hundred time steps and used a total of $\approx 9 \cdot 10^{11}$ computational particles (ions and electrons).

efficiently and reliably. None of the latter can be taken for granted in high-performance computing. To this end, we tested the output performance for a set of representative file types in the large-scale PIC simulation on the Cray XC40 system. In some cases, the performance was optimized by adjusting the HDF5 library parameters. The results are given in Table 4.2 and demonstrate excellent performance for the considered data types. Note that these results can be highly system-dependent.[1]

Data type	Format	Size	Throughput
3D field data	HDF5	$\approx$ 27 GB/file	$\approx$ 1.2 GB/s
2D slices	HDF5	$\approx$ 15 MB/file	$\approx$ 800 MB/s
Checkpoint data	Binary	$\approx$ 64 TB/checkpoint	$\approx$ 270 GB/s

Table 4.2: OSIRIS data output performance on the Lustre file system of Cray XC40.

4.3 Design of the physical simulation setup

In the author's experience, careful design of the simulation setup is crucial for achieving a fast and efficient transition to fully developed, strong turbulence in fully kinetic simulations. In contrast with turbulence in neutral fluids described by the Navier-Stokes equation, a high degree of randomness and/or statistical isotropy in the initial perturbation or in the external turbulence forcing may easily translate into a predominantly linear, and possibly high-frequency response of the plasma. The reason for the qualitative difference between neutral-fluid and plasma turbulence is that plasmas, unlike regular fluids, support a very large number of linear modes [304]. This property is especially noticeable in 3D simulations,

[1]For example, on the SuperMUC system at the Leibniz-Rechenzentrum, the output of checkpoint data was a quite significant limiting factor for the maximal size of the massively parallel simulations.

which give more room for different types of linear response compared to the simplified two-dimensional (2D) simulations. Below we give guidelines for achieving strongly turbulent regimes based on the simulation runs presented in this Thesis. We mention that at least some of the aspects discussed below are presently not universally appreciated in the kinetic turbulence simulation community.

The key physical aspects considered for the design of simulation runs presented in this Thesis can be divided into the following categories:

- Type of initial perturbation or external forcing,
- Physical simulation box dimensions,
- Plasma parameters, such as the ion and electron beta.

The first point is arguably the most essential one. One might wonder why is the type of initialization or external forcing essential, given that turbulence is believed to be a natural constituent of many weakly collisional plasmas, regardless of the precise features of the system under consideration. Is it not reasonable to expect that turbulence will eventually develop from almost any unstable configuration? The answer is in principle yes. However, many unstable configurations may in practice require a vast amount of scale separation (in space and time) and a large supply of energy, before a fully developed turbulent cascade eventually emerges. For instance, in the solar wind it takes more than one decade in wavenumber space before the fluctuations transition into a proper inertial range type of cascade with a Kolmogorov-like $\sim k^{-5/3}$ magnetic energy spectrum (e.g., [33]). Above the transition scale, a range frequently referred to as the outer scale or energy containing scale with a $\sim k^{-1}$ spectrum exists.[2] In order to spend computational resources wisely, it is therefore crucial to achieve a fast and efficient transition to turbulence within the system size limits of present state-of-the-art simulations. Various approaches have been employed to achieve this goal [77, 81, 87, 252, 295, 305]. For the simulation runs presented in Chapters 5, 6, and 7, we employ one particular technique [39, 43, 78, 87, 305], where the initial perturbation or external forcing *itself* mimics the intrinsic properties of plasma turbulence at the scale of the simulation box.

At kinetic scales, the phenomenology of plasma turbulence is presently less understood compared to the inertial, magnetohydrodynamic (MHD) range [32, 41, 188]. Once the turbulent cascade transitions into the kinetic range, the number of possible linear solutions increases and significant collisionless damping may occur [4, 40, 52, 306]. In view of these circumstances, we employ here computational domains slightly larger than the characteristic ion kinetic scales, where the transition into the kinetic range occurs. In the latter case, the phenomenology of MHD turbulence may be used to guide the choice of initial condition or the type of external forcing. This approach has also the advantage that it does not strictly enforce any particular type of kinetic-scale fluctuations, thus allowing the sub-ion

[2]The so-called energy containing range of the solar wind is believed to consist of a mixture of outward propagating Alfvén waves, magnetically dominated force-free structures, and of a subdominant population of nonlinearly interacting fluctuations [218].

scale turbulence to attain its most natural state. Ideally, even much larger computational domains, covering several hundred ion inertial lengths, should be employed for maximal realism. Present state-of-the-art capabilities permit computational domains with linear sizes of a few ten d_i in fully kinetic, 3D explicit PIC simulations. Somewhat larger domains are accessible with substantial artificial reductions in the ion-electron mass ratio to values as low as $m_i/m_e \approx 25$, or even less. While reduced values of the mass ratio are almost inevitable at present [40, 77, 269], we do not fully adhere to the latter simplification, since our aim is to investigate the sub-ion scale range.

Decades of numerical and observational studies have demonstrated that the turbulence at MHD scales is predominantly low-frequency [141, 235], Alfvénic [139, 234, 307, 308], and inherently anisotropic [138, 140, 160, 200, 201, 209, 309], with turbulent eddies elongated along the local field-parallel direction (see Sec. 3.2). Furthermore, MHD theory tells that nonlinear interaction occurs only between counterpropagating Alfvén wave packets [136, 184, 297, 310]. Our simulations take into account these properties. In practice, this means that the kinetic turbulence is seeded at the tail of the MHD range by Alfvénic fluctuations, corresponding to counterpropagating, shear Alfvén waves with $k_\parallel < k_\perp$. These perturbations are incorporated into the fully kinetic model in a way which tries to avoid a spurious high-frequency response of the plasma. For decaying simulations we set up the fluid velocity profiles by locally shifting the ion and electron velocity distributions during initialization. Similarly, we explicitly initialize a self-consistent electric current according to $\mathbf{J} = (c/4\pi)\nabla \times \mathbf{B}$, by adding an additional shift to the electron velocity distribution. Similar considerations are made for forced turbulence runs [9, 161, 305]. Further details are provided in Appendices A and B. Therein, the reader can find a detailed description of an MHD-like initial condition and of an external forcing scheme, which were used to obtain the results presented in Chapters 6 and 7.

Having discussed the initialization, external forcing, and simulation box dimensions, brings us to the last point, which pertains to the selection of plasma parameters. We mostly choose representative parameters for the near-Earth, free streaming solar wind, which is a $\beta \sim 1$ plasma with an ion-electron temperature ratio of order unity [27, 32]. The choice of parameters "typical" for the solar wind is motivated by the abundance of observational data for this regime, against which the simulation results can be compared. Here, it is important to acknowledge a few caveats. First, there is a large variability in the plasma beta and in the ion-electron temperature ratio values across different solar wind periods, as well as in astrophysical plasmas generally [18, 32]. Secondly, while β and T_i/T_e do fall within the typical range, other (perhaps less significant) parameters that make up these two ratios differ from their realistic values. For instance, the electron beta can be expressed as $\beta_e = (\omega_{pe}/\Omega_{ce})^2(v_{\mathrm{th},e}/c)^2$. In line with the vast majority of present fully kinetic, electromagnetic simulations of space plasma turbulence [77, 82, 311, 312], neither the electron plasma to cyclotron frequency ratio, nor the electron thermal speed as a fraction of c, are chosen close to their realistic values.[3] Such artificial adjustment is

[3]Many computational works do not state these values explicitly, but it is usually possible to at least roughly estimate ω_{pe}/Ω_{ce} and $v_{\mathrm{th},e}/c$ from the other given simulation parameters.

almost mandatory in present electromagnetic, explicit PIC simulations due to the harsh computational constraints. The ω_{pe}/Ω_{ce} ratio is typically assigned a lower than realistic value and the $v_{\mathrm{th},e}/c$ ratio a higher. The former may give rise to charge separation at electron scales, whereas the latter eventually yields relativistic electrons. As long as the electron-scale dynamics remains to a good approximation quasi-neutral and non-relativistic, the artificial adjustments are considered acceptable [78, 116]. In practice, many computational studies use $\omega_{pe}/\Omega_{ce} \gtrsim 2$ and $v_{\mathrm{th},e}/c \lesssim 0.25$.[4] A number of other simplifications are also made. In 3D we mostly—although not exclusively (see Chapter 6)—consider globally balanced regimes with a near-zero normalized cross-helicity σ_c (see Sec. 3.2). Especially the fast streams of the solar wind frequently exhibit high levels of imbalance [217–219]. All presently known kinetic range turbulence phenomenologies implicitly assume $\sigma_c \approx 0$ for simplicity. Because a major objective of ours is to critically examine the leading kinetic range theories, we mainly focus on globally balanced regimes. As already implied, the ion-electron mass ratio is artificially reduced in our simulations, compared to a real hydrogen plasma. We use either $m_i/m_e = 100$ or $m_i/m_e = 64$. These values were chosen as a reasonable compromise among the competing desires for MHD-sized domains on one hand, and large scale-separations between ions and electrons on the other hand. Significantly higher mass ratios could be achieved in massively parallel 2D simulations.[5] Astrophysical magnetized plasma turbulence is in principle inherently 3D [51, 59] and certain aspects of it (e.g., the $k_\parallel(k_\perp)$ anisotropy) are ill-defined in 2D. For this reason, we focus our main effort on massively parallel 3D simulations. Finally, all particle distributions are loaded as isotropic Maxwellians at the start of the simulation. This choice is made for simplicity. Preexisting, strongly anisotropic and non-Maxwellian background distributions could give rise to a number of fast-growing kinetic instabilities [93], and further complicate an already elaborate physical interpretation. In this respect, we can once more emphasize that the present understanding of sub-ion scale, weakly collisional plasma turbulence is rather scarce and only very few 3D fully kinetic simulations were devoted to it so far [77, 252, 269]. Thus, it seems natural to consider first a more simplified scenario, before thinking of advanced topics, such as kinetic turbulence in a strongly non-Maxwellian and temperature-anisotropic mean background.[6]

To conclude this section, we give an overview of the main physical properties of our simulation runs in Table 4.3. Each row corresponds to a different Chapter of the Thesis. The numerical parameters are discussed in the next section.

[4] For reference, some characteristic values for the solar wind would be $\omega_{pe}/\Omega_{ce} \sim 10^2$ and $v_{\mathrm{th},e}/c \sim 5{\cdot}10^{-3}$ [27].

[5] Note that an increase of the simulation size by a factor of α (in each dimension) prolongs the aggregate computing time by a factor of $\sim \alpha^3$ and $\sim \alpha^4$ in 2D and 3D, respectively. The extra power comes from the large-scale turbulence eddy turnover time, which is proportional to the system size.

[6] Evidently, strong temperature anisotropies and non-Maxwellian features can (and do) develop in kinetic simulations directly as a result of the turbulent dynamics [38, 49, 132]. Note that most kinetic instabilities have peak growth rates on scales $k_\perp \rho_s \lesssim 1$ [93, 95, 188, 289, 313], whereas the turbulently generated (local) anisotropies tend to peak around $k_\perp \rho_s \sim 1$. Moreover, on the typical time scales covered in fully kinetic simulations, bulk plasma heating is usually too slow (and/or insufficiently anisotropic) to generate a strong *global* temperature anisotropy.

Ch.	Type	Initialization/forcing	β_i	T_i/T_e	m_i/m_e	ϵ	$L_\perp/d_i$	$L_\perp/L_z$
5	2D, decaying	large-scale $\mathbf{u}_\perp$ and $\mathbf{b}_\perp$ perturbations	0.5, 0.1	≈ 1.0	100	0.15, 0.3, 0.1, 0.2	25.1	n/a
6	3D, decaying	counterpropagating, oblique Alfvén waves	0.5	≈ 1.0	64	0.4	17.0	0.4
7	3D, forced	low-frequency, ext. current drive	0.56	≈ 1.1	100	≈ 0.5	18.9	0.39

Table 4.3: Overview of physical simulation parameters. The parameter $\epsilon \approx \delta u/v_A \approx \delta b/B_0$ denotes the (initial) root-mean-square turbulence fluctuation amplitude.

4.4 Choice of numerical parameters

Let us now discuss the choice of numerical parameters for our PIC simulations of plasma turbulence. General constraints on the time step and grid spacing are imposed by the standard numerical stability requirements for the explicit PIC scheme (see Sec. 2.2). Thus, the grid spacing needs to be comparable to the Debye length (in any direction) and the time step is determined by the CFL condition based on the speed of light. Here, we use grid spacing between $\approx \lambda_D$ and $\approx 1.5 \cdot \lambda_D$ and we integrate the equations with CFL parameters around ≈ 0.95. Cells slightly larger than λ_D are permitted when high-order particle shapes are used, which reduce the numerical self-heating [106]. Regarding the total number of time steps, we integrate the equations for as long as needed to reach a fully developed turbulent state. For simulations of Alfvénic, space plasma turbulence, this time amounts to around $\gtrsim 10^5$ time steps.

In the rest of this section, we devote a few words to one particularly important numerical aspect, which is the mitigation of the background thermal noise in particle-based kinetic simulations (see also Sec. 2.2.2). First, we note that a high *relative* level of the thermal noise is not an exact synonym for the lack of velocity-space resolution. The degree to which the thermal fluctuations mask the smooth, self-consistent plasma response is problem dependent, whereas the velocity-space resolution is determined directly by the number of particles in a given volume.[7] Apart from having a dependence on the plasma parameters, the relative strength of the noise can even vary between different quantities in a single simulation [40]. For some problem types, the thermal noise may not be a particularly significant factor. The simulations of kinetic range space plasma turbulence happen to fall in the other category, and therefore, we provide here some details on how we coped with the particle noise.

Below, we base our discussion of particle noise around a few concrete examples, taken

[7]Thermal noise in the electromagnetic fields may be roughly estimated from equilibrium statistical mechanics [62, 63, 116]. This shows that its relative strength decays with the number of particles per Debye length and grows with the ratio of the particle thermal to the fluctuating, self-consistent field energy. Thus, high-beta and low-amplitude turbulent fluctuations are the most challenging case.

from our simulations. Some of these results were published in Refs. [40, 78]. As already mentioned, the relative strength of noise increases with the plasma beta and drops with the turbulence fluctuation amplitude. This is the main practical reason why we use only moderately low fluctuation amplitudes and why we do not perform simulations with betas much higher than $\beta \approx 1$. Even when doing so, it is still beneficial to try to reduce the noise even further. The most straightforward way is to increase the number of computational particles. We use of the order of one hundred particles per cell per species in 3D and between several hundred and a thousand in 2D, which is comparable to the values reported for similar simulations [48, 77, 269, 312].

Given the memory and computing limitations of present state-of-the-art simulations, we also employ two additional, somewhat less common, techniques for reducing the noise. The first one pertains to the choice of the particle spline interpolation. The vast majority of fully kinetic PIC codes uses linear splines. In OSIRIS, an efficient implementation of high-order (quadratic and cubic) splines is readily available and it is exploited here as a means for reducing the noise and improving the energy conservation. An example is given in Fig. 4.2, which compares the spectra from decaying 3D turbulence simulations (see Chapter 6) for different numbers of particles per cell per species (N_{ppc}) and for different particle spline interpolations. The results clearly show that cubic splines are much superior to the more standard linear splines in terms of the noise properties at high (perpendicular) wavenumbers. The simulation with $N_{ppc} = 64$ and cubic splines gives results comparable to the run with $N_{ppc} = 125$ and linear splines, in terms of noise in the electron density spectrum. In terms of the noise in the magnetic field, even the simulation with only $N_{ppc} = 32$ and cubic splines gives much lower noise levels, compared to the run with linear splines. It is important to acknowledge that higher order splines require many more floating point operations per step. However, the most serious bottleneck for present large-scale 3D simulations is quite often represented by the amount of data that a given supercomputer and its file system can handle. It is therefore the opinion of the author that higher-order (quadratic or cubic) splines should be preferred for this particular problem type.

Finally, given that the self-consistent turbulent dynamics of interest is typically relatively low-frequency, a significant reduction of the noise is also possible by averaging the raw simulation data over a short time window [40, 77, 118]. Indeed, when the fluctuation amplitudes in the self-consistent fields are relatively low, it may happen that a considerable fraction of the smooth field response is merely "covered up" by the noise [113]. We illustrate the technique based on the 2D simulations from Chapter 5, which were published in Ref. [40]. In Figure 4.3 we show the contour plots of the electric field (E_x and E_z) and of the out-of-plane electric current (J_z), with and without short-time averaging. In all cases shown, the short-time average was performed over a window of duration $\Delta t = 0.5\Omega_{ci}^{-1}$. It is clearly seen that the noise is substantially reduced by short-time averaging, while at the same time, it preserves the turbulent structures that evolve on a slower time scale. Further insight is obtained by considering the turbulent spectra shown in Fig. 4.4. In terms of the spectra, the background thermal noise may be directly estimated as follows. For each turbulence simulation, we perform a corresponding thermal plasma run with the exact same parameters (including a mean magnetic field) as in the turbulence simulation. The

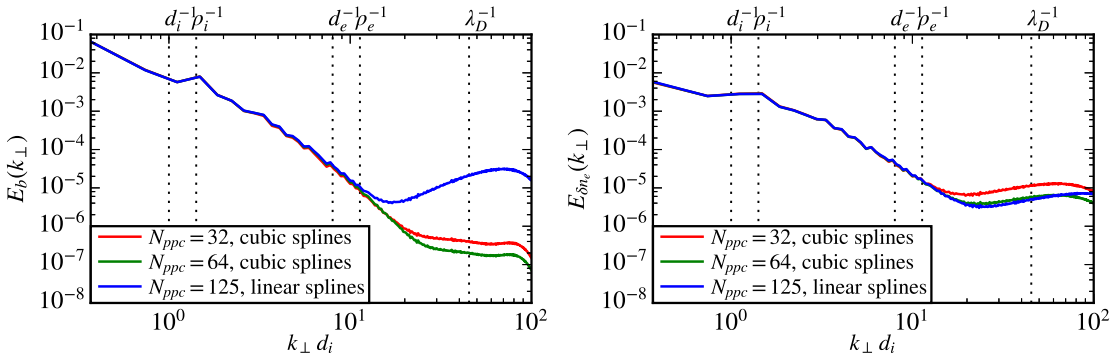

Figure 4.2: Turbulent spectra of the magnetic field (left) and of the electron density (right), obtained from PIC simulations with different particle counts and different orders of spline interpolation. All curves shown above correspond to 3D simulations of decaying turbulence (Chapter 6). The flattening of the spectra at high $k_\perp$ is due to the noise.

kinetic equations are integrated for a few thousand time steps, until the thermal noise spectra reach a quasi-steady state. The final noise estimates are plotted in Fig. 4.4 with dashed lines. This clearly shows how the turbulence simulations become dominated by noise at high wavenumbers. Moreover, it is evident that (i) different fields are affected by the noise differently, and (ii) the runs with a lower turbulence amplitude (ϵ) are generally more influenced by the noise. Same as for the 2D simulations, we also employ short-time averages in the 3D simulations. In the latter case, we perform the averages over shorter time windows because the time evolution in 3D tends to be faster than in 2D [87].

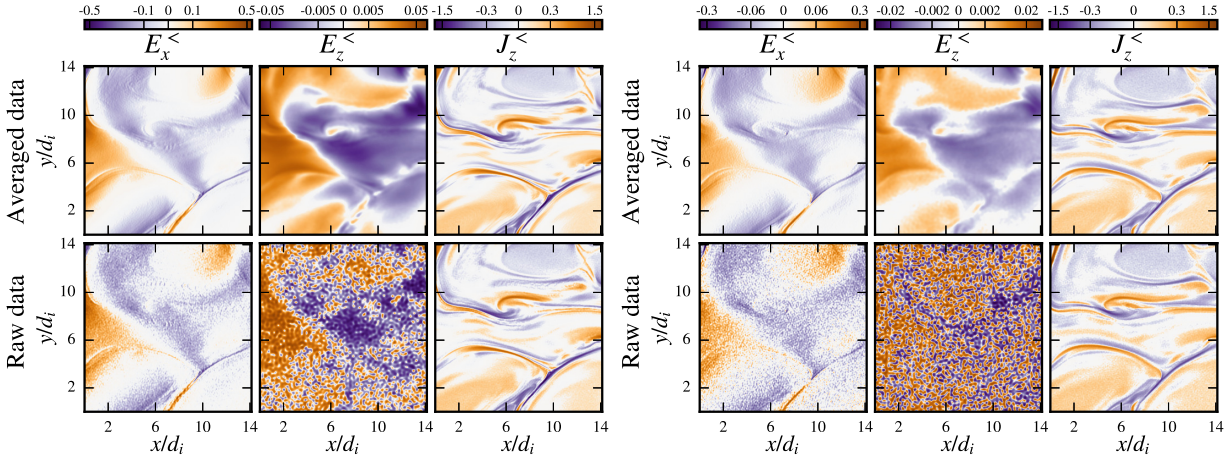

Figure 4.3: Turbulent field structure with and without short-time averaging of the raw simulation data. The initial fluctuation amplitudes were $\epsilon = \delta b/B_0 = 0.2$ (left panel) and $\epsilon = 0.1$ (right panel). The ion beta was $\beta_i = 0.1$. Only a subpart of the whole 2D domain is shown. All fields have been additionally low-pass filtered to wavenumbers $k_\perp < 4/d_e$. 625 particles per cell per species with cubic spline interpolation were used in both simulations.

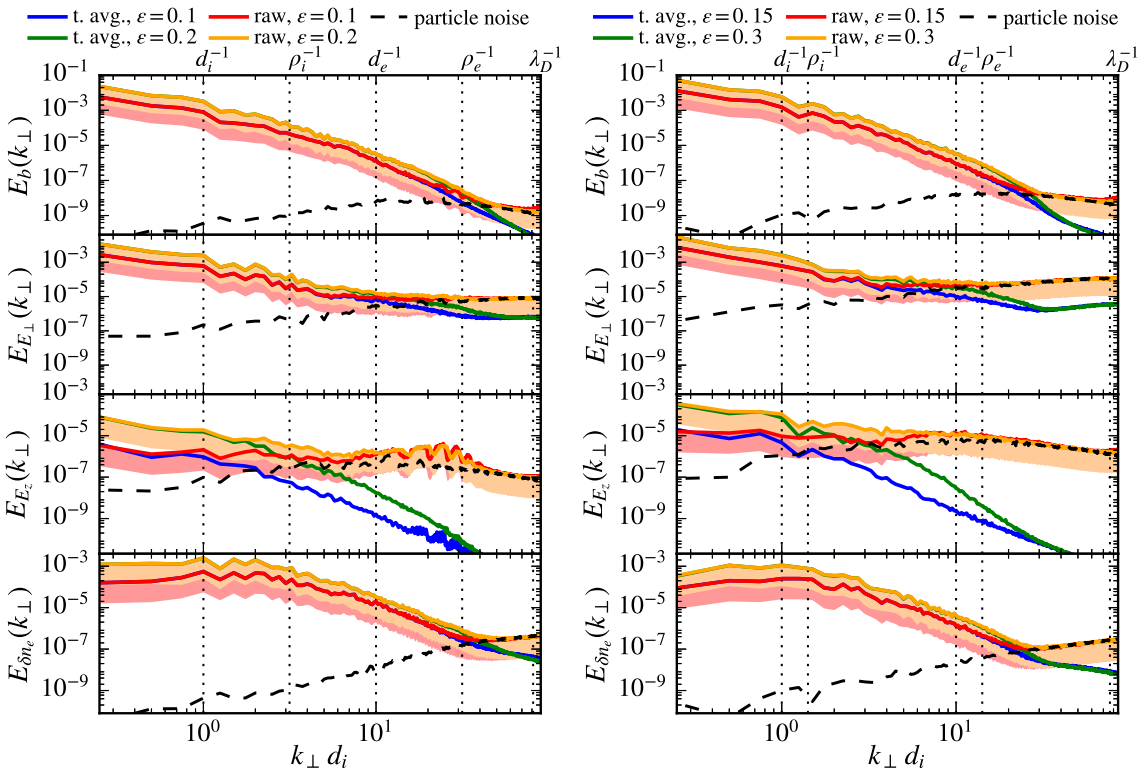

Figure 4.4: Effect of short-time averaging on the turbulent spectra in relation to the background thermal particle noise. Results were obtained from 2D simulations (Chapter 5) with $\beta_i = 0.1$ (left) and $\beta_i = 0.5$ (right) and for different turbulence amplitudes ϵ.

To summarize, we give an overview of our main simulation parameters in Table 4.4. Among others, we also list the typical amount of CPU hours required for a single simulation of a given type. Further details for each simulation are provided in the following chapters, where our main results are presented.

Ch.	$N_{\text{particles}}$	N_{grid}	N_{steps}	N_{cores}	Interpolation	Core-h/run
5	$7.5 \cdot 10^9$, $5.2 \cdot 10^9$	1920^2, 2048^2	$\approx 2 \cdot 10^5 - 5 \cdot 10^5$	4,096	cubic	$\approx$ 500 k
6	$1.2 \cdot 10^{11}$	$768^2 \times 1536$	$\approx 1.3 \cdot 10^5$	32,768	cubic	$\approx$ 4 M
7	$5.0 \cdot 10^{11}$	$928^2 \times 1920$	$\approx 2.7 \cdot 10^5$	49,152	quadratic	$\approx$ 10 M

Table 4.4: Overview of the numerical simulation parameters.

Chapter 5

Comparison of kinetic models in collisionless plasma turbulence

This Chapter is the first in a sequence to present the main results of this Thesis. Here, we report the results of a detailed kinetic model comparison in two-dimensional (2D), kinetic range plasma turbulence. Apart from the fully kinetic description, we also include for reference the results from the reduced-kinetic models described in Sec. 2.3. The results shown below have been published as an article in the Astrophysical Journal [40].

This study represents the first of its kind, direct comparison of the fully kinetic (FK), hybrid-kinetic (HK), and gyrokinetic (GK) models in kinetic range, collisionless plasma turbulence. The need for such a comparison was clearly pointed out in the community [314], but it was not until this study that the most prominent kinetic models (fully kinetic, gyrokinetic, and hybrid-kinetic) were directly compared in a turbulent regime, relevant to space and astrophysical plasmas. The project was led by the author of this Thesis, who specified the simulation setup and the choice of diagnostics (in close correspondence with the coauthors), performed the fully kinetic simulations, produced the figures, and provided a written interpretation of the results, taking into account helpful suggestions and comments from the coauthors. The reduced-kinetic simulations were performed by the coauthors. In particular, S. S. Cerri, A. Bañón Navarro, and C. Willmott provided, respectively, the hybrid-kinetic, gyrokinetic, and KREHM simulation results. Besides analyzing the fully kinetic simulation output data, the author also carried out the calculation of the turbulent spectra and spectral ratios, the calculation of scale-filtered mean J_z values, and the computation of the statistics of magnetic field increments for all reduced-kinetic models included in the comparison.

We emphasize that the dilemma on the choice of the appropriate (reduced) kinetic model is not a pure modeling question as much as it is presently a critical physics question. The subject would concern only modeling if we already had a complete understanding of how kinetic plasma turbulence works across different regimes. However, a comprehensive understanding is currently lacking, and for this reason, detailed model comparisons are crucial in order to conclusively identify the key physical mechanisms that dominate the kinetic range turbulence. We also stress that the reduced-kinetic models involved in the

comparison (HK, GK, and KREHM) are by no means trivial, and they may be obtained rigorously from the fully kinetic description in certain physical limits (see Sec. 2.3). In recent years, distinct and somewhat contradictory views on the applicability of different reduced-kinetic models have been advocated in the community [4, 5, 38, 50, 188]. In this context, the present study might also help in resolving some of the controversies.

The rest of this Chapter is organized as follows. In Sec. 5.1 we describe the simulation setup and the choice of the plasma parameters. The results are presented in Sec. 5.2. Several aspects of the kinetic turbulence are considered. First, we analyze in Sec. 5.2.1 the real space structure of the turbulent fields and intermittency. In Sec. 5.2.2 we consider the global energy budget and the bulk plasma heating, followed by an analysis of the spectral features in Sec. 5.2.3. Finally, in Sec. 5.2.4 we analyze non-thermal features in the particle distribution function. We conclude the Chapter with a summary of our main findings in Sec. 5.3.

5.1 Problem description and simulation setup

The simulation setup for the comparison was chosen as a compromise between the desire for maximal physical realism and computational accessibility of the problem. In particular, we chose to study decaying, 2D plasma turbulence with an out-of-plane mean magnetic field. Certain aspects of collisionless plasma turbulence are inherently three-dimensional (3D) [51, 59]. However, 3D kinetic simulations presently require state-of-the-art computing resources (see Chapters 6 and 7). Based on our experience with the project, any reasonably successful and comprehensive kinetic model comparison requires a series of test runs, before an acceptable final set of simulation parameters (for *all* models involved) is even determined. Moreover, it is advantageous if the final set of simulations involves a range of different turbulence regimes in order to better illustrate the key differences between the models. All of the above objectives would be extremely difficult to achieve in present 3D kinetic simulations. It is for this reason that we adopt here a 2D simulation setup. Nevertheless, based on existing literature, we still expect our simplified setup to capture at least some of the key aspects of collisionless plasma turbulence [38, 87, 134, 315].

As far as the initial condition goes, we adopt a frequently used initial condition known as the 2D Orszag-Tang vortex [316]. The initial perpendicular fluid velocity $\mathbf{u}_\perp$ and the perpendicular fluctuating magnetic field $\mathbf{b}_\perp$ are given by

$$\mathbf{u}_\perp = \delta u \Big(-\sin(2\pi y/L),\, \sin(2\pi x/L) \Big), \tag{5.1}$$

$$\mathbf{b}_\perp = \delta b \Big(-\sin(2\pi y/L),\, \sin(4\pi x/L) \Big), \tag{5.2}$$

where L is the size of the periodic square, δu is the initial root-mean-square (RMS) fluid velocity, and δb is the initial RMS fluctuating magnetic field. A mean magnetic field $\mathbf{B}_0 = B_0 \hat{\mathbf{e}}_z$ is prescribed in the out-of-plane (z) direction. In the FK and HK models, the fluid velocities are initialized by locally shifting the (Maxwellian) particle velocity distributions. In the GK model and KREHM, the perpendicular velocity distributions

are gyrotropic by construction (i.e., they depend only on $v_\perp = |\mathbf{v}_\perp|$), so that the same method is not feasible. Instead, the initial perpendicular velocities in GK and KREHM are determined from the electrostatic potential, which gives rise to fluid motion via the $E \times B$ drift [152, 317]. The electric current is initialized self-consistently according to Ampere's law:

$$J_z = \frac{c}{4\pi}\frac{2\pi\delta b}{L}\Big(2\cos(4\pi x/L) + \cos(2\pi y/L)\Big). \tag{5.3}$$

The latter follows automatically from (5.2) in the HK and GK models (due to the neglect of the displacement current), whereas in the FK model, both J_z and $\mathbf{b}_\perp$ have to be specified explicitly. Finally, in the FK model, we also explicitly initialize a self-consistent perpendicular electric field given by

$$\mathbf{E}_\perp = -\frac{1}{c}\mathbf{u}_\perp \times \mathbf{B}_0, \tag{5.4}$$

which is the lowest order contribution in the magnetohydrodynamic (MHD), strong guide field regime.

We perform a series of simulations for different plasma parameters. The main parameters varied between the runs are the ion beta

$$\beta_i = 8\pi n_0 T_i / B_0^2 \tag{5.5}$$

and the initial fluctuation amplitude

$$\epsilon = \delta b / B_0 = \delta u / v_A, \tag{5.6}$$

where v_A is the Alfvén speed. All basic plasma parameters used in this (or any other) Chapter are defined according to Appendix C. When comparing the results in the time domain, we use the (integral scale) *eddy turnover time* τ_0 as the elementary time unit:

$$\tau_0 = \frac{L}{2\pi\delta u}. \tag{5.7}$$

By normalizing time to τ_0 we can directly compare the results obtained from different models and for different plasma parameters [318].

To summarize, we list our main simulation runs and their corresponding physical parameters in Table 5.1. A total of four different simulations are considered; two for each ion beta ($\beta_i = 0.1, 0.5$). Since ϵ is not a free parameter in GK and KREHM (see Sec. 2.3), only a single simulation is performed for each β_i in the latter case. A reduced ion-electron mass ratio of 100 is used, mainly due to the computational constraints for the FK model. All HK simulations are performed with the generalized Ohm's law (2.30), which includes electron inertia effects. Each simulation is evolved for about six large-scale eddy turnover times and the size of the periodic simulation domain L is fixed to about 25 ion inertial lengths.

The FK, HK, GK, and KREHM simulations are performed using the kinetic codes OSIRIS [60, 298], HVM [128], GENE [319], and Viriato [152], respectively. A detailed list

Run	β_i	ϵ	m_i/m_e	T_i/T_e	L/d_i
A1	0.1	0.2	100	1	8π
A2	0.1	0.1	100	1	8π
B1	0.5	0.3	100	1	8π
B2	0.5	0.15	100	1	8π

Table 5.1: List of simulation runs with their main plasma parameters: the ion beta (β_i), the initial turbulence fluctuation amplitude (ϵ), the ion-electron mass ratio (m_i/m_e), the ion-electron temperature ratio (T_i/T_e), and the box size L in units of d_i.

of numerical simulation parameters for all the codes is given in Ref. [40]. Here, we provide details for the FK particle-in-cell (PIC) simulations, since these are the ones performed by the author. Regarding the numerical parameters for the other models, we only mention briefly that the numerical grid resolution was different for each model. This choice was made out of convenience, since the smallest physical scale differs between the models. In the HK model and KREHM the smallest physical scale is the electron inertial length, in GK it is the electron thermal gyroradius, and in the FK model it is the Debye length. All FK PIC simulations employ cubic spline interpolation, combined with a second-order, compensated low-pass filter for the electric current and for the electromagnetic fields felt by the particles [63]. To reduce the particle noise, we additionally short-time average the raw data over a window of duration $\Delta t = 0.5\Omega_{ci}^{-1}$, before calculating the turbulent spectra and the values given in Table 5.3. For a detailed discussion of the time averaging, see Sec. 4.4 and Ref. [40]. The remaining numerical parameters for the FK PIC simulations are listed in Table 5.2.

Run	N_{grid}	N_{ppc}	$\Delta x/\lambda_D$	$v_{\text{th},e}/c$	ω_{pe}/Ω_{ce}
A1	2048^2	625	1.0	0.174	1.822
A2	2048^2	625	1.0	0.174	1.822
B1	1920^2	1024	1.0	0.185	3.820
B2	1920^2	1024	1.0	0.185	3.820

Table 5.2: Numerical parameters for the OSIRIS fully kinetic simulations. N_{grid}, N_{ppc}, Δx, $v_{\text{th},e}$, and ω_{pe}/Ω_{ce} denote, respectively, the number of spatial grid points, the number of particles per cell per species, the grid spacing, the electron thermal speed, and the electron plasma to cyclotron frequency ratio.

5.2 Results

We now turn to the main results of the 2D kinetic model comparison. The presentation is logically divided into several subsections, according to the different types of physical properties considered. As much as possible within the model assumptions, all diagnostics are implemented in normalized in an equivalent way for every kinetic model.

5.2.1 Spatial field structure and intermittency

We begin the analysis and interpretation by considering the real space structure of the turbulent fields. In Fig. 5.1 we show the contour plots of the out-of-plane electric current, rescaled by $1/\epsilon$. Overall, a good agreement between all the models is found, except perhaps in the $\beta_i = 0.5$ run with KREHM. This is understandable, since KREHM is obtained as the low-beta limit of GK (see Sec. 2.3.3). On the other hand, KREHM agrees well with the rest of the simulations for $\beta_i = 0.1$, even though its formal range of validity is limited to $\beta_i \lesssim m_e/m_i = 0.01$ for our choice of the reduced mass ratio. This is the first in a series of examples from this Thesis, where a certain result, obtained from a simplified model, remains accurate well beyond its formal limit of validity. Looking at Fig. 5.1, it is also seen that the turbulent field structure changes only very little with the fluctuation amplitude ϵ.[1] Moreover, the field structure depends more strongly on the plasma beta and on the details of the kinetic model.

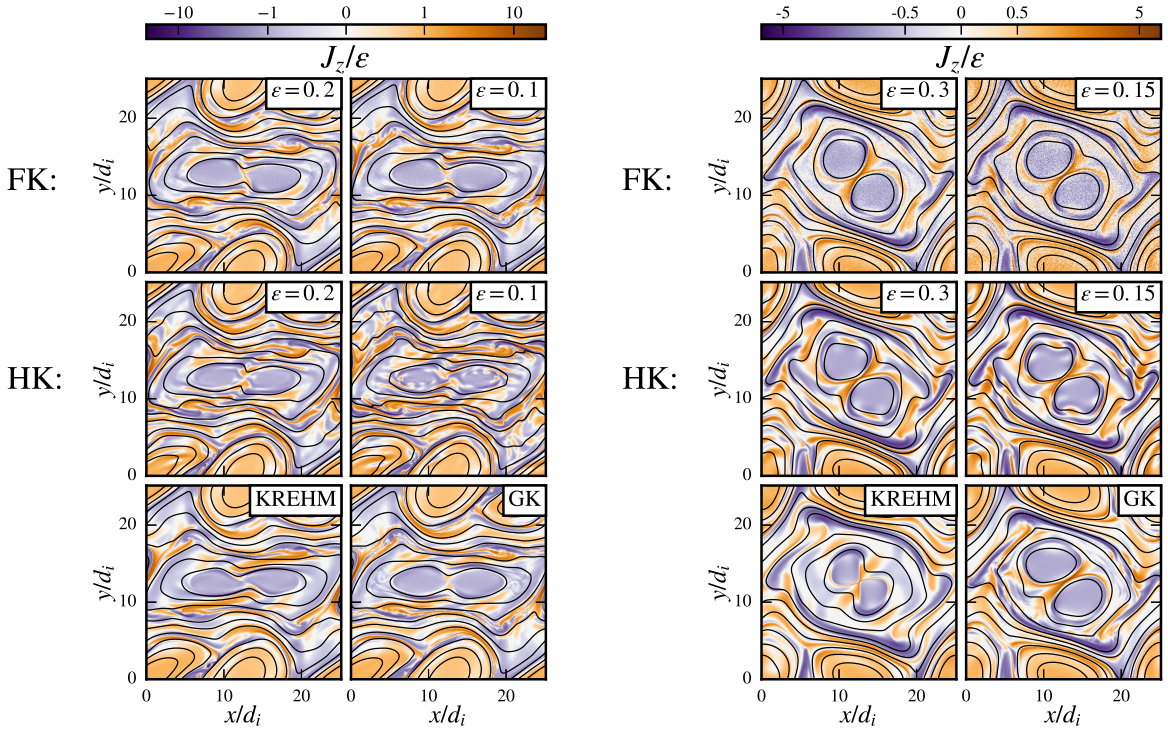

Figure 5.1: Snapshots of J_z/ϵ at around 3.1 eddy turnover times for $\beta_i = 0.1$ (left) and $\beta_i = 0.5$ (right). The color scale is doubly logarithmic, with a narrow linear scale around zero to connect the positive and negative extremal values. Black lines represent the contours of the parallel vector potential A_z.

A more quantitative perspective is provided in Table 5.3, where we list the RMS values

[1] We make this claim with some caution. The structure would certainly change significantly once the sonic Mach number $M_s \sim \epsilon/\sqrt{\beta_i}$ reaches values close to unity or higher [320]. However, supersonic regimes are not considered here.

of J_z/ϵ at around 4.7 eddy turnover times. Here, we employ short-time averaged data from the FK simulations to remove any artifacts from the particle noise. Only a single value for each β_i is reported for the GK and KREHM simulations because ϵ is not a free parameter in these two models. Perhaps the most notable feature is the excess electric current in the HK model. As argued in the following (see also Ref. [40]), the origin of the excess current is likely related to the lack of electron Landau damping in the HK approximation with fluid electrons. The first piece of evidence in support of the claim is obtained by determining the range of scales, over which the difference in the RMS value accumulates. The latter can be determined by considering the RMS values of the low-pass filtered J_z, versus the filter cutoff wavenumber K (Fig. 5.2). As seen in Fig. 5.2, the main difference accumulates over the range of scales $1/\rho_i \lesssim k_\perp \lesssim 1/d_e$, which are still well-resolved in the HK simulations (see Sec. 5.2.3). Thus, the excess current in the HK model appears to be predominantly of physical rather than numerical origin, and for obvious reasons the physical origin must be related to the lack of electron kinetic effects.

$J_z^{\mathrm{rms}}/\epsilon$				
	$\beta_i = 0.1$		$\beta_i = 0.5$	
	$\epsilon = 0.2$	$\epsilon = 0.1$	$\epsilon = 0.3$	$\epsilon = 0.15$
FK	1.09	1.24	0.85	0.93
HK	1.31	1.44	1.08	1.24
GK	1.13		0.91	
KREHM	1.12		0.82	

Table 5.3: RMS values of J_z/ϵ obtained from different kinetic models. The values have been computed at around 4.7 eddy turnover times in the simulation.

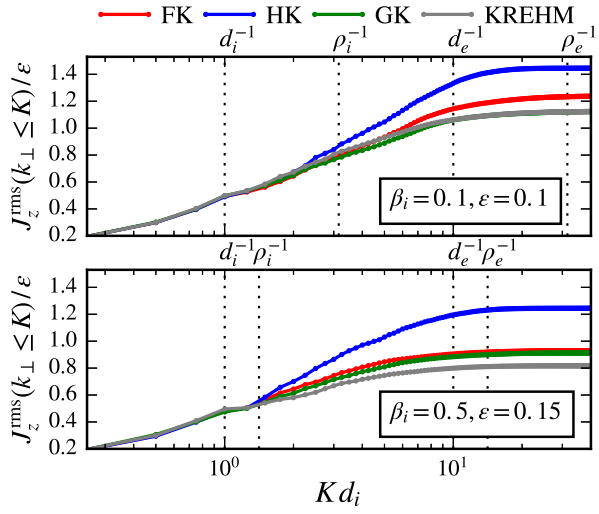

Figure 5.2: RMS low-pass filtered J_z versus the filter cutoff wavenumber K.

A distinct feature revealed by the snapshots in Fig. 5.1 is the emergence of strong

electric current sheets.[2] This property is fully consistent with a number of previous works (e.g., [46, 48, 53, 295]), which related the current sheet formation to the intermittency of (kinetic) plasma turbulence. Motivated by these previous works, we now characterize the intermittency of the turbulence as obtained from different kinetic models. Classically, the phenomenon of intermittency is described as a scale-dependent departure from self-similarity in turbulent flows [99]. In a more loose sense, the term sometimes refers to any turbulence statistics with a heavy tailed, non-Gaussian probability distribution function (e.g., [146]), which may or may not be scale-dependent. The most frequent and straightforward scale decomposition to study intermittency are the two-point field increments, defined as

$$\Delta_x b_y(\ell) = b_y(\mathbf{r} + \ell\hat{\mathbf{e}}_x) - b_y(\mathbf{r}). \tag{5.8}$$

We consider here the increments of the y component of the fluctuating magnetic field $\mathbf{b}$, with relative displacements ℓ in the x direction. Of course, the increments may be in principle evaluated for any component in any given direction. To improve confidence in the results, we average the statistics of $\Delta_x b_y(\ell)$ over a time interval between 4.4 and 5 eddy turnover times in each simulation. The statistics of the perpendicular magnetic field increments are shown in Fig. 5.3. In accordance with our expectations, the probability distribution functions develop increasing levels of large-amplitude, non-Gaussian fluctuations with decreasing scale ℓ. What is perhaps more surprising is that all models capture the intermittency reasonably well, regardless of their physical approximations. This result appears to be consistent with the presently somewhat unconventional view of Ref. [188], which argues that the intermittency of fluidlike quantities should depend little on kinetic physics. On the other hand, notable differences between the models are seen at the very tails of the probability distribution functions. These rare, extremal values carry the largest statistical uncertainties, related to finite sampling artifacts [321, 322]. Moreover, the most intense events could be affected by the choice of the numerical resolution, which is in our case different for each model. It is therefore to early to say if the minor quantitative differences are predominantly physical or not and further studies will be necessary to clarify this point.

To characterize the level of intermittency in even greater detail, we calculate the flatness of the field increments, defined as $F_{\Delta_x b_y}(\ell) = \langle \Delta_x b_y(\ell)^4 \rangle / \langle \Delta_x b_y(\ell)^2 \rangle^2$, where $\langle \dots \rangle$ denotes a space average. Large values of the flatness above the Gaussian value of 3 are indicators of intermittency. As seen in the right panel of Fig. 5.3, the statistics slowly depart from the Gaussian value of 3 with decreasing scale. A relatively large deviation from the FK model is seen in the HK results. As already implied in the previous paragraph, this result could depend significantly on the choice of numerical parameters. In particular, the discrepancy is larger for $\beta_i = 0.1$, in which case the smallest resolved scale in the HK model ($\approx d_e$) is further away from the the smallest, well-resolved scale of the FK model ($\approx \rho_e$).[3]

[2] The sheets are perhaps not seen most clearly in Fig. 5.1 due to the choice of the doubly logarithmic color scale. In linear scale, the moderate-amplitude fluctuations are hardly visible and only a few sheetlike structures stand out.

[3] The smallest well-resolved scale is the scale, beyond which the turbulent spectra artificially steepen or flatten due to numerical effects related, for instance, to low-pass filtering or particle noise (see Sec. 5.2.3).

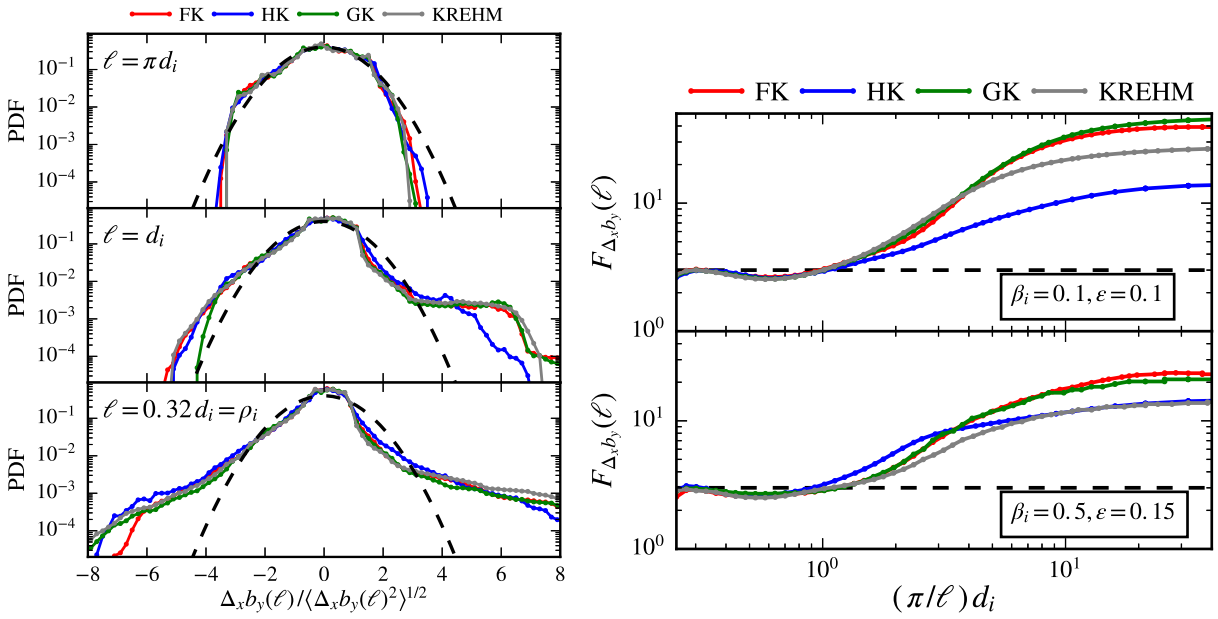

Figure 5.3: Statistics of perpendicular magnetic field increments. Left panel: Probability distribution functions at different scales for $\beta_i = 0.1$. Right panel: Flatness of the magnetic field increments. Dashed lines in left panel show for reference a (normalized) Gaussian probability distribution.

5.2.2 Global energy budget

Insight into the partitioning of the energy in the turbulent cascade can be obtained by calculating the global energy time traces, separately for each channel. We divide the mean energy into

$$M = \left\langle |\mathbf{b}|^2/8\pi \right\rangle, \qquad K_i = \left\langle n_i m_i |\mathbf{u}_i|^2/2 \right\rangle, \tag{5.9}$$

$$I_i = \left\langle 3 n_i T_i/2 \right\rangle, \qquad I_e = \left\langle 3 n_e T_e/2 \right\rangle, \tag{5.10}$$

where M is the fluctuating magnetic field energy, K_i is the ion fluid kinetic energy, I_i is the ion internal energy, I_e is the electron internal energy, and $\langle \dots \rangle$ represents a space average. By averaging the local values over the whole periodic domain, any contributions due to spatial energy transport are eliminated and only the net energy gain or loss for each channel remains. The remaining forms of energy, the electric field and electron fluid energy, represent only a very small fraction of the total fluctuating energy (around $\approx$1%). We also consider the mean "turbulent energy" [188], hereafter $E(t)$, which we define as the sum of electromagnetic and species fluid energies:[4]

$$E = \left\langle |\mathbf{b}|^2/8\pi + |\mathbf{E}|^2/8\pi + \sum_s n_s m_s |\mathbf{u}_s|^2/2 \right\rangle. \tag{5.11}$$

[4]We do not include the electric field energy, except for the FK model, since it is ordered out of the energy budget in the non-relativistic limit.

To highlight the conversions between different forms of energy, we compute the relative change for each channel (with respect to $t = 0$), normalized to the initial turbulent energy $E_0 = E(0)$.

The definition of the internal energies in GK and KREHM requires some additional clarification. Due to the GK expansion of the particle distribution function around a mean static background $F_{0s}(v)$, only the non-thermal part of the species internal energy is tracked explicitly, whereas any thermalized species energy, lost via (hyper)collisional and (hyper)diffusive terms, is considered "dissipated." The dissipated energy should be counted as part of the internal energy in order to make contact with the full-f HK and FK models.[5] More specifically, we estimate the internal energies in GK and KREHM as

$$\delta I_s = \left\langle \int \frac{T_{0s}\delta f_s^2}{2F_{0s}} \mathrm{d}^3\mathbf{v} - \frac{n_{0s}m_s|\delta\mathbf{u}_s|^2}{2} \right\rangle + \int_0^t \mathcal{D}_s \mathrm{d}t' \,, \tag{5.12}$$

where $\delta S_s = -\langle \int \mathrm{d}^3\mathbf{v}\, \delta f_s^2/2F_{0s} \rangle$ is the fluctuating species entropy [131], $\delta\mathcal{F}_s = -T_{0s}\delta S_s$ is the perturbed free energy, and $\mathcal{D}_s$ is the average dissipation rate, occurring due to (hyper)collisional and (hyper)diffusive terms in the GK equations. Only δI_e is estimated for KREHM, since ion heating is ordered out of the model by construction [102]. The first term on the right-hand side of (5.12) corresponds to the non-equilibrium part of the internal energy [87, 323]. The last term represents the net dissipated fluctuating free energy. In the FK and HK models, the latter remains part of the internal energy in the form of thermal fluctuations. We mention that the net dissipative terms are relatively large and cannot be neglected in the internal energy estimates. In the GK simulation runs, hypercollisionality amounts to about 56% and 67% of δI_e and to around 5% and 14% of δI_i at the end of each simulation for $\beta_i = 0.1$ and $\beta_i = 0.5$, respectively.

The final results for the bulk evolution of different energy channels are shown in Fig. 5.4. Overall, the moderate differences between the models are fully consistent with the physical assumptions of each model. The partitioning of the bulk energy in GK turbulence matches more closely the FK results for lower values of the fluctuation amplitude ϵ, while the general dependence on β_i appears to be well captured. Similarly, KREHM is much more accurate for $\beta_i = 0.1$, which is a natural consequence of its low-beta assumption. The HK simulations agree well with the FK model predictions in terms of the ion quantities, whereas a slight excess energy is seen in the magnetic field, which may be in part attributed to the lack of electron heating.[6] Perhaps the most interesting aspect is the dissipation of the total turbulent energy (5.11) and its partitioning between the ions and electrons for different values of β_i and ϵ. Note that we refer here to bulk dissipation and heating in a more loose, coarse-grained sense. In other words, we do not explicitly distinguish the properly thermalized (i.e., dissipated) energy from the non-thermal fluctuations. Such frequently used terminology [252, 325, 326] is motivated by the fact that the *global* species internal

[5] This aspect was not fully appreciated in some previous works [323].

[6] In the HK simulations, any cascaded energy not lost via ion heating is eventually dissipated by numerical low-pass filters [324]. This energy would be in reality converted to electron heat [46]. At least for the particular choice of HK simulation parameters used, the numerical filters do not fully compensate for the actual electron heating observed in other models.

energies are smooth and strictly monotonically increasing functions of time. Thus, from a practical standpoint, an explicit distinction between irreversible (collisional) heating and energy transfer to non-thermal fluctuations is perhaps not crucial from the *global* energy budget perspective.[7]

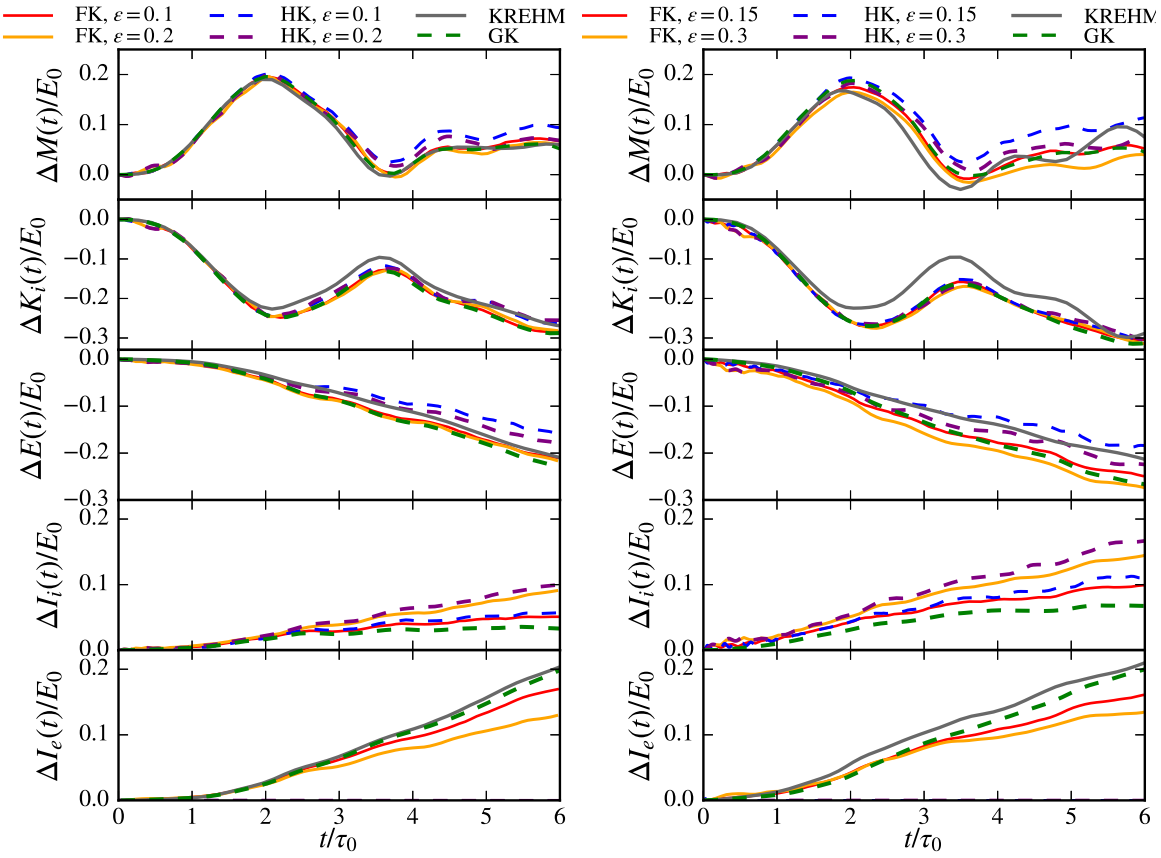

Figure 5.4: Mean energy time traces for $\beta_i = 0.1$ (left) and $\beta_i = 0.5$ (right). Shown from top to bottom are the relative changes in magnetic energy, ion fluid energy, turbulent energy (5.11), ion internal energy, and electron internal energy.

With the above-mentioned simplification in mind, let us now briefly discuss the bulk ion and electron heating (i.e., the species internal energy gain) in the kinetic plasma turbulence. In consistency with other works [6, 18], the ion heating increases going from $\beta_i = 0.1$ to $\beta_i = 0.5$, whereas the electron heating is relatively unchanged. The trend may be anticipated from linear Landau and transit-time damping of kinetic Alfvén waves (KAWs) [6]. The total turbulent energy dissipation (i.e., the decay of $E(t)$) depends only very little on ϵ. In contrast, the relative ion heating increases with ϵ, whereas the electron heating drops. The latter is observed independently of the beta. Consequently, the $\epsilon \to 0$ limit employed in

[7] In contrast, *locally* in real space the energy transfer to/from the particles is highly oscillatory and not sign-definite [54, 98, 292].

GK tends to underestimate the ion-electron heating ratio, compared to a situation with a finite ϵ. On the other hand, the convergence of the FK results towards the GK limit proceeds at a relatively fast rate upon decreasing the fluctuation amplitude. The question how acceptable is the GK approximation for predicting the ion and electron heating rates is therefore situation-dependent. In many practical situations, such as solar wind turbulence, the effective fluctuation amplitudes are expected to be small [4], and in such cases GK might provide a reasonable, although perhaps not entirely accurate [55], estimate of the ion and electron heating. It may be also worth commenting on the possible physical origin of the enhanced ion heating with increasing ϵ. Based on global time traces alone, it is difficult to make any definitive conclusions, but a reasonable possibility would appear to be stochastic ion heating [55, 147, 148], which depends strongly on ϵ and is ordered out of the GK model by definition. Finally, the ion heating estimates obtained from the HK and FK models are very similar, as expected. To the extent that the electron heating serves merely as an ultimate small-scale turbulent energy sink [18], the ion-electron heating ratio can be accurately obtained from the HK model. This possibility is perhaps slightly at odds with our results, given the observed excess magnetic energy in the HK model. However, it is important to acknowledge that our simulations likely provide an incomplete picture since (i) our turbulence is 2D and decaying, and (ii) our scale separation between ions and electrons has been artificially reduced.

5.2.3 Spectral features

We now turn to the spectral features of the turbulent solutions. We base our analysis on the one-dimensional (1D) perpendicular wavenumber spectra. According to a standard procedure, the 1D spectra are obtained by dividing the $\mathbf{k}_\perp$ plane into discrete shells of width $\Delta k_\perp = 2\pi/L$, followed by a summation over the squared Fourier-mode amplitudes contained in each shell. The shells are centered at integer values of $\Delta k_\perp = 2\pi/L$. The spectra from the FK simulations are calculated using the short-time averaged data to reduce contributions from the thermal particle noise. We study the spectra of several quantities in order to obtain a reasonably comprehensive view of the spectral features of the kinetic turbulence. More specifically, we consider the total fluctuating magnetic field spectrum $E_b(k_\perp)$, the electron density spectrum $E_{\delta n_e}(k_\perp)$, the perpendicular electric field spectrum $E_{E_\perp}(k_\perp)$, and the parallel fluctuating magnetic field spectrum $E_{b_z}(k_\perp)$. All spectra are normalized such that the sum over all spectral shells yields a (fixed) constant. In this way, we compensate for the differences in the bulk energy variations between different models at any given time in the simulation. In addition, we average the (normalized) spectra over a time interval from 4.4 to 5 eddy turnover times.

The 1D turbulent energy spectra are compared in Fig. 5.5. First, we comment on the differences in the smallest well-resolved scale between different models, which were already touched upon in Sec. 5.2.1. The smallest well-resolved scale is in practice limited by hyperdiffusive terms and numerical low-pass filters in the HK, GK, and KREHM simulations, and by particle noise in the FK PIC simulations. Inspection of the results shown in Fig. 5.5 reveals that this scale is roughly comparable to $\ell_\perp/\pi \approx 1/k_\perp \approx d_e$ for the HK simulations

and to $\ell_\perp/\pi \approx 1/k_\perp \approx \rho_e$ or so for the rest. It should be understood that any model differences are physically meaningful only over the well-resolved range of scales. With this aspect in mind, it can be noticed that all kinetic models produce very similar spectra, except perhaps the HK model, which yields somewhat shallower magnetic spectra at sub-ion scales. The shallower HK spectra are consistent with the excess RMS electric current and with the excess mean magnetic energy reported in previous sections. Since the shallower spectra are observed over the well-resolved range, the difference can be presumably attributed to the lack of electron Landau damping in the HK model.

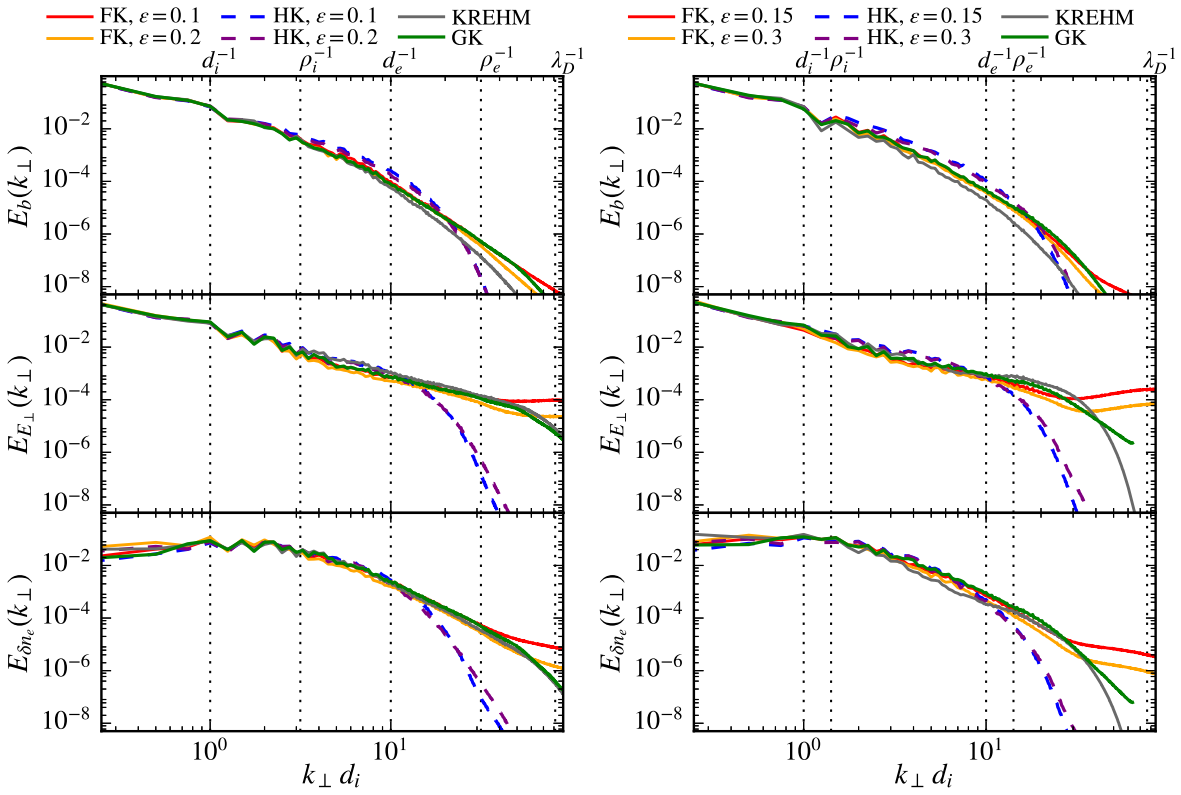

Figure 5.5: 1D turbulent wavenumber spectra for $\beta_i = 0.1$ (left) and $\beta_i = 0.5$ (right). Vertical dotted lines indicate different kinetic plasma scales. Shown from top to bottom are the fluctuating magnetic, perpendicular electric, and electron density spectra.

The possibility that the HK spectra have shallower slopes at sub-ion scales due to the lack of electron Landau damping was further investigated in Ref. [40]. To this end, an additional set of KREHM simulations was carried in the *isothermal* electron limit (simulations were performed by C. Willmott), with $\delta T_{\parallel e}$ in (2.43) set to zero. Since electron Landau damping is the only heating channel available in KREHM [102], the isothermal limit helps to clarify its relative importance. We show these results for reference in Fig. 5.6. It is seen that the isothermal electron limit of KREHM agrees well with the HK results, albeit with some minor differences for $\beta_i = 0.5$, which are a natural consequence of the low-beta assumption of KREHM. On the other hand, when the isothermal electron assumption is

relaxed, the KREHM spectra match much more closely the FK results.

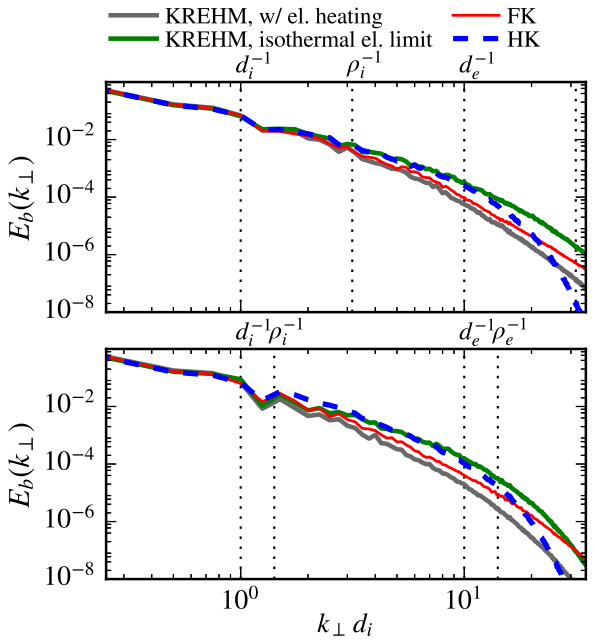

Figure 5.6: KREHM magnetic energy spectra with and without electron heating (i.e., Landau damping) for $\beta_i = 0.1$ (top) and $\beta_i = 0.5$ (bottom). For comparison, we also show the corresponding HK and FK spectra. Note that the $k_\perp \gtrsim 1/d_e$ range in the HK results is affected by numerical artifacts related to low-pass filtering.

Next, to study the spectral properties in greater detail, we calculate the ratios of the 1D spectra, as described in Sec. 3.3.4. The turbulent field ratios have been frequently considered as a diagnostic for detecting the presence of wavelike features by comparison with linear theory predictions [144, 145, 236, 237]. For the case of KAWs in the idealized limit $1/\rho_i \ll k_\perp \ll 1/\rho_e$, the analytical predictions are given by (3.61) and (3.65)–(3.67). Before proceeding, it is important to mention a significant limitation of our 2D simulation setup with an out-of-plane guide field $\mathbf{B}_0 = B_0\hat{\mathbf{e}}_z$. Many relevant kinetic-scale waves exist for highly oblique, yet not purely perpendicular propagation angles with respect to the mean magnetic field. In our 2D geometry, the wave vectors are purely perpendicular to $\mathbf{B}_0$. On the other hand, this does not imply that the *local* parallel wavenumber $k_\parallel$ is zero (see Sec. 3.2.2). Indeed, the large-scale perpendicular magnetic fluctuations may act as a *local* guide field on the smaller-scale fluctuations and give rise to a local parallel wavenumber $k_\parallel \approx \mathbf{b}_\perp^< \cdot \mathbf{k}_\perp / B_0$, where $\mathbf{b}_\perp^<$ is a low-pass filtered $\mathbf{b}_\perp$ with a cutoff scale around $\approx k_\perp/2$ [40, 78, 87, 144]. In this way, the small-scale fluctuations acquire a small but finite effective $k_\parallel$, which supports the existence of various linear modes such as KAWs. Nevertheless, it is still worth to remember that a considerable amount of degrees of freedom is inevitably lost in 2D geometry. In particular, the so-called effective $k_\parallel$ is not a free parameter but depends directly on the magnetic field fluctuations, whereas in 3D, modes with arbitrary $k_\parallel$ may be populated. With these caveats in mind, we now proceed with the spectral ratios analysis.

The spectral ratios are shown in Fig. 5.7. At kinetic scales for $\beta_i = 0.5$, the FK results agree remarkably well with the GK simulations, where KAWs are the only relevant linear modes at kinetic scales [4, 131]. Thus, we are able to demonstrate by means of model comparisons, that the kinetic range turbulent fluctuations in a $\beta \sim 1$ plasma are predominantly of KAW type, even when the full range of kinetic physics is taken into account. Here, the result is strictly speaking limited to 2D turbulence, but we will show in Chapters 6 and 7 that it carries over remarkably well to the full 3D geometry. Notable deviations from the GK approximation are seen only at large scales ($k_\perp \lesssim 1/d_i$). For $\beta_i = 0.1$, some of these deviations carry over to kinetic scales, although to a limited degree.

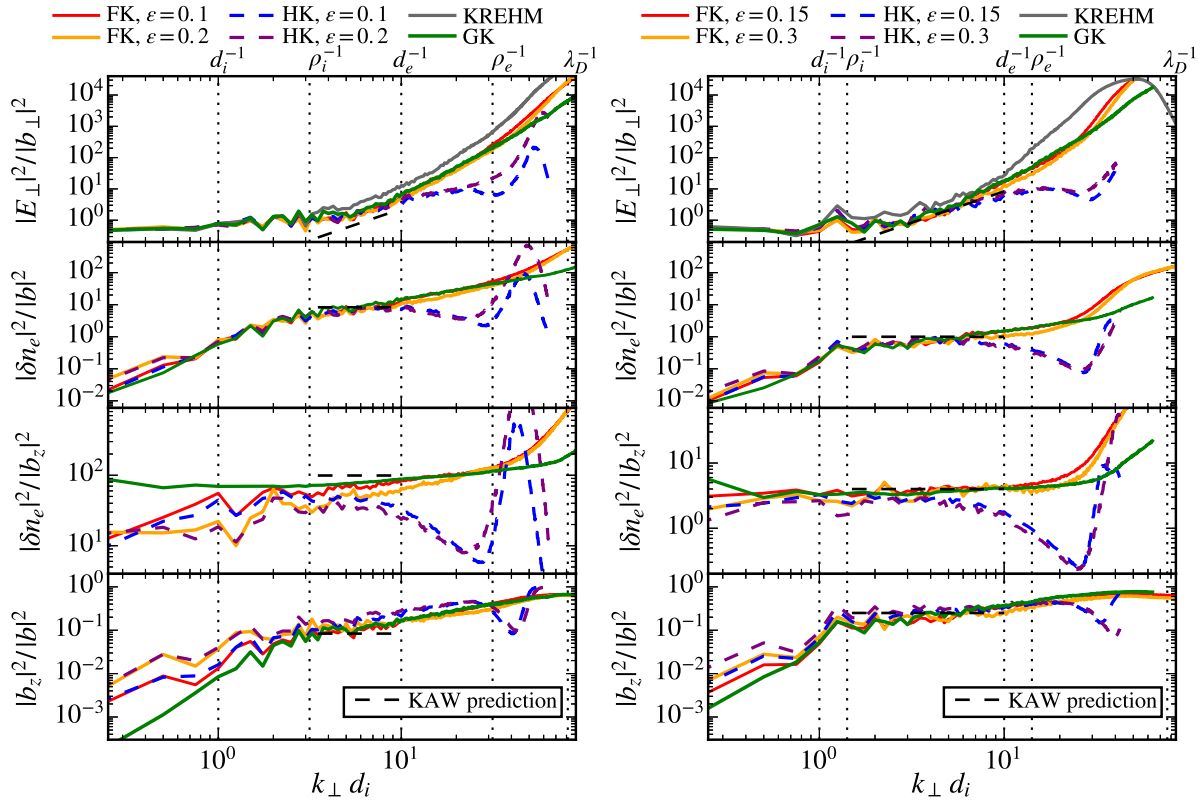

Figure 5.7: Spectral ratios of the 1D spectra for $\beta_i = 0.1$ and $\beta_e = 0.5$. Black dashed lines indicate the asymptotic KAW predictions, formally valid for $1/\rho_i \ll k_\perp \ll 1/d_e$.

The discrepancy between the FK and GK models at large scales and nature of the HK turbulent ratios at kinetic scales was investigated in Ref. [40] further, based on numerical solutions of the HK and GK dispersion relations [52, 327]. The numerical solutions of the dispersion relations were obtained by D. Told and the main physical interpretation was given by the author. Here, we only briefly summarize the main points. In short, considering the assumptions of each model and the damping rates of various linear modes, the fast magnetosonic modes and the (generalized) ion Bernstein waves were identified as

the possible source of the deviations between the FK and GK models.[8] Both the fast waves and ion Bernstein modes are ordered out of GK. For our choice of simulation parameters, the fast mode would be subject to ion cyclotron resonance at around $k_\perp \approx 1/d_i$ (assuming highly oblique propagation angles). Beyond $k_\perp \approx 1/d_i$, the energy in the fast modes may be channeled via mode conversion into ion Bernstein waves. Such conversion could be relevant in the $\beta_i = 0.1$ regime (but not for $\beta_i = 0.5$), because the GK ratios deviate in that case even for wavenumbers $k_\perp \gtrsim 1/d_i$. It is also worth mentioning that the Bernstein waves at $\omega > \Omega_{ci}$ are weakly damped in the HK model, whereas in the FK description they are additionally subject to electron damping. This could potentially explain why the FK ratios tend to converge onto the GK results with increasing $k_\perp$, whereas the HK ratios do not exactly share the same trend. Finally, linear theory predicts an abrupt change in the spectral ratios around $k_\perp d_i \approx 10$ if the KAWs were exposed to significant cyclotron resonance around $\omega \approx \Omega_{ci}$. No such change is seen in our turbulent solutions, in consistency with the arguments against cyclotron resonance given in Sec. 3.3.2 and in Ref. [4].

5.2.4 Non-thermal fluctuations in the particle distribution function

Finally, we consider the non-thermal fluctuations in the particle distribution function. Detailed studies of the particle velocity space are challenging in FK PIC simulations, due to the finite sampling of the velocity space with computational particles. However, a relatively robust measure may be obtained by considering the amount of deviation from a local Maxwellian velocity distribution [38, 132]. In particular, we study here the so-called non-thermal free energy fluctuations [39, 228, 256, 328]:

$$\delta\widetilde{\mathcal{E}}_s(\mathbf{r}) = \int \frac{T_{0s}\delta\widetilde{f}_s^2}{2F_{0s}}\,\mathrm{d}^3\mathbf{v}\,, \tag{5.13}$$

where $\delta\widetilde{f}_s$ is a modified, perturbed distribution function with vanishing lowest three moments (density, fluid velocity, and temperature) and F_{0s} is the equilibrium background distribution. In this way, direct contributions from fluidlike quantities are eliminated and $\delta\widetilde{\mathcal{E}}_s$ may be used to probe *where* (in real space) the largest non-thermal fluctuations occur. In the FK and HK models we define $\delta\widetilde{f}_s = f_s - F_{0s}$, where F_{0s} is the *local* Maxwellian with the same lowest three moments as the total f_s. In KREHM, and equivalent expression may be defined based on an expansion of g_e (Eq. (2.40)) in a Hermite basis for $v_\parallel$ (see Refs. [40, 101, 102, 256]). Due to the limited availability of advanced diagnostics required for this particular analysis, our study of non-thermal fluctuations is rather limited in scope but it nevertheless reveals some intriguing properties of the kinetic turbulence.

The spatial distribution of the non-thermal fluctuations in the FK, HK, and KREHM simulations is shown in Fig. 5.8. Due to the above-mentioned limitations, we only consider the electron fluctuations in the FK model and KREHM, based on the $v_\perp$-integrated velocity

[8] For some additional linear results and discussions on fast waves and ion Bernstein modes, see Refs. [142, 229, 240].

distribution, and the ion non-equilibrium fluctuations in the HK model. The restriction to the $v_\parallel$ coordinate for the electrons can be motivated physically based on previous works, which showed that the electron distribution develops fine structures predominantly in the parallel component [49, 87, 98, 296]. In consistency with previous works employing related diagnostics [38, 49, 132], we observe highly non-uniform spatial distributions of the non-thermal free energy. Instead of being distributed randomly, we find that these fluctuations cluster around the saddle points of the parallel vector potential A_z, which correspond in 2D to sites of magnetic reconnection. As is well known, reconnection converts magnetic energy into fluid kinetic energy by changing the topology of the magnetic field [329]. As an extension of previous studies of laminar (i.e., non-turbulent) kinetic-scale reconnection [101, 296], we find that the energy release by reconnection leads to enhanced non-thermal fluctuations, which may eventually convert into heat by cascading to progressively finer scales in velocity space [69, 98, 101]. For the electrons, the results point toward a close relationship between reconnection and Landau damping in kinetic plasma turbulence, since Landau damping is known to preferentially generate fine structures in the $v_\parallel$ coordinate of the perturbed velocity distribution [102].

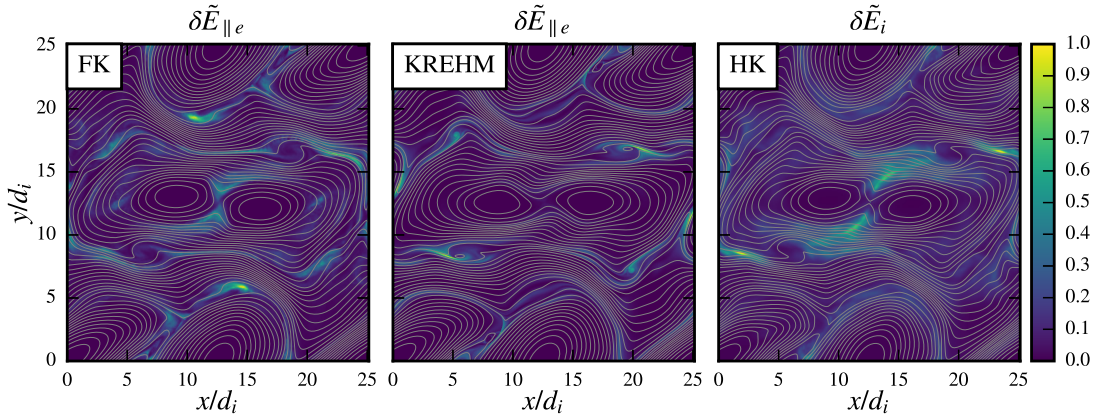

Figure 5.8: Spatial distribution of the non-thermal fluctuations at around 4.7 eddy turnover times for $\beta_i = 0.1$. The color scale is normalized to the maximum value for each plot. Overplotted are the contours of the parallel vector potential A_z.

It may be also of some interest to quantify how anisotropic the particle distributions are *on average*. In this context, two relevant measures are

$$A_s = \left\langle \frac{P_{\perp s}}{P_{\parallel s}} - 1 \right\rangle, \qquad A\varnothing_s = \left\langle 2\frac{|P_{\perp s1} - P_{\perp s2}|}{P_{\perp s1} + P_{\perp s2}} \right\rangle, \tag{5.14}$$

where A_s is the mean pressure/temperature anisotropy with respect to the direction of the magnetic field, $A\varnothing_s$ is the mean species agytrotropy [330], and $\langle \cdots \rangle$ represents a space average. Both measures are defined in terms of the species pressure tensor P_s, where $P_{\parallel s} = \hat{\mathbf{e}}_\parallel \hat{\mathbf{e}}_\parallel : \mathsf{P}_s$, $P_{\perp s} = (\mathrm{Tr}(\mathsf{P}_s) - P_{\parallel s})/2$, $\hat{\mathbf{e}}_\parallel = \mathbf{B}/|\mathbf{B}|$, and $P_{\perp s1}$, $P_{\perp s2}$ are the two eigenvalues of P_s in the plane perpendicular to $\hat{\mathbf{e}}_\parallel$. The mean species temperature anisotropies and

agyrotropies at the end of each FK PIC simulation are reported in Table 5.4. These values are calculated here in addition to the results reported in the published article [40]. A slight, ϵ-dependent average departure from isotropy is seen in the electron temperature anisotropy, A_e, and in the ion agyrotropy, $A\varnothing_i$. The increased values of the parallel electron temperature may be related to Landau damping. Overall, the obtained average values of A_s and $A\varnothing_s$ are relatively small, such that the particle velocity distributions can be considered *on average* isotropic to a reasonable approximation. It appears that the kinetic turbulence alone is not a very efficient mechanism to produce a globally anisotropic particle distribution; at least not on the typical time scales covered in present FK simulations.

β_i	ϵ	A_i	A_e	$A\varnothing_i$	$A\varnothing_e$
0.1	0.2	0.010	−0.108	0.098	0.016
0.1	0.1	0.000	−0.047	0.049	0.014
0.5	0.3	−0.005	−0.06	0.096	0.013
0.5	0.15	−0.004	−0.02	0.048	0.012

Table 5.4: Space-averaged values of the species temperature anisotropy A_s and agyrotropy $A\varnothing_s$, obtained from the FK model towards the end of each PIC simulation at around 6 eddy turnover times.

5.3 Summary and conclusions

We performed a detailed comparison of different kinetic descriptions of 2D collisionless plasma turbulence, with application to space and astrophysical plasmas. This is the first time that the prominent fully kinetic (FK), gyrokinetic (GK), and hybrid-kinetic (HK) models were directly compared in a turbulent regime over the kinetic range of scales. The approach allowed us to conclusively identify some of the key properties of the kinetic turbulence and to highlight the strengths and limitations of various reduced-kinetic descriptions. The main findings include the following:

- All models describe the kinetic-scale turbulent structures reasonably well. The only notable exception is the low-beta KREHM approximation, which is inaccurate for $\beta_i = 0.5$, as expected. The intermittency of the magnetic field is not particularly sensitive to the level of detail included in the kinetic description. At the very tails of the probability distribution functions of magnetic field increments, we do observe clear quantitative differences. However, the latter result might be very sensitive to the exact choice of numerical parameters and further studies will be necessary to clarify if the quantitative differences are indeed physical.

- The conversion of the bulk turbulent energy into ion and electron internal energy depends on the turbulence fluctuation amplitude ϵ and on the (ion) beta β_i. For a finite ϵ, GK tends to underestimate the ion-electron heating ratio. On the other

hand, the general β_i-dependence of the heating ratio appears to be reasonably well captured by GK. The ion heating obtained from the HK model matches the FK predictions. The total (effective) turbulent dissipation in the HK model, occurring due to small-scale numerical filtering and ion heating, appears to be somewhat slower compared to other models, which explicitly resolve electron kinetic features (or at least a part of it).

- A good overall agreement is found in terms of the turbulent spectra, but a closer inspection revels discrepancies. The HK model produces somewhat shallower magnetic spectral slopes at sub-ion scales, which may be presumably attributed to the lack of electron Landau damping. Perhaps somewhat surprisingly, a shallower slope for the magnetic field spectrum is observed at wavenumbers only slightly larger than $\approx 1/\rho_i$ (for our choice of the reduced mass ratio, $m_i/m_e = 100$). The FK and GK spectra are in remarkable agreement at kinetic scales for $\beta_i = 0.5$, which demonstrates the dominance of KAW-like fluctuations in the kinetic turbulence. The $\beta_i = 0.1$ regime appears to be slightly more complex and shows minor disagreements between the FK and GK models at kinetic scales, which could be possibly attributed to ion Bernstein modes. At large scales ($k_\perp \lesssim 1/d_i$), a fraction of the energy is carried by fast magnetosonic waves, which are ordered out of GK, but are well-described by the HK and FK models.

- An inspection of non-thermal free energy fluctuations implies a close relation between (electron) Landau damping and reconnection in kinetic-scale plasma turbulence, similarly as previously demonstrated in studies of laminar kinetic-scale reconnection [101, 296]. The result also supports the conjecture of Ref. [54], which argues that Landau damping in a turbulent plasma can be spatially highly non-uniform.

- KREHM delivers surprisingly accurate results already for $\beta_i = 0.1$, even though its formal range of validity is limited to $\beta_i \lesssim 0.01$ for our choice of the reduced mass ratio.

We emphasize that the conclusions, as they stand, are strictly speaking applicable only to the particular set of examples studied. We have already commented on the limitations of 2D simulations [51, 59]. It is by no means obvious that the above conclusions could be directly applied in 3D, but in the following Chapters 6 and 7 we show that several results in fact *do* carry over to 3D. A similar remark can be made regarding the question of forced versus decaying turbulence. In the following, we present both forced and decaying 3D fully kinetic simulations and we do not observe any obvious changes in the turbulent properties when the system is forced instead of decaying. Finally, an inherent limitation of our simulations is admittedly the use of a reduced ion-electron mass ratio. A realistic mass ratio might diminish the differences between the FK and HK models at sub-ion scales, as well as potentially expose a departure from the KAW turbulence phenomenology deep in the sub-ion range, close to the electron scales [226]. No definitive conclusion on the effects of the reduced mass ratio can be made at this point. On the other hand, it is worth

mentioning that significant electron kinetic effects close to ion scales have been reported even in studies employing realistic mass ratios [52, 98].

In conclusion, by means of direct model comparisons we were able to clearly expose the strengths and limits of reduced-kinetic approximations for describing weakly collisional turbulence in space and astrophysical plasmas. Any turbulence property correctly reproduced by a reduced-kinetic model directly eliminates the relevance of the neglected kinetic effects for predicting that particular feature. For example, in the $\beta \sim 1$ regime our results readily establish that the kinetic range spectral properties can be predicted from the physics of the GK model, without the need to invoke any effects beyond GK (at least for setups similar to the ones studied here). Finally, the present study might also provide valuable hints for other model comparisons in kinetic plasma turbulence. The need for a comprehensive set of comparisons was clearly pointed out in the so-called "Turbulent Dissipation Challenge" [314].

Chapter 6

3D fully kinetic study of kinetic Alfvén turbulence

We now present the first set of our three-dimensional (3D) fully kinetic simulations of plasma turbulence. Here, we consider decaying turbulence for vanishing and non-vanishing values of the normalized mean cross-helicity σ_c (see Sec. 3.2). Most of the results included in this Chapter have been published as an article in Physical Review Letters [78].

Only a very limited number of 3D fully kinetic computational studies of astrophysical and space plasma turbulence have been performed to date (e.g., [77, 82, 83, 269]). Previous works focused on diverse aspects, such as intermittent turbulent heating and structure formation [77, 269], whistler wave turbulence [82, 331], bulk plasma heating by kinetic Alfvén wave (KAW) turbulence [252], or particle acceleration in highly relativistic regimes [9]. On the other hand, it was never investigated if a critically balanced cascade of KAWs (see Sec. 3.3) develops naturally from first physics principles, as the turbulence transitions from the magnetohydrodynamic (MHD) into the sub-ion range. Moreover, supposing the latter answer was (largely) affirmative, it was unclear if the obtained turbulent spectra would bear any similarities with previous results based on the gyrokinetic approximation [36, 39, 42, 85, 205]. This gap in the literature was the main motivation for the work presented below. All simulations were performed by the author on the SuperMUC system at the Leibniz-Rechenzentrum under project number "pr74vi." The author of this Thesis also analyzed the data to obtain the results shown below, produced the figures, and wrote the published paper [78]. The original calculations of the local scale-dependent anisotropy, presented in Ref. [78] (in Fig. 4 of the main letter and in Fig. 1 of the supplement), were performed by A. Mallet. The latter result is reproduced here independently by the author, yielding estimates consistent with those of Ref. [78].

The rest of the Chapter is organized is follows. We provide numerical simulation details in Sec. 6.1, followed by the main results in Sec. 6.2. The results include an overview of the spatio-temporal dynamics (Sec. 6.2.1), turbulence spectra and spectral ratios (Sec. 6.2.2), and the local anisotropy (Sec. 6.2.3). We also consider some additional aspects. In Sec. 6.2.4 we study the effects of a mean cross-helicity on the kinetic range turbulence, and in Sec. 6.2.5 we analyze the ion and electron energy fluctuations, computed along their self-consistent

trajectories. A summary of our results and the conclusions are given in Sec. 6.3.

6.1 Simulation details

Before presenting the main results, we first describe the simulation setup. Two different simulations are performed using the fully kinetic particle-in-cell (PIC) code OSIRIS (see Chapter 4). A detailed description of the initial condition for the decaying turbulence is given in Appendix A. It is important to note that the initialization is limited to large scales above ρ_i and does not *a priori* constrain the kinetic fluctuations to be KAW-like. Other simulation parameters are given below.

Both 3D simulations have identical parameters, except for the initial value of the normalized mean cross-helicity

$$\sigma_c = \frac{\langle |\mathbf{z}_\perp^+|^2 - |\mathbf{z}_\perp^-|^2 \rangle}{\langle |\mathbf{z}_\perp^+|^2 + |\mathbf{z}_\perp^-|^2 \rangle}, \tag{6.1}$$

where $\mathbf{z}_\perp^\pm$ are the Elsässer variables (see Sec. 3.2). We initialize σ_c at $t = 0$ to $\sigma_{c0} = 0$ in the first run and to $\sigma_{c0} = -0.45$ in the second run. Values of σ_c close to zero correspond to so-called balanced (MHD) turbulence with an equal flux of shear Alfvén wave packets propagating parallel ($\mathbf{z}_\perp^-$) and antiparallel ($\mathbf{z}_\perp^+$) to the mean magnetic field $\mathbf{B}_0 = B_0\hat{\mathbf{e}}_z$. Large values of $|\sigma_c|$ close to unity correspond to strongly imbalanced regimes, which are typical for the fast streams of the solar wind [32, 218]. The slow streams, on the other hand, are typically only moderately imbalanced. Most existing turbulence phenomenologies (implicitly) assume $\sigma_c \approx 0$. We therefore take our balanced simulation with $\sigma_{c0} \approx 0$ as the main reference for comparison with the KAW turbulence phenomenology.

The spatial resolution in both simulations is $(N_x, N_y, N_z) = (768, 768, 1536)$ with 64 particles per cell per species. The fields and particle current are interpolated with cubic splines, which significantly reduce the particle noise compared to lower-order splines (see Sec. 4.4). To further reduce noise and grid aliasing effects, a second-order compensated binomial filter is applied to the electric current and to the fields felt by the particles at each time step [63]. During each simulation, the total net energy of the fields and particles is conserved up to 0.04%. An elongated periodic box with dimensions $L_\perp = 17.0d_i$ and $L_z = 42.4d_i$ in directions perpendicular and parallel to $\mathbf{B}_0$, respectively, is chosen and a reduced ion-electron mass ratio of $m_i/m_e = 64$ is used. We adopt the reduced mass ratio in order to make the simulation tractable on the computational resource employed. Ion and electron velocity distributions are initialized as Maxwellians with equal temperatures, yielding an (initial) species beta of $\beta_s = 8\pi n_0 T_s/B_0^2 = 0.5$. The electron plasma to cyclotron frequency ratio is set to $\omega_{pe}/\Omega_{ce} = 2.83$. A different phase is chosen for each initialized Alfvén wave mode and the initial value of σ_c is controlled by adjusting the phase difference according to Eq. (A.12) of Appendix A. The initial turbulence fluctuation amplitude $\epsilon = \delta u/v_A = \delta b/B_0$ is chosen so as to satisfy critical balance at the box scale: $\epsilon = L_\perp/L_z \approx 0.4$. To reduce particle noise, we employ short-time averages (see Sec. 4.4) when analyzing the turbulent spectra and the local spectral anisotropy. In particular, we

average the raw field data over a time interval of $\Delta t = 2.4\Omega_{ce}^{-1}$ and $\Delta t = 11.9\Omega_{ce}^{-1}$ for the run with $\sigma_{c0} = 0$ and $\sigma_{c0} = -0.45$, respectively. Before calculating the local anisotropy, we downsample the grid data by a factor of 2 in each dimension to speed up the computation.[1] Note that the simulations employ a large resolution in order to (marginally) resolve the Debye scale. The actual kinetic scales of interest are well represented at a reduced grid resolution. For a list of commonly used symbols and plasma parameter definitions see Appendix C.

6.2 Results

We now present the results of the massively parallel 3D kinetic simulations. Sections 6.2.1 to 6.2.3 focus on the comparison of the globally balanced turbulence ($\sigma_{c0} \approx 0$) results with phenomenological expectations for KAW turbulence (see Sec. 3.3). The imbalanced regime is considered in Secs. 6.2.4 and 6.2.5.

6.2.1 Spatio-temporal evolution

The first set of the results serves as a rough illustration of the spatio-temporal dynamics. To this end, we show in Fig. 6.1 the global time traces of the magnetic energy and of the mean squared electric current, together with a spatial snapshot of the current in a well-developed turbulent state. Throughout this Chapter, we normalize time to the large-scale Alfvén transit time, $t_A = L_z/v_A$, and we analyze the spectra at different times in the simulation. Consistent with a strong turbulence regime, characterized by critical balance [4, 136], the system reaches a well-develop turbulent state in a time comparable to t_A. The magnetic energy undergoes a relatively rapid decay due to ion and electron heating. By the end of the simulation, the ion and the electron internal energies increase by 17% and by 15%, respectively. Thus, it may be inferred that the ion-electron heating ratio is close to unity. The bulk fluid energy equals the fluctuating magnetic energy at $t = 0$ (as a result of our initialization) and decays at a similar rate as the latter. In contrast, the electric current undergoes a transient period, during which it is rapidly amplified, before it eventually fades away. The current amplification is believed to be a generic feature of the transition to strong plasma turbulence and it may be attributed to current sheet formation [53, 132, 208, 210, 264, 297].[2] It was recently proposed that current sheet formation could be explained in terms of nonlinear interactions between counterpropagating Alfvén wave packets [297]. Our results are in principle consistent with the idea, since the current sheets develop on a time scale of $\sim t_A$, which is the natural interaction time for a strong, large-scale Alfvén wave collision.

[1] We low-pass filter the data to $k < k_{\max}/2$ beforehand to avoid any grid aliasing effects.

[2] An animation, showing how the current sheets form in our 3D kinetic simulation, is available as part of the supplemental material for Ref. [78].

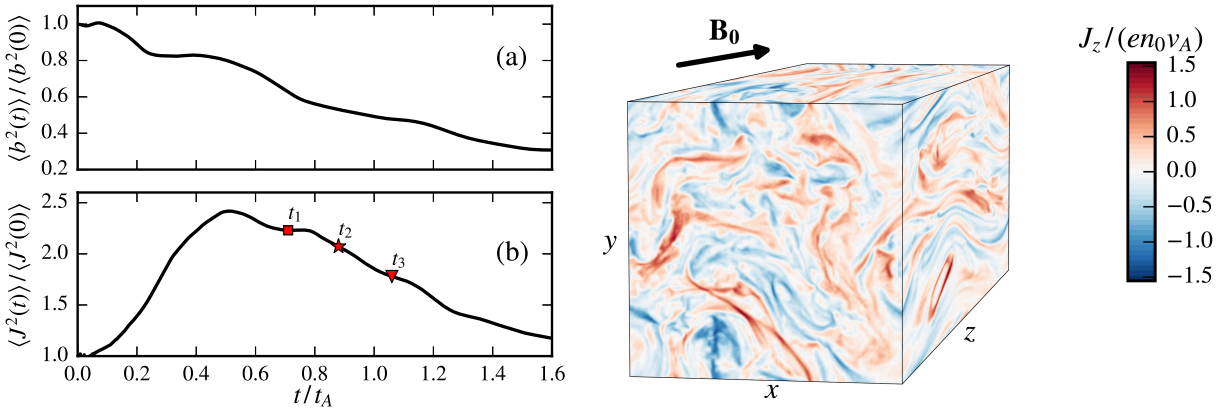

Figure 6.1: Left: Global time traces of the fluctuating magnetic energy (a) and of the mean squared electric current (b). The traces are normalized to the values at $t = 0$. The markers in panel (b) indicate the times at which we analyze the spectra ($t_1/t_A = 0.71, t_2/t_A = 0.88$, $t_3/t_A = 1.06$). Right: Snapshot of the parallel electric current at time t_2 in the simulation.

6.2.2 Turbulent spectra and spectral ratios

Next, we consider the one-dimensional (1D) perpendicular wavenumber spectra of the decaying turbulence. In Fig. 6.2 we show the power spectra of the $\mathbf{b}$, $\mathbf{E}_\perp$, and δn_e fields at time $t_1 = 0.71 t_A$. Qualitatively very similar results are obtained at later times in the simulation (not shown). The results from our 3D fully kinetic simulation appear to be consistent with *in situ* spacecraft measurements of the solar wind [27, 235, 255] and show similar features as the turbulent spectra previously obtained from various reduced-kinetic 3D simulations [36, 39, 47]. Indeed, the magnetic spectra at sub-ion scales of the solar wind typically exhibit spectral exponents around -2.8 [27, 235], which is similar to what is observed in our simulation. However, due to the reduced mass ratio of 64, a precise spectral exponent cannot be established because the magnetic spectrum progressively steepens upon approaching electron scales. The latter trend is also observed in spacecraft measurements and in gyrokinetic simulations employing realistic proton-electron mass ratios [27, 39, 43].

Essentially, according to the KAW turbulence phenomenology (see Sec. 3.3.3), the magnetic and electron density spectra are expected to reach equipartition at sub-ion scales in appropriately normalized units. From (3.66), we obtain the linear KAW prediction $|b/B_0|^2 \approx |\delta n_e/n_0|^2$ for $\beta = \beta_i + \beta_e \approx 1$, which is consistent with our simulation results over the (narrow) range between the ion and electron scales. This key result demonstrates, based on a first principles 3D kinetic simulation, that the sub-ion scale turbulence is highly compressible, as anticipated for a turbulent cascade of KAWs [59, 145]. The alternative whistler turbulence model [59, 80, 81, 143, 244, 245] predicts only negligible density fluctuations and cannot explain this result. A closer look at Fig. 6.2 shows that the density spectrum, while in approximate equipartition with the magnetic spectrum, is somewhat shallower than the latter. Present phenomenological predictions for KAW turbulence assume exact energy equipartition between $|\delta n_e|^2$ and $|\mathbf{b}_\perp|^2$ in the normalized

units and cannot predict the difference in the spectral slopes (see Sec. 3.3.3). While this trend appears to be present in a number of simulations [39, 59, 134], its possible physical origin has been rarely discussed to our knowledge. The difference could be attributed to the finite extent of the sub-ion range, determined by the square root of m_i/m_e. However, we believe there is no strong basis to argue that the density and magnetic field ought to be in precise equipartition, even if the sub-ion range is taken to be asymptotically large. The motivation comes from the fact that the electron reduced MHD equations (see Sec. 3.3.1) cannot be brought into a perfectly symmetric form for δn_e and $\mathbf{b}_\perp$ (or equivalently, for $\mathbf{b}_\parallel$ and $\mathbf{b}_\perp$).[3] Instead, as already noted by Boldyrev *et al.* [59], a deviation from exact equipartition may be also an inherent property of nonlinear KAW turbulence dynamics, analogous to the residual energy phenomenon in MHD turbulence [213, 219, 222, 223].

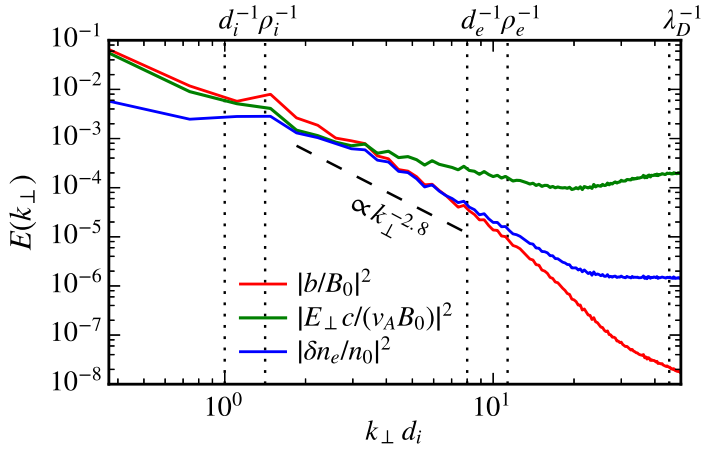

Figure 6.2: Turbulent spectra of the magnetic ($\mathbf{b}$), perpendicular electric ($\mathbf{E}_\perp$), and electron density (δn_e) fluctuations at time $t_1 = 0.71 t_A$. A -2.8 slope is shown for reference. Dotted vertical lines indicate various kinetic plasma scales. The flattening of the spectra in the range $k_\perp \gtrsim 20/d_i$ is due to particle noise.

To obtain further insight into the nature of the kinetic range fluctuations, we calculate the ratios of the 1D spectra. The results computed at different times in the simulation are shown in Fig. 6.3. For reference, we show the spectral ratios obtained from a 2D gyrokinetic simulation with $\beta_i = \beta_e = 0.5$ and $m_i/m_e = 100$ from Chapter 5 (gyrokinetic simulation data were provided by A. Bañón Navarro). An excellent agreement between the fully kinetic and gyrokinetic results is found between the ion and electron scales. The ratios are also in good agreement with the linear asymptotic KAW predictions (3.65)–(3.67). The amount of kinetic physics present in the gyrokinetic model (see Sec. 2.3.2) is in general quite heavily constrained, since the fluctuations are assumed to be strongly anisotropic ($k_\parallel/k_\perp \ll 1$), small-amplitude ($\delta b/B_0 \ll 1$), and of low-frequency ($\omega/\Omega_{ci} \ll 1$). With these assumptions,

[3]For a formulation of electron reduced MHD in terms of $\mathbf{b}_\parallel$ and $\mathbf{b}_\perp$, see Cho and Lazarian [241]. They use a parallel derivative of the form $\nabla_\parallel = (1 + b_\parallel/B_0)\partial/\partial z + (\mathbf{b}_\perp/B_0)\cdot\nabla_\perp$. Assuming the ordering (3.34), the $(b_\parallel/B_0)\partial/\partial z$ term is small and can be neglected.

KAWs are the only relevant linear modes at sub-ion scales [4, 131]. Considering the fact that we resolve frequencies up to $\omega \sim \omega_{pe} \gg \Omega_{ci}$, our 3D simulation domain is only moderately elongated in the direction parallel to $\mathbf{B}_0$, and that our fluctuations are relatively large, the agreement with linear KAW predictions and gyrokinetics is quite remarkable and indicates a certain robustness of KAW turbulence, well beyond the physical limits that have been frequently adopted in its theoretical and computational studies [4, 5, 36, 42, 56, 59].

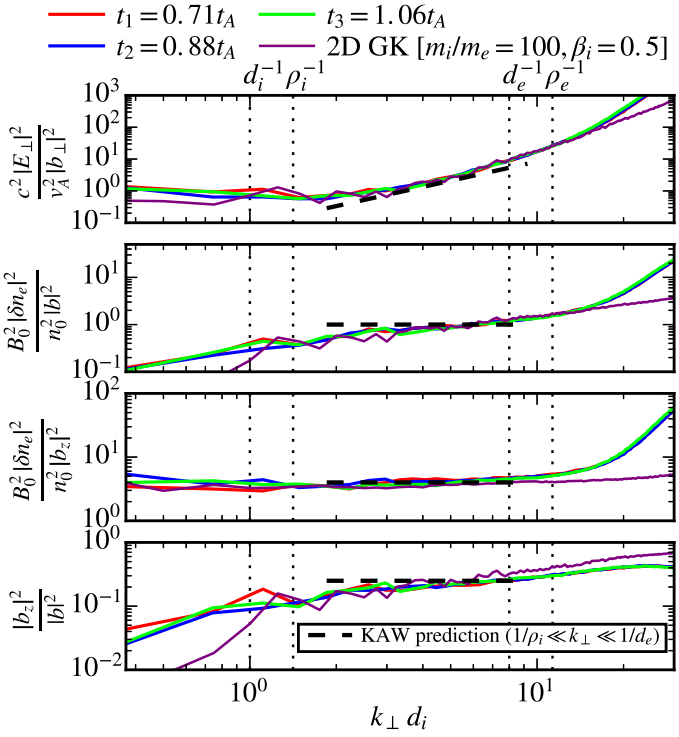

Figure 6.3: Spectral field ratios at different times in the 3D fully kinetic simulation. For reference, we show the ratios from a 2D gyrokinetic simulation, presented in Chapter 5. The black dashed lines indicate the linear asymptotic KAW predictions (3.65)–(3.67).

6.2.3 Local scale-dependent anisotropy

Given the results shown above, it may be concluded that the kinetic range turbulence is predominantly composed of fluctuations with polarization properties of KAWs. However, based on spectral ratios alone it is difficult to judge on the relevance of wavelike features in strongly nonlinear plasma turbulence. One might ask, what if the KAW spectral ratio predictions happen to fall, by chance, in some general class of kinetic turbulence, not necessarily related to any sort of wave activity? This critical concern may be clarified by considering the *local* spectral anisotropy $k_\parallel(k_\perp)$, where $k_\parallel$ is characteristic wavenumber measured along the local mean magnetic field at perpendicular scale $\lambda \sim 1/k_\perp$ (see Sec. 3.2.2). If the linear footprint of KAWs is indeed preserved in a state of strong turbulence, as

anticipated by the critical balance conjecture [4, 5, 136], a scale-dependent anisotropy should be observed, such that the linear and nonlinear terms approximately balance. In particular, the scale-dependent ratio of linear (KAW) to nonlinear time scales $\chi = \tau_\mathrm{l}/\tau_\mathrm{nl}$ may be inferred from the anisotropy as $\chi(k_\perp) \approx k_\perp \delta b_{\perp k_\perp}/[k_\parallel(k_\perp) B_0]$, where $\delta b_{\perp k_\perp}$ is a typical fluctuation amplitude at perpendicular scale $\lambda \sim 1/k_\perp$ [4, 241, 245]. The definition may be qualitatively explained by the fact that KAW packets disperse with a relatively fast parallel velocity (Eq. (3.55)), whereas the perpendicular wave dispersion is negligible. Thus, according to critical balance, the parallel dynamics of a localized eddy is characterized by wave dispersive effects, whereas its perpendicular evolution is governed by nonlinear turbulence interactions.

From a technical perspective, the *local* anisotropy is considerably more challenging to estimate than the energy spectrum and very few attempts have been made to evaluate the local anisotropy in kinetic range plasma turbulence [205, 241, 245, 253]. In MHD turbulence, the anisotropy is traditionally estimated with the help of two-point field increments, $\delta\mathbf{b}(\mathbf{r}_0, \mathbf{r}) = \mathbf{b}(\mathbf{r}_0 + \mathbf{r}) - \mathbf{b}(\mathbf{r}_0)$, computed in directions parallel and perpendicular to the local mean field [138, 157, 159, 160]. However, two-point increments have a poor scale selectivity in spectral space and cannot extract the true scaling of any signal with a spectrum steeper than $E(k) \propto k^{-3}$ in a given spatial direction [146, 169, 241]. Phenomenological treatments of KAW turbulence predict very steep parallel wavenumber spectra, the standard prediction being $E(k_\parallel) \propto k_\parallel^{-5}$ (see Sec. 3.3.3). Thus, two-point field increments cannot be used. To overcome the limitations of two-point increments, Cho and Lazarian [241, 245] proposed a local anisotropy estimate based on a sequence of spectral band-pass filters in $k_\perp$. Here, we follow their approach, which can be summarized as follows.[4] At a given $k_\perp = \sqrt{k_x^2 + k_y^2}$ scale, a local fluctuating field $\delta\mathbf{b}_{k_\perp}(\mathbf{r})$ and a local mean field $\mathbf{B}_{0k_\perp}(\mathbf{r})$ are extracted. The fluctuating field is obtained by eliminating the Fourier modes with wavenumbers greater than $2k_\perp$ or smaller than $k_\perp/2$. The local mean field is obtained by low-pass filtering the total field to wavenumbers smaller than $k_\perp/2$. It is important to use a band-pass filter of logarithmic width to extract the scale-dependent fluctuations.[5] An effective, scale-dependent $k_\parallel$ is then estimated as

$$k_\parallel(k_\perp) \approx \frac{\langle |\mathbf{B}_{0k_\perp} \cdot \nabla \delta\mathbf{b}_{k_\perp}|^2 \rangle^{1/2}}{\langle |\delta\mathbf{b}_{k_\perp}|^2 \rangle^{1/2} \langle |\mathbf{B}_{0k_\perp}|^2 \rangle^{1/2}}, \tag{6.2}$$

where $\langle \dots \rangle$ represents a space average.

Estimates of the local anisotropy and of the nonlinearity parameter at time $t_2 = 0.88 t_A$ in our simulation are shown in Fig. 6.4. Similar results are obtained for times $t_1 = 0.71 t_A$ and $t_3 = 1.06 t_A$ [78]. The local anisotropy scalings of 3D fully kinetic, sub-ion scale plasma

[4] Known alternatives include multi-point field increments or the indirect inference of $k_\parallel$ from the $k_\perp - \omega$ energy spectrum [205]. A detailed discussion on multi-point increments and their limitations is given in Cho and Lazarian [241]. The frequency spectrum method of TenBarge and Howes [205] rests on the assumption that each frequency can be unambiguously associated with a given $k_\parallel$, which may not be appropriate if linear modes other than KAWs are permitted by the model.

[5] Essentially, the scale extraction should be reasonably well localized both in real space and in spectral space. A filter of fixed (absolute) width in $k_\perp$ is very badly localized in real space.

turbulence have been so far reported in the literature only for the simulations performed in the scope of this Thesis [78, 161]. Between the ion and electron scales, we find a strong scale-dependent anisotropy, which yields a nonlinearity parameter of order unity. As implied by this simple estimate, it appears that the sub-ion range turbulence is close to a state of critical balance ($\chi \sim 1$) between the linear KAW and nonlinear time.[6] It also happens so, that the slope of $k_\parallel(k_\perp)$ on the logarithmic graph is roughly 1/3, in consistency with the standard prediction for a critically balanced KAW cascade [4, 5]. It would be incorrect to confuse this result as a validation of the assumptions used in deriving the standard KAW turbulence predictions (see Sec. 3.3.3), which neglect any corrections due to dissipation or intermittency. Indeed, in its most simple version the model also predicts an energy spectrum of the form $E(k_\perp) \propto k_\perp^{-7/3}$, which is inconsistent with our results. Potential reasons for spectral indices steeper than $-7/3$ have been widely discussed in recent literature [16, 56, 86, 233, 332]. Without taking sides on the open issue, we only mention here that a sub-ion scale energy spectrum steeper than $\sim k_\perp^{-7/3}$ is not necessarily incompatible with an anisotropy exponent of $\simeq 1/3$ or similar when various extensions of the basic KAW turbulence phenomenology are taken into account. In conclusion, while the exact form of the KAW turbulence spectral scalings is presently an open question, our work demonstrates—in terms of fully kinetic 3D simulations—the general feasibility of kinetic range turbulence models based on the physics of KAWs and critical balance.

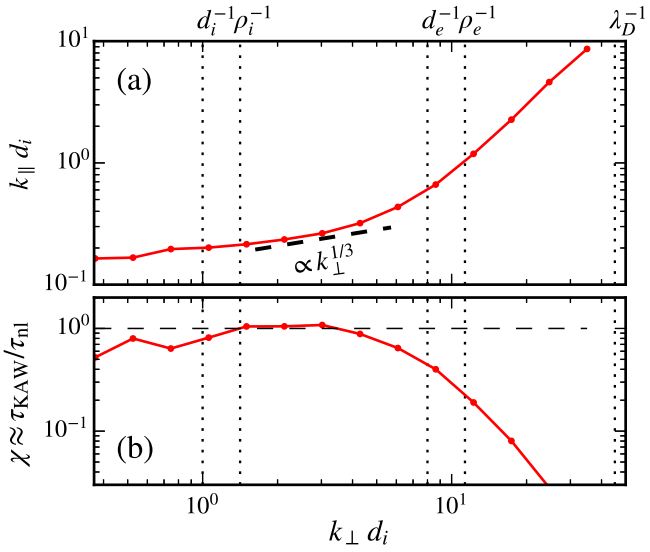

Figure 6.4: Local spectral anisotropy of the 3D decaying kinetic turbulence (a) at time $t_2 = 0.88 t_A$ in the simulation. The bottom panel (b) shows the nonlinearity parameter χ, which can be inferred from the anisotropy.

[6] The steepening of the anisotropy curve close to electron scales and beyond is most likely a consequence of particle noise. However, it is not entirely unimaginable that the slope steepens at electron scales for physical reasons [247]. In either case, our definition of χ is not appropriate at scales $k_\perp \gtrsim 1/d_e$, because it does not account for electron inertia.

6.2.4 Impact of cross-helicity on the sub-ion scale turbulence

So far we have considered an idealized regime of balanced turbulence, characterized by (nearly) vanishing values of the normalized cross-helicity σ_c. However, plasma turbulence in many natural systems (notably in the fast solar wind [218]) may be far from $\sigma_c \approx 0$. It is therefore of interest to study the impact of a mean cross-helicity on the kinetic range turbulence. To this end, we perform a second 3D PIC simulation of decaying turbulence with $\sigma_{c0} = -0.45$ at $t = 0$ (see Sec. 6.1) and we carry out the same analysis as in previous sections.

In Fig. 6.5 we compare the global time traces of the fluctuating magnetic energy and of the mean squared current in the balanced and imbalanced simulations. Most notably, the simulation with $\sigma_{c0} = -0.45$ reaches lower values of the peak electric current, which may be considered as a sign of reduced nonlinear activity. The result can be naturally explained in the framework of MHD turbulence, where nonlinear interaction occurs only between counterpropagating Alfvén wave packets [136, 184, 310]. The nonlinear MHD interaction is therefore maximized for $\sigma_c = 0$ and vanishes for $|\sigma_c| = 1$, which corresponds to states with purely copropagating Alfvén waves. In the simulation with $\sigma_{c0} = -0.45$, the electron heating is slightly reduced compared to the $\sigma_{c0} = 0$ case. By the end of the simulation, the electron internal energy increases by 11% and the ion one by 16%. It may be also worth noting that the level of imbalance slowly increases with time in the simulation with $\sigma_{c0} = -0.45$. For instance, at time $t_2 = 0.88 t_A$ we obtain $\sigma_c = -0.59$.

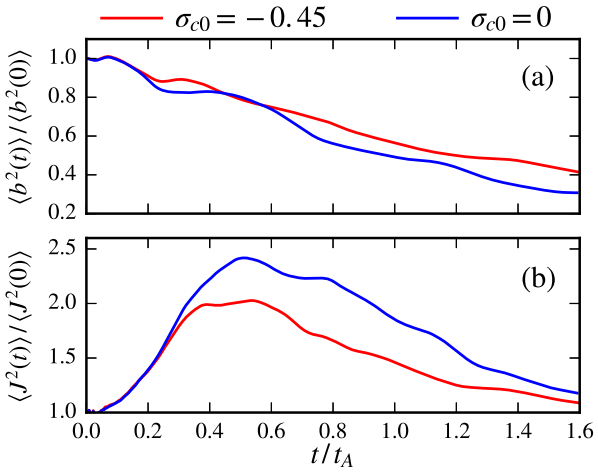

Figure 6.5: Comparison of global time traces between the balanced ($\sigma_{c0} = 0$) and imbalanced ($\sigma_{c0} = -0.45$) kinetic turbulence simulations.

In the kinetic range, the same line of reasoning as in MHD turbulence does not apply directly because KAWs are dispersive, so that copropagating wave packets can catch up with each other and interact [5]. Instead, what may be expected is that the energy will be passed on into the kinetic range at a somewhat slower rate due to the reduced nonlinear transfer from the largest (MHD-like) scales. This is supported by the results shown in

Fig. 6.6, where we compare the turbulence spectra at time $t_1 = 0.71 t_A$ in both simulations. The spectral energy at scales $k_\perp \lesssim 1/d_i$ of the imbalanced simulation exceeds the energy of the balanced simulation, whereas at kinetic scales the opposite is observed. On small kinetic scales far from the transition, the spectral slopes appear to be relatively insensitive to the large-scale imbalance. Moreover, the magnetic and electron density spectra remain in approximate equipartition, according to the KAW turbulence predictions. Good agreement with linear KAW predictions is also found in terms of the spectral ratios (see supplemental material for Ref. [78]).

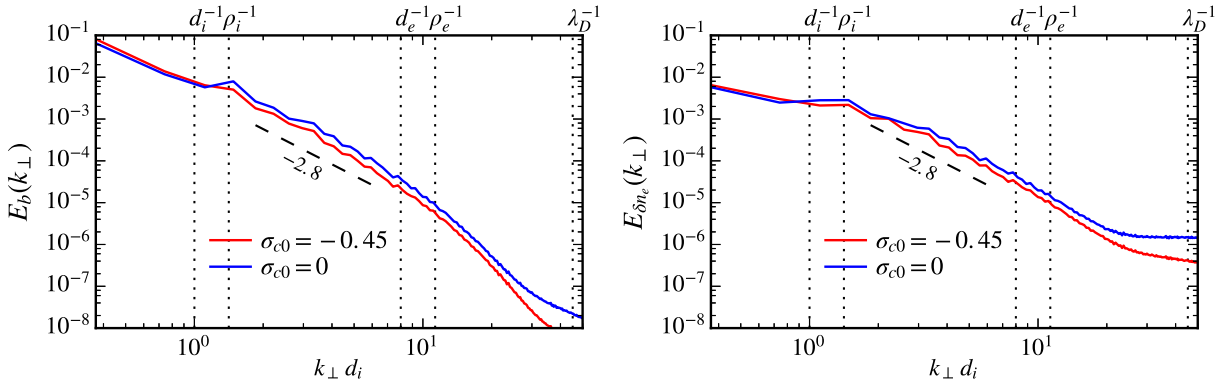

Figure 6.6: Impact of a mean cross-helicity on the kinetic range turbulence spectrum. Left panel compares the magnetic spectra and the right panel shows the electron density spectra.

Finally, Fig. 6.4 compares the local anisotropy and the nonlinearity parameter estimates. Both runs give similar results, albeit with some minor differences. In particular, the nonlinearity parameter is reduced at sub-ion scales and the slope of the anisotropy curve is slightly shallower for $\sigma_{c0} = -0.45$. Both features can be interpreted as a sign of reduced nonlinear interaction. On the other hand, the differences are altogether only moderate, such that the kinetic turbulence remains reasonably close to a state of critical balance.

In summary, we confirmed that our results are not very sensitive to the exact level of the mean cross-helicity. Therefore, we expect our qualitative conclusions to be applicable to a wide range realistic scenarios with moderate levels of imbalance in the Elsässer fields $\mathbf{z}^\pm$, such as kinetic turbulence in the slow solar wind streams. The results also give hope that the KAW turbulence phenomenology could be formally extended to regimes with $\sigma_c \neq 0$. A theoretical attempt along these lines is yet to be made, in contrast to MHD turbulence where various extensions have already been proposed (e.g., [220, 221]).

6.2.5 Lagrangian particle statistics

It may be also of some interest to consider the turbulence statistics computed along the self-consistent ion and electron trajectories (i.e., in the Lagrangian particle frame). Such analysis may give useful insight into the mechanisms behind particle energization and acceleration in kinetic plasma turbulence. Here, we consider an ensemble of 4,096 randomly

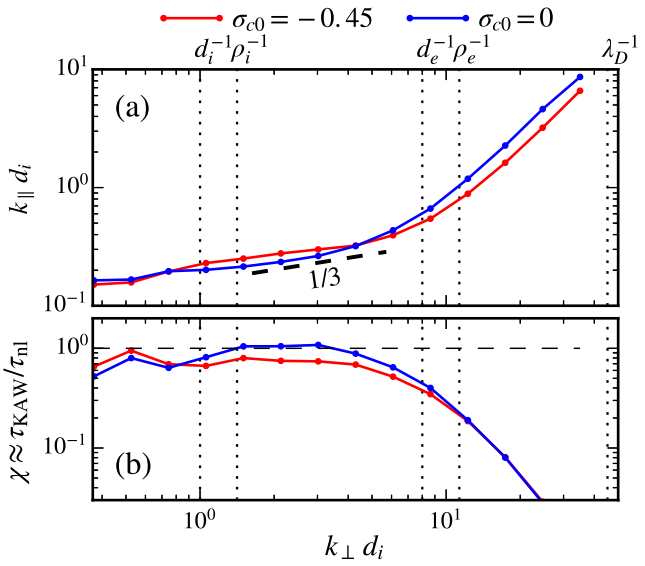

Figure 6.7: Impact of a large-scale imbalance on the local anisotropy of the 3D kinetic range turbulence. The estimates are compared at time $t_2 = 0.88t_A$ in the simulations.

selected ion and electron macroparticles in the 3D PIC simulation with $\sigma_{c0} = -0.45$. In the context of 3D fully kinetic simulations aimed at solar wind turbulence, the results shown below are to our knowledge the first attempt along these lines. Without going into an in-depth analysis we merely point out some of the interesting possibilities that the particle tracking diagnostics can offer.

In what follows, we split each particle's instantaneous velocity $\mathbf{v}_s(t)$ into a parallel and perpendicular part as $v_{\parallel s} = \hat{\mathbf{e}}_\parallel \cdot \mathbf{v}_s$ and $\mathbf{v}_{\perp s} = \mathbf{v}_s - \hat{\mathbf{e}}_\parallel \hat{\mathbf{e}}_\parallel \cdot \mathbf{v}_s$, where $\hat{\mathbf{e}}_\parallel = \mathbf{B}(t)/|\mathbf{B}(t)|$ is the direction of the *total* magnetic field, interpolated along the particle trajectory. Due to the limited sample size of tracked particles, we average below the normalized probability distribution functions (PDFs) over a time interval between $\approx 0.5t_A$ and $\approx 1.6t_A$. Since the turbulence is decaying, the averaging cannot be strictly justified but it is adopted here as a necessity in order to obtain reasonably well-behaved statistical estimates.

In Fig. 6.8 (left panel) we show the PDFs of the instantaneous energy transfer to/from the particles, split between the parallel and perpendicular contributions as $\mathrm{d}W_{\parallel s}/\mathrm{d}t = q_s \mathbf{v}_{\parallel s}(t) \cdot \mathbf{E}(t)$ and $\mathrm{d}W_{\perp s}/\mathrm{d}t = q_s \mathbf{v}_{\perp s}(t) \cdot \mathbf{E}(t)$, respectively. The instantaneous energy transfer that a particle experiences along its self-consistent path is highly oscillatory and features a considerable fraction of large-amplitude "kicks." The PDFs are nearly symmetric functions and are characterized by exponentially decaying tails with shallower exponents for the parallel transfer. Essentially, in an infinitesimal amount of time, a given particle has nearly equal probability of gaining or loosing energy. A more visual representation of the particle dynamics is shown in the right panel of Fig. 6.8, which displays a few sample electron trajectories. Different types of particle motion can be identified, ranging from the highly energetic passing particles to velocity reversals at the magnetic mirrors.

As shown above, the instantaneous energy transfer is highly oscillatory and tells little

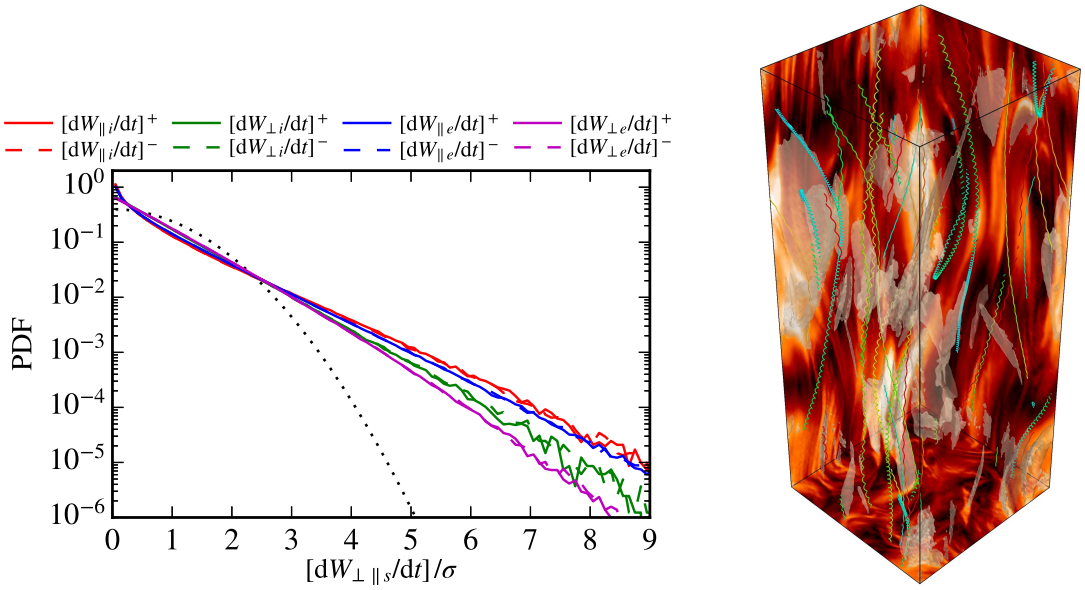

Figure 6.8: Particle energization in 3D kinetic plasma turbulence. Left panel: Distribution of the instantaneous energy transfer to/from the particles, $dW_{\perp\parallel s}/dt = q_s \mathbf{v}_{\perp\parallel s}(t) \cdot \mathbf{E}(t)$, sampled along the particle trajectories. Dotted line shows a normal Gaussian distribution for reference. Right: Visual representation of a few sample electron trajectories. The colored sides of the box and the isosurfaces represent $|\mathbf{E}|$. The trajectories are colored according to the instantaneous particle energy.

about the fact that the particles gain energy on average as the turbulent energy dissipates. It is therefore more instructive to consider the Lagrangian energy increments over a finite time scale τ.[7] For an appropriate, physically motivated choice $\tau \gtrsim \tau_0$ it may be expected that the net energy transfer will be positive and the PDFs of the energy increments will be non-symmetric. In the context of our fully kinetic simulations, it is of some particular interest to study the perpendicular heating, which may arise (among others) from the stochastic scattering of the particles on finite-amplitude, low-frequency electromagnetic fluctuations [55, 147, 148, 334]. In short, when the gyroscale fluctuations exceed a critical amplitude, the particle perpendicular motion becomes stochastic and decorrelates on a time scale $\tau_{0s} \sim (\Omega_{cs}\epsilon_s)^{-1}$, where ϵ_s is a relative strength of gyroscale fluctuations [148]. For moderately low betas, ϵ_s can be estimated as $\epsilon_s \sim \delta u_{\rho_s}/v_{\perp s}$, where δu_{ρ_s} is an effective $E \times B$ drift amplitude on scale $\lambda \sim \rho_s$. On longer time scales ($\tau \gg \tau_{0s}$), the stochastic motion leads to energy-space diffusion, resulting in a net statistical energy gain if the particle distribution f_s is a decreasing function of $v_\perp$ [148]. Stochastic heating is a mechanism ordered out of gyrokinetics by construction [188], since it violates the conservation of the magnetic moment $\mu_s = m_s|\gamma_s \mathbf{v}_{\perp s}|^2/(2|\mathbf{B}|)$. Given these circumstances, we characterize the perpendicular energization in terms of the fractional changes in the magnetic moment. In principle, μ_s should not contain contributions from large-scale (fluid) drift motion [335].

[7] Our idea was inspired by an analysis of Lagrangian particles in fluid turbulence [333].

To improve our estimates, we thus transform the perpendicular velocities into the local frame of $\mathbf{u}_{E\times B} = c(\mathbf{E}\times\mathbf{B})/B^2$, before calculating μ_s. The $\mathbf{u}_{E\times B}$ drift is estimated from the local fields, interpolated along each particle's trajectory. Since the drift is well-defined only for low-frequency motion of the (effective) guiding center, $\mathbf{u}_{E\times B}(t)$ is low-pass filtered to (Lagrangian) frequencies below $\Omega_{cs}/2$, before performing the velocity transformation.

The PDFs of the fractional changes in μ_s for two different Lagrangian increments τ are displayed in Fig. 6.9. We take the characteristic decorrelation time for stochastic motion $\tau_{0s} \sim (\Omega_{cs}\epsilon_s)^{-1}$ as the reference time scale and we calculate the PDFs for $\tau_1 = \tau_{0s}/4$ and $\tau_2 = 4\tau_{0s}$. For simplicity, we estimate $\epsilon_s \approx \delta b_{\rho_s}/B_0$, where δb_{ρ_s} is a typical gyroscale magnetic fluctuation amplitude (evaluated using a band-pass filter). From this we obtain, $\epsilon_i \approx 0.14$ and $\epsilon_e \approx 0.03$.[8] Since the fluctuations at the electron Larmor scale are nearly a factor of ≈ 5 smaller than the ones at ion scales, it is reasonable to expect that the stochastic heating would be much more efficient for the ions. This is implicitly supported by our results in Fig. 6.9. In particular, the fractional changes in the ion magnetic moment increase substantially for Lagrangian increments longer than the decorralation time scale τ_{0i} and the PDFs acquire a distinct non-symmetric shape with very large violations of μ_i at the tails of the distribution. For electrons, the latter trend is not observed as clearly as for the ions. It is also seen that the average increase of μ_i is facilitated by a fraction of ions, which heavily violate the magnetic moment conservation. Supporting evidence is also provided by a visual inspection of the ion trajectories, which exhibit highly irregular perpendicular motion (not shown). Altogether, these results imply that stochastic ion motion may be a viable perpendicular heating mechanism in KAW turbulence, whenever the ion gyroscale fluctuations cannot be assumed small. As a side note, we also performed an equivalent analysis for a thermal plasma PIC simulation and we found substantially smaller violations of μ conservation for both ions and electrons. This indicates that the trends seen in Fig. 6.9 are of physical rather than numerical origin.

In addition to the Lagrangian particle statistics, we also show in Fig. 6.10 for reference the global particle velocity distributions toward the end 3D fully kinetic simulation. We visualize the distributions in the reduced $v_\parallel - v_\perp$ space by averaging f_s over fixed shells in the $\mathbf{v}_\perp$ plane. A very close look at the figure shows that the core electron distribution has a slightly larger parallel spread, whereas the ion core distribution is somewhat elongated in the perpendicular direction. The latter is consistent with the possibility of perpendicular stochastic ion heating, although there might be also other kinetic processes contributing to the slightly increased perpendicular spread. Interestingly, an excess population of ions is found at large positive values of $v_\parallel$ in the range $v_\parallel \gtrsim v_{\mathrm{th},i}$. Recall that the velocity distributions are obtained here from the imbalanced turbulence simulation. For our choice of the (initial) cross-helicity, there is an excess of large-scale shear Alfvén waves propagating in the positive parallel direction. These waves transition into an imbalanced flux of KAWs around the ion gyroscale, where resonant ion heating via the Landau resonance is possible

[8] We also considered a definition of ϵ_s based on the average $\delta u_{\rho_s}/v_{\mathrm{th},s}$ ratio, where δu_{ρ_s} is the RMS, band-pass filtered $\mathbf{u}_{E\times B}$ drift in the (Lagrangian) frequency range: $\Omega_{cs}/2 \le \omega \le 2\Omega_{cs}$. This gives estimates consistent with those based on $\delta b_{\rho_s}/B_0$, within a difference of $\approx 15\%$.

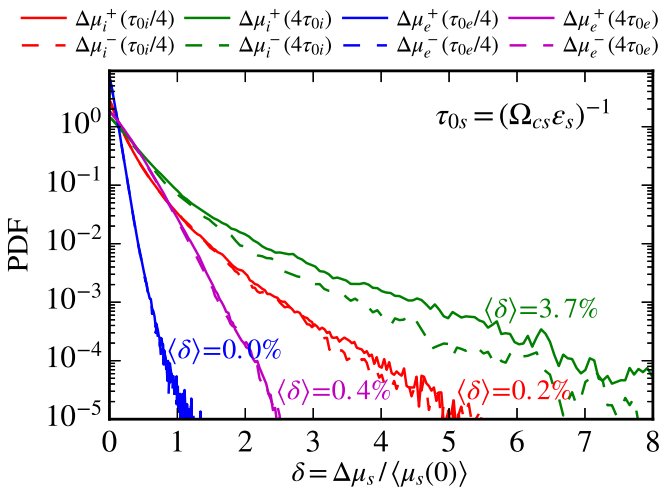

Figure 6.9: Statistics of the fractional change in the magnetic moment $\Delta\mu_s(\tau)$ in a given time scale τ. Solid and dashed lines represent positive and negative fractional increments, respectively. The mean fractional changes are reported with colored labels on the graph.

[54, 131]. Since the KAW frequency is comparable to $\omega \sim k_\parallel v_A$ at ρ_i and because our ion beta $\beta_i = v_{\mathrm{th},i}^2/v_A^2 \approx 0.5$, it is expected that the ions with parallel velocities comparable to or larger than $v_{\mathrm{th},i}$ will resonate with KAWs most efficiently. Furthermore, due to the imbalance, the resonant wave-particle interaction should be stronger for positive $v_\parallel$. Our result in Fig. 6.10 is consistent with such interpretation and provides in this sense circumstantial evidence for resonant ion heating via Landau damping in KAW turbulence. For the electrons, the slightly increased parallel spread of the core may as well be a sign of Landau damping, although no clear conclusion can be made based on the results at hand.

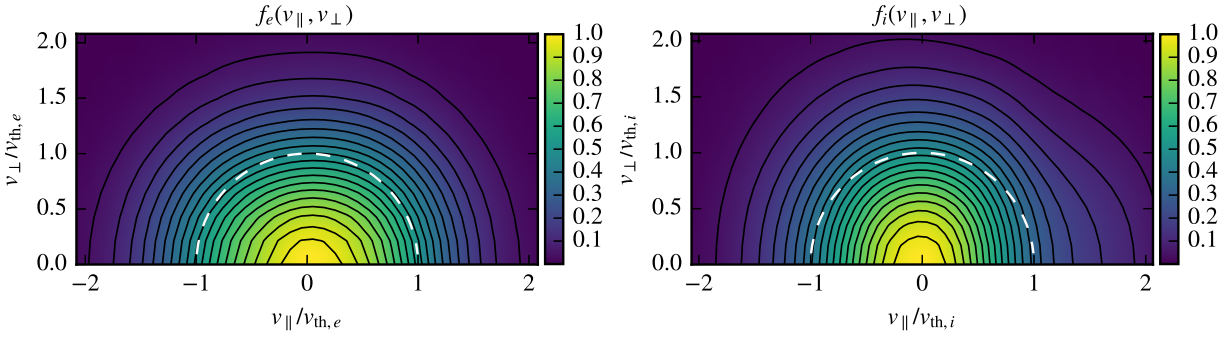

Figure 6.10: Global electron (left) and ion (right) velocity distribution functions toward the end of the turbulence simulation with $\sigma_{c0} = -0.45$, visualized in the $v_\parallel - v_\perp$ plane. White dashed lines show for reference a circle with radius $v_{\mathrm{th},s}$ to help recognizing the deviations of the core from an isotropic Maxwellian.

A reader may find it perhaps somewhat surprising that the deviations of the global ion and electron velocity distributions from an isotropic Maxwellian are relatively moderate

and that the distributions are rather well-behaved and smooth, despite the presence of a turbulent cascade. The latter can be heuristically explained based on the following argument. Let us ask, what is the amount of turbulent energy, ΔE, available to energize the particles compared to the energy in the thermal background $E_{\rm th}$? On the eddy turnover time scale, an amount of $\Delta E \sim \delta b^2$ energy can be cascaded to small scales and energize the particles. Thus, on time scales comparable to an eddy turnover time, the fraction of available energy is $\Delta E/E_{\rm th} \sim \beta^{-1}(\delta b/B_0)^2$. If the plasma beta is of order unity, the available energy is a relatively small fraction of the thermal background, even for moderate fluctuation amplitudes $\epsilon = \delta b/B_0$. This shows that, at least on the time scales accessible in present 3D fully kinetic simulations, there is typically not a lot of energy available for strong global deformations of the particle velocity distribution, unless perhaps in the tails of the distribution where there are not many particles.[9] In conjunction, a number of processes may act to restore a state close to equilibrium on longer time scales, including an effective (numerical) collisionality [69, 97, 98, 131].

6.3 Summary and conclusions

We performed a set of fully kinetic 3D simulations of decaying plasma turbulence, covering the transition from the tail of the MHD turbulence into the sub-ion range and beyond. The physical parameters are chosen to mimic the conditions found in the slow streams of the solar wind at around 1 AU, where the plasma beta and ion-electron temperature ratio are typically both close to unity. The initial fluctuations at the start of each simulation are limited to scales above the ion gyroradius and the initialized shear Alfvén waves are only moderately oblique. It is therefore not evident that KAW turbulence would naturally develop at sub-ion scales of the fully kinetic simulations. Other possibilities, such as whistler wave turbulence [80–82, 143, 244, 245], cannot be *a priori* ruled out. However, we find that the sub-ion scale spectral ratios are well consistent with theoretical expectations for KAW turbulence. We also estimate the local spectral anisotropy and the ratio of linear to nonlinear turbulence time scales χ. Between the ion and the electron scales, we obtain a strong scale-dependent anisotropy with $k_\parallel < k_\perp$ and a nonlinearity parameter of order unity ($\chi \sim 1$), in broad agreement with critical balance [4, 5, 136].

A number of additional aspects of the 3D kinetic plasma turbulence are also studied. By varying the initial level of the normalized cross-helicity, σ_{c0}, between the two runs we show that the KAW turbulence scalings are not very sensitive to moderate variations in the cross-helicity, which are naturally found in the slow solar wind [32]. On the other hand, slight differences can be still seen compared to the balanced regime with $\sigma_{c0} = 0$. In particular, the sub-ion range nonlinear interaction is weakened as $|\sigma_{c0}|$ is increased to a value above zero. Finally, we analyze the particle energy increments in the Lagrangian frame and obtain evidence for the violation of the magnetic moment conservation via perpendicular

[9] Note, however, that even a relatively small anisotropy in the distribution function can lead to kinetic instabilities, in particular if the plasma beta is large [11, 149, 151].

stochastic ion heating [148]. The global ion velocity distributions exhibit also signatures of resonant parallel heating via the Landau resonance with KAWs.

Even though we resolve the full range of 3D kinetic physics, it is fair to mention the limitations imposed by present computational constraints for our massively parallel computations. Most notably, we use a reduced ion-electron mass ratio of 64, which reduces the scale separation between the ions and electrons by a factor of ≈ 5.4, compared to a proton-electron plasma. No definitive answer can be given regarding the impact of the reduced mass ratio, although it should be noted that our results are in good agreement with *in situ* solar wind measurements [27, 145, 235, 276], as well as with gyrokinetic simulations employing realistic mass ratios [36, 39]. For what is worth, in the following Chapter 7 we present a 3D fully kinetic simulation with $m_i/m_e = 100$ and external forcing. No significant qualitative differences are found compared to the results presented in this Chapter. Significantly improved parameters for fully kinetic simulations will have to await the next generation of supercomputers. Here we demonstrated, for the first time based on fully kinetic 3D simulations, that the sub-ion range turbulent fluctuations in a $\beta \sim 1$ plasma naturally evolve towards a state consistent with the phenomenology of KAW turbulence. As such, our results improve confidence in the KAW turbulence phenomenology and shed light on some of the ongoing debates in the field [50, 188, 226, 227].

Chapter 7

Kinetic turbulence in astrophysical plasmas: waves and/or structures?

For many years, the question of the relative importance of wavelike features and coherent structures has intrigued astrophysical and space plasma turbulence researchers. The debate on waves and structures emerged historically in the context of magnetohydrodynamic (MHD) turbulence [136, 336–338] and shifted more recently towards the kinetic range of scales [48, 53, 188, 235, 238, 277, 339]. Wavelike interpretations of magnetized plasma turbulence defy the classical Kolmogorov picture of Navier-Stokes turbulence [99], where linear physics is of no particular interest. Many natural turbulent systems are, however, not of the standard Navier-Stokes type and may support waves. Prominent examples include magnetized plasmas, rapidly rotating, and/or stratified fluid flows [340]. The question then arises how does the linear response affect the turbulent dynamics, and in particular the nonlinear formation of turbulent structures [53, 337, 341].

A far reaching phenomenological interpretation of turbulence in systems that support waves emerged with the critical balance conjecture of Goldreich and Sridhar [136] for MHD plasma turbulence (see Sec. 3.2). Their seminal contribution later paved the way for many highly significant works on astrophysical plasma turbulence [4, 5, 14, 206], and since then, the concept of critical balance received attention even in fields outside of plasma physics [190, 342, 343]. It is important to note that critical balance is essentially a statement about the persistence of wavelike features in strongly nonlinear turbulence. However, the phenomenology put forward by Goldreich and Sridhar makes no explicit connection to the pervasive structure formation in plasma turbulence [13, 210, 277, 295, 344], nor does it account for the resulting intermittency of the turbulent fields [37, 57, 58, 254, 345]. The latter aspect is presently the subject of ongoing investigations [58, 188, 277, 297, 346], since it is not immediately obvious how structure formation—an inherently nonlinear process—should come into play, if strong plasma turbulence were to preserve a linear wave footprint.

In this Chapter, we straightforwardly address the dilemma on waves and structures in kinetic plasma turbulence by means of a joint analysis of observational and simulation data. In particular, we introduce a novel set of diagnostic measures to study the interplay between

large-amplitude structures and wavelike features in kinetic range plasma turbulence. The simulation results are obtained from an externally driven, three-dimensional (3D) fully kinetic turbulence simulation, and the observational data are based on *in situ* measurements from the Cluster [274] and MMS [275] spacecraft. Most of the results shown below are presently available as a preprint article ([161], submitted to Physical Review X). The author of the Thesis performed the kinetic simulation, devised the generalized spectral ratio definitions (see Sec. 7.1.4), analyzed the observational and simulation data, produced the figures, and wrote the draft paper [161], taking into account a number of valuable comments and suggestions from the coauthors. A preliminary analysis of spacecraft measurements (not shown) was carried out by C. H. K. Chen, who also proposed the original project and provided the observational data.

The rest of this Chapter is organized as follows. In Sec. 7.1 we detail the scientific methods used to obtain our results. This includes an overview of the kinetic simulation (Sec. 7.1.1), a description of solar wind spacecraft data (Sec. 7.1.2), wavelet analysis techniques (Sec. 7.1.3), and the generalized spectral ratio definitions (Sec. 7.1.4). The results of the analysis are presented in Sec. 7.2. The turbulence statistics are characterized by calculating the scale-dependent flatness (Sec. 7.2.1). We then depict the structure formation in the simulation and discuss its relation to the spatial variability of the local wavelet spectra (Sec. 7.2.2). Moreover, we show that the kinetic-scale structures are to a good approximation pressure balanced (Sec. 7.2.3). Finally, we present the generalized spectral field ratios, estimated from simulation and observational data (Sec. 7.2.4). To order unity, we find that the large-amplitude structures *themselves* approximately satisfy the linear field ratio predictions for kinetic Alfvén waves (KAWs). The implications of this quantitative evidence are discussed in Sec. 7.3, where we demonstrate the possibility of a scale-dependent and intermittent alignment between the perpendicular electron fluid velocity and the magnetic field. Similar to angular alignment in MHD turbulence [158–160, 206, 207], we argue that the alignment may lead to a progressive and intermittent weakening of the nonlinearity in KAW turbulence. We conclude the Chapter with a summary of our main results in Sec. 7.4.

7.1 Methods

In the following, we provide technical details on the kinetic simulation, the selection of spacecraft data, the wavelet analysis techniques, and on the generalized spectral field ratios. In addition, we also present the magnetic spectra and the local spectral anisotropy estimates, obtained from the driven 3D kinetic simulation. The details provided below are essential for a complete understanding of the main results presented in Sec. 7.2.

7.1.1 Driven 3D fully kinetic simulation

The fully kinetic, particle-in-cell (PIC) simulation is performed with the OSIRIS code (see Chapter 4). The Cray XC40, Shaheen, at the King Abdullah University of Science &

Technology (KAUST) in Thuwal, Saudi Arabia was utilized for the reported numerical results. The simulation ran on 49,152 CPU cores for a total time of about 10 million aggregate computing hours. Unlike in the few previous 3D fully kinetic simulations aimed at solar wind, sub-ion range turbulence [77, 78, 269], we include an external forcing and we evolve the kinetic equations until a quasi-steady turbulent state emerges. The spatial resolution is $(N_x, N_y, N_z) = (928, 928, 1920)$ with 150 particles per cell per species. Quadratic spline interpolation is used for the current deposit and for the interpolation of the Lorentz force. A second-order compensated binomial filter is applied to the electric current and to the electromagnetic fields felt by the particles at each step [63]. A mean magnetic field $\mathbf{B}_0$ is imposed in the z direction. The electron plasma to cyclotron frequency ratio is $\omega_{pe}/\Omega_{ce} = 2.86$ and the ion-electron (reduced) mass ratio is $m_i/m_e = 100$. The physical box dimensions are $(L_x, L_y, L_z) = (18.9, 18.9, 48.3)d_i$. For a list of common plasma parameters and their definitions see Appendix C. The external forcing, described in Appendix B, is included in the form of a time-varying external electric current $\mathbf{J}_{\rm ext}$ [305]. We apply $\mathbf{J}_{\rm ext}$ at the lowest wavenumbers. The mean frequency of the forcing is $\omega_0 = 0.9 \cdot \omega_{A0}$, where $\omega_{A0} = 2\pi v_A/L_z$ is the lowest shear Alfvén wave frequency, and the temporal decorrelation rate is $\gamma_0 = 0.6 \cdot \omega_0$. At the start of simulation, the ion and electron velocity distributions are isotropic Maxwellians with $\beta_i \approx \beta_e \approx 0.5$. To reduce particle noise in the subsequent analysis, we short-time average the raw simulation data over a time window of duration $\Delta t = 2.0 \cdot \Omega_{ce}^{-1}$.

In Fig. 7.1 we illustrate the approach towards a statistically steady turbulent state in the simulation. We employ a strong external current drive, such that the fluctuation amplitudes towards the end of the simulation approximately satisfy the large-scale, critical balance condition: $\delta b/B_0 \approx L_\perp/L_z \approx 0.4$ (Fig. 7.1, top panel). The plasma beta slightly increases during the simulation as a result of ion and electron heating. At the end of the simulation, we obtain $\beta_i \approx 0.56$ and $\beta_e \approx 0.51$ in terms of the space-averaged local beta values. The evolution of the one-dimensional (1D) magnetic energy spectrum is shown in bottom panel of Fig. 7.1. The steady-state spectrum is in reasonable agreement with spacecraft measurements, showing typical spectral exponents around -2.8 at sub-ion scales, while steeper exponents are measured close to electron scales and beyond [27, 235]. Similar to Ref. [134], we further reduce the particle noise by filtering out the noise-dominated modes with $k_z d_i > 12$ (see inset of Fig. 7.1).

An important piece of information is obtained from the local spectral anisotropy estimates presented in Fig. 7.2 (see Sec. 6.2.3 for additional details). At sub-ion scales, the $k_\parallel(k_\perp)$ relation indicates a strong, scale-dependent anisotropy with an approximate slope of 1/3 on the logarithmic graph, in agreement with previous results from Chapter 6. For reference, we include an alternative anisotropy estimate obtained using a two-dimensional (2D) Halo wavelet decomposition in $k_\perp$ ([347, 348], see also Sec. 7.1.3), instead of a sharp band-pass filter [78, 241].[1] From the anisotropy, we infer the typical ratio of linear (KAW) to nonlinear time scales, $\chi = \tau_{\rm L}/\tau_{\rm NL} \approx k_\perp \delta b_{\perp k_\perp}/[k_\parallel(k_\perp)B_0]$, where $\delta b_{\perp k_\perp}$ is a typical

[1]The *local* mean magnetic field is in that case defined via a Gaussian low-pass filter with the same spread in $k_\perp$ as the analyzing wavelet.

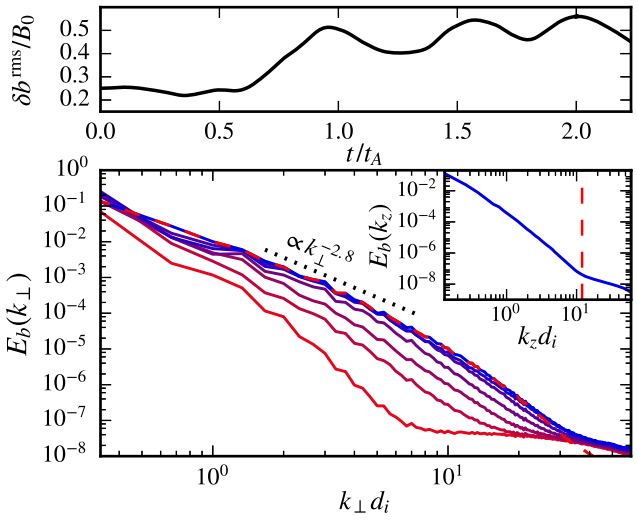

Figure 7.1: Approach towards a statistically steady state in the 3D PIC simulation. Top: Time evolution of the root-mean-square fluctuating magnetic field. Bottom: 1D magnetic energy spectrum as a function of $k_\perp$ from $t/t_A = 0.66$ (solid red curve) to $t/t_A = 2.24$ (blue curve), where $t_A = L_z/v_A$. Dashed red line shows the $k_\perp$ spectrum at $t/t_A = 2.24$, after the noise-dominated modes with $k_z d_i > 12$ (see inset) have been removed.

fluctuation amplitude at perpendicular scale $\lambda \sim 1/k_\perp$ [4, 78, 241, 245]. Even though the fluctuation amplitudes in our simulation are relatively large, the linear time scale appears to be on average comparable to the nonlinear time scale. In order to make nonlinear effects dominant ($\chi \gg 1$), the 3D turbulence would need to sustain a quasi-2D state, which would correspond to a nearly flat curve for the spectral anisotropy. This essential piece of evidence implies that the linear, wave-crossing time scale is of clear dynamic relevance and motivates a further exploration of the turbulence wavelike features.

7.1.2 Spacecraft data

Solar wind data for the analysis are obtained from the Cluster [274] and MMS [275] space missions. In particular, we select 7 hours of Cluster measurements and a 159 second long interval from MMS. The intervals chosen were previously studied by Chen *et al.* [242] and Gershman *et al.* [278], respectively. During the measurement, the Cluster spacecraft were in the free streaming solar wind far from the Earth's foreshock. The MMS measurements, on the other hand, were taken in the Earth's magnetosheath [247] at a location well separated from the bow shock and from the magnetopause. The mean plasma beta ratios are $\beta_i \approx 0.26$ and $\beta_e \approx 0.62$ for Cluster and $\beta_i \approx 0.27$ and $\beta_e \approx 0.03$ for the MMS interval. As is regularly done, we convert the spacecraft frame frequencies $f_{\rm sc}$ to (perpendicular) wavenumbers $k_\perp$ by invoking the Taylor hypothesis [34, 35]: $k_\perp \approx 2\pi f_{\rm sc}/(|\mathbf{V}_{\rm SW}| \sin\theta_{BV})$, where $\mathbf{V}_{\rm SW}$ is the mean solar wind speed and θ_{BV} is the mean angle between $\mathbf{B}_0$ and $\mathbf{V}_{\rm SW}$ during the

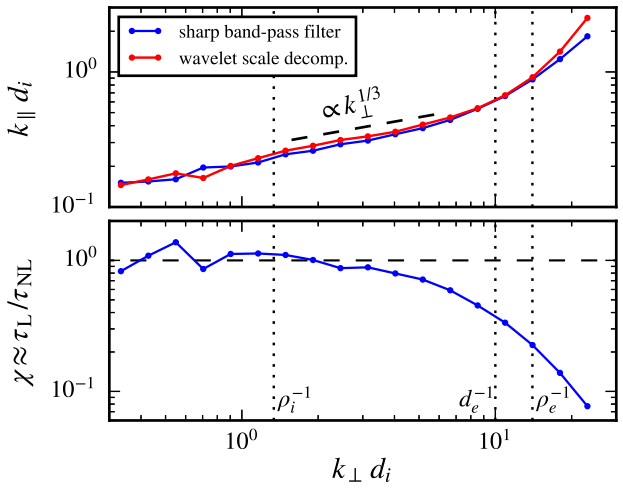

Figure 7.2: Local spectral anisotropy (top) and the typical ratio of linear to nonlinear time scales (bottom), estimated at the final stage of the forced 3D kinetic simulation.

measurement.[2] For Cluster, $\theta_{BV} \approx 76°$ so that the $\sin\theta_{BV}$ factor can be neglected, whereas for the MMS data $\theta_{BV} \approx 14°$ [278]. The average angle between $\mathbf{B}_0$ and the wave vector $\mathbf{k}$, estimated in Ref. [278] using the k-filtering technique [279], is very close to 90 degrees for the selected MMS interval, thus justifying the conversion to $k_\perp$ even though θ_{BV} is relatively small.

The analyzed data includes magnetic field measurements from Cluster and the magnetic field and electron density measurements from MMS. High-resolution electron density measurements are not available from Cluster. This is the main reason why we include here the MMS data, even though the MMS interval is rather short and generally less suitable for the intermittency analysis than the Cluster interval, which covers many typical turbulence correlation times [293]. Better suited data from MMS are presently not available to our knowledge [278]. We also mention that the accessible range of scales is limited by the various measurement uncertainties. In terms of perpendicular wavenumbers (estimated using Taylor's hypothesis), the analysis is limited to $k_\perp \lesssim 10/d_i$ for Cluster and to $k_\perp \lesssim 1/d_e$ for the MMS interval.

7.1.3 Wavelet scale decomposition

Since our aim is to study the impact of spatially localized structures on the spectral field ratios, we require a scale decomposition with a good localization in both configuration and spectral space. Wavelet transforms appear as a natural choice for the task [169, 347]. Here, we adopt complex-valued Morlet wavelets [347–349], which have been often utilized in recent years as a tool for the analysis of *in situ* solar wind turbulence measurements [200, 277, 346, 350]. The 1D Morlet wavelet basis functions ψ^{1D} can be represented in

[2] Here we also implicitly assume a strong spectral anisotropy with $k \approx k_\perp \gg k_\parallel$.

spectral space as band-pass filters of the form

$$\widehat{\psi}_s^{1D}(k) = \Theta(k) \exp\left(\frac{-(k-k_s)^2}{2(k_s/k_0)^2}\right), \tag{7.1}$$

where $k_0 = 6$ is a dimensionless parameter [347], $\Theta(k) = 1$ for $k > 0$ and zero otherwise, and k_s is a characteristic wavenumber scale. The wavelet scale s can be expressed as $s = k_0/k_s$. For some signal $f(x)$, the Morlet wavelet transform $\widetilde{f}_s(x)$ at a given scale s is obtained from the inverse Fourier transform of $\widehat{f}\,\widehat{\psi}_s$, where $\widehat{f}$ is the Fourier-transformed original signal. The wavenumbers $\{k_s\}$ are logarithmically spaced and increase in fractional powers of 2. The choice of the number of scales per octave is, however, somewhat arbitrary due to the inherent information redundancy associated with continuous wavelet transforms [349]. Based on the complex wavelet coefficients, a local and scale-dependent fluctuation can be defined as $\delta f_s(x) = c_1\,\mathrm{Re}\{\widetilde{f}_s(x)\}$ and a local spectrum as $E_f(k_s, x) = c_2|\widetilde{f}_s(x)|^2/k_s$, where $\mathrm{Re}\{\dots\}$ is the real part, and the constants c_1 and c_2 can be determined from the exact parameters of the transform [347, 349]. We set $c_1 = c_2 = 1$ since the choice of normalization does not affect our results. In the following, we omit the scale subscript s but it is to be understood that all quantities depend on scale.

The *local and scale-dependent* fluctuations and the *local* spectra, defined in terms of the 1D Morlet transform, form the basis for our analysis of simulation and observational data. More specifically, in the next section we define a set of generalized spectral field ratios based on the wavelet transform coefficients. When analyzing finite time series with Morlet wavelets, edge distortions may occur due to the assumed signal periodicity. This can be avoided by discarding a fraction of the wavelet coefficients close to the edges. To this end, we skip about 5 s on each side of the Cluster interval and about 7 s at the edges of the MMS trace. In order to establish a one-to-one correspondence between solar wind measurements and the simulation, we construct a set of 1D traces from the 3D simulation by mimicking a spacecraft fly-through over the periodic box [351]. A set of 100 uniformly distributed virtual spacecraft paths are analyzed to improve the statistics. For all paths, we choose a direction $\hat{\mathbf{n}} = (0.949, 0.292, 0.122)$ and we extract the field variations along the lines parallel to $\hat{\mathbf{n}}$ using cubic spline interpolation.[3] Each line starts in the $z = 0$ plane and ends at $z = L_z$, during which time the linear trajectory covers a total distance of nearly $400d_i$. Similarly as for the solar wind data, we avoid edge effects by skipping the wavelet coefficients within a distance of $19d_i$ from the edges of each interval.

In Sec. 7.2.2 we also employ a 2D Morlet transform, which is a generalization of its 1D counterpart [347, 348]. The 2D basis functions can be written in spectral space as

$$\widehat{\psi}_{s,\phi}^{2D}(k_x, k_y) = \exp\left(\frac{-\left[(k_x - k_s\cos\phi)^2 + (k_y - k_s\sin\phi)^2\right]}{2(k_s/k_0)^2}\right), \tag{7.2}$$

where ϕ determines the direction to be analyzed in the $x-y$ plane. Additionally, we set $\widehat{\psi}_{s,\phi}^{2D}(0,0) = 0$. Here, we use the 2D Morlet transform to study the field structure at different

[3] This particular direction was chosen because the corresponding lines of extraction traverse the periodic box relatively uniformly and at a highly oblique angle with respect to $\mathbf{B}_0 = (0, 0, B_0)$.

perpendicular planes of the 3D fully kinetic simulation. Twelve angular directions in the range $\phi \in [0, \pi)$ are used to compute the coefficients and the results are later averaged over different angles. The angular averaging of the local wavelet spectra is performed *after* taking the squared modulus of the wavelet coefficients. In this way, we avoid contributions from the variations in the complex phase, thus highlighting the true spatial variability of the power spectrum [352].

7.1.4 Generalized field ratios

Let us now define a new set of diagnostic measures, which can be viewed as generalizations of the standard spectral field ratios ([40, 143, 145, 236], see also Sec. 3.3.4) to higher order statistics. The first set is based on the ratios of the scale-dependent moments of the fluctuations:

$$\left(\frac{\langle|\delta n_e|^m\rangle}{\langle|\delta b_\perp|^m\rangle}\right)^{2/m}, \qquad \left(\frac{\langle|\delta n_e|^m\rangle}{\left\langle|\delta b_\parallel|^m\right\rangle}\right)^{2/m}, \qquad \left(\frac{\left\langle|\delta b_\parallel|^m\right\rangle}{\langle|\delta b_\perp|^m\rangle}\right)^{2/m}, \tag{7.3}$$

where m is the order of the moment, $\langle \dots \rangle$ denotes a space average, and δn_e, $\delta b_\parallel$, and $\delta b_\perp$ are, respectively, the fluctuating electron density, the parallel, and the perpendicular magnetic fluctuations at a given wavelet extracted scale. For $m = 2$ we recover the usual spectral field ratios. On the other hand, as the order m is increased, the large-amplitude fluctuations are assigned higher statistical weights and the ratios become progressively more sensitive to the fluctuations at the tails of the probability distribution functions (PDFs). In this sense, the ratios of the moments can be used to probe if the higher-amplitude fluctuations satisfy the linear KAW field ratio predictions (3.61), (3.65), and (3.66).

In the following, we consider moments up to $m = 6$. When estimating high-order moments from finite time series, care has to be taken because the tails of the PDFs may not be sufficiently sampled [321, 322]. To recover more reliable estimates we follow Kiyani *et al.* [322] (see also Ref. [263]) and remove a very small fraction of the largest fluctuations at each scale, until the moments appear reasonably converged. For Cluster data with $N \approx 6.3 \cdot 10^5$ samples, we find that removing 0.005% of the largest fluctuations appears to be sufficient, which amounts to about 30 samples. For consistency, we clip the same small fraction in the simulation. Due to the short duration of the MMS interval, relatively large fractions would have to be removed to recover more reliable estimates, at which point only the core of the PDF would be left. Therefore, we do not attempt any clipping when calculating the scale-dependent moments from the MMS data.

The ratios of the scale-dependent moments are global measures, in a sense that the moments are averaged over the whole ensemble. A more local measure can be defined based on the ratios of the conditionally averaged local wavelet spectra:

$$\frac{\langle|\widetilde{n}_e|^2\,|\mathrm{LIM} > \xi\rangle}{\langle|\widetilde{b}_\perp|^2\,|\mathrm{LIM} > \xi\rangle}, \qquad \frac{\langle|\widetilde{n}_e|^2\,|\mathrm{LIM} > \xi\rangle}{\langle|\widetilde{b}_\parallel|^2\,|\mathrm{LIM} > \xi\rangle}, \qquad \frac{\langle|\widetilde{b}_\parallel|^2\,|\mathrm{LIM} > \xi\rangle}{\langle|\widetilde{b}_\perp|^2\,|\mathrm{LIM} > \xi\rangle}, \tag{7.4}$$

where LIM is the so-called local intermittency measure [347, 352] and ξ is the threshold for the conditional average. The LIM is defined as the local wavelet spectrum normalized by its average value at a given scale. Non-Gaussian turbulent fluctuations give rise to large spatial variations in the local spectra and the locations where LIM > 1 correspond to energetic events that contain above-average fractions of the total spectral energy. Based on physical considerations, we define here the LIM as

$$\mathrm{LIM}(k_s, x) \equiv \frac{E_{KA}(k_s, x)}{\langle E_{KA}(k_s, x) \rangle_x}, \tag{7.5}$$

where $E_{KA} = |\widetilde{b}_\perp/B_0|^2 + [\beta(2+\beta)/4]\,|\widetilde{n}_e/n_0|^2$ is the local kinetic-Alfvén spectral energy density (see Eq. (3.58)), B_0 is the mean magnetic field strength, n_0 is the mean density, and $\beta = \beta_i + \beta_e$ is the total plasma beta. Our choice can be justified *a posteriori* based on our results, which show that the sub-ion range fluctuations carry significant density fluctuations, in consistency with the KAW turbulence phenomenology. A single, physically motivated choice for the LIM has also the clear advantage of constraining all conditional averages in (7.4) to the exact same spatial locations. In the case of Cluster data which lack the electron density measurements, we infer $|\widetilde{n}_e|^2$ from $|\widetilde{b}_\parallel|^2$ by invoking the linearized pressure balance (3.61), which is a necessary condition for the existence of the low-frequency KAWs.

We consider a range of different thresholds for the conditional average from $\xi = 1$ up to $\xi = 16$. By progressively increasing the threshold, we study how the spectral field ratios vary within the most intense structures, which may contain relatively large amounts of energy while occupying only very small volume fractions (typically less than $\sim 1\%$). However, as the threshold is increased further and further, the conditional ratios may eventually become even energetically insignificant. To focus on the ratios which are still of some energetic relevance, we discard any conditional averages that amount to less than 1% of the total kinetic-Alfvén energy at a given scale.

In what follows, we employ the newly introduced statistical measures to study the relation between large-amplitude structures and wavelike physics in kinetic range plasma turbulence. It is *a priori* not obvious that the generalized ratios should bear any resemblance with the standard spectral ratios, which are based on the Fourier amplitudes and ignore the presence of localized coherent structures. However, by comparison with linear KAW predictions we show that even the large-amplitude structures carry certain wavelike features, albeit with a slight tendency to deviate further from the linear predictions when compared to the total ensemble of fluctuations.

7.2 Results

Below, we present the main results of the joint analysis of observational and simulation data. Before doing so, it is worth clarifying a few essential aspects. First, to ease the comparison with the beta-dependent linear KAW predictions, we employ the following

natural normalizations (see Sec. 3.3.1):

$$n_e' = \left[\frac{\beta(2+\beta)}{4}\right]^{1/2} \frac{n_e}{n_0}, \qquad \mathbf{b}_\perp' = \frac{\mathbf{b}_\perp}{B_0}, \qquad \mathbf{b}_\parallel' = \left(\frac{2+\beta}{\beta}\right)^{1/2} \frac{\mathbf{b}_\parallel}{B_0}. \tag{7.6}$$

In the above units, the fluctuations are expected to reach equipartition at sub-ion scales,

$$\left\langle |\delta n_e'|^2 \right\rangle \approx \left\langle |\delta \mathbf{b}_\perp'|^2 \right\rangle \approx \left\langle |\delta \mathbf{b}_\parallel'|^2 \right\rangle \approx E_{KA}'/2, \tag{7.7}$$

according to the asymptotic KAW turbulence predictions and independently of the precise value of the (variable) order-unity plasma beta. In the following sections, we drop the prime signs but it is to be understood that all fields are normalized according to (7.6), unless noted otherwise.

Similar to previous works [146, 237], the parallel and perpendicular field components are defined everywhere relative to a local mean magnetic field as

$$\widetilde{b}_\parallel = \hat{\mathbf{e}}_{\rm loc} \cdot \widetilde{\mathbf{b}}, \qquad \widetilde{\mathbf{b}}_\perp = \widetilde{\mathbf{b}} - \widetilde{b}_\parallel \hat{\mathbf{e}}_{\rm loc}, \tag{7.8}$$

where $\hat{\mathbf{e}}_{\rm loc} = \mathbf{B}_{\rm loc}/|\mathbf{B}_{\rm loc}|$ is the direction of the local mean field $\mathbf{B}_{\rm loc}$, obtained from a Gaussian low-pass filter with the same spectral width σ_s as the analyzing wavelet at that scale (i.e., $\sigma_s = k_s/k_0$). Once the parallel and perpendicular components are obtained at a given scale, we normalize the wavelet coefficients according to (7.6).

We clarify, that we do *not* consider here a regime of weak wave turbulence [243]. Instead, our primary interest is strong turbulence, where the nonlinear terms cannot be assumed small. Therefore, we make no expectation that the turbulent fluctuations are truly waves in a classical sense of the term when we refer to wavelike properties. Moreover, we expect the relation (7.7) to hold only in terms of statistical averages, evaluated at least over an appreciable spatial subdomain. Indeed, when the fluctuations are composed of *many* modes with different wavenumbers, no general linear relation similar to (7.7) can be obtained locally in real space. It is, however, plausible that the KAW field polarizations are restored in a weak sense even locally with the aid of nonlinear effects [56, 353], if the linear response is able to keep up with the nonlinear evolution, as anticipated by critical balance [136, 159, 190]. Finally, an exception to the above is the relation between $\delta n_e'$ and $\delta b_\parallel'$. The latter two fields are expected to locally satisfy a linearized pressure balance condition (cf., Eq. (3.61)):

$$\delta n_e'(x) = -\delta b_\parallel'(x). \tag{7.9}$$

The pressure balance is a quite general property of low-frequency dynamics and it is not exclusive to KAWs. If satisfied at kinetic scales, the pressure balance helps eliminating several ambiguities associated with the potential role of high-frequency fluctuations, such as whistler waves [80–82, 143, 245, 247]. It is therefore still an important property for the identification of KAW-like fluctuations.[4] In contrast, the equipartition between $|\delta n_e'|^2$ and $|\delta b_\perp'|^2$ (or equivalently, between $|\delta b_\parallel'|^2$ and $|\delta b_\perp'|^2$) is deduced directly from the (asymptotic) KAW dispersion relation (see Sec. 3.3.2) and cannot be derived from pressure balance alone. With all these aspects in mind, we now proceed to our main results.

[4] We also note that a purely linear relation between $\delta n_e'$ and $\delta b_\parallel'$ implies that the scale-dependent fluctuations are sufficiently small that they can be expanded around a local mean background.

7.2.1 Scale-dependent flatness

We first characterize the kinetic range intermittency in the solar wind measurements and in the simulation in terms of the scale-dependent flatness $F(k_\perp) = \langle|\delta f|^4\rangle/\langle|\delta f|^2\rangle^2$, where $\delta f \in \{\delta n_e, \delta b_\parallel, \delta b_\perp\}$ represents a wavelet decomposed fluctuation [169]. Values of F above 3 are associated with non-Gaussian, heavy tailed PDFs. The results are shown in Fig. 7.3. Errorbars are included on the plot to illustrate the statistical uncertainties. To estimate the errorbars, we calculate the moments separately on a number of subsets of the original sample and use these as input for a jackknife error estimate [354].

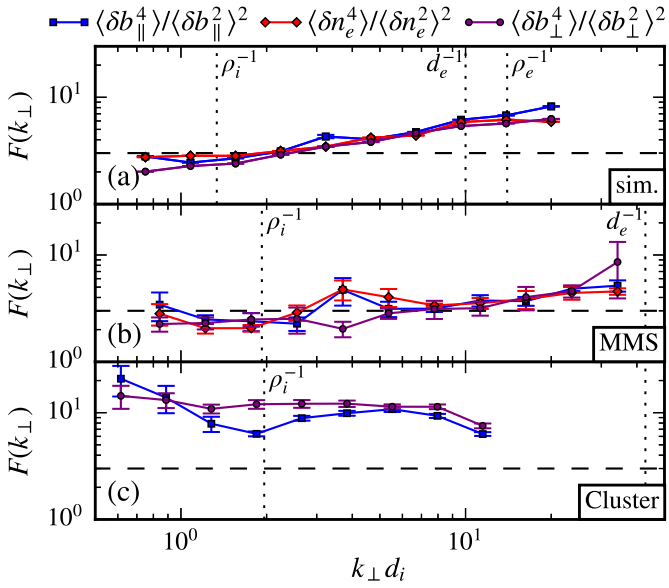

Figure 7.3: Scale-dependent flatness obtained from the 3D fully kinetic simulation (a), from the MMS (b), and Cluster measurements (c).

At sub-ion scales, which are of our primary interest here, all three analyzed fields follow similar statistical trends (separately for each dataset) and the kinetic turbulence is characterized by large-amplitude, intermittent events that give rise to values of the flatness above 3. The departure from normal, Gaussian statistics is generally largest in the Cluster dataset, which contains a large sample of small-scale fluctuations from the free streaming, turbulent solar wind. In agreement with previous works [146, 254], Cluster measurements show that the kinetic range magnetic field statistics are non-Gaussian, but at the same time only weakly scale-dependent. Another study of turbulence in the free solar wind [263] reported a similar trend for the density statistics, with values of F comparable to our Cluster results for $\delta b_\parallel$ and $\delta b_\perp$. The MMS interval is less intermittent and the statistics are rather inaccurate due to the very small size of the sample. However, at a few scales, the flatness still appears to be above the the Gaussian value of 3. The simulation data features a steady increase of the flatness with $k_\perp$ at a very similar rate for all three fields, thus indicating a close dynamic correspondence between the density and different components of

the turbulent magnetic field. Unlike in the Cluster measurements, we do not clearly observe a saturation of the flatness, presumably due to the limited size of the 3D kinetic simulation.

7.2.2 Spatial field structure and local wavelet spectra

In the simulation, the turbulent kinetic-scale structures can be visualized and studied directly in real space. In Fig. 7.4 we show the contour plots of the parallel electric current, $J_z = (c/4\pi)(\nabla \times \mathbf{b}_\perp)_z$, and of the parallel vorticity of the electron flow, $\omega_{ez} = (\nabla \times \mathbf{u}_{\perp e})_z$. Note that ω_{ez} is proportional to the perpendicular Laplacian of the density in electron reduced MHD (see Eq. (3.44) in Sec. 3.3.1).[5] We choose to plot the current and the vorticity to better highlight the kinetic-scale structure of the turbulent fields, which is not seen as clearly in the density and magnetic field data, unless the large, energy-containing scales are filtered out. The structures form mostly sheetlike patterns, elongated in the direction of the mean magnetic field. The strong anisotropy is qualitatively consistent with the more quantitative estimates from Fig. 7.2. Interestingly, the most intense small-scale structures in the vorticity are preferentially aligned with the electric current sheets in the field-perpendicular plane. We will come back to this aspect in Sec. 7.3.

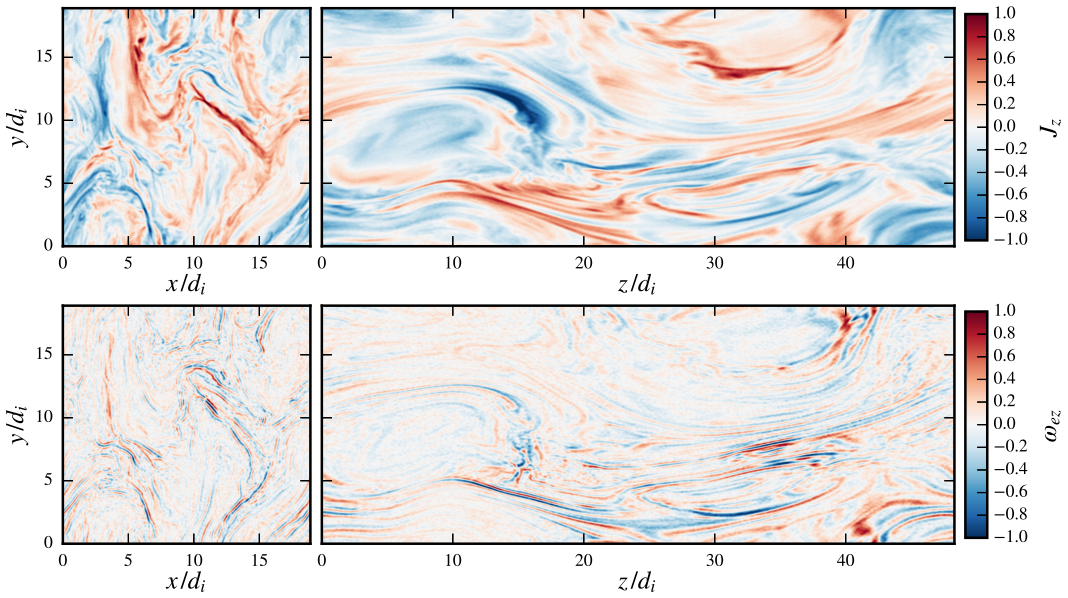

Figure 7.4: 2D contour plots of J_z (top) and of ω_{ez} (bottom), obtained from the 3D driven fully kinetic simulation (units are arbitrary). The left side shows the structures in a given field-perpendicular plane and the right side shows 2D slices along the parallel (z) direction.

Further insight into structure formation can be obtained by visualizing the 2D Morlet wavelet coefficients of δn_e, $\mathbf{b}_\parallel$ and $\mathbf{b}_\perp$. In Figs. 7.5(a)–7.5(c) we show the sub-ion range field

[5] We confirmed that $\nabla_\perp^2 n_e$ has indeed a structure very similar to $\omega_{ez} = (\nabla \times \mathbf{u}_{\perp e})_z$ in our PIC simulation. However, ω_{ez} is somewhat less affected by the particle noise.

structure by summing up the wavelet extracted fluctuations over the range $k_\perp \in [5, 10]d_i$, using 8 scales per octave. We find nearly identical δn_e and $\delta b_\parallel$ patterns, which indicates that the linearized pressure balance (7.9) is indeed satisfied to a good approximation. Even though we allow for the full range of (high-frequency) kinetic physics in the simulation, the natural turbulent dynamics at sub-ion scales appears to be of the low-frequency type. The spatial patterns inferred from scale-filtered fields can be somewhat misleading due to the spurious signal oscillations that may occur as a result of the filtering [347]. To highlight the true spatial variability of the energy density across different scales it is more appropriate to visualize the local wavelet spectra, shown in Figs. 7.5(d)–7.5(i). We find a nonuniform spatial distribution of the local spectral density. Furthermore, the spectral peaks are concentrated around the same spatial locations at different scales. This local correlation across different scales is a typical property of coherent turbulent structures [346, 347, 352]. Although no apparent local relation exists between δn_e and $\delta b_\perp$ according to KAW turbulence theory, their corresponding wavelet spectra suggest a weak local coupling. This points towards the importance of nonlinear effects in shaping the local turbulent fluctuations.

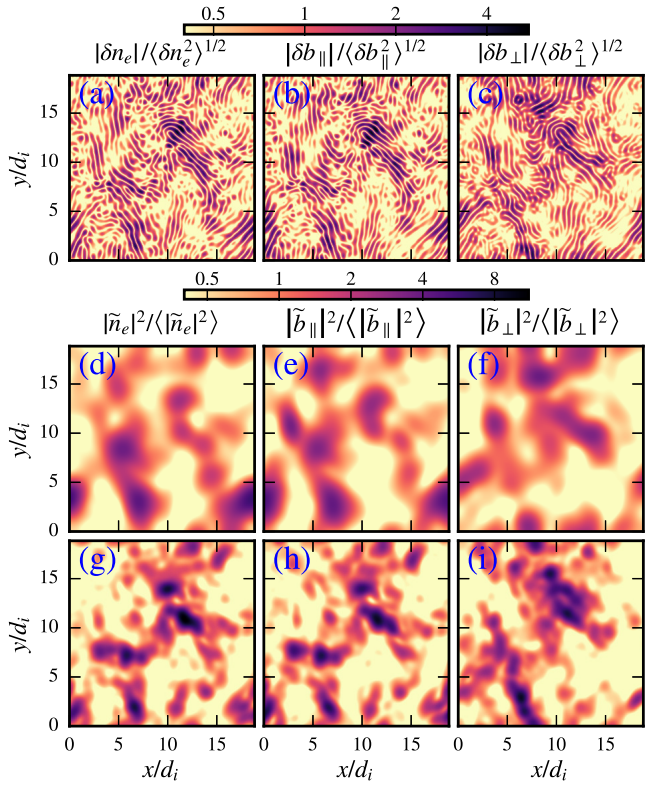

Figure 7.5: Turbulent fluctuations in the range $k_\perp \in [5, 10]d_i$ (a)-(c) and the local wavelet spectra at scales $k_\perp d_i = 5$ (d)-(f) and $k_\perp d_i = 10$ (g)-(i). A logarithmic scale is used and the low-amplitude fluctuations are clipped to the lowest value on the color map to highlight the more intense fluctuations.

7.2.3 Wavelet cross coherence

To further validate the linearized pressure balance (7.9) and the resulting anti-correlation between δn_e and $\delta b_\parallel$, we employ the wavelet cross coherence [247, 346, 355]. Large values of the squared cross coherence close to unity correspond to strong local phase synchronizations between two signals. The results of the cross coherence analysis, applied to MMS data and to a single 1D trace from the simulation, are shown in Fig. 7.6. Arrows on the plot indicate the local phase difference between δn_e and $\delta b_\parallel$. At sub-ion scales, we find a strong anti-correlation, consistent with the linearized pressure balance (7.9), as well as with previous results based on MMS measurements [247, 278].[6]

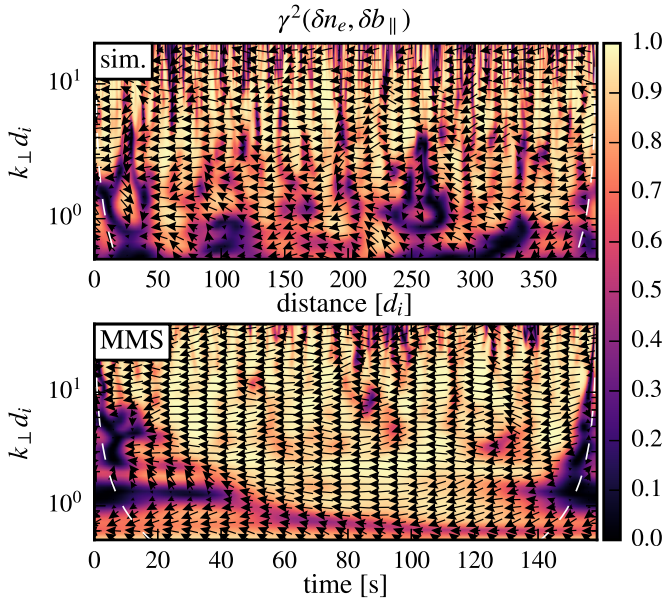

Figure 7.6: Wavelet squared cross coherence between $\delta b_\parallel$ and δn_e from the simulation (a) and MMS data (b). The orientation of the arrows relative to the positive horizontal axis indicates the phase difference. Dashed white lines represent the cone of influence [349].

We also considered the cross coherence between $\delta b_\parallel$ and different components of $\delta b_\perp$ (not shown). The turbulent $\delta b_\parallel$ and $\delta b_\perp$ fields generally do not exhibit a high cross coherence, unlike a single KAW where they are locked into a 90 degree phase difference (see Sec. 3.3.2). However, at the rare times of high coherence we often find a relative phase difference close to 90 degrees (see also Ref. [270]).

[6] At scales around $k_\perp \sim 1/d_i$ of the simulation, a few events notably violate the pressure balance. A possible reason is that the large-scale fluctuations in the simulation may be too large to allow for a linearization of the magnetic pressure around a local mean background.

7.2.4 Spectral field ratios of the large-amplitude structures

Finally, we present the generalized spectral field ratios. The results obtained from the Cluster, MMS, and simulation datasets are shown in Fig. 7.7. In the adopted beta-dependent field normalizations, values close to unity are expected for all the ratios at sub-ion scales, according to the asymptotic linear KAW predictions. In Figs. 7.7(a)–7.7(f) we display the moment ratios (7.3). The conditional ratios (7.4), conditioned on a given LIM threshold, are shown in Figs. 7.7(g)–7.7(l). The standard field ratios are recovered for $m = 2$ in terms of the moments, and for $\xi = 0$ in terms of the conditional averages of the wavelet spectra. As the order m or the threshold ξ is increased, the ratios become progressively more sensitive to the large-amplitude events. Note that "large-amplitude" refers here to the above-average field amplitudes compared to their scale-dependent typical values. In real space, these energetic events are not distributed randomly, but instead form distinct localized patterns (see Fig. 7.5), typically attributed to turbulent structures. The main difference between the moment ratios and the conditional ratios is that the former assign higher statistical weights to large-amplitude events but do not discard the rest, whereas the latter extract the ratios from the most energetic structures only.

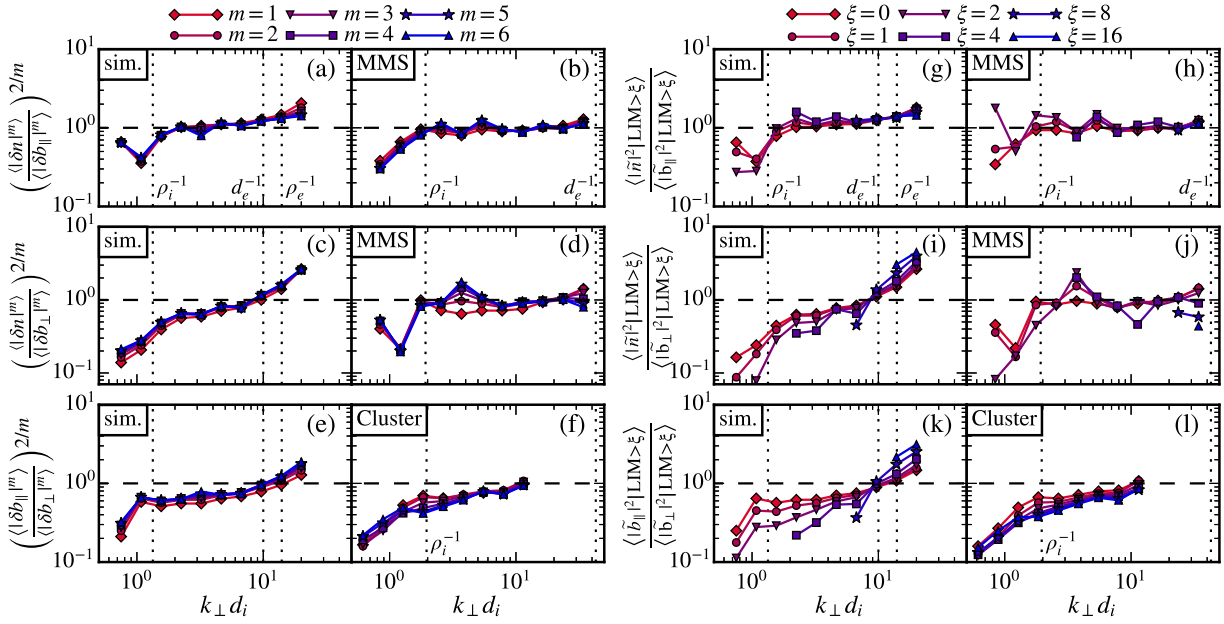

Figure 7.7: Generalized spectral field ratios obtained from the Cluster, MMS, and simulation data (see text for further details). The moment ratios (7.3) are displayed in the left panel and the conditional ratios (7.4) are shown in the right panel. Dashed horizontal lines indicate the asymptotic KAW linear predictions.

At sub-ion scales, we observe that the generalized ratios satisfy the linear KAW predictions to order unity. This is found consistently in the simulation as well as in the observational data, thus indicating a certain robustness of the result. The linear predictions are most accurately satisfied for the generalized spectral ratios of $|\delta n_e|^2$ to $|\delta b_\parallel|^2$ (Fig. 7.7,

top row), which can be interpreted as a direct consequence of the linear pressure balance (7.9), studied in the previous sections. The moment ratios depend only very weakly on the order of the moment m. Thus, the approximate agreement with linear KAW predictions appears to be satisfied not only in terms of "typical" fluctuations but also in the sense higher moments of the distributions. It is also worth noticing that the ratios converge closer towards the KAW predictions below the ion Larmor scale ρ_i rather than below the inertial scale d_i. The latter is as well consistent with the KAW turbulence phenomenology, where ρ_i is considered as the relevant transition scale [5].

Unlike the moment ratios, the conditional ratios reveal a slight tendency of the energetic structures to deviate further from the linear wave predictions.[7] The trend is not seen for the ratios of $|\delta n_e|^2$ to $|\delta b_\parallel|^2$, which are linearly related in real space due to pressure balance. This indicates that the deviations seen for the other two ratios (Figs. 7.7(i)–7.7(l)) may be possibly interpreted as signs of nonlinear effects related to structure formation and intermittency. The latter statement deserves some clarification. The conditional averages of the local wavelet spectra may be also evaluated over the locations with *less* energy than the average on a given scale. In this way, we can study the spectral scalings of the low-amplitude background fluctuations without contributions from turbulent structures. In Fig. 7.8 we compare the magnetic compressibility ratios of the background fluctuations with LIM < 1 against the ratios for the entire ensemble. Similar results are obtained for the electron compressibility (not shown). We find that the background fluctuations satisfy the linear predictions more accurately than the entire population, which includes significant contributions from the turbulent structures. This result suggests that structure formation may be a possible reason for the order unity deviations from linear predictions, often seen in simulations and space observations of plasma turbulence (e.g., [145, 146]). On the other hand, while quantitatively measurable, the overall impact of the structures is relatively moderate and even the large-amplitude fluctuations themselves preserve the linear wave predictions to a certain degree.

7.3 Discussion

Using a set of newly defined diagnostic measures, we have demonstrated that both the background fluctuations as well as the turbulent structures preserve wavelike signatures to order unity. Let us now discuss some of the implications of this result.

First, it seems that all observed features can be reasonably explained in terms of the KAW turbulence phenomenology. Other known phenomenologies, such as whistler wave turbulence [80, 81, 143, 245], cannot explain our results. In particular, whistler turbulence is weakly compressible and of the high-frequency type. As such, it is characterized by only

[7] In the simulation, the degree of apparent deviation is perhaps somewhat misleading because the points that deviate most strongly are energetically not very significant. For example, in Figs. 7.7(i) and 7.7(k) the two outliers with $\xi = 4$ and one with $\xi = 8$ amount to 3.0%, 8.3%, and 2.5% of the scale-dependent kinetic-Alfvén energy, respectively (from the leftmost to the rightmost outlier in the $1/\rho_i < k_\perp < 1/d_e$ range).

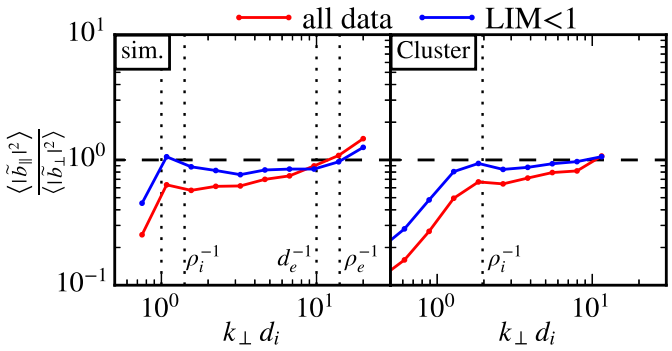

Figure 7.8: Magnetic compressibility ratio of the background fluctuations (LIM < 1) compared to the total population.

minor density fluctuations and it does not satisfy the (linearized) pressure balance, in direct contradiction with our results. In Fig. 7.2 we estimate $k_\parallel d_i < 1$ in the sub-ion range, in which case the whistlers would be also quite strongly damped [59, 145]. Figure 7.2 is also a crucial piece of evidence in general support of a wavelike interpretation. Indeed, at sub-ion scales we estimate $\chi = \tau_\mathrm{L}/\tau_\mathrm{NL} \lesssim 1$, which indicates that the typical KAW time scale is no less significant than the typical nonlinear time scale. Putting aside a large body of observational evidence in support of KAWs in the solar wind (see Podesta [238] for a recent review), one could perhaps suppose that the spectral ratios match the KAW predictions due to some other (yet unknown) property not related to any wave activity. However, this view is inconsistent with our estimates of the nonlinearity parameter χ.

Two key questions that remain to be answered are: (i) How are the structures formed nonlinearly in kinetic range turbulence? (ii) And how is it that a linear wave footprint is apparently preserved in the process? Regarding the former, we note that the structure formation may involve a range of different phenomena, such as nonlinear wave steepening and solitons [356, 357], constructive interference between wave packets [297, 358], or nonlinear wave refraction [353]. Presently, it seems difficult to narrow down the list to a single, mostly likely option. Some observational evidence for solition-like structures exists, but it is presently unclear whether these structures are generated dynamically by the turbulence itself or if they are created by other processes and merely coexist with the turbulence [277, 359]. Judging by our simulation results, the turbulent structures appear to be dynamically evolving on relatively short time scales, unlike solitons. The nonlinear interference between localized wave packets could be a viable explanation. In particular, in Ref. [297] a mechanism for the generation of current sheets in MHD range turbulence via Alfvén wave packet collisions was proposed and later confirmed in gyrokinetic simulations [358]. A direct extension of the model into the sub-ion range is, however, not straightforward, since the KAWs are essentially dispersive, unlike the MHD shear Alfvén waves. Finally, an interesting exposition was given in Refs. [353, 360], where it was argued that coherent structures form naturally in (decaying) KAW turbulence due to nonlinear refraction of KAWs at the locations of strong magnetic shear.

On the latter issue on why the wavelike features can be preserved at all within the turbulent structures, we investigate a more concrete possibility. Following a remark from Boldyrev and Perez [56], we note that the nonlinear term in the electron reduced MHD equation (3.46) for $\partial\psi/\partial t$ can be written as: $[cB_0\beta/(8\pi n_0^2 e)](\hat{\mathbf{e}}_z\times\nabla_\perp\psi)\cdot\nabla_\perp n_e = \mathbf{u}_{\perp e}\cdot\nabla_\perp\psi = \mathbf{u}_{\perp e}\cdot(\mathbf{b}_\perp\times\hat{\mathbf{e}}_z)$. Thus, we see that the flux function ψ is advected in the perpendicular plane with velocity $\mathbf{u}_{\perp e}\propto\nabla_\perp n_e\times\hat{\mathbf{e}}_z$, forcing the gradients of ψ to become aligned with the gradients of n_e [56]. In analogy with MHD turbulence, if $\mathbf{u}_{\perp e}$ ($\nabla_\perp n_e$) and $\mathbf{b}_\perp$ ($\nabla_\perp\psi$) are aligned perfectly, the nonlinearity in the equation for $\partial\psi/\partial t$ vanishes and only the linear term remains. Further borrowing ideas from MHD turbulence, we now investigate the possibility that an effective alignment exists in the kinetic range, in a scale-dependent [206, 212] and intermittent manner [57, 58, 160, 207].[8] To this end, we define a set of alignment angles θ_m as:

$$\sin^m\theta_m = \frac{\langle|\delta\mathbf{u}_{\perp e}\times\delta\mathbf{b}_\perp|^m\rangle}{\langle|\delta\mathbf{u}_{\perp e}|^m|\delta\mathbf{b}_\perp|^m\rangle}, \tag{7.10}$$

where $\delta\mathbf{u}_{\perp e}$ and $\delta\mathbf{b}_\perp$ are the local, scale-dependent fluctuations, and m determines the order of the statistics.[9] In our case, these are wavelet decomposed fields extracted along a given 1D trace. Same as for the generalized ratios, we define the perpendicular field components relative to the local mean field direction. The above definition closely follows Mallet *et al.* [160], where it was used to study intermittent alignment in MHD turbulence. The results are shown in Fig. 7.9. Essentially, we show that a scale-dependent and intermittent alignment exists in our simulation, although the resolved range of scales is too narrow to determine any precise scalings for θ_m.[10] In analogy with MHD turbulence [160, 206, 212], it seems that the turbulent fields in our simulation become progressively more aligned and more intermittent with decreasing scale (see also Fig. 7.3). Moreover, for higher orders m we obtain a stronger alignment at the smallest scales. This indicates that the small-scale turbulent structures are more aligned on average than the rest. That the structures are indeed aligned can be confirmed also visually from Fig. 7.4. Note that we observe here the phenomenon in *driven* kinetic turbulence, and hence, the alignment cannot be interpreted as a dynamic relaxation process [361], but is instead a property of the steady state kinetic range turbulence.

Based on the above result, it may be worth considering the possibility that the kinetic-scale alignment is a significant feature, which helps preserving a KAW-like character of the structures via local depletions of the nonlinearity. The aspect certainly requires

[8] Note that Boldyrev and Perez [56] employ the advection argument to explain the formation of sheetlike structures in KAW turbulence, but they do not explicitly consider nor mention the associated weakening of the nonlinearity or the possibility of a scale-dependent alignment.

[9] In principle, the alignment could be also defined in terms of $\nabla_\perp\psi$ and $\nabla_\perp n_e$, but (7.10) is a bit less sensitive to the particle noise and it also seems more appropriate to use around the transition into the sub-ion range.

[10] We obtain broadly similar results using the more traditional two-point field increments. A more notable difference from the wavelet decomposition is that a stronger alignment for higher m is found at *any* $k_\perp\gtrsim 1/d_i$.

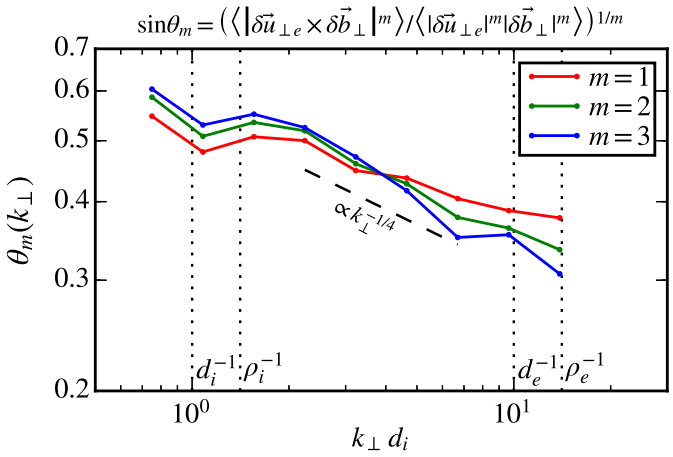

Figure 7.9: Angular alignment measures in 3D kinetic plasma turbulence for different orders m. An MHD-like $-1/4$ slope [206, 212] is shown for reference only.

further investigation before any definitive conclusion can be made, but the possibility seems promising in our opinion. We discussed the depletion of the nonlinearity in Eq. (3.46) for $\partial\psi/\partial t$, but we did not touch upon Eq. (3.45) for $\partial n_e/\partial t$. The nonlinear term for $\partial n_e/\partial t$ depends on ψ only and takes the form: $(c/4\pi)(\hat{\mathbf{e}}_z \times \nabla_\perp\psi)\cdot\nabla_\perp\nabla_\perp^2\psi = \mathbf{b}_\perp\cdot\nabla_\perp J_z$. This is analogous to the nonlinearity in 2D fluid turbulence, where the depletion is a known phenomenon (e.g., [362, 363]). Moreover, a wide class of different solutions may (locally) satisfy $\mathbf{b}_\perp\cdot\nabla_\perp J_z \approx 0$. For sheetlike structures, J_z exhibits the strongest gradients in directions (nearly) transverse to $\mathbf{b}_\perp$, so it seems reasonable to expect that the nonlinearity is weakened also in the equation for $\partial n_e/\partial t$. In MHD turbulence, the alignment has been traditionally discussed in relation to the ideal conservation of the cross-helicity [206], whereas an alternative interpretation has been given more recently [57]. One might wonder what would be a corresponding conserved quantity for the alleged alignment in sub-ion scale turbulence. We would tend to side with the view of Ref. [57] that interprets alignment as an inherent intermittency effect. However, a corresponding ideal conserved quantity would be presumably the cross-correlation $H_{KA} = \langle\delta n_e\psi\rangle$ (see Eq. 3.59).

7.4 Summary

We performed a joint analysis of observational and 3D kinetic simulation data to study the waves and structures emerging at sub-ion scales in turbulent astrophysical plasmas. The simulation results are obtained from a massively parallel, 3D fully kinetic simulation with external turbulence forcing, and the observational data are obtained from *in situ* Cluster and MMS spacecraft measurements. A new set of diagnostic measures was designed to test the wavelike turbulence predictions for the spatially localized, large-amplitude structures.

The kinetic-scale turbulence in the solar wind and in our numerical simulation exhibits non-Gaussian, intermittent statistics, thus indicating the presence of turbulent structures.

These are manifested in the simulation mostly in the form of pressure-balanced sheets extending from ion to electron scales and beyond. By applying the newly defined generalized field ratios to solar wind measurements and to the simulation data, we find that the kinetic-scale structures themselves approximately preserve the linear KAW signatures, although a gradual trend of deviation from the linear predictions is also seen. This quantitative evidence suggests that structures are not immune to wave physics and vice versa. Furthermore, all analyzed properties of the sub-ion scale fluctuations are consistent with the phenomenology of KAW turbulence [4, 5, 59], whereas known alternatives (e.g., whistler turbulence [80, 81, 143, 245]) cannot explain our results. To support our interpretation, we calculate the local spectral anisotropy in the simulation and we explore a previously unknown possibility of dynamic alignment in KAW turbulence. The anisotropy estimates imply a balance between the linear (KAW) and nonlinear turbulence time scales, and the alignment measures suggest that the nonlinearity might be depleted within the structures. The latter phenomenon may be a reason why the nonlinearly generated, large-amplitude structures are able to preserve a linear KAW footprint.

Our study gives credence to an interpretation similar to recent developments in MHD turbulence [58, 159, 297]. Namely, it opens the possibility to describe the sub-ion scale structures within the framework of strong KAW turbulence. We emphasize that we consider here *strong* turbulence, where the nonlinearities cannot be assumed small. Therefore, the structures should not be viewed as waves in a classical sense, but rather in the spirit of critical balance [5, 136, 159, 190], as fully nonlinear entities which preserve a linear KAW signature during their evolution. Finally, our general method of analysis employed here is not exclusively limited to kinetic turbulence in astrophysical plasmas and we hope it might find a range of interesting possibilities in other turbulent systems supporting waves [340]. An immediate extension of the method lends itself in the context of MHD range turbulence, where the generalized field ratios could be used to investigate the impact of structure formation on the so-called Alfvén ratio [32, 345].

Chapter 8

Conclusions

In this Thesis, we carried out a set of massively parallel kinetic simulations to investigate the nature of kinetic-scale turbulence in weakly collisional space and astrophysical plasmas. Stimulated by increasingly accurate *in situ* space observations [32, 41] and by the need for improved models of ion/electron turbulent heating [3, 6, 7, 24, 364], kinetic simulations of astrophysical plasma turbulence gained popularity in recent years [36, 47, 78, 98, 134, 269]. The vast majority of previous studies employed a number of simplifications of the first principles kinetic plasma description, such as reduced two-dimensional geometries [46, 48, 49, 132, 144] and/or various modeling approximations [36, 38, 39, 47, 88]. Here, we focused instead our main effort on three-dimensional (3D), fully kinetic, fully electromagnetic studies without *ad hoc* physical approximations.

The 3D turbulence simulations with fully kinetic ions and electrons, presented in this Thesis, are among the first of their kind in the field. We extensively compare our simulations with existing theories, observational data, and reduced-kinetic models, thus significantly improving confidence in our results and their physical interpretation. In this way, we are able to provide a fresh perspective on some of the ongoing vigorous debates in the community [38, 188, 226, 227], with important implications for plasma turbulence in the observationally accessible solar wind [32]. By inference, our findings could be also relevant to other turbulent astrophysical plasmas, such as the warm interstellar medium [19–21] and hot accretion flows [3, 11, 17, 18]. A more specific account of the main scientific results and accomplishments of this work is provided in the short summary below.

8.1 Summary

Employing massively parallel, first principles kinetic simulations we explicitly addressed the following key open questions:

- Which are most essential physical effects that should be retained in a model to accurately describe different properties and regimes of kinetic-scale turbulence in weakly collisional astrophysical plasmas (Chapter 5)?

- Is critically balanced kinetic Alfvén wave (KAW) turbulence indeed a natural state, considering the full range of possible 3D kinetic and electromagnetic effects at sub-ion scales of low-collisionality plasmas (Chapter 6)?
- What is the relative importance of waves and coherent structures in kinetic, astrophysical plasma turbulence and how are these two seemingly different aspects related (Chapter 7)?

The importance of improving our understanding in these areas has been recognized by numerous experts from the field [32, 53, 188, 277, 314]. For each of our main objectives, we employed a first-of-a-kind approach as explained in the following.

Comparison of kinetic models in collisionless plasma turbulence

In Chapter 5 we presented the first direct comparison of the prominent fully kinetic, gyrokinetic, and hybrid-kinetic models in a turbulent setup, relevant to space and astrophysical plasmas [40]. For a plasma beta and ion-electron temperature ratio both close to unity, the gyrokinetic simulations correctly reproduce the kinetic range turbulent spectra obtained from the fully kinetic description. This explicitly shows that the sub-ion scale turbulent spectra can be explained by gyrokinetics for typical solar wind parameters ($\beta \sim T_i/T_e \sim 1$), at least within the limits of the simplified simulation setup adopted in our comparison. Considering the physical assumptions used in deriving the gyrokinetic model, our results also directly imply that the sub-ion scale turbulent fluctuations are predominantly of the KAW type. In terms of turbulent heating, gyrokinetics reproduces the total heating (i.e., the combined ion and electron internal energy gain) reasonably well, but tends to underestimate the ion-electron heating ratio, if the turbulence fluctuation amplitudes cannot be assumed small. The difference could be possibly attributed to a portion of energy dissipated via stochastic ion heating [147, 148], which is presumably taken up by electron heating in the gyrokinetic approximation. We also highlighted the importance of electron kinetic effects, which give rise to somewhat steeper sub-ion scale spectra, compared to a hybrid-kinetic model with fluid electrons. Finally, all (reduced) models predict similar statistical properties for the scale-dependent magnetic fluctuations, which indicates that the intermittency of the turbulent fields may not be very sensitive to the level of detail included in the kinetic plasma description.

3D fully kinetic study of kinetic Alfvén turbulence

In Chapter 6 we investigated if a critically balanced KAW cascade develops naturally at sub-ion scales, in regimes reminiscent of solar wind turbulence [78]. We addressed this question for the first time using a 3D fully kinetic description, without physical approximations that may artificially favor KAW turbulence. Two decaying turbulence simulations were carried out by initializing a set of counterpropagating, shear Alfvén waves, with wavelengths larger than the ion Larmor radius. By analyzing the spectral properties, we demonstrated the natural development of a sub-ion scale cascade, consistent with theoretical expectations for

KAW turbulence. This result significantly improves confidence in the KAW energy cascade phenomenology [4, 5] and facilitates a certain progress in the theoretical understanding of space and astrophysical plasma turbulence. In addition, we also studied the impact of a non-vanishing mean cross-helicity on kinetic range turbulence, and the particle velocity-space statistics. We showed that a moderate mean cross-helicity, typical for the slow solar wind streams, does not significantly affect the sub-ion scale turbulence properties. Finally, by analyzing the self-consistent ion trajectories and their global velocity distributions, we obtained evidence for both stochastic and resonant Landau heating of ions in KAW turbulence.

Kinetic turbulence in astrophysical plasmas: waves and/or structures?

In Chapter 7 we jointly analyzed kinetic simulation data and a set of *in situ* space plasma turbulence measurements to investigate the interplay between wavelike features and structures, emerging in kinetic-scale plasma turbulence [161]. The simulation data were obtained from a massively parallel, 3D fully kinetic turbulence simulation with external forcing, and the observational data were acquired from high-resolution Cluster [274] and MMS [275] spacecraft measurements. A set of new diagnostic measures was introduced to probe if the large-amplitude turbulent structures exhibit any signatures of wave physics, typically associated with the moderate-amplitude background fluctuations. We observed that the large-amplitude, kinetic-scale structures themselves preserve the KAW signatures to order unity, although some gradual trends of deviation from linear wave predictions are also seen. Based on our results and contrary to a presently common view, we advocate the possibility that wavelike features and structure formation go hand in hand in kinetic-scale astrophysical plasma turbulence. To avoid confusion, we emphasize that the turbulent structures should not be viewed as waves in a casual sense, but instead as fully nonlinear entities that preserve a linear wave signature during their evolution. Finally, we discuss the implications of our results and explore a previously unknown possibility of angular alignment between the perpendicular electron fluid velocity and the magnetic field in KAW turbulence.

8.2 Outlook

3D electromagnetic plasma simulations with fully kinetic ions and electrons are an exciting area with a growing potential. With continuing advances in high-performance computing, it may be anticipated that the range of accessible problems will only increase further and significantly impact the future directions in the field of plasma physics and perhaps across disciplines. A comprehensive account of all the future possibilities would be almost endless. For this reason, let us focus here only on kinetic turbulence in astrophysical plasmas, which is the primary subject of this Thesis.

The key themes for future directions in the field are in our opinion the following:

- How does kinetic plasma turbulence operate across the diverse range of regimes and environments found in astrophysical plasmas?

- How do other prominent astrophysical plasma phenomena, such as particle acceleration and electromagnetic radiation, magnetic reconnection, and kinetic instabilities relate to kinetic plasma turbulence?

In relation to the first theme, it may be argued that many previous studies focused (too) often on a relatively narrow range of regimes, mostly in the desire to mimic "typical" conditions found in the solar wind, where kinetic turbulence is relatively well documented observationally. However, theoretical and observational results suggest that the physical conditions in turbulent astrophysical plasmas are generally highly variable [5, 365], ranging from magnetic to kinetic pressure dominated states, or from non-relativistic to highly-relativistic scenarios. In fact, even the solar wind alone exhibits relatively large variations in plasma parameters [32]. Last but not least, many turbulent plasma environments may be subject to significant background fields not of the magnetic type (e.g., mean velocity shear). These aspects have been largely overlooked in fully kinetic studies until very recently [9, 96, 302, 366].

Let us give a brief example. In low-electron-beta plasmas, a new turbulence regime may exist at scales below the electron inertial scale, recently termed inertial kinetic Alfvén turbulence [247]. Such regime may be particularly relevant to the solor corona and to the Earth's magnetosheath. A theoretical analysis similar to phenomenological treatments of KAW turbulence was given in Ref. [247], where it was argued that KAWs transition into so-called inertial kinetic Alfvén waves (iKAWs) at sub-electron scales. A preliminary study in this parameter range was recently carried out by the author. To this end, a 3D fully kinetic simulation was performed on the Shaheen II supercomputer at the KAUST Supercomputing Laboratory. The turbulence was decaying and the species (initial) beta ratios were $\beta_i = 0.8$ and $\beta_e = 0.06$. The results shown in Fig. 8.1 are indeed indicative of the iKAW regime, but also point out computational challenges specific to the problem. In particular, the simulation exposed a tendency of iKAW turbulence towards quasi-neutrality violation, the degree of which may be exaggerated if the electron plasma to cyclotron frequency ratio falls short of its realistic value (see Ref. [366] for complementary and more in-depth results).[1]

Regarding the second main theme listed above, it was recently recognized that kinetic turbulence may significantly affect and be affected by a range of fundamental plasma processes, such as magnetic reconnection [16, 89, 264], particle acceleration [9], and kinetic instabilities [11, 133]. These aspects are of considerable practical interest for predicting the radiation spectra from astrophysical objects [22], the evolution of ion and electron velocity distribution functions throughout the heliosphere [28], and magnetic field generation by dynamo action in collisionless plasmas [12], to name a few. Most investigations along these lines have been so far conducted with various reduced models, whereas existing 3D

[1] As explained in Chapter 4, realistic values of the ω_{pe}/Ω_{ce} ratio may be in practice extremely difficult to achieve.

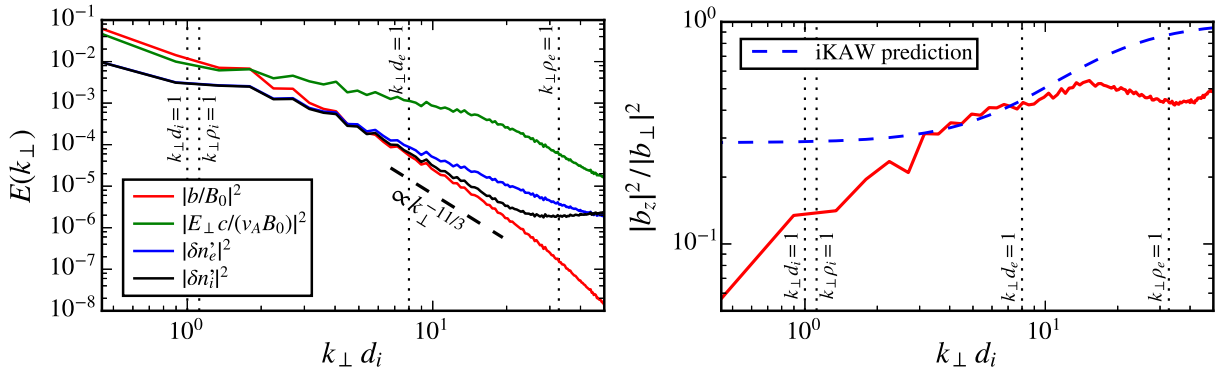

Figure 8.1: Preliminary results on iKAW turbulence. Left: Turbulent spectra of the magnetic and perpendicular electric fields, and of the ion and electron densities. Right: Magnetic compressibility ratio. Dashed lines indicate the iKAW turbulence predictions [247], formally obtained for $1/d_e \ll k_\perp \ll 1/\rho_e$.

fully kinetic studies are only few [9, 89]. We anticipate that first principles, 3D kinetic simulations will enable important breakthroughs in these areas in the future.

Appendix A

An initial condition for decaying 3D turbulence simulations

In this appendix we give a detailed example of an initial condition appropriate for fully kinetic simulations of decaying Alfvénic turbulence. This particular initialization was used for the fully kinetic turbulence simulations presented in Ref. [78] and in Chapter 6. A very similar type of initial condition was originally introduced in the gyrokinetic study by Li *et al.* [87] as a particular 3D formulation of the 2D Orszag-Tang vortex [316]. The formulation introduced in Ref. [87] was further generalized and adapted for fully kinetic PIC simulations by the author.

Due to the large number of possible linear modes supported at kinetic scales it is beneficial to restrict the initial perturbation to wavelengths exceeding the characteristic plasma kinetic scales. In the latter case, the task is considerably simplified since the phenomenology of MHD turbulence may be used to guide the choice of initial condition. An MHD scale initialization has also the advantage that it does not strictly enforce any type of fluctuations at kinetic scales, thus allowing the kinetic turbulence to evolve towards its most natural state. According to the MHD theory, nonlinear interaction occurs only between counterpropagating, perpendicularly polarized Alfvén wave packets. Here we describe an initial condition which takes into account these properties. We assume that the decaying turbulence evolves in a periodic box of size $L_\perp$ and L_z in directions perpendicular and parallel to the mean field $\mathbf{B}_0 = B_0\hat{\mathbf{e}}_z$, respectively. In terms of the perpendicular fluid velocity $\mathbf{u}_\perp = (u_x, u_y)$ and magnetic field $\mathbf{B}_\perp = (B_x, B_y)$, the initial condition can be written as follows:

$$\frac{u_x}{\epsilon v_A} = \cos(k_{\perp,0}y + a)\sin(k_{z,0}z) - \sin(k_{\perp,0}y + b)\cos(k_{z,0}z), \tag{A.1}$$

$$\frac{u_y}{\epsilon v_A} = \sin(k_{\perp,0}x + c)\cos(k_{z,0}z) - \cos(2k_{\perp,0}x + d)\sin(k_{z,0}z), \tag{A.2}$$

$$\frac{B_x}{\epsilon B_0} = \cos(k_{\perp,0}y + b)\sin(k_{z,0}z) - \sin(k_{\perp,0}y + a)\cos(k_{z,0}z), \tag{A.3}$$

$$\frac{B_y}{\epsilon B_0} = \sin(2k_{\perp,0}x + d)\cos(k_{z,0}z) - \cos(k_{\perp,0}x + c)\sin(k_{z,0}z), \tag{A.4}$$

where $k_{\perp,0} = 2\pi/L_\perp$, $k_{z,0} = 2\pi/L_z$, $\epsilon = \delta u_\perp/v_A = \delta B_\perp/B_0$ is the initial turbulence amplitude, and (a, b, c, d) is an arbitrary set of phases. Artificial symmetries in the field configuration can be avoided by choosing a different phase for each mode. The addition of random phases was motivated here by the 2D generalization of the Orszag-Tang vortex by Biskamp and Welter [208]. The 3D formulation of Li *et al.* [87] is obtained for $a = b = c = d = 0$. A self-consistent electric current is specified additionally according to the Ampere's law:

$$\frac{4\pi J_x}{c\epsilon B_0} = k_{z,0}\Big[\cos(k_{\perp,0}x + c)\cos(k_{z,0}z) + \sin(2k_{\perp,0}x + d)\sin(k_{z,0}z)\Big], \tag{A.5}$$

$$\frac{4\pi J_y}{c\epsilon B_0} = k_{z,0}\Big[\cos(k_{\perp,0}y + b)\cos(k_{z,0}z) + \sin(k_{\perp,0}y + a)\sin(k_{z,0}z)\Big], \tag{A.6}$$

$$\frac{4\pi J_z}{c\epsilon B_0} = k_{\perp,0}\Big\{\Big[\sin(k_{\perp,0}x + c) + \sin(k_{\perp,0}y + b)\Big]\sin(k_{z,0}z) \tag{A.7}$$

$$+\Big[2\cos(2k_{\perp,0}x + d) + \cos(k_{\perp,0}y + a)\Big]\cos(k_{z,0}z)\Big\}. \tag{A.8}$$

This can be achieved in a PIC code by locally shifting the ion and electron velocity distributions, such that ion and electron fluid velocities satisfy $\mathbf{u}_i = \mathbf{u}_\perp$ and $\mathbf{u}_e = \mathbf{u}_\perp - \mathbf{J}/(en_0)$. The initialization of a self-consistent current is omitted in many PIC simulations of turbulence in the literature in the hope that the plasma will "self-adjust" to the initial perturbation. While this is true to some degree, it is worth mentioning that this self-adjustment takes place via a rather undesired rapid transient response originating from the displacement current in the Maxwell equations. Finally, note that under the requirement for strong turbulence ϵ is *not* an arbitrary parameter. According to the critical balance conjecture for strong turbulence ($\delta B_\perp/B_0 \approx k_\parallel/k_\perp$), the large-scale fluctuation amplitude is essentially determined by the elongation of the simulation box:

$$\epsilon \approx L_\perp/L_z. \tag{A.9}$$

This is another aspect not always fully appreciated in present literature.

There is nothing special about the above set of expressions other that they satisfy the desired physical properties and that they are straightforward to implement in a PIC code. Many alternative initializations with equivalent physical properties may be specified. The physical interpretation of the above initial condition becomes more obvious by rewriting Eqs. (A.1)–(A.4) in terms of the Elsässer fields $\mathbf{z}^\pm_\perp = \mathbf{u}_\perp \pm \mathbf{b}_\perp$, where $\mathbf{b}_\perp = (v_A/B_0)\mathbf{B}_\perp$, as:

$$\frac{z^\pm_x}{\epsilon v_A} = \mp\sin(k_{\perp,0}y \mp k_{z,0}z + a) - \sin(k_{\perp,0}y \mp k_{z,0}z + b), \tag{A.10}$$

$$\frac{z^\pm_y}{\epsilon v_A} = \sin(k_{\perp,0}x \mp k_{z,0}z + c) \pm \sin(2k_{\perp,0}x \mp k_{z,0}z + d). \tag{A.11}$$

This evidently corresponds to counterpropagating, shear Alfvén waves with wavenumbers $(k_{\perp,0}, 0, \pm k_{z,0})$, $(0, k_{\perp,0}, \pm k_{z,0})$, and $(2k_{\perp,0}, 0, \pm k_{z,0})$. The mean normalized cross-helicity σ_c

(see Sec. 3.2) can be obtained analytically as

$$\sigma_c = \frac{\langle |\mathbf{z}_\perp^+|^2 - |\mathbf{z}_\perp^-|^2 \rangle}{\langle |\mathbf{z}_\perp^+|^2 + |\mathbf{z}_\perp^-|^2 \rangle} = \frac{2\langle \mathbf{u}_\perp \cdot \mathbf{b}_\perp \rangle}{\langle |\mathbf{u}_\perp|^2 + |\mathbf{b}_\perp|^2 \rangle} = \frac{1}{2}\cos(a-b). \tag{A.12}$$

Thus, the initial condition may be used to study balanced ($\sigma_c \approx 0$) as well as moderately imbalanced ($|\sigma_c| \approx 1/2$) regimes with an appropriate choice of the phases. The nonlinear interaction is maximized for $\sigma_c = 0$.

Appendix B

External turbulence forcing implementation in OSIRIS

In this appendix we describe a variant of the so-called Langevin antenna [305], which was recently implemented in the OSIRIS code by the author of this Thesis. The antenna implementation was then utilized for the 3D fully kinetic simulation presented in Ref. [161] and in Chapter 7. Because the Langevina antenna scheme was originally developed in the context of gyrokinetics, a few minor modifications are necessary to adapt the method for the fully kinetic, electromagnetic model. For the model-specific modifications, we mainly follow the recent work by Zhdankin *et al.* [9], with a few additions of our own.

The Langevin antenna is implemented as an external, time-varying electric current $\mathbf{J}_{\text{ext}}$ in the Maxwell equation for the time change of the electric field:

$$\frac{\partial \mathbf{E}}{\partial t} = c\nabla \times \mathbf{B} - 4\pi(\mathbf{J} + \mathbf{J}_{\text{ext}}). \tag{B.1}$$

Magnetic field fluctuations are induced only indirectly through the electric field response to the external current. However, since we are interested in the low-frequency regime, the external current may be associated with an external magnetic field via $\mathbf{J}_{\text{ext}} = (c/4\pi)\nabla \times \mathbf{B}_{\text{ext}}$. In the following, we describe the evolution of the antenna in terms of $\mathbf{B}_{\text{ext}}$ even though it is actually the external current, and not the external magnetic field, that is incorporated into the final equations.

We consider a set of perpendicularly polarized modes with complex amplitudes $\{b_{n,\mathbf{k}}\}$ at time step n in the simulation. The magnetic field corresponding to the antenna current may be written as

$$\mathbf{B}_{\text{ext}}(\mathbf{r}) = \frac{1}{\sqrt{N}} \sum_{\mathbf{k}} \text{Re}\left\{ \frac{\mathbf{k}_\perp \times \hat{\mathbf{e}}_z}{k_\perp} b_{n,\mathbf{k}} \exp(\text{i}\,\mathbf{k}\cdot\mathbf{r}) \right\}, \tag{B.2}$$

where $\mathbf{k}_\perp = (k_x, k_y)$, the mean field $\mathbf{B}_0 = B_0\hat{\mathbf{e}}_z$ is in the z direction, the sum runs over all the N forced modes, and $\text{Re}\{\dots\}$ is the real part.[1] In practice, one should keep in mind

[1]The actual implementation does not include the $1/\sqrt{N}$ normalization for the amplitude. The desired antenna amplitude should be therefore divided by $\sqrt{N}$ in the code input file.

that the numerical (Yee) grid is staggered [62, 63] so that different components of $\mathbf{B}_{\text{ext}}$ should be evaluated at different spatial locations, displaced by half a grid cell relative to each other. The $\mathbf{B}_{\text{ext}}$ update also needs to include a sufficient number of so-called ghost cells in each spatial direction and on each MPI [303] compute node. The complex amplitude of each forced mode evolves according to a discretized Langevin type equation [305]:

$$b_{0,\mathbf{k}} = \delta B_0 \exp(\mathrm{i}\varphi_{\mathbf{k}}), \tag{B.3}$$

$$C_{n+1} = 1 + \Delta t r\Big(\delta\overline{B} - \delta B_n\Big)/\delta\overline{B}, \tag{B.4}$$

$$\delta B_{n+1} = C_{n+1}\delta B_n, \tag{B.5}$$

$$b_{n+1,\mathbf{k}} = C_{n+1} b_{n,\mathbf{k}} \exp\Big(-(\mathrm{i}\omega_0 + \gamma_0)\Delta t\Big) + \delta B_{n+1}\sqrt{12\gamma_0\Delta t}\, u_{n,\mathbf{k}}, \tag{B.6}$$

where Δt is the simulation time step, $u_{n,\mathbf{k}}$ is a random number with real and imaginary parts between -1/2 and 1/2, ω_0 is the antenna frequency, γ_0 is the decorrelation rate, $\varphi_{\mathbf{k}}$ is an initial random phase, and δB_n is the instantaneous mean amplitude, which smoothly evolves towards the mean target amplitude $\delta\overline{B}$ at a growth rate r. The smooth transition towards the target amplitude $\delta\overline{B}$ is an optional feature not present in the original version by TenBarge *et al.* [305]. It may be used to smoothly adjust the mean amplitude during runtime and/or to smoothly increase the amplitude from $t = 0$ towards the maximal target value. By choosing $\delta B_0 = \delta\overline{B}$, the mean amplitude is kept constant, unless adjusted during runtime. The choice $\delta B_0 = \delta\overline{B}$ is usually the preferred setting.

At each time step, the external current is calculated as $\mathbf{J}_{\text{ext}} = (c/4\pi)\nabla \times \mathbf{B}_{\text{ext}}$ and added to the self-consistent plasma current $\mathbf{J}$. This operation is performed right after the deposit of the self-consistent plasma current and before the advance of the Maxwell equations. During initialization at $t = 0$, we set $\mathbf{B}(t = 0) = \mathbf{B}_0 + \mathbf{B}_{\text{ext}}$ in order to avoid a strong transient response to the external current in Eq. (B.1). At later times, however, the self-consistent field $\mathbf{B}$ evolves freely according to the Maxwell equations, supplemented with $\mathbf{J}_{\text{ext}}$. The $\nabla \times \mathbf{B}_{\text{ext}}$ term is calculated using the same finite difference numerical derivatives as for the rest of the integration scheme. This assures the $\mathbf{J}_{\text{ext}}$ is (numerically) divergence free to machine precision. Once the internal and external currents have been combined, the complex amplitudes and the external field are updated according to (B.2)–(B.6). The new complex amplitudes $\{b_{n+1,\mathbf{k}}\}$ are calculated on a single MPI node and distributed to all the other nodes using the MPI interface.

Whenever using the antenna, a particular choice of the forced wavenumbers and of the antenna parameters ω_0, γ_0, and $\delta\overline{B}$ (as well as the optional r and δB_0) is necessary. Some general guidelines for choosing the antenna parameters are given in TenBarge *et al.* [305]. To prevent the kinetic-scale turbulence from being directly affected by the antenna, it is best to restrict the forcing to large scales exceeding the kinetic scales of the plasma. In our particular implementation, the forcing is restricted to $N = 8$ different wave vectors: $(1, 0, \pm 1)$, $(0, 1, \pm 1)$, $(-1, 0, \pm 1)$, and $(0, -1, \pm 1)$ in units of $(2\pi/L_x, 2\pi/L_y, 2\pi/L_z)$. Note that only one half of the forced modes is evolved according to (B.6). The other half is calculated based on the reality condition: $b_{-\mathbf{k}} = b^*_{\mathbf{k}}$. If the box dimensions (L_x, L_y, L_z) exceed the plasma kinetic scales, the antenna frequency and decorrelation rate may be

chosen as a fraction of the shear Alfvén wave frequency: $\omega_A = v_A k_z$, where v_A is the Alfvén speed. In the latter case the antenna mimics the turbulent, MHD scale energy transfer from scales larger than the simulation box [305]. Some typical values used in a production run would be $\omega_0 \approx 0.9 \cdot (2\pi v_A/L_z)$ and $\gamma_0 \approx 0.6 \cdot \omega_0$.[2] The choice of the mean antenna amplitude is a somewhat more delicate task. A rough estimate may be obtained from the critical balance conjecture [136] for strong turbulence:

$$\delta\overline{B} \approx B_0 L_\perp / L_z. \tag{B.7}$$

However, the external input from the antenna is in practice combined with the nonlinear response of the plasma to produce a total fluctuation amplitude exceeding the antenna mean target amplitude. The estimate (B.7) is therefore more of an upper bound. Empirically, in the author's experience, amplitudes of about $\delta\overline{B} \approx (1/2) \cdot B_0 L_\perp / L_z$ are usually sufficient to achieve critical balance ($k_\parallel/k_\perp \approx \delta B/B_0$) at the box scale. The mean target amplitude may be additionally smoothly tuned during runtime in order to match the critical balance condition more closely. Finally, note that the (complex) amplitudes of individual modes contain a rather large random component (second term in Eq. (B.6)) and the total external power input is relatively unsteady, whenever the decorrelation rate γ_0 is comparable to ω_0. Various extensions of the scheme could be possibly developed in the future to make the power input more steady. One possibility worth exploring would be to employ a similar procedure as for Navier-Stokes forced turbulence [367] and eliminate the correlation between the external (random) force and the turbulent (self-consistent) fields. This would amount to initializing the random part of the external current $\widetilde{\mathbf{J}}_{\text{ext}}$ (the one due to the second term in Eq. (B.6)) at each step and for each $\mathbf{k}$ under the constraint $\widetilde{\mathbf{J}}_{\text{ext},\mathbf{k}} \cdot \mathbf{E}^*_{\mathbf{k}} = 0$, where $\mathbf{E}$ is the self-consistent electric field. In that case the instantaneous correlation between $\widetilde{\mathbf{J}}_{\text{ext}}$ and $\mathbf{E}$ would be eliminated and the external power input would be likely more steady.

[2] If one desires to adjust the mean amplitude during runtime, a growth rate r satisfying $\omega_0 \ll r \ll \omega_{pe}$, where ω_{pe} is the plasma frequency, is recommended.

Appendix C

List of plasma parameters

A weakly collisional, magnetized plasma is characterized by several kinetic scales and parameters, which critically impact the nature of the kinetic turbulence. The interplay between different plasma parameters is essential for the design of fully kinetic simulations with explicit PIC codes, which need to resolve all the characteristic plasma scales. Many of these parameters are referenced throughout this Thesis. In this Appendix, we provide for clarity their definitions. As in the rest of the Thesis, we use Gaussian units and we neglect any relativistic corrections in the parameter definitions.

In Table C.1 we list the physical quantities used in the definitions of the parameters. Out of these quantities, we may define several characteristic plasma scales, all of which emerge naturally from the physical processes involved. The characteristic frequencies are:

$$\omega_{ps} = \sqrt{\frac{4\pi q_s^2 n_0}{m_s}}, \qquad \Omega_{cs} = \frac{q_s B_0}{m_s c}, \tag{C.1}$$

where ω_{ps} is the species plasma frequency and Ω_{cs} is the species cyclotron frequency. Next, the typical velocities are:

$$v_{\mathrm{th},s} = \sqrt{\frac{2T_{0s}}{m_s}}, \qquad v_A = \frac{B_0}{\sqrt{4\pi n_0 m_i}}, \tag{C.2}$$

where $v_{\mathrm{th},s}$ is the species thermal velocity and v_A is the Alfvén wave speed. Above, the kinetic temperature T_{0s} is defined as

$$T_{0s} = \left\langle \frac{m_s}{3n_s} \int (\mathbf{v} - \mathbf{u}_s)^2 f_s \, \mathrm{d}^3\mathbf{v} \right\rangle,$$

where f_s is the particle distribution function, $\mathbf{u}_s$ is the species fluid velocity, n_s is the species density, and $\langle \cdots \rangle$ denotes a space average. Finally, the characteristic kinetic length scales in a plasma are:

$$\lambda_D = \sqrt{\frac{T_{0e}}{4\pi n_0 e^2}} = \frac{v_{\mathrm{th},e}}{\sqrt{2}\,\omega_{pe}}, \qquad d_s = \frac{c}{\omega_{ps}}, \qquad \rho_s = \frac{v_{\mathrm{th},s}}{\Omega_{cs}}, \tag{C.3}$$

Symbol	Quantity
c	speed of light
e	elementary charge
q_s	species charge
m_s	species mass
T_{0s}	species mean temperature
n_0	mean number density
B_0	magnitude of mean magnetic field

Table C.1: List of quantities used in the definitions of the plasma parameters. The subscript $s \in \{i, e\}$ is the species index.

where λ_D is the Debye shielding distance, d_s is the species inertial scale or skin depth, and ρ_s is the species thermal gyroradius.

The gross plasma features are mainly determined by various dimensionless parameters, constructed from the typical plasma scales. Below, we define the dimensionless parameters as the ratios of global, space-averaged quantities. Alternatively, the ratios may be also computed first locally and averaged later. A key parameter is the species beta:

$$\beta_s = \frac{8\pi n_0 T_{0s}}{B_0^2} = \left(\frac{\omega_{ps}}{\Omega_{cs}}\right)^2 \left(\frac{v_{\mathrm{th},s}}{c}\right)^2 = \left(\frac{\rho_s}{d_s}\right)^2, \tag{C.4}$$

which gives the ratio of the kinetic to magnetic pressure. Essentially, the plasma beta determines the scale separation between the species inertial and gyroradius scale. The ion and electron betas separately obey the following relations:

$$\beta_i = \frac{v_{\mathrm{th},i}^2}{v_A^2}, \qquad \beta_e = \frac{m_e}{m_i}\frac{v_{\mathrm{th},e}^2}{v_A^2}. \tag{C.5}$$

Another important set of parameters are:

$$\frac{\omega_{pe}}{\Omega_{ce}} = \frac{\rho_e}{\sqrt{2}\,\lambda_D}, \qquad \frac{c}{v_{\mathrm{th},e}} = \frac{d_e}{\sqrt{2}\,\lambda_D}. \tag{C.6}$$

For the plasma to remain non-relativistic and quasi-neutral at electron kinetic scales, the above ratios should be (reasonably) large. It is also useful to recall that the separation between the ion and electron scales is set by the square root of the mass ratio. Finally, the collisionality is controlled by the so-called plasma parameter:

$$\Lambda = 4\pi n_0 \lambda_D^3 = \frac{1}{\sqrt{4\pi}} \left(\frac{n_0^{-1/3}}{e^2 T_{0e}^{-1}}\right)^{3/2}, \tag{C.7}$$

which has to be very large for collisions to be weak.

Bibliography

[1] J. A. Krommes, "Fundamental Statistical Descriptions of Plasma Turbulence in Magnetic Fields," Phys. Rep. **360**, 1 (2002).

[2] A. A. Schekochihin and S. C. Cowley, "Turbulence and Magnetic Fields in Astrophysical Plasmas," in *Magnetohydrodynamics: Historical Evolution and Trends*, edited by S. Molokov, R. Moreau, and H. K. Moffatt (Springer, Dordrecht, 2007) pp. 85–115.

[3] E. Quataert and A. Gruzinov, "Turbulence and Particle Heating in Advection-Dominated Accretion Flows," Astrophys. J. **520**, 248 (1999).

[4] G. G. Howes, S. C. Cowley, W. Dorland, G. W. Hammett, E. Quataert, and A. A. Schekochihin, "A Model of Turbulence in Magnetized Plasmas: Implications for the Dissipation Range in the Solar Wind," J. Geophys. Res. **113**, A05103 (2008).

[5] A. A. Schekochihin, S. C. Cowley, W. Dorland, G. W. Hammett, G. G. Howes, E. Quataert, and T. Tatsuno, "Astrophysical Gyrokinetics: Kinetic and Fluid Turbulent Cascades in Magnetized Weakly Collisional Plasmas," Astrophys. J. Suppl. Ser. **182**, 310 (2009).

[6] G. G. Howes, "A Prescription for the Turbulent Heating of Astrophysical Plasmas," Mon. Not. R. Astron. Soc. **409**, L104 (2010).

[7] B. D. G. Chandran, T. J. Dennis, E. Quataert, and S. D. Bale, "Incorporating Kinetic Physics into a Two-Fluid Solar-Wind Model with Temperature Anisotropy and Low-Frequency Alfvén-Wave Turbulence," Astrophys. J. **743**, 197 (2011).

[8] I. Zhuravleva, E. Churazov, A. A. Schekochihin, S. W. Allen, P. Arévalo, A. C. Fabian, W. R. Forman, J. S. Sanders, A. Simionescu, R. Sunyaev, A. Vikhlinin, and N. Werner, "Turbulent Heating in Galaxy Clusters Brightest in X-Rays," Nature (London) **515**, 85 (2014).

[9] V. Zhdankin, G. R. Werner, D. A. Uzdensky, and M. C. Begelman, "Kinetic Turbulence in Relativistic Plasma: From Thermal Bath to Nonthermal Continuum," Phys. Rev. Lett. **118**, 055103 (2017).

[10] R. Kulsrud and E. G. Zweibel, "On the Origin of Cosmic Magnetic Fields," Rep. Prog. Phys. **71**, 046901 (2008).

[11] M. W. Kunz, J. M. Stone, and E. Quataert, "Magnetorotational Turbulence and Dynamo in a Collisionless Plasma," Phys. Rev. Lett. **117**, 235101 (2016).

[12] F. Rincon, F. Califano, A. A. Schekochihin, and F. Valentini, "Turbulent Dynamo in a Collisionless Plasma," Proc. Natl. Acad. Sci. USA **113**, 3950 (2016).

[13] W. H. Matthaeus and S. L. Lamkin, "Turbulent Magnetic Reconnection," Phys. Fluids **29**, 2513 (1986).

[14] A. Lazarian and E. T. Vishniac, "Reconnection in a Weakly Stochastic Field," Astrophys. J. **517**, 700 (1999).

[15] S. Boldyrev and N. F. Loureiro, "Magnetohydrodynamic Turbulence Mediated by Reconnection," Astrophys. J. **844**, 125 (2017).

[16] N. F. Loureiro and S. Boldyrev, "Collisionless Reconnection in Magnetohydrodynamic and Kinetic Turbulence," Astrophys. J. **850**, 182 (2017).

[17] F. Yuan and R. Narayan, "Hot Accretion Flows Around Black Holes," Annu. Rev. Astron. Astrophys. **52**, 529 (2014).

[18] Y. Kawazura, M. Barnes, and A. A. Schekochihin, "Thermal Disequilibration of Ions and Electrons by Collisionless Plasma Turbulence," arXiv:1807.07702.

[19] B. G. Elmegreen and J. Scalo, "Interstellar Turbulence I: Observations and Processes," Annu. Rev. Astron. Astrophys. **42**, 211 (2004).

[20] M. Haverkorn and S. R. Spangler, "Plasma Diagnostics of the Interstellar Medium with Radio Astronomy," Space Sci. Rev. **178**, 483 (2013).

[21] B. M. Gaensler, M. Haverkorn, B. Burkhart, K. J. Newton-McGee, R. D. Ekers, A. Lazarian, N. M. McClure-Griffiths, T. Robishaw, J. M. Dickey, and A. J. Green, "Low-Mach-Number Turbulence in Interstellar Gas Revealed by Radio Polarization Gradient," Nature (London) **478**, 214 (2011).

[22] D. A. Uzdensky, "Relativistic Turbulence with Strong Synchrotron and Synchrotron Self-Compton Cooling," Mon. Not. R. Astron. Soc. **477**, 2849 (2018).

[23] R. Bühler and R. Blandford, "The Surprising Crab Pulsar and its Nebula: A Review," Rep. Prog. Phys. **77**, 066901 (2014).

[24] R. Bruno and V. Carbone, "The Solar Wind as a Turbulence Laboratory," Living Rev. Solar Phys. **10**, 2 (2013).

[25] N. Meyer-Vernet, *Basics of the Solar Wind* (Cambridge University Press, Cambridge, 2007).

[26] E. N. Parker, "Dynamics of the Interplanetary Gas and Magnetic Fields," Astrophys. J. **128**, 664 (1958).

[27] O. Alexandrova, J. Saur, C. Lacombe, A. Mangeney, J. Mitchell, S. J. Schwartz, and P. Robert, "Universality of Solar-Wind Turbulent Spectrum from MHD to Electron Scales," Phys. Rev. Lett. **103**, 165003 (2009).

[28] E. Marsch, "Kinetic Physics of the Solar Corona and Solar Wind," Living Rev. Solar Phys. **3**, 1 (2006).

[29] E. N. Parker, "Dynamical Theory of the Solar Wind," Space Sci. Rev. **4**, 666 (1965).

[30] J. D. Richardson and C. W. Smith, "The Radial Temperature Profile of the Solar Wind," Geophys. Res. Lett. **30**, 1206 (2003).

[31] P. J. Coleman Jr., "Turbulence, Viscosity, and Dissipation in the Solar-Wind Plasma," Astrophys. J. **153**, 371 (1968).

[32] C. H. K. Chen, "Recent Progress in Astrophysical Plasma Turbulence from Solar Wind Observations," J. Plasma Phys. **82**, 535820602 (2016).

[33] K. H. Kiyani, K. T. Osman, and S. Chapman, "Dissipation and Heating in Solar Wind Turbulence: From the Macro to the Micro and Back Again," Phil. Trans. R. Soc. A **373**, 20140155 (2015).

[34] G. I. Taylor, "The Spectrum of Turbulence," Proc. R. Soc. A **164**, 476 (1938).

[35] G. G. Howes, K. G. Klein, and J. M. TenBarge, "Validity of the Taylor Hypothesis for Linear Kinetic Waves in the Weakly Collisional Solar Wind," Astrophys. J. **789**, 106 (2014).

[36] G. G. Howes, J. M. TenBarge, W. Dorland, E. Quataert, A. A. Schekochihin, R. Numata, and T. Tatsuno, "Gyrokinetic Simulations of Solar Wind Turbulence from Ion to Electron Scales," Phys. Rev. Lett. **107**, 035004 (2011).

[37] P. Wu, S. Perri, K. Osman, M. Wan, W. H. Matthaeus, M. A. Shay, M. L. Goldstein, H. Karimabadi, and S. Chapman, "Intermittent Heating in Solar Wind and Kinetic Simulations," Astrophys. J. Lett. **763**, L30 (2013).

[38] S. Servidio, F. Valentini, D. Perrone, A. Greco, F. Califano, W. H. Matthaeus, and P. Veltri, "A Kinetic Model of Plasma Turbulence," J. Plasma Phys. **81**, 325810107 (2015).

[39] D. Told, F. Jenko, J. M. TenBarge, G. G. Howes, and G. W. Hammett, "Multiscale Nature of the Dissipation Range in Gyrokinetic Simulations of Alfvénic Turbulence," Phys. Rev. Lett. **115**, 025003 (2015).

[40] D. Grošelj, S. S. Cerri, A. Bañón Navarro, C. Willmott, D. Told, N. F. Loureiro, F. Califano, and F. Jenko, "Fully Kinetic versus Reduced-Kinetic Modeling of Collisionless Plasma Turbulence," Astrophys. J. **847**, 28 (2017).

[41] O. Alexandrova, C. H. K. Chen, L. Sorriso-Valvo, T. S. Horbury, and S. D. Bale, "Solar Wind Turbulence and the Role of Ion Instabilities," Space Sci. Rev. **178**, 101 (2013).

[42] G. G. Howes, W. Dorland, S. C. Cowley, G. W. Hammett, E. Quataert, A. A. Schekochihin, and T. Tatsuno, "Kinetic Simulations of Magnetized Turbulence in Astrophysical Plasmas," Phys. Rev. Lett. **100**, 065004 (2008).

[43] J. M. TenBarge, G. G. Howes, and W. Dorland, "Collisionless Damping at Electron Scales in Solar Wind Turbulence," Astrophys. J. **774**, 139 (2013).

[44] D. Winske, L. Yin, N. Omidi, H. Karimabadi, and K. Quest, "Hybrid Simulation Codes: Past, Present and Future—A Tutorial," in *Space Plasma Simulation*, edited by J. Büchner, M. Scholer, and C. T. Dum (Springer, Berlin, Heidelberg, 2003) pp. 136–165.

[45] M. W. Kunz, J. M. Stone, and X.-N. Bai, "Pegasus: A New Hybrid-Kinetic Particle-in-Cell Code for Astrophysical Plasma Dynamics," J. Comput. Phys. **259**, 154 (2014).

[46] L. Franci, S. Landi, L. Matteini, A. Verdini, and P. Hellinger, "High-Resolution Hybrid Simulations of Kinetic Plasma Turbulence at Proton Scales," Astrophys. J. **812**, 21 (2015).

[47] S. S. Cerri, S. Servidio, and F. Califano, "Kinetic Cascade in Solar-Wind Turbulence: 3D3V Hybrid-Kinetic Simulations with Electron Inertia," Astrophys. J. Lett. **846**, L18 (2017).

[48] M. Wan, W. H. Matthaeus, H. Karimabadi, V. Roytershteyn, M. Shay, P. Wu, W. Daughton, B. Loring, and S. C. Chapman, "Intermittent Dissipation at Kinetic Scales in Collisionless Plasma Turbulence," Phys. Rev. Lett. **109**, 195001 (2012).

[49] C. T. Haynes, D. Burgess, and E. Camporeale, "Reconnection and Electron Temperature Anisotropy in Sub-Proton Scale Plasma Turbulence," Astrophys. J. **783**, 38 (2014).

[50] W. H. Matthaeus, S. Servidio, and P. Dmitruk, "Comment on *Kinetic Simulations of Magnetized Turbulence in Astrophysical Plasmas*," Phys. Rev. Lett. **101**, 149501 (2008).

[51] G. G. Howes, "The Inherently Three-Dimensional Nature of Magnetized Plasma Turbulence," J. Plasma Phys. **81**, 325810203 (2015).

[52] D. Told, J. Cookmeyer, F. Muller, P. Astfalk, and F. Jenko, "Comparative Study of Gyrokinetic, Hybrid-Kinetic and Fully Kinetic Wave Physics for Space Plasmas," New J. Phys. **18**, 065011 (2016).

[53] W. H. Matthaeus, M. Wan, S. Servidio, A. Greco, K. T. Osman, S. Oughton, and P. Dmitruk, "Intermittency, Nonlinear Dynamics and Dissipation in the Solar Wind and Astrophysical Plasmas," Phil. Trans. R. Soc. A **373**, 20140154 (2015).

[54] K. G. Klein, G. G. Howes, and J. M. TenBarge, "Diagnosing Collisionless Energy Transfer using Field-Particle Correlations: Gyrokinetic Turbulence," J. Plasma Phys. **83**, 535830401 (2017).

[55] A. Mallet, K. G. Klein, B. D. G. Chandran, D. Grošelj, I. W. Hoppock, T. A. Bowen, C. S. Salem, and S. D. Bale, "Interplay Between Intermittency and Dissipation in Collisionless Plasma Turbulence," arXiv:1807.09301.

[56] S. Boldyrev and J. C. Perez, "Spectrum of Kinetic-Alfvén Turbulence," Astrophys. J. Lett. **758**, L44 (2012).

[57] B. D. G. Chandran, A. A. Schekochihin, and A. Mallet, "Intermittency and Alignment in Strong RMHD Turbulence," Astrophys. J. **807**, 39 (2015).

[58] A. Mallet and A. A. Schekochihin, "A Statistical Model of Three-Dimensional Anisotropy and Intermittency in Strong Alfvénic Turbulence," Mon. Not. R. Astron. Soc. **466**, 3918 (2017).

[59] S. Boldyrev, K. Horaites, Q. Xia, and J. C. Perez, "Toward a Theory of Astrophysical Plasma Turbulence at Subproton Scales," Astrophys. J. **777**, 41 (2013).

[60] R. A. Fonseca, L. O. Silva, F. S. Tsung, V. K. Decyk, W. Lu, C. Ren, W. B. Mori, S. Deng, S. Lee, T. Katsouleas, and J. C. Adam, "OSIRIS: A Three-Dimensional, Fully Relativistic Particle in Cell Code for Modeling Plasma Based Accelerators," Lecture Notes in Comput. Sci. **2331**, 342 (2002).

[61] R. A. Fonseca, J. Vieira, F. Fiuza, A. Davidson, F. S. Tsung, W. B. Mori, and L. O. Silva, "Exploiting Multi-Scale Parallelism for Large Scale Numerical Modelling of Laser Wakefield Accelerators," Plasma Phys. Control. Fusion **55**, 124011 (2013).

[62] J. M. Dawson, "Particle Simulation of Plasmas," Rev. Mod. Phys. **55**, 403 (1983).

[63] C. K. Birdsall and A. B. Langdon, *Plasma Physics via Computer Simulation* (Taylor & Francis Group, New York, 2005).

[64] Y. L. Klimontovich, *The Statistical Theory of Non-Equilibrium Processes in a Plasma* (MIT Press, Cambridge, Mass., 1967).

[65] R. L. Liboff, *Kinetic Theory: Classical, Quantum, and Relativistic Descriptions*, 3rd ed. (Springer, New York, 2003).

[66] T. J. M. Boyd and J. J. Sanderson, *The Physics of Plasmas* (Cambridge University Press, Cambridge, 2003).

[67] G. Lapenta, "Particle Simulations of Space Weather," J. Comput. Phys. **231**, 795 (2012).

[68] M. Melzani, C. Winisdoerffer, R. Walder, D. Folini, J. M. Favre, S. Krastanov, and P. Messmer, "Apar-T: Code, Validation, and Physical Interpretation of Particle-in-Cell Results," Astron. Astrophys. **558**, A133 (2013).

[69] G. L. Eyink, "Cascades and Dissipative Anomalies in Nearly Collisionless Plasma Turbulence," Phys. Rev. X **8**, 041020 (2018).

[70] Y. L. Klimontovich, "Physics of Collisionless Plasma," Phys.-Usp. **40**, 21 (1997).

[71] P. H. Yoon, L. F. Ziebell, E. P. Kontar, and R. Schlickeiser, "Weak Turbulence Theory for Collisional Plasmas," Phys. Rev. E **93**, 033203 (2016).

[72] M. N. Rosenbluth, W. M. MacDonald, and D. L. Judd, "Fokker-Planck Equation for an Inverse-Square Force," Phys. Rev. **107**, 1 (1957).

[73] P. Helander and D. J. Sigmar, *Collisional Transport in Magnetized Plasmas* (Cambridge University Press, Cambridge, 2002).

[74] P. H. Chavanis, "Kinetic Theory of Spatially Homogeneous Systems with Long-Range Interactions: I. General Results," Eur. Phys. J. Plus **127**, 19 (2012).

[75] A. A. Schekochihin and S. C. Cowley, "Turbulence, Magnetic Fields, and Plasma Physics in Clusters of Galaxies," Phys. Plasmas **13**, 056501 (2006).

[76] S. Markidis, G. Lapenta, and Rizwan-uddin, "Multi-Scale Simulations of Plasma with iPIC3D," Math. Comput. Simulat. **80**, 1509 (2010).

[77] V. Roytershteyn, H. Karimabadi, and A. Roberts, "Generation of Magnetic Holes in Fully Kinetic Simulations of Collisionless Turbulence," Phil. Trans. R. Soc. A **373**, 20140151 (2015).

[78] D. Grošelj, A. Mallet, N. F. Loureiro, and F. Jenko, "Fully Kinetic Simulation of 3D Kinetic Alfvén Turbulence," Phys. Rev. Lett. **120**, 105101 (2018).

[79] J. Juno, A. Hakim, J. TenBarge, E. Shi, and W. Dorland, "Discontinuous Galerkin Algorithms for Fully Kinetic Plasmas," J. Comput. Phys. **353**, 110 (2018).

[80] S. Galtier and A. Bhattacharjee, "Anisotropic Weak Whistler Wave Turbulence in Electron Magnetohydrodynamics," Phys. Plasmas **10**, 3065 (2003).

[81] S. Saito, S. P. Gary, H. Li, and Y. Narita, "Whistler Turbulence: Particle-in-Cell Simulations," Phys. Plasmas **15**, 102305 (2008).

[82] S. P. Gary, O. Chang, and J. Wang, "Forward Cascade of Whistler Turbulence: Three-Dimensional Particle-in-Cell Simulations," Astrophys. J. **755**, 142 (2012).

[83] O. Chang, S. P. Gary, and J. Wang, "Energy Dissipation by Whistler Turbulence: Three-Dimensional Particle-in-Cell Simulations," Phys. Plasmas **21**, 052305 (2014).

[84] Y. Narita, R. Nakamura, W. Baumjohann, K.-H. Glassmeier, U. Motschmann, B. Giles, W. Magnes, D. Fischer, R. B. Torbert, C. T. Russell, R. J. Strangeway, J. L. Burch, Y. Nariyuki, S. Saito, and S. P. Gary, "On Electron-Scale Whistler Turbulence in the Solar Wind," Astrophys. J. Lett. **827**, L8 (2016).

[85] J. M. TenBarge and G. G. Howes, "Current Sheets and Collisionless Damping in Kinetic Plasma Turbulence," Astrophys. J. Lett. **771**, L27 (2013).

[86] T. Passot and P. L. Sulem, "A Model for the Non-Universal Power Law of The Solar Wind Sub-Ion-Scale Magnetic Spectrum," Astrophys. J. Lett. **812**, L37 (2015).

[87] T. C. Li, G. G. Howes, K. G. Klein, and J. M. TenBarge, "Energy Dissipation and Landau Damping in Two- and Three-Dimensional Plasma Turbulence," Astrophys. J. Lett. **832**, L24 (2016).

[88] S. Kobayashi, F. Sahraoui, T. Passot, D. Laveder, P. L. Sulem, S. Y. Huang, P. Henri, and R. Smets, "Three-Dimensional Simulations and Spacecraft Observations of Sub-Ion Scale Turbulence in the Solar Wind: Influence of Landau Damping," Astrophys. J. **839**, 122 (2017).

[89] W. Daughton, V. Roytershteyn, H. Karimabadi, L. Yin, B. J. Albright, B. Bergen, and K. J. Bowers, "Role of Electron Physics in the Development of Turbulent Magnetic Reconnection in Collisionless Plasmas," Nat. Phys. **7**, 539 (2011).

[90] R. A. Treumann and W. Baumjohann, "Collisionless Magnetic Reconnection in Space Plasmas," Front. Phys. **1**, 31 (2013).

[91] A. Mallet, A. A. Schekochihin, and B. D. G. Chandran, "Disruption of Alfvénic Turbulence by Magnetic Reconnection in a Collisionless Plasma," J. Plasma Phys. **83**, 905830609 (2017).

[92] T. D. Phan, J. P. Eastwood, M. A. Shay, J. F. Drake, B. U. Ö.. Sonnerup, M. Fujimoto, P. A. Cassak, M. Øieroset, J. L. Burch, R. B. Torbert, A. C. Rager, J. C. Dorelli, D. J. Gershman, C. Pollock, P. S. Pyakurel, C. C. Haggerty, Y. Khotyaintsev, B. Lavraud, Y. Saito, M. Oka, R. E. Ergun, A. Retino, O. Le Contel, M. R. Argall, B. L. Giles, T. E. Moore, F. D. Wilder, R. J. Strangeway, C. T. Russell, P. A. Lindqvist, and W. Magnes, "Electron Magnetic Reconnection Without Ion Coupling in Earth's Turbulent Magnetosheath," Nature (London) **557**, 202 (2018).

[93] S. P. Gary, "Short-Wavelength Plasma Turbulence and Temperature Anisotropy Instabilities: Recent Computational Progress," Phil. Trans. R. Soc. A **373**, 20140149 (2015).

[94] L. Sironi and R. Narayan, "Electron Heating by the Ion Cyclotron Instability in Collisionless Accretion Flows. I. Compression-Driven Instabilities and the Electron Heating Mechanism," Astrophys. J. **800**, 88 (2015).

[95] K. G. Klein, B. L. Alterman, M. L. Stevens, D. Vech, and J. C. Kasper, "Majority of Solar Wind Intervals Support Ion-Driven Instabilities," Phys. Rev. Lett. **120**, 205102 (2018).

[96] V. Zhdankin, D. A. Uzdensky, G. R. Werner, and M. C. Begelman, "Electron and Ion Energization in Relativistic Plasma Turbulence," arXiv:1809.01966.

[97] O. Pezzi, F. Valentini, and P. Veltri, "Collisional Relaxation of Fine Velocity Structures in Plasmas," Phys. Rev. Lett. **116**, 145001 (2016).

[98] A. Bañón Navarro, B. Teaca, D. Told, D. Groselj, P. Crandall, and F. Jenko, "Structure of Plasma Heating in Gyrokinetic Alfvénic Turbulence," Phys. Rev. Lett. **117**, 245101 (2016).

[99] U. Frisch, *Turbulence: The Legacy of A. N. Kolmogorov* (Cambridge University Press, Cambridge, 1995).

[100] G. L. Eyink and K. R. Sreenivasan, "Onsager and the Theory of Hydrodynamic Turbulence," Rev. Mod. Phys. **78**, 87 (2006).

[101] N. F. Loureiro, A. A. Schekochihin, and A. Zocco, "Fast Collisionless Reconnection and Electron Heating in Strongly Magnetized Plasmas," Phys. Rev. Lett. **111**, 025002 (2013).

[102] A. Zocco and A. A. Schekochihin, "Reduced Fluid-Kinetic Equations for Low-Frequency Dynamics, Magnetic Reconnection, and Electron Heating in Low-Beta Plasmas," Phys. Plasmas **18**, 102309 (2011).

[103] V. Bratanov, F. Jenko, D. Hatch, and S. Brunner, "Aspects of Linear Landau Damping in Discretized Systems," Phys. Plasmas **20**, 022108 (2013).

[104] H. Okuda and C. K. Birdsall, "Collisions in a Plasma of Finite-Size Particles," Phys. Fluids **13**, 2123 (1970).

[105] R. W. Hockney, "Measurement of Collision and Heating Times in a Two-Dimensional Thermal Computer Plasma," J. Comput. Phys. **8**, 19 (1971).

[106] E. Cormier-Michel, B. A. Shadwick, C. G. R. Geddes, E. Esarey, C. B. Schroeder, and W. P. Leemans, "Unphysical Kinetic Effects in Particle-in-Cell Modeling of Laser Wakefield Accelerators," Phys. Rev. E **78**, 016404 (2008).

[107] J. P. Verboncoeur, "Particle Simulation of Plasmas: Review and Advances," Plasma Phys. Control. Fusion **47**, A231 (2005).

[108] J. Villasenor and O. Buneman, "Rigorous Charge Conservation for Local Electromagnetic Field Solvers," Comput. Phys. Commun. **69**, 306 (1992).

[109] T. Z. Esirkepov, "Exact Charge Conservation Scheme for Particle-in-Cell Simulation with an Arbitrary Form-Factor," Comput. Phys. Commun. **135**, 144 (2001).

[110] K. J. Bowers, B. J. Albright, L. Yin, B. Bergen, and T. J. T. Kwan, "Ultrahigh Performance Three-Dimensional Electromagnetic Relativistic Kinetic Plasma Simulation," Phys. Plasmas **15**, 055703 (2008).

[111] V. K. Decyk, "Energy and Momentum Conservation Theorems for Electrostatic Simulations," J. Comput. Phys. **56**, 461 (1984).

[112] L. D. Landau, "On the Vibrations of the Electronic Plasma," Zh. Eksp. Teor. Fiz. **16**, 574 (1946).

[113] T. Grismayer, J. E. Fahlen, V. K. Decyk, and W. B. Mori, "On the Time-Dependent Resonant Width for Landau Damping: Theory and PIC Simulation," Plasma Phys. Control. Fusion **53**, 074011 (2011).

[114] D. Montgomery and C. W. Nielson, "Thermal Relaxation in One- and Two-Dimensional Plasma Models," Phys. Fluids **13**, 1405 (1970).

[115] I. Jechart, T. Katsouleas, and J. Dawson, "Anomalous Thermal Relaxation of a Two-Dimensional Magnetized Plasma," Phys. Fluids **30**, 65 (1987).

[116] R. S. Hughes, J. Wang, V. K. Decyk, and S. P. Gary, "Effects of Variations in Electron Thermal Velocity on the Whistler Anisotropy Instability: Particle-in-Cell Simulations," Phys. Plasmas **23**, 042106 (2016).

[117] P. A. Muñoz, P. Kilian, and J. Büchner, "Instabilities of Collisionless Current Sheets Revisited: The Role of Anisotropic Heating," Phys. Plasmas **21**, 112106 (2014).

[118] P. A. Muñoz, J. Büchner, and P. Kilian, "Turbulent Transport in 2D Collisionless Guide Field Reconnection," Phys. Plasmas **24**, 022104 (2017).

[119] G. G. M. Coppa, G. Lapenta, G. Dellapiana, F. Donato, and V. Riccardo, "Blob Method for Kinetic Plasma Simulation with Variable-Size Particles," J. Comput. Phys. **127**, 268 (1996).

[120] T. Abel, O. Hahn, and R. Kaehler, "Tracing the Dark Matter Sheet in Phase Space," Mon. Not. R. Astron. Soc. **427**, 61 (2012).

[121] O. Hahn and R. E. Angulo, "An Adaptively Refined Phase–Space Element Method for Cosmological Simulations and Collisionless Dynamics," Mon. Not. R. Astron. Soc. **455**, 1115 (2016).

[122] J. Kates-Harbeck, S. Totorica, J. Zrake, and T. Abel, "Simplex-in-Cell Technique for Collisionless Plasma Simulations," J. Comput. Phys. **304**, 231 (2016).

[123] D. Verscharen, E. Marsch, U. Motschmann, and J. Müller, "Kinetic Cascade Beyond Magnetohydrodynamics of Solar Wind Turbulence in Two-Dimensional Hybrid Simulations," Phys. Plasmas **19**, 022305 (2012).

[124] T. Parashar, M. Shay, P. A. Cassak, and W. H. Matthaeus, "Kinetic Dissipation and Anisotropic Heating in a Turbulent Collisionless Plasma," Phys. Plasmas **16**, 032310 (2009).

[125] B. J. Vasquez, S. A. Markovskii, and B. D. G. Chandran, "Three-Dimensional Hybrid Simulation Study of Anisotropic Turbulence in the Proton Kinetic Regime," Astrophys. J. **788**, 178 (2014).

[126] J. Byers, B. Cohen, W. Condit, and J. Hanson, "Hybrid Simulations of Quasineutral Phenomena in Magnetized Plasma," J. Comput. Phys. **27**, 363 (1978).

[127] D. S. Harned, "Quasineutral Hybrid Simulation of Macroscopic Plasma Phenomena," J. Comput. Phys. **47**, 452 (1982).

[128] F. Valentini, P. Trávníček, F. Califano, P. Hellinger, and A. Mangeney, "A Hybrid-Vlasov Model Based on the Current Advance Method for the Simulation of Collisionless Magnetized Plasma," J. Comput. Phys. **225**, 753 (2007).

[129] E. A. Frieman and L. Chen, "Nonlinear Gyrokinetic Equations for Low-Frequency Electromagnetic Waves in General Plasma Equilibria," Phys. Fluids **25**, 502 (1982).

[130] A. J. Brizard and T. S. Hahm, "Foundations of Nonlinear Gyrokinetic Theory," Rev. Mod. Phys. **79**, 421 (2007).

[131] G. G. Howes, S. C. Cowley, W. Dorland, G. W. Hammett, E. Quataert, and A. A. Schekochihin, "Astrophysical Gyrokinetics: Basic Equations and Linear Theory ," Astrophys. J. **651**, 590 (2006).

[132] F. Valentini, S. Servidio, D. Perrone, F. Califano, W. H. Matthaeus, and P. Veltri, "Hybrid Vlasov-Maxwell Simulations of Two-Dimensional Turbulence in Plasmas," Phys. Plasmas **21**, 082307 (2014).

[133] P. Hellinger, L. Matteini, S. Landi, A. Verdini, L. Franci, and P. M. Trávníček, "Plasma Turbulence and Kinetic Instabilities at Ion Scales in the Expanding Solar Wind," Astrophys. J. Lett. **811**, L32 (2015).

[134] L. Franci, S. Landi, A. Verdini, L. Matteini, and P. Hellinger, "Solar Wind Turbulent Cascade from MHD to Sub-Ion Scales: Large-Size 3D Hybrid Particle-in-Cell Simulations," Astrophys. J. **853**, 26 (2018).

[135] J. A. Krommes, "The Gyrokinetic Description of Microturbulence in Magnetized Plasmas," Annu. Rev. Fluid Mech. **44**, 175 (2012).

[136] P. Goldreich and S. Sridhar, "Toward a Theory of Interstellar Turbulence. II. Strong Alfvénic Turbulence," Astrophys. J. **438**, 763 (1995).

[137] W. H. Matthaeus, M. L. Goldstein, and D. A. Roberts, "Evidence for the Presence of Quasi-Two-Dimensional Nearly Incompressible Fluctuations in the Solar Wind," J. Geophys. Res. **95**, 20673 (1990).

[138] J. Cho and E. Vishniac, "The Anisotropy of Magnetohydrodynamic Alfvénic Turbulence," Astrophys. J. **539**, 273 (2000).

[139] J. Cho and A. Lazarian, "Compressible Magnetohydrodynamic Turbulence: Mode Coupling, Scaling Relations, Anisotropy, Viscosity-Damped Regime and Astrophysical Implications," Mon. Not. R. Astron. Soc. **345**, 325 (2003).

[140] R. T. Wicks, T. S. Horbury, C. H. K. Chen, and A. A. Schekochihin, "Power and Spectral Index Anisotropy of the Entire Inertial Range of Turbulence in the Fast Solar Wind," Mon. Not. R. Astron. Soc. **407**, L31 (2010).

[141] G. G. Howes, S. D. Bale, K. G. Klein, C. H. K. Chen, C. S. Salem, and J. M. TenBarge, "The Slow-Mode Nature of Compressible Wave Power in Solar Wind Turbulence," Astrophys. J. Lett. **753**, L19 (2012).

[142] J. J. Podesta, "The Need to Consider Ion Bernstein Waves as a Dissipation Channel of Solar Wind Turbulence," J. Geophys. Res. **117**, A07101 (2012).

[143] S. P. Gary and C. W. Smith, "Short-Wavelength Turbulence in the Solar Wind: Linear Theory of Whistler and Kinetic Alfvén Fluctuations," J. Geophys. Res. **114**, A12105 (2009).

[144] S. S. Cerri, F. Califano, F. Jenko, D. Told, and F. Rincon, "Subproton-Scale Cascades in Driven Hybrid-Kinetic Plasma Turbulence," Astrophys. J. Lett. **882**, L12 (2016).

[145] C. H. K. Chen, S. Boldyrev, Q. Xia, and J. C. Perez, "Nature of Subproton Scale Turbulence in the Solar Wind," Phys. Rev. Lett. **110**, 225002 (2013).

[146] K. H. Kiyani, S. C. Chapman, F. Sahraoui, B. Hnat, O. Fauvarque, and Y. V. Khotyaintsev, "Enhanced Magnetic Compressibility and Isotropic Scale Invariance at Sub-Ion Larmor Scales in Solar Wind Turbulence," Astrophys. J. **763**, 10 (2013).

[147] L. Chen, Z. Lin, and R. White, "On Resonant Heating Below the Cyclotron Frequency," Phys. Plasmas **8**, 4713 (2001).

[148] B. D. G. Chandran, B. Li, B. N. Rogers, E. Quataert, and K. Germaschewski, "Perpendicular Ion Heating by Low-Frequency Alfvén-Wave Turbulence in the Solar Wind," Astrophys. J. **720**, 503 (2010).

[149] A. A. Schekochihin, S. C. Cowley, R. M. Kulsrud, G. W. Hammett, and P. Sharma, "Plasma Instabilities and Magnetic Field Growth in Clusters of Galaxies," Astrophys. J. **629**, 139 (2005).

[150] M. W. Kunz, A. A. Schekochihin, and J. M. Stone, "Firehose and Mirror Instabilities in a Collisionless Shearing Plasma," Phys. Rev. Lett. **112**, 205003 (2014).

[151] M. W. Kunz, I. G. Abel, K. G. Klein, and A. A. Schekochihin, "Astrophysical Gyrokinetics: Turbulence in Pressure-Anisotropic Plasmas at Ion Scales and Beyond," J. Plasma Phys. **84**, 715840201 (2018).

[152] N. F. Loureiro, W. Dorland, L. Fazendeiro, A. Kanekar, A. Mallet, M. S. Vilelas, and A. Zocco, "Viriato: A Fourier–Hermite Spectral Code for Strongly Magnetized Fluid–Kinetic Plasma Dynamics," Comput. Phys. Commun. **206**, 45 (2016).

[153] H. Politano and A. Pouquet, "von Kármán–Howarth Equation for Magnetohydrodynamics and its Consequences on Third-Order Longitudinal Structure and Correlation Functions," Phys. Rev. E **57**, R21(R) (1998).

[154] S. Galtier, "von Kármán–Howarth equations for Hall Magnetohydrodynamic Flows," Phys. Rev. E **77**, 015302 (2008).

[155] G. L. Eyink and T. D. Drivas, "Cascades and Dissipative Anomalies in Compressible Fluid Turbulence," Phys. Rev. X **8**, 011022 (2018).

[156] G. L. Eyink and T. D. Drivas, "Cascades and Dissipative Anomalies in Relativistic Fluid Turbulence," Phys. Rev. X **8**, 011023 (2018).

[157] J. Maron and P. Goldreich, "Simulations of Incompressible Magnetohydrodynamic Turbulence," Astrophys. J. **554**, 1175 (2001).

[158] J. C. Perez, J. Mason, S. Boldyrev, and F. Cattaneo, "On the Energy Spectrum of Strong Magnetohydrodynamic Turbulence," Phys. Rev. X **2**, 041005 (2012).

[159] A. Mallet, A. A. Schekochihin, and B. D. G. Chandran, "Refined Critical Balance in Strong Alfvénic Turbulence," Mon. Not. R. Astron. Soc. **449**, L77 (2015).

[160] A. Mallet, A. A. Schekochihin, B. D. G. Chandran, C. H. K. Chen, T. S. Horbury, R. T. Wicks, and C. C. Greenan, "Measures of Three-Dimensional Anisotropy and Intermittency in Strong Alfvénic Turbulence," Mon. Not. R. Astron. Soc. **459**, 2130 (2016).

[161] D. Grošelj, C. H. K. Chen, A. Mallet, R. Samtaney, K. Schneider, and F. Jenko, "Kinetic Turbulence in Astrophysical Plasmas: Waves and/or Structures?" arXiv:1806.05741.

[162] A. N. Kolmogorov, "The Local Structure of Turbulence in Incompressible Viscous Fluid for Very Large Reynolds Numbers," Dokl. Akad. Nauk SSSR **30**, 301 (1941), [English translation: Proc. R. Soc. Lond. A **434**, 9 (1991)].

[163] A. N. Kolmogorov, "Dissipation of Energy in the Locally Isotropic Turbulence," Dokl. Akad. Nauk SSSR **32**, 16 (1941), [English translation: Proc. R. Soc. Lond. A **434**, 15 (1991)].

[164] A. M. Obukhov, "On the Distribution of Energy in the Spectrum of Turbulent Flow," Dokl. Akad. Nauk SSSR **32**, 22 (1941).

[165] C. F. von Weizsäcker, "Das Spektrum der Turbulenz bei Großen Reynoldsschen Zahlen," Z. Phys. **124**, 614 (1948).

[166] W. Heisenberg, "On the Theory of Statistical and Isotropic Turbulence," Proc. R. Soc. Lond. A **195**, 402 (1948).

[167] L. Onsager, "Statistical Hydrodynamics," Nuovo Cimento, Suppl. **6**, 279 (1949).

[168] H. Aluie and G. Eyink, "Localness of Energy Cascade in Hydrodynamic Turbulence. II. Sharp Spectral Filter," Phys. Fluids **21**, 115108 (2009).

[169] M. Farge and K. Schneider, "Wavelet Transforms and their Applications to MHD and Plasma Turbulence: A Review," J. Plasma Phys. **81**, 435810602 (2015).

[170] R. H. Kraichnan, "Inertial-Range Transfer in Two- and Three-Dimensional Turbulence," J. Fluid Mech. **47**, 525 (1971).

[171] J. A. Domaradzki and D. Carati, "An Analysis of the Energy Transfer and the Locality of Nonlinear Interactions in Turbulence," Phys. Fluids **19**, 085112 (2007).

[172] P. D. Mininni, "Scale Interactions in Magnetohydrodynamic Turbulence," Annu. Rev. Fluid Mech. **43**, 377 (2011).

[173] T. Ishihara, T. Gotoh, and Y. Kaneda, "Study of High–Reynolds Number Isotropic Turbulence by Direct Numerical Simulation," Annu. Rev. Fluid Mech. **41**, 165 (2009).

[174] G. L. Eyink, "Locality of Turbulent Cascades," Physica D **207**, 91 (2005).

[175] L. F. Richardson, *Weather Prediction by Numerical Process* (Cambridge University Press, London, 1922).

[176] D. Biskamp, *Magnetohydrodynamic Turbulence* (Cambridge University Press, Cambridge, 2003).

[177] D. Verscharen, C. H. K. Chen, and R. T. Wicks, "On Kinetic Slow Modes, Fluid Slow Modes, and Pressure-Balanced Structures in the Solar Wind," Astrophys. J. **840**, 106 (2017).

[178] A. M. Obukhov, "Structure of the Temperature Field in Turbulent Flows," Izv. Akad. Nauk SSSR Ser. Geogr. Geofiz. **13**, 58 (1949).

[179] S. Corrsin, "On the Spectrum of Isotropic Temperature Fluctuations in an Isotropic Turbulence," J. Applied Phys. **22**, 469 (1951).

[180] Y. Lithwick and P. Goldreich, "Compressible Magnetohydrodynamic Turbulence in Interstellar Plasmas," Astrophys. J. **562**, 279 (2001).

[181] R. Meyrand, A. Kanekar, W. Dorland, and A. A. Schekochihin, "Fluidization of Collisionless Plasma Turbulence," arXiv:1808.04284.

[182] W. M. Elsasser, "The Hydromagnetic Equations," Phys. Rev. **79**, 183 (1950).

[183] R. S. Iroshnikov, "Turbulence of a Conducting Fluid in a Strong Magnetic Field," Astron. Zh. **40**, 742 (1963), [English translation: Sov. Astron. **7**, 566 (1964)].

[184] R. H. Kraichnan, "Intertial-Range Spectrum of Hydromagnetic Turbulence," Phys. Fluids **8**, 1385 (1965).

[185] J. V. Shebalin, W. H. Matthaeus, and M. D. Montgomery, "Anisotropy in MHD Turbulence due to a Mean Magnetic Field," J. Plasma Phys. **29**, 525 (1983).

[186] S. Oughton, E. R. Priest, and W. H. Matthaeus, "The Influence of a Mean Magnetic Field on Three-Dimensional Magnetohydrodynamic Turbulence," J. Fluid Mech. **280**, 95 (1994).

[187] P. Goldreich and S. Sridhar, "Toward a Theory of Interstellar Turbulence. I. Weak Alfvénic Turbulence," Astrophys. J. **432**, 612 (1994).

[188] G. G. Howes, "A Dynamical Model of Plasma Turbulence in the Solar Wind," Phil. Trans. R. Soc. A **373**, 20140145 (2015).

[189] S. Boldyrev, "On the Spectrum of Magnetohydrodynamic Turbulence," Astrophys. J. Lett. **626**, L37 (2005).

[190] S. V. Nazarenko and A. A. Schekochihin, "Critical Balance in Magnetohydrodynamic, Rotating and Stratified Turbulence: Towards a Universal Scaling Conjecture," J. Fluid Mech. **677**, 134 (2011).

[191] S. Galtier, S. V. Nazarenko, A. C. Newell, and A. Pouquet, "A Weak Turbulence Theory for Incompressible Magnetohydrodynamics," J. Plasma Phys. **63**, 447 (2000).

[192] A. A. Schekochihin, S. Nazarenko, and T. A. Yousef, "Weak Alfvén-Wave Turbulence Revisited," Phys. Rev. E **85**, 036406 (2012).

[193] P. Goldreich and S. Sridhar, "Magnetohydrodynamic Turbulence Revisited," Astrophys. J. **485**, 680 (1997).

[194] S. Boldyrev and J. C. Perez, "Spectrum of Weak Magnetohydrodynamic Turbulence," Phys. Rev. Lett. **103**, 225001 (2009).

[195] R. Meyrand, S. Galtier, and K. H. Kiyani, "Direct Evidence of the Transition from Weak to Strong Magnetohydrodynamic Turbulence," Phys. Rev. Lett. **116**, 105002 (2016).

[196] H. Aluie and G. Eyink, "Scale Locality of Magnetohydrodynamic Turbulence," Phys. Rev. Lett. **104**, 081101 (2010).

[197] B. Teaca, D. Carati, and J. A. Domaradzki, "On the Locality of Magnetohydrodynamic Turbulence Scale Fluxes," Phys. Plasmas **18**, 112307 (2011).

[198] J. C. Higdon, "Density Fluctuations in the Interstellar Medium: Evidence for Anisotropic Magnetogasdynamic Turbulence. I - Model and Astrophysical Sites," Astrophys. J. **285**, 109 (1984).

[199] J. Cho, A. Lazarian, and E. T. Vishniac, "Simulations of Magnetohydrodynamic Turbulence in a Strongly Magnetized Medium," Astrophys. J. **564**, 291 (2002).

[200] T. S. Horbury, M. Forman, and S. Oughton, "Anisotropic Scaling of Magnetohydrodynamic Turbulence," Phys. Rev. Lett. **101**, 175005 (2008).

[201] J. J. Podesta, "Dependence of Solar-Wind Power Spectra on the Direction of the Local Mean Magnetic Field," Astrophys. J. **698**, 986 (2009).

[202] W.-C. Müller, D. Biskamp, and R. Grappin, "Statistical Anisotropy of Magnetohydrodynamic Turbulence," Phys. Rev. E **67**, 066302 (2003).

[203] W. H. Matthaeus, S. Oughton, S. Ghosh, and M. Hossain, "Scaling of Anisotropy in Hydromagnetic Turbulence," Phys. Rev. Lett. **81**, 2056 (1998).

[204] J. A. Tessein, C. W. Smith, B. T. MacBride, W. H. Matthaeus, M. A. Forman, and J. E. Borovsky, "Spectral Indices for Multi-Dimensional Interplanetary Turbulence at 1 AU," Astrophys. J. **692**, 684 (2009).

[205] J. M. TenBarge and G. G. Howes, "Evidence of Critical Balance in Kinetic Alfvén Wave Turbulence Simulations," Phys. Plasmas **19**, 055901 (2012).

[206] S. Boldyrev, "Spectrum of Magnetohydrodynamic Turbulence," Phys. Rev. Lett. **96**, 115002 (2006).

[207] A. Beresnyak and A. Lazarian, "Polarization Intermittency and Its Influence on MHD Turbulence," Astrophys. J. Lett. **640**, L175 (2006).

[208] D. Biskamp and H. Welter, "Dynamics of Decaying Two-Dimensional Magnetohydrodynamic Turbulence," Phys. Fluids B **1**, 1964 (1989).

[209] C. H. K. Chen, A. Mallet, A. A. Schekochihin, T. S. Horbury, R. T. Wicks, and S. D. Bale, "Three-Dimensional Structure of Solar Wind Turbulence," Astrophys. J. **758**, 120 (2012).

[210] V. Zhdankin, D. A. Uzdensky, J. C. Perez, and S. Boldyrev, "Statistical Analysis of Current Sheets in Three-Dimensional Magnetohydrodynamic Turbulence," Astrophys. J. **771**, 124 (2013).

[211] A. Pouquet, M. Meneguzzi, and U. Frisch, "Growth of Correlations in Magnetohydrodynamic Turbulence," Phys. Rev. A **33**, 4266 (1986).

[212] J. Mason, F. Cattaneo, and S. Boldyrev, "Dynamic Alignment in Driven Magnetohydrodynamic Turbulence," Phys. Rev. Lett. **97**, 255002 (2006).

[213] S. Boldyrev, J. C. Perez, J. E. Borovsky, and J. J. Podesta, "Spectral Scaling Laws in Magnetohydrodynamic Turbulence Simulations and in the Solar Wind," Astrophys. J. Lett. **741**, L19 (2011).

[214] A. Beresnyak, "Spectral Slope and Kolmogorov Constant of MHD Turbulence," Phys. Rev. Lett. **106**, 075001 (2011).

[215] A. Beresnyak, "Basic Properties of Magnetohydrodynamic Turbulence in the Inertial Range," Mon. Not. R. Astron. Soc. **422**, 3495 (2012).

[216] A. Mallet, A. A. Schekochihin, and B. D. G. Chandran, "Disruption of Sheet-like Structures in Alfvénic Turbulence by Magnetic Reconnection," Mon. Not. R. Astron. Soc. **468**, 4862 (2017).

[217] J. J. Podesta and J. E. Borovsky, "Scale Invariance of Normalized Cross-Helicity Throughout the Inertial Range of Solar Wind Turbulence," Phys. Plasmas **17**, 112905 (2010).

[218] R. T. Wicks, D. A. Roberts, A. Mallet, A. A. Schekochihin, T. S. Horbury, and C. H. K. Chen, "Correlations at Large Scales and the Onset of Turbulence in the Fast Solar Wind," Astrophys. J. **778**, 177 (2013).

[219] C. H. K. Chen, S. D. Bale, C. S. Salem, and B. A. Maruca, "Residual Energy Spectrum of Solar Wind Turbulence," Astrophys. J. **770**, 125 (2013).

[220] Y. Lithwick, P. Goldreich, and S. Sridhar, "Imbalanced Strong MHD Turbulence," Astrophys. J. **655**, 269 (2007).

[221] A. Beresnyak and A. Lazarian, "Strong Imbalanced Turbulence," Astrophys. J. **682**, 1070 (2008).

[222] W.-C. Müller and R. Grappin, "Spectral Energy Dynamics in Magnetohydrodynamic Turbulence," Phys. Rev. Lett. **95**, 114502 (2005).

[223] J. J. Podesta, D. A. Roberts, and M. L. Goldstein, "Spectral Exponents of Kinetic and Magnetic Energy Spectra in Solar Wind Turbulence," Astrophys. J. **664**, 543 (2007).

[224] R. Grappin, W.-C. Müller, and A. Verdini, "Alfvén-Dynamo Balance and Magnetic Excess in Magnetohydrodynamic Turbulence," Astron. Astrophys. **589**, A131 (2016).

[225] D. Shaikh and G. P. Zank, "Spectral Features of Solar Wind Turbulent Plasma," Mon. Not. R. Astron. Soc. **400**, 1881 (2009).

[226] J. J. Podesta, J. E. Borovsky, and S. P. Gary, "A Kinetic Alfvén Wave Cascade Subject to Collisionless Damping Cannot Reach Electron Scales in the Solar Wind at 1 AU," Astrophys. J. **712**, 685 (2010).

[227] W. H. Matthaeus, S. Oughton, K. T. Osman, S. Servidio, M. Wan, S. P. Gary, M. A. Shay, F. Valentini, V. Roytershteyn, H. Karimabadi, and S. C. Chapman, "Nonlinear and Linear Timescales near Kinetic Scales in Solar Wind Turbulence," Astrophys. J. **790**, 155 (2014).

[228] A. A. Schekochihin, S. C. Cowley, W. Dorland, G. W. Hammett, G. G. Howes, G. G. Plunk, E. Quataert, and T. Tatsuno, "Gyrokinetic Turbulence: A Nonlinear Route to Dissipation through Phase Space," Plasma Phys. Control. Fusion **50**, 124024 (2008).

[229] G. G. Howes, "Limitations of Hall MHD as a Model for Turbulence in Weakly Collisional Plasmas," Nonlin. Processes Geophys. **16**, 219 (2009).

[230] P. Henri, S. S. Cerri, F. Califano, F. Pegoraro, C. Rossi, M. Faganello, O. Šebek, P. M. Trávníček, P. Hellinger, J. T. Frederiksen, A. Nordlund, S. Markidis, R. Keppens, and G. Lapenta, "Nonlinear Evolution of the Magnetized Kelvin-Helmholtz Instability: From Fluid to Kinetic Modeling," Phys. Plasmas **20**, 102118 (2013).

[231] S. S. Cerri, L. Franci, F. Califano, S. Landi, and P. Hellinger, "Plasma Turbulence at Ion Scales: A Comparison Between Particle in Cell and Eulerian Hybrid-Kinetic Approaches," J. Plasma Phys. **83**, 705830202 (2017).

[232] O. Pezzi, T. N. Parashar, S. Servidio, F. Valentini, C. L. Vásconez, Y. Yang, F. Malara, W. H. Matthaeus, and P. Veltri, "Revisiting a Classic: The Parker-Moffatt Problem," Astrophys. J. **834**, 166 (2017).

[233] G. G. Howes, J. M. TenBarge, and W. Dorland, "A Weakened Cascade Model for Turbulence in Astrophysical Plasmas," Phys. Plasmas **18**, 102305 (2011).

[234] S. D. Bale, P. J. Kellogg, F. S. Mozer, T. S. Horbury, and H. Reme, "Measurement of the Electric Fluctuation Spectrum of Magnetohydrodynamic Turbulence," Phys. Rev. Lett. **94**, 215002 (2005).

[235] F. Sahraoui, M. L. Goldstein, G. Belmont, P. Canu, and L. Rezeau, "Three Dimensional Anisotropic k Spectra of Turbulence at Subproton Scales in the Solar Wind," Phys. Rev. Lett. **105**, 131101 (2010).

[236] C. S. Salem, G. G. Howes, D. Sundkvist, S. D. Bale, C. C. Chaston, C. H. K. Chen, and F. S. Mozer, "Identification of Kinetic Alfvén Wave Turbulence in the Solar Wind," Astrophys. J. Lett. **745**, L9 (2012).

[237] J. M. TenBarge, J. J. Podesta, K. G. Klein, and G. G. Howes, "Interpreting Magnetic Variance Anisotropy Measurements in the Solar Wind," Astrophys. J. **753**, 107 (2012).

[238] J. J. Podesta, "Evidence of Kinetic Alfvén Waves in the Solar Wind at 1 AU," Sol. Phys. **286**, 529 (2013).

[239] O. W. Roberts, S. Toledo-Redondo, D. Perrone, J. Zhao, Y. Narita, D. Gershman, R. Nakamura, B. Lavraud, C. P. Escoubet, B. Giles, J. Dorelli, C. Pollock, and J. Burch, "Ion-Scale Kinetic Alfvén Turbulence: MMS Measurements of the Alfvén Ratio in the Magnetosheath," Geophys. Res. Lett. **45**, 7974 (2018).

[240] R. A. López, A. F. Viñas, J. A. Araneda, and P. H. Yoon, "Kinetic Scale Structure of Low-Frequency Waves and Fluctuations," Astrophys. J. **845**, 60 (2017).

[241] J. Cho and A. Lazarian, "Simulations of Electron Magnetohydrodynamic Turbulence," Astrophys. J. **701**, 236 (2009).

[242] C. H. K. Chen, L. Matteini, D. Burgess, and T. S. Horbury, "Magnetic Field Rotations in the Solar Wind at Kinetic Scales," Mon. Not. R. Astron. Soc. **453**, L64 (2015).

[243] S. Nazarenko, *Wave Turbulence* (Springer, Berlin, 2011).

[244] D. Biskamp, E. Schwartz, A. Zeiler, A. Celani, and J. F. Drake, "Electron Magnetohydrodynamic Turbulence," Phys. Plasmas **6**, 751 (1999).

[245] J. Cho and A. Lazarian, "The Anisotropy of Electron Magnetohydrodynamic Turbulence," Astrophys. J. Lett. **615**, L41 (2004).

[246] F. Sahraoui, G. Belmont, and M. L. Goldstein, "New Insight into Short-Wavelenght Solar Wind Fluctuations from Vlasov Theory," Astrophys. J. **748**, 100 (2012).

[247] C. H. K. Chen and S. Boldyrev, "Nature of Kinetic Scale Turbulence in the Earth's Magnetosheath," Astrophys. J. **842**, 122 (2017).

[248] S. P. Gary, "Low-Frequency Waves in a High-Beta Collisionless Plasma: Polarization, Compressibility and Helicity," J. Plasma Phys. **35**, 431 (1986).

[249] J. V. Hollweg, "Kinetic Alfvén Wave Revisited," J. Geophys. Res. **104**, 14811 (1999).

[250] E. Camporeale and D. Burgess, "Comparison of Linear Modes in Kinetic Plasma Models," J. Plasma Phys. **83**, 535830201 (2017).

[251] J. T. Dahlin, J. F. Drake, and M. Swisdak, "Electron Acceleration in Three-Dimensional Magnetic Reconnection with a Guide Field," Phys. Plasmas **22**, 100704 (2015).

[252] R. S. Hughes, S. P. Gary, J. Wang, and T. N. Parashar, "Kinetic Alfvén Turbulence: Electron and Ion Heating by Particle-in-Cell Simulations," Astrophys. J. Lett. **847**, L14 (2017).

[253] P. L. Sulem, T. Passot, D. Laveder, and D. Borgogno, "Influence of the Nonlinearity Parameter on the Solar Wind Sub-Ion Magnetic Energy Spectrum: FLR-Landau Fluid Simulations," Astrophys. J. **818**, 66 (2016).

[254] K. H. Kiyani, S. C. Chapman, Y. V. Khotyaintsev, M. W. Dunlop, and F. Sahraoui, "Global Scale-Invariant Dissipation in Collisionless Plasma Turbulence," Phys. Rev. Lett. **103**, 075006 (2009).

[255] C. H. K. Chen, C. S. Salem, J. W. Bonnell, F. S. Mozer, and S. D. Bale, "Density Fluctuation Spectrum of Solar Wind Turbulence between Ion and Electron Scales," Phys. Rev. Lett. **109**, 035001 (2012).

[256] A. A. Schekochihin, J. T. Parker, E. G. Highcock, P. J. Dellar, W. Dorland, and G. W. Hammett, "Phase Mixing versus Nonlinear Advection in Drift-Kinetic Plasma Turbulence," J. Plasma Phys. **82**, 905820212 (2016).

[257] R. W. Gould, T. M. O'Neil, and J. H. Malmberg, "Plasma Wave Echo," Phys. Rev. Lett. **19**, 219 (1967).

[258] H. Wu, D. Verscharen, R. T. Wicks, C. H. K. Chen, J. He, and G. Nicolaou, "The Fluid-Like Behavior of Kinetic Alfvén Turbulence in Space Plasma," arXiv:1808.09763.

[259] G. G. Howes, A. J. McCubbin, and K. G. Klein, "Spatially Localized Particle Energization by Landau Damping in Current Sheets Produced by Strong Alfvén Wave Collisions," J. Plasma Phys. **84**, 905840105 (2018).

[260] W. Dorland and G. W. Hammett, "Gyrofluid Turbulence Models with Kinetic Effects," Phys. Fluids B **5**, 812 (1993).

[261] T. Tatsuno, W. Dorland, A. A. Schekochihin, G. G. Plunk, M. Barnes, S. C. Cowley, and G. G. Howes, "Nonlinear Phase Mixing and Phase-Space Cascade of Entropy in Gyrokinetic Plasma Turbulence," Phys. Rev. Lett. **103**, 015003 (2009).

[262] S. S. Cerri, M. W. Kunz, and F. Califano, "Dual Phase-Space Cascades in 3D Hybrid-Vlasov-Maxwell Turbulence," Astrophys. J. Lett. **856**, L13 (2018).

[263] C. H. K. Chen, L. Sorriso-Valvo, J. Šafránková, and Z. Němeček, "Intermittency of Solar Wind Density Fluctuations from Ion to Electron Scales," Astrophys. J. Lett. **789**, L8 (2014).

[264] S. S. Cerri and F. Califano, "Reconnection and Small-Scale Fields in 2D-3V Hybrid-Kinetic Driven Turbulence Simulations," New J. Phys. **19**, 025007 (2017).

[265] R. Fitzpatrick and F. Porcelli, "Collisionless Magnetic Reconnection with Arbitrary Guide Field," Phys. Plasmas **11**, 4713 (2004).

[266] R. Fitzpatrick and F. Porcelli, "Erratum: Collisionless Magnetic Reconnection with Arbitrary Guide Field [Phys. Plasmas 11, 4713 (2004)]," Phys. Plasmas **14**, 049902 (2007).

[267] L. Franci, S. S. Cerri, F. Califano, S. Landi, E. Papini, A. Verdini, L. Matteini, F. Jenko, and P. Hellinger, "Magnetic Reconnection as a Driver for a Sub-Ion-Scale Cascade in Plasma Turbulence," Astrophys. J. Lett. **850**, L16 (2017).

[268] D. Biskamp, H. Welter, and M. Walter, "Statistical Properties of Two-Dimensional Magnetohydrodynamic Turbulence," Phys. Fluids B **2**, 3024 (1990).

[269] M. Wan, W. H. Matthaeus, V. Roytershteyn, H. Karimabadi, T. Parashar, P. Wu, and M. Shay, "Intermittent Dissipation and Heating in 3D Kinetic Plasma Turbulence," Phys. Rev. Lett. **114**, 175002 (2015).

[270] J. He, C. Tu, E. Marsch, and S. Yao, "Do Oblique Alfvén/Ion-Cyclotron or Fast-Mode/Whistler Waves Dominate the Dissipation of Solar Wind Turbulence Near the Proton Inertial Length?" Astrophys. J. Lett. **745**, L8 (2012).

[271] K. G. Klein, G. G. Howes, J. M. TenBarge, and J. J. Podesta, "Physical Interpretation of the Angle-Dependent Magnetic Helicity Spectrum in the Solar Wind: The Nature of Turbulent Fluctuations Near the Proton Gyroradius Scale," Astrophys. J. **785**, 138 (2014).

[272] L. Franci, A. Verdini, L. Matteini, S. Landi, and P. Hellinger, "Solar Wind Turbulence from MHD to Sub-Ion Scales: High-Resolution Hybrid Simulations," Astrophys. J. Lett. **804**, L39 (2015).

[273] F. Sahraoui, M. L. Goldstein, P. Robert, and Y. V. Khotyaintsev, "Evidence of a Cascade and Dissipation of Solar-Wind Turbulence at the Electron Gyroscale," Phys. Rev. Lett. **102**, 231102 (2009).

[274] C. P. Escoubet, M. Fehringer, and M. Goldstein, "*Introduction* The Cluster Mission," Ann. Geophys. **19**, 1197 (2001).

[275] J. L. Burch, T. E. Moore, R. B. Torbert, and B. L. Giles, "Magnetospheric Multiscale Overview and Science Objectives," Space Sci. Rev. **199**, 5 (2016).

[276] C. H. K. Chen, T. S. Horbury, A. A. Schekochihin, R. T. Wicks, O. Alexandrova, and J. Mitchell, "Anisotropy of Solar Wind Turbulence between Ion and Electron Scales," Phys. Rev. Lett. **104**, 255002 (2010).

[277] D. Perrone, O. Alexandrova, A. Mangeney, M. Maksimovic, C. Lacombe, V. Rakoto, J. C. Kasper, and D. Jovanovic, "Compressive Coherent Structures at Ion Scales in the Slow Solar Wind," Astrophys. J. **826**, 196 (2016).

[278] D. J. Gershman, A. F.-Viñas, J. C. Dorelli, M. L. Goldstein, J. Shuster, L. A. Avanov, S. A. Boardsen, J. E. Stawarz, S. J. Schwartz, C. Schiff, B. Lavraud, Y. Saito, W. R. Paterson, B. L. Giles, C. J. Pollock, R. J. Strangeway, C. T. Russell, R. B. Torbert, T. E. Moore, and J. L. Burch, "Energy Partitioning Constraints at Kinetic Scales in Low-β Turbulence," Phys. Plasmas **25**, 022303 (2018).

[279] F. Sahraoui, G. Belmont, M. L. Goldstein, and L. Rezeau, "Limitations of Multispacecraft Data Techniques in Measuring Wave Number Spectra of Space Plasma Turbulence," J. Geophys. Res. **115**, A04206 (2010).

[280] O. Alexandrova, C. Lacombe, A. Mangeney, R. Grappin, and M. Maksimovic, "Solar Wind Turbulent Spectrum at Plasma Kinetic Scales," Astrophys. J. **760**, 121 (2012).

[281] J. J. Podesta and S. P. Gary, "Magnetic Helicity Spectrum of Solar Wind Fluctuations as a Function of the Angle with Respect to the Local Mean Magnetic Field," Astrophys. J. **734**, 15 (2011).

[282] G. G. Howes and E. Quataert, "On the Interpretation of Magnetic Helicity Signatures in the Dissipation Range of Solar Wind Turbulence," Astrophys. J. Lett. **709**, L49 (2010).

[283] A. V. Gordeev, A. S. Kingsep, and L. I. Rudakov, "Electron Magnetohydrodynamics," Phys. Rep. **243**, 215 (1994).

[284] R. Meyrand, K. H. Kiyani, Ö. D. Gürcan, and S. Galtier, "Coexistence of Weak and Strong Wave Turbulence in Incompressible Hall Magnetohydrodynamics," Phys. Rev. X **8**, 031066 (2018).

[285] Y. Narita, S. P. Gary, S. Saito, K.-H. Glassmeier, and U. Motschmann, "Dispersion Relation Analysis of Solar Wind Turbulence," Geophys. Res. Lett. **38**, L05101 (2011).

[286] C. Perschke, Y. Narita, S. P. Gary, U. Motschmann, and K.-H. Glassmeier, "Dispersion Relation Analysis of Turbulent Magnetic Field Fluctuations in Fast Solar Wind," Ann. Geophys. **31**, 1949 (2013).

[287] C. Lacombe, O. Alexandrova, L. Matteini, O. Santolík, N. Cornilleau-Wehrlin, A. Mangeney, Y. de Conchy, and M. Maksimovic, "Whistler Mode Waves and the Electron Heat Flux in the Solar Wind: *Cluster* Observations," Astrophys. J. **796**, 5 (2014).

[288] D. Stansby, T. S. Horbury, C. H. K. Chen, and L. Matteini, "Experimental Determination of Whistler Wave Dispersion Relation in the Solar Wind," Astrophys. J. Lett. **829**, L16 (2016).

[289] K. Horaites, P. Astfalk, S. Boldyrev, and F. Jenko, "Stability Analysis of Core–Strahl Electron Distributions in the Solar Wind," Mon. Not. R. Astron. Soc. **480**, 1499 (2018).

[290] F. Sahraoui, S. Y. Huang, G. Belmont, M. L. Goldstein, A. Rétino, P. Robert, and J. De Patoul, "Scaling of the Electron Dissipation Range of Solar Wind Turbulence," Astrophys. J. **777**, 15 (2013).

[291] Y. Narita and E. Marsch, "Kinetic Slow Mode in the Solar Wind and its Possible Role in Turbulence Dissipation and Ion Heating," Astrophys. J. **805**, 24 (2015).

[292] Y. Yang, W. H. Matthaeus, T. N. Parashar, P. Wu, M. Wan, Y. Shi, S. Chen, V. Roytershteyn, and W. Daughton, "Energy Transfer Channels and Turbulence Cascade in Vlasov-Maxwell Turbulence," Phys. Rev. E **95**, 061201(R) (2017).

[293] K. T. Osman, W. H. Matthaeus, J. T. Gosling, A. Greco, S. Servidio, B. Hnat, S. C. Chapman, and T. D. Phan, "Magnetic Reconnection and Intermittent Turbulence in the Solar Wind," Phys. Rev. Lett. **112**, 215002 (2014).

[294] T. Parashar and W. H. Matthaeus, "Propinquity of Current and Vortex Structures: Effects on Collisionless Plasma Heating," Astrophys. J. **832**, 57 (2016).

[295] H. Karimabadi, V. Roytershteyn, M. Wan, W. H. Matthaeus, W. Daughton, P. Wu, M. Shay, B. Loring, J. Borovsky, E. Leonardis, S. C. Chapman, and T. K. M. Nakamura, "Coherent Structures, Intermittent Turbulence, and Dissipation in High-Temperature Plasmas," Phys. Plasmas **20**, 012303 (2013).

[296] R. Numata and N. F. Loureiro, "Ion and Electron Heating During Magnetic Reconnection in Weakly Collisional Plasmas," J. Plasma Phys. **81**, 305810201 (2015).

[297] G. G. Howes, "The Dynamical Generation of Current Sheets in Astrophysical Plasma Turbulence," Astrophys. J. Lett. **827**, L28 (2016).

[298] R. A. Fonseca, S. F. Martins, L. O. Silva, J. W. Tonge, F. S. Tsung, and W. B. Mori, "One-to-One Direct Modeling of Experiments and Astrophysical Scenarios: Pushing the Envelope on Kinetic Plasma Simulations," Plasma Phys. Control. Fusion **50**, 124034 (2008).

[299] S. F. Martins, R. A. Fonseca, L. O. Silva, and W. B. Mori, "Ion Dynamics and Acceleration in Relativistic Shocks," Astrophys. J. **695**, L189 (2009).

[300] K. M. Schoeffler, N. F. Loureiro, R. A. Fonseca, and L. O. Silva, "Magnetic-Field Generation and Amplification in an Expanding Plasma," Phys. Rev. Lett. **112**, 175001 (2014).

[301] T. Grismayer, M. Vranic, J. L. Martins, R. A. Fonseca, and L. O. Silva, "Seeded QED Cascades in Counterpropagating Laser Pulses," Phys. Rev. E **95**, 023210 (2017).

[302] G. Inchingolo, T. Grismayer, N. F. Loureiro, R. A. Fonseca, and L. O. Silva, "Fully Kinetic Large-Scale Simulations of the Collisionless Magnetorotational Instability," Astrophys. J. **859**, 149 (2018).

[303] Message Passing Interface Forum, *MPI: A Message-Passing Interface Standard, Version 3.0* (High-Performance Computing Center Stuttgart, 2012).

[304] T. H. Stix, *Waves in Plasmas* (AIP-Press, New York, 1992).

[305] J. M. TenBarge, G. G. Howes, W. Dorland, and G. W. Hammett, "An Oscillating Langevin Antenna for Driving Plasma Turbulence Simulations," Comput. Phys. Commun. **185**, 578 (2014).

[306] O. Stawicki, S. P. Gary, and H. Li, "Solar Wind Magnetic Fluctuation Spectra: Dispersion versus Damping," J. Geophys. Res. **106**, 8273 (2001).

[307] J. W. Belcher and L. Davis, "Large-Amplitude Alfvén Waves in the Interplanetary Medium, 2," J. Geophys. Res. **76**, 3534 (1971).

[308] R. Bruno, B. Bavassano, and U. Villante, "Evidence for Long Period Alfvén Waves in the Inner Solar System," J. Geophys. Res. **90**, 4373 (1985).

[309] W. H. Matthaeus, S. Ghosh, S. Oughton, and D. A. Roberts, "Anisotropic Three-Dimensional MHD Turbulence," J. Geophys. Res. **101**, 7619 (1996).

[310] G. G. Howes and K. D. Nielson, "Alfvén Wave Collisions, the Fundamental Building Block of Plasma Turbulence. I. Asymptotic Solution," Phys. Plasmas **20**, 072302 (2013).

[311] P. Wu, M. Wan, W. H. Matthaeus, M. A. Shay, and M. Swisdak, "von Kárman Energy Decay and Heating of Protons and Electrons in a Kinetic Turbulent Plasma," Phys. Rev. Lett. **111**, 121105 (2013).

[312] W. Daughton, T. K. M. Nakamura, H. Karimabadi, V. Roytershteyn, and B. Loring, "Computing the Reconnection Rate in Turbulent Kinetic Layers by using Electron Mixing to Identify Topology," Phys. Plasmas **21**, 052307 (2014).

[313] K. G. Klein and G. G. Howes, "Predicted Impacts of Proton Temperature Anisotropy on Solar Wind Turbulence," Phys. Plasmas **22**, 032903 (2015).

[314] T. N. Parashar, C. Salem, R. T. Wicks, H. Karimabadi, S. P. Gary, and W. H. Matthaeus, "Turbulent Dissipation Challenge: A Community-Driven Effort," J. Plasma Phys. **81**, 905810513 (2015).

[315] M. Wan, W. H. Matthaeus, V. Roytershteyn, T. N. Parashar, P. Wu, and H. Karimabadi, "Intermittency, Coherent Structures and Dissipation in Plasma Turbulence," Phys. Plasmas **23**, 042307 (2016).

[316] S. A. Orszag and C.-M. Tang, "Small-Scale Structure of Two-Dimensional Magnetohydrodynamic Turbulence," J. Fluid Mech. **90**, 129 (1979).

[317] R. Numata, G. G. Howes, T. Tatsuno, M. Barnes, and W. Dorland, "AstroGK: Astrophysical Gyrokinetics Code," J. Comput. Phys. **229**, 9347 (2010).

[318] T. Parashar, W. H. Matthaeus, M. A. Shay, and M. Wan, "Transition from Kinetic to MHD Behavior in a Collisionless Plasma," Astrophys. J. **811**, 112 (2015).

[319] F. Jenko, W. Dorland, M. Kotschenreuther, and B. N. Rogers, "Electron Temperature Gradient Driven Turbulence," Phys. Plasmas **7**, 1904 (2000).

[320] J. M. Picone and R. B. Dahlburg, "Evolution of the Orszag–Tang Vortex System in a Compressible Medium. II. Supersonic Flow," Phys. Fluids B **3**, 29 (1991).

[321] T. Dudok de Wit, "Can High-Order Moments be Meaningfully Estimated from Experimental Turbulence Measurements?" Phys. Rev. E **70**, 055302(R) (2004).

[322] K. Kiyani, S. C. Chapman, and B. Hnat, "Extracting the Scaling Exponents of a Self-Affine, Non-Gaussian Process from a Finite-Length Time Series," Phys. Rev. E **74**, 051122 (2006).

[323] J. M. TenBarge, W. Daughton, H. Karimabadi, G. G. Howes, and W. Dorland, "Collisionless Reconnection in the Large Guide Field Regime: Gyrokinetic versus Particle-in-Cell Simulations," Phys. Plasmas **21**, 020708 (2014).

[324] S. K. Lele, "Compact Finite Difference Schemes with Spectral-like Resolution," J. Comput. Phys. **103**, 16 (1992).

[325] S. P. Gary, R. S. Hughes, and J. Wang, "Whistler Turbulence Heating of Electrons and Ions: Three-Dimensional Particle-in-Cell Simulations," Astrophys. J. **816**, 102 (2016).

[326] W. H. Matthaeus, T. N. Parashar, M. Wan, and P. Wu, "Turbulence and Proton-Electron Heating in Kinetic Plasma," Astrophys. J. Lett. **827**, L7 (2016).

[327] D. Told, J. Cookmeyer, P. Astfalk, and F. Jenko, "A Linear Dispersion Relation for the Hybrid Kinetic-Ion/Fluid-Electron Model of Plasma Physics," New J. Phys. **18**, 075001 (2016).

[328] A. Bañón Navarro, P. Morel, M. Albrecht-Marc, D. Carati, F. Merz, T. Görler, and F. Jenko, "Free Energy Cascade in Gyrokinetic Turbulence," Phys. Rev. Lett. **106**, 055001 (2011).

[329] E. G. Zweibel and M. Yamada, "Magnetic Reconnection in Astrophysical and Laboratory Plasmas," Annu. Rev. Astron. Astrophys. **47**, 291 (2009).

[330] J. Scudder and W. Daughton, ""Illuminating" Electron Diffusion Regions of Collisionless Magnetic Reconnection using Electron Agyrotropy," J. Geophys. Res. **113**, A06222 (2008).

[331] O. Chang, S. P. Gary, and J. Wang, "Whistler Turbulence Forward Cascade Versus Inverse Cascade: Three-Dimensional Particle-in-Cell Simulations," Astrophys. J. **800**, 87 (2015).

[332] R. Meyrand and S. Galtier, "Anomalous $k_\perp^{-8/3}$ Spectrum in Electron Magnetohydrodynamic Turbulence," Phys. Rev. Lett. **111**, 264501 (2013).

[333] H. Xu, A. Pumir, G. Falkovich, E. Bodenschatz, M. Shats, H. Xia, N. Francois, and G. Boffetta, "Flight-Crash Events in Turbulence," Proc. Natl. Acad. Sci. USA **111**, 7558 (2014).

[334] Q. Xia, J. C. Perez, B. D. G. Chandran, and E. Quataert, "Perpendicular Ion Heating by Reduced Magnetohydrodynamic Turbulence," Astrophys. J. **776**, 90 (2013).

[335] R. Lehe, I. J. Parrish, and E. Quataert, "The Heating of Test Particles in Numerical Simulations of Alfvénic Turbulence," Astrophys. J. **707**, 404 (2009).

[336] G. P. Zank and W. H. Matthaeus, "Waves and Turbulence in the Solar Wind," J. Geophys. Res. **97**, 17189 (1992).

[337] C.-Y. Tu and E. Marsch, "MHD Structures, Waves and Turbulence in the Solar Wind: Observations and Theories," Space Sci. Rev. **73**, 1 (1995).

[338] P. Veltri, "MHD Turbulence in the Solar Wind: Self-Similarity, Intermittency and Coherent Structures," Plasma Phys. Control. Fusion **41**, A787 (1999).

[339] D. Sundkvist, A. Retinò, A. Vaivads, and S. D. Bale, "Dissipation in Turbulent Plasma due to Reconnection in Thin Current Sheets," Phys. Rev. Lett. **99**, 025004 (2007).

[340] P. A. Davidson, *Turbulence in Rotating, Stratified and Electrically Conducting Fluids* (Cambridge University Press, New York, 2013).

[341] F. S. Godeferd and F. Moisy, "Structure and Dynamics of Rotating Turbulence: A Review of Recent Experimental and Numerical Results," Appl. Mech. Rev. **67**, 030802 (2015).

[342] D. Proment, S. Nazarenko, and M. Onorato, "Quantum Turbulence Cascades in the Gross-Pitaevskii Model," Phys. Rev. A **80**, 051603 (2009).

[343] N. Yokoyama and M. Takaoka, "Identification of a Separation Wave Number Between Weak and Strong Turbulence Spectra for a Vibrating Plate," Phys. Rev. E **89**, 012909 (2014).

[344] D. Sundkvist, V. Krasnoselskikh, P. K. Shukla, A. Vaivads, M. André, S. Buchert, and H. Réme, "*In Situ* Multi-Satellite Detection of Coherent Vortices as a Manifestation of Alfvénic Turbulence," Nature (London) **436**, 825 (2005).

[345] C. Salem, A. Mangeney, S. D. Bale, and P. Veltri, "Solar Wind Magnetohydrodynamics Turbulence: Anomalous Scaling and Role of Intermittency," Astrophys. J. **702**, 537 (2009).

[346] S. Lion, O. Alexandrova, and A. Zaslavsky, "Coherent Events and Spectral Shape at Ion Kinetic Scales in the Fast Solar Wind Turbulence," Astrophys. J. **824**, 47 (2016).

[347] M. Farge, "Wavelet Transforms and their Applications to Turbulence," Annu. Rev. Fluid Mech. **24**, 395 (1992).

[348] J. F. Kirby, "Which Wavelet Best Reproduces the Fourier Power Spectrum?" Comput. Geosci. **31**, 846 (2005).

[349] C. Torrence and G. P. Compo, "A Practical Guide to Wavelet Analysis," Bull. Am. Meteorol. Soc. **79**, 61 (1998).

[350] O. Alexandrova, V. Carbone, P. Veltri, and L. Sorriso-Valvo, "Small-Scale Energy Cascade of the Solar Wind Turbulence," Astrophys. J. **674**, 1153 (2008).

[351] A. Greco, P. Chuychai, W. H. Matthaeus, S. Servidio, and P. Dmitruk, "Intermittent MHD Structures and Classical Discontinuities," Geophys. Res. Lett. **35**, L19111 (2008).

[352] J. Ruppert-Felsot, M. Farge, and P. Petitjeans, "Wavelet Tools to Study Intermittency: Application to Vortex Bursting," J. Fluid Mech. **636**, 427 (2009).

[353] P. W. Terry and K. W. Smith, "Coherence and Intermittency of Electron Density in Small-Scale Interstellar Turbulence," Astrophys. J. **665**, 402 (2007).

[354] J. Shao and D. Tu, *The Jackknife and Bootstrap* (Springer, New York, 1995).

[355] A. Grinsted, J. C. Moore, and S. Jevrejeva, "Application of the Cross Wavelet Transform and Wavelet Coherence to Geophysical Time Series," Nonlin. Processes Geophys. **11**, 561 (2004).

[356] V. I. Petviashvili and O. A. Pokhotelov, *Solitary Waves in Plasmas and in the Atmosphere* (Gordon and Breach, New York, 1992).

[357] D. J. Wu and J. K. Chao, "Recent Progress in Nonlinear Kinetic Alfvén Waves," Nonlin. Processes Geophys. **11**, 631 (2004).

[358] J. L. Verniero, G. G. Howes, and K. G. Klein, "Nonlinear Energy Transfer and Current Sheet Development in Localized Alfvén Wavepacket Collisions in the Strong Turbulence Limit," J. Plasma Phys. **84**, 905840103 (2018).

[359] M. L. Stevens and J. C. Kasper, "A Scale-Free Analysis of Magnetic Holes at 1 AU," J. Geophys. Res. **112**, A05109 (2007).

[360] K. W. Smith and P. W. Terry, "Damping of Electron Density Structures and Implications for Interstellar Scintillation," Astrophys. J. **730**, 133 (2011).

[361] W. H. Matthaeus, A. Pouquet, P. D. Mininni, P. Dmitruk, and B. Breech, "Rapid Alignment of Velocity and Magnetic Field in Magnetohydrodynamic Turbulence," Phys. Rev. Lett. **100**, 085003 (2008).

[362] S. Servidio, M. Wan, W. H. Matthaeus, and V. Carbone, "Local Relaxation and Maximum Entropy in Two-Dimensional Turbulence," Phys. Fluids **22**, 125107 (2010).

[363] A. V. Pushkarev and W. J. T. Bos, "Depletion of Nonlinearity in Two-Dimensional Turbulence," Phys. Fluids **26**, 115102 (2014).

[364] S. R. Cranmer and A. A. van Ballegooijen, "Alfvénic Turbulence in the Extended Solar Corona: Kinetic Effects and Proton Heating," Astrophys. J. **594**, 573 (2003).

[365] D. A. Uzdensky and S. Rightley, "Plasma Physics of Extreme Astrophysical Environments," Rep. Prog. Phys. **77**, 036902 (2014).

[366] V. Roytershteyn, S. Boldyrev, G. L. Delzanno, C. H. K. Chen, D. Grošelj, and N. F. Loureiro, "Numerical Study of Inertial Kinetic-Alfvén Turbulence," Astrophys. J. (to be published), arXiv:1810.12428.

[367] K. Alvelius, "Random Forcing of Three-Dimensional Homogeneous Turbulence," Phys. Fluids **11**, 1880 (1999).

Acknowledgements

It is my pleasure to thank everyone who has supported me in various ways during my time as a PhD student. First, I would like to thank Frank Jenko for the guidance and support that I received during my PhD project. I am especially grateful that he has given me the opportunity to work on a very exciting and ambitious project, which involved many international collaborations with leading experts, as well as a long research stay at UCLA. Very special thanks go to Nuno Loureiro, who has been like a mentor to me and who has always provided me with incredibly stimulating and insightful feedback on my research. I also thank my advisor at the LMU, Hartmut Zohm, for his support in preparing this Thesis. Furthermore, I wish to thank Frank Tsung, Viktor Decyk, and Warren Mori for the many helpful discussions on particle-in-cell simulations during my stay at UCLA. Last but not least, I would like to acknowledge my numerous collaborators with whom it has been truly a pleasure to interact with. This includes, in particular, Alfred Mallet, Chris Chen, Silvio Cerri, Alejandro Bañón Navarro, Daniel Told, Chris Willmott, Francesco Califano, Kai Schneider, Ravi Samtaney, Vadim Roytershteyn, Patricio Muñoz, and Jörg Büchner. My PhD project would have been much less successful if I did not have the privilege to be involved in so many fruitful collaborations.

On a more personal note, I would like to kindly thank all my colleagues at IPP, with whom I have enjoyed spending time also outside of work. Many of them I consider as good friends. Finally, I am indebted to my relatives, especially my parents, who have always been incredibly supportive of my pursuit of science. Many thanks go also to my love Anja, who bore with me during the busy months of writing this Thesis.